

# UC Berkeley

## UC Berkeley Electronic Theses and Dissertations

### Title

Understanding Radiation Physics and Chemistry of Extreme Ultraviolet Resists

### Permalink

<https://escholarship.org/uc/item/2t16b8s0>

### Author

Ma, Jonathan Han Son

### Publication Date

2021

Peer reviewed|Thesis/dissertation

Understanding Radiation Physics and Chemistry of Extreme Ultraviolet Resists

By

Jonathan Hanson Ma

A dissertation submitted in partial sanctification of the

requirements for the degree of

Doctor of Philosophy

in

Physics

in the

Graduate Division

of the

University of California, Berkeley

Committee in charge:

Doctor Patrick Naulleau, Co-chair

Professor Naomi Ginsberg, Co-chair

Professor Andrew Neureuther

Professor Jeffery Neaton

Fall 2021



## Abstract

### Understanding Radiation Physics and Chemistry of Extreme Ultraviolet Resists

by

Jonathan Hanson Ma

Doctor of Philosophy in Physics

University of California, Berkeley

Doctor Patrick Naulleau, Co-chair

Professor Naomi Ginsberg, Co-chair

Extreme Ultraviolet Lithography (EUVL) has been introduced to meet the need for smaller feature sizes. EUVL imaging chemistry is revolutionary because of ionizing radiation is involved. Novel physical and chemical processes has made material development more akin to shooting in the dark. In this work, the author delineates the material challenge of EUV photo-sensitization at the molecular level, presents investigations in elucidating sensitization mechanisms and explores new possibilities. The author argues that chemical activation, which connects EUV photon absorption and generation of reactive species, is one of the main driver of resist performance. Three electron spectroscopy techniques are introduced and characterized to interrogate the electron cascade subsequent to photo-ionization. These experiments mainly answer questions about how reactive radical cations and slow electrons are generated. For example, the size of this cascade was found to be between 1 to 4 nanometers in various materials. Once the radical cations are cooled and the slow electrons have attached to electron acceptors, existing computational chemistry techniques are used to understand the subsequent generation of active species. Specifically, photo acid generators (PAG) and a prototypical organo-tin oxo cluster are studied in detail. This study revealed that the said organo-tin oxo cluster reacts to both ionization and electron attachment with similar chemical outcomes, thus partially explaining its superior performance. Manipulating dose by modifying interface dipole is also investigated. Finally, consolidating what he has learned along the way, the author discusses possibilities in EUV material engineering.



## ACKNOWLEDGEMENTS

It has been a long yet fruitful journey, one eventful enough to qualify itself as an adventure. Therefore I would like to acknowledge a few people.

To begin with, I would like to thank are my advisors Patrick Naulleau and Andy Neureuther. When I first saw Andy's "blurb" (in his exact wording) regarding an opening at the Center of X-ray Optics, I was already a couple of years into graduate school and, in colloquial terms, things did not quite work out. It was a gamble for me to essentially restart graduate school near the end of my fourth year and I assume it was a even bigger gamble for Patrick and Andy to take me in.

What followed were probably the most productive years of my life thus far. Through these years I have achieved so much more than I could have imagined. Had Patrick and Andy decided not to give me that opportunity, my life for sure would have been very different.

The trust and freedom that they have given me in my research have allowed me to push my limits. On top of that, their effective approach to research problems, where they always try to combine first-principal scientific thinking with the pragmatism of engineering, has profound and lasting influences on me and will serve a cornerstone of whatever I will achieve in the future.

This work would not have been possible without Gregory Wallraff. His knowledge in chemistry, material science, and lithography has been invaluable to say the least. Not only did he teach me almost all I know about resist chemistry, his experience, knowledge, candor, and intuition always point us to the right places. The breadth and depth of EUV resist chemistry is rather daunting but he always puts things in perspective and knows which battles to choose.

I would also like to thank Dr. James Blackwell for his support, especially for being a vocal advocate for rational mechanistic study. While our group was trying to bring the community towards more rational material design, his support came in as a boost of confidence, both for me personally and for our group as a whole.

My collaborators were also instrumental to my work. Rudy Wojtecki, Craig Needham and Sonia Castellanos were not at all stingy about sharing their knowledge and they all tried to be as open as possible with their research and they genuinely wanted me to succeed. It has also been a pleasure working and brainstorming ideas with Harvey MacKenzie and Dr Ian Manners.

Also, there are Luke and Stuart, my colleagues. The three of us all have rather different focuses. So they have filled me in with a lot of context. Moreover, they have been the perfect sounding boards for a lot of research ideas.

There have been numerous other people whom I have worked with at LBL. First of all, there is Isvar Cordova. He was like a big brother to me and Luke. He had helped me a lot with navigating the Advanced Light Source, both literally and metaphorically. Also, he is a pretty good devil's advocate and that made answering questions at conferences a lot easier. Having the full support from the beam line principal investigator is pivotal to doing research at the ALS. We definitely had

that from Cheng Wang and particularly Eric Guilickson, the “biggest scatter brain”.

The opportunity for my research would not have existed without the CXRO’s strong track record. So I would like to acknowledge everyone who has helped made it what it is today. In particular there are a few interesting encounters. The breadth of Warren Holcomb’s knowledge always surprises me. He knows how to keep things running and more importantly, from breaking down. Also he taught me about HSA accounts and never buying a used Honda Integra unless I know what I’m doing—they get stolen a lot! As our collaborations picked up momentum things got shipped a lot and Sara Lee has made it simpler than ever before. Thanks Sara. Seno has been around for quite a while and he knows every detail like account numbers and the fact that some of us at some point would need some decongestant drugs and he was more than happy to share his personal stash.

My computational work was made possible by David Prendergast, who provided us with the resources at the Molecular Foundry. His postdoc Han Wang has been helpful in bouncing ideas around. Like Isvar, he is often the devil’s advocate (Maybe it’s part of a post-doc researcher’s job requirements) yet that inadvertently galvanized my knowledge and instincts in quantum and computational chemistry.

I would like to thank my department advisor Naomi Ginsberg. She has been very supportive since the very beginning. Continuing exposure to her group’s research has consolidated my intuition in physical chemistry, which has turned out to be very beneficial over the years. I would also like to thank the rest of my qualifying exam committee, which includes professors Jeffrey Neaton and Ramamoorthy Ramesh, for providing me with valuable feedback in my qualification exam.

My long term roommates Kenneth Hung and Matthew Diamond were the best grad school buddies and I would like to thank them as well. As the “in-house” statistician, Kenneth has given me numerous crash courses on statistics and data analysis. Matthew is the guy who always has interesting ideas when it comes to food, music and TV shows. In grad school where creativity matters, that is definitely a plus.

Last but not the least I would like to thank my parents who have been supportive in this endeavor no matter what.

Date: 11/25/2021

**Jonathan Ma**

## TABLE OF CONTENTS

<b>ABSTRACT</b>	1
<b>ACKNOWLEDGEMENT</b>	i
<b>LIST OF FIGURES</b>	viii
<b>LIST OF TABLES</b>	xi
<b>1 Introduction</b>	<b>1</b>
1.1 Preface	1
1.2 Motivation and Context	2
1.2.1 Extreme Ultraviolet Lithography and photo resist	2
1.2.2 New challenges facing EUV resists	2
1.3 EUV resist chemistry and chemical activation	3
1.3.1 Resist chemistry	3
1.3.2 EUV specific challenges on resist chemistry	4
1.3.3 Chemical Activation as the Subject of this study	5
<b>2 Electron Driven Radiation Chemistry in EUV</b>	<b>7</b>
2.1 Radiation Chemistry in EUV	7
2.1.1 Primary photoionization	7
2.1.2 Secondary Electron Cascade	8
2.1.3 Generation of reactive species	12
2.1.4 Electron capture	13
2.1.5 The key challenges	14
2.1.6 Relevance of e-beam resist	15
2.2 Structure of the thesis	15

<b>3</b>	<b>Experimental Investigation of Electron Processes</b>	<b>17</b>
3.1	Introduction . . . . .	17
3.2	Condensed Phase Photoemission . . . . .	17
3.2.1	Background . . . . .	17
3.2.2	Experimental Setup . . . . .	18
3.2.3	Photoemission measurements . . . . .	19
3.3	Total Electron Yield Experiment . . . . .	23
3.3.1	Experimental Setup . . . . .	23
3.3.2	Data processing . . . . .	23
3.3.3	Charging . . . . .	24
3.3.4	Data interpretation . . . . .	24
3.3.5	Time dependence of TEY and Fitting model . . . . .	25
3.3.6	The rising component, electron capture, and implications for EUV molecular engineering . . . . .	26
3.4	Electron Attenuation Length Experiment . . . . .	27
3.4.1	Background . . . . .	27
3.4.2	Experimental Setup . . . . .	28
3.4.3	Experimental Results . . . . .	31
3.4.4	Relevance EUV Lithography . . . . .	34
3.4.5	Direction for Development—Energy Resolution . . . . .	36
3.5	Combining TEY, EAL and EUV absorption measurements . . . . .	37
<b>4</b>	<b>Inferring Internal Electron Energy Spectrum with Monte Carlo Electron Trajectory Simulation</b>	<b>39</b>
4.1	Background . . . . .	39
4.2	Monte Carlo Electron Trajectory Simulation—An Overview . . . . .	39
4.3	The Monte Carlo Scheme . . . . .	40
4.4	Scattering Mechanisms . . . . .	42
4.4.1	Electron-nuclei elastic scattering . . . . .	42
4.4.2	Dielectric model . . . . .	43

4.4.3	Phonon/vibrational scattering . . . . .	48
4.4.4	Electron capture . . . . .	48
4.4.5	Scattering mechanisms used in this study . . . . .	48
4.5	Model setup and results . . . . .	49
4.6	Correlation Adjusted Mean Free Path Approach . . . . .	50
4.7	Results . . . . .	51
<b>5</b>	<b>Photo Acid Generators in EUV</b>	<b>53</b>
5.1	Introduction . . . . .	53
5.2	Electron Attachment . . . . .	54
5.3	Ab-Initio Molecular Dynamics of Photo Acid Generators . . . . .	59
5.3.1	Internal Excitation . . . . .	59
5.3.2	Electron Attachment . . . . .	61
5.3.3	Reactions after S-C bond cleavage . . . . .	62
5.4	Relative Importance between Internal Excitation and Electron Attachment . . . . .	63
5.4.1	Existing Experimental Investigations . . . . .	63
5.4.2	Reports on DUV insensitive EUV PAGs . . . . .	63
5.4.3	Possible Causes for Low DUV sensitivity . . . . .	64
5.4.4	Failure mode 1—Optical Absorption . . . . .	65
5.4.5	Failure mode 2—Fragmentation Dynamics . . . . .	66
5.4.6	Limitations of the Current Molecular Dynamics Computation Scheme . . . . .	67
5.5	Assessing the Accuracy of Molecular Dynamics Simulation Using Spin Flip Methods	68
5.6	Between PAG activation and acid generation . . . . .	71
5.6.1	The independent mechanism . . . . .	72
5.6.2	Rendezvous Mechanisms . . . . .	73
5.6.3	The Two Rendezvous Mechanisms . . . . .	76
5.6.4	Unmediated Deprotonation in Last Minute Rendezvous . . . . .	77
5.6.5	Mediated Deprotonation—Rendezvous-Relay Mechanism . . . . .	80
5.6.6	Summary and Prospects on Deprotonation . . . . .	80
<b>6</b>	<b>Mechanistic Advantages of Organometallic Resists</b>	<b>83</b>

6.1	Introduction . . . . .	83
6.2	Computation Methodology . . . . .	85
6.3	Origin of Sensitivity . . . . .	86
6.3.1	Overview . . . . .	86
6.3.2	One electron redox . . . . .	88
6.3.3	Tin-Carbon Thermal Chemistry . . . . .	91
6.3.4	Proton transfer . . . . .	92
6.4	Tin-Carbon Chemistry—Complex Environments and Formulation Considerations . . . . .	95
6.4.1	Ionic dissociation . . . . .	95
6.4.2	Ethyl substitution . . . . .	99
6.4.3	Dielectric medium . . . . .	101
6.5	Conclusion . . . . .	102
<b>7</b>	<b>Recording Materials Interface EUV Sensitivity Engineering with Self Assembled Monolayers</b>	<b>104</b>
7.1	Introduction . . . . .	104
7.2	Origin of Head Group Sensitivity—the Hypothesis . . . . .	106
7.2.1	The Elusive Head Group Dependence . . . . .	106
7.2.2	Interface Dipole Moment, Work Function and Electron Transmission . . . . .	106
7.3	Divide and Conquer . . . . .	108
7.4	SAM-SAM interaction . . . . .	109
7.5	Tilt Dependence of Interface Work function . . . . .	112
7.5.1	Substrates and Computational Method . . . . .	112
7.5.2	Binding Site and Acid Base Reaction . . . . .	113
7.5.3	Tilt dependence . . . . .	115
7.5.4	Evaluating work function shift . . . . .	117
7.6	Results . . . . .	118
7.6.1	Unsubstituted Hydroxamic Acid . . . . .	118
7.6.2	Methyl Hydroxamic Acid . . . . .	119
7.7	Additional Discussion . . . . .	121

7.7.1	Substrate Matters—Comparison with Copper Substrate . . . . .	121
7.7.2	Additional Knobs . . . . .	122
<b>8</b>	<b>Ongoing Endeavors—Ferrocene Based Resists</b>	<b>123</b>
8.1	Charge transfer nature . . . . .	123
8.2	Polyferrocene . . . . .	127
8.3	Additional Contrast Handles . . . . .	128
8.4	Spontaneous scission . . . . .	129
8.5	Mediated Scission . . . . .	131
8.5.1	Anion Attack . . . . .	133
8.5.2	Radical Attack . . . . .	135
8.5.3	Anion Attack after radical attack . . . . .	136
8.6	Lingering Questions . . . . .	137
8.6.1	Can Polyferrocene be an Electron Acceptor . . . . .	137
8.6.2	Where does Spontaneous Scission Stand? . . . . .	138
8.7	Summary . . . . .	138
<b>9</b>	<b>Prospects</b>	<b>139</b>
	<b>REFERENCES</b> . . . . .	<b>144</b>
	<b>LIST OF PUBLICATIONS</b> . . . . .	<b>166</b>

## LIST OF FIGURES

3.1	Photoemission Spectrometry Schematic . . . . .	18
3.2	Photoemission Spectrometer Setup . . . . .	19
3.3	PES spectrum of a photo resist . . . . .	20
3.4	Tougarrrd Scattering Background . . . . .	21
3.5	Recovery of Primary Electron Spectrum . . . . .	21
3.6	Underlayer injection . . . . .	22
3.7	PES spectra of underlayers . . . . .	22
3.8	Experimental setup of TEY . . . . .	23
3.9	TEY traces of various polymers . . . . .	26
3.10	EAL overlayer technique . . . . .	29
3.11	Electrical Scheme of EAL experiment . . . . .	30
3.12	X-ray photoelectron spectra . . . . .	33
3.13	Electron Attenuation Length Data . . . . .	35
4.1	Monte-Carlo trajectory simulation scheme . . . . .	41
4.2	Schematic of the electron Monte Carlo simulation . . . . .	49
4.3	Scattering mean free path . . . . .	50
4.4	Scattering correlation . . . . .	51
4.5	Efficacy of correlation adjusted scattering mean free path . . . . .	52
5.1	Assessment of predictive power of a single functional/basis combination . . . . .	55
5.2	Predictive powers of different functional/basis combination . . . . .	56
5.3	PAGs investigated . . . . .	57
5.4	Computational vertical electron affinity of four onium PAG cations . . . . .	58
5.5	Computational vertical electron affinities versus dose to clear . . . . .	59



5.6	Results for internal excitation AIMD calculations. . . . .	61
5.7	The distributions of bond lengths before and after AIMD simulations initiated with electron attachment at ground state. . . . .	62
5.8	EUV vs DUV excitation . . . . .	64
5.9	Possible DUV failure modes . . . . .	65
5.10	Optical absorption spectra computed with TDDFT . . . . .	66
5.11	Fragmentation yield from AIMD computations . . . . .	66
5.12	Potential energy surfaces computed with TDDFT . . . . .	69
5.13	Potential energy surfaces computed with SF-TDDFT . . . . .	70
5.14	Deprotonation energy of PS and PHS monomers in vacuum or media . . . . .	79
5.15	Proton solvation energy of a prototypical amide trimer . . . . .	82
6.1	The structure of $\text{Sn}_{12}\text{Me}_{12}(\text{OH})_2$ . . . . .	85
6.2	reaction free energies for $\text{Sn}_{12}\text{Me}_{12}(\text{OH})_2$ . . . . .	87
6.3	Frontier Orbitals of $[(\text{Me}-\text{Sn})_{12}\text{O}_{14}(\text{OH})_6](\text{CHO}_2)_2$ . . . . .	89
6.4	$\text{Sn}_{12}\text{Me}_{12}\text{A}_2$ clusters at various degrees of cage deprotonation . . . . .	93
6.5	First and second ionic dissociation energies of the cluster with the hydroxide anion. . . . .	95
6.6	Reaction free energies for $[\text{Sn}_{12}\text{Me}_{12}]^{2+}$ . . . . .	96
6.7	Structure of $[\text{Sn}_{12}\text{Me}_{12}\text{OH}]^+$ . . . . .	97
6.8	Reaction free energies for $[\text{Sn}_{12}\text{Me}_{12}\text{OH}]^+$ . . . . .	98
6.9	Summary . . . . .	102
7.1	EUV absorption estimates of self assembled monolayers . . . . .	107
7.2	Dipole moments of various head groups . . . . .	108
7.3	Angle resolved NEXAFS spec of hydroxamic acid SAMs on metal oxide surfaces . . . . .	109
7.4	Energy of free standing unsubstituted hydroxamic acid . . . . .	110
7.5	Energy of free standing methyl hydroxamic acid . . . . .	111
7.6	A schematic of the tilt dependence geometry computation . . . . .	117
7.7	Work function shift extraction . . . . .	118
7.8	Tilt dependence of work function-unsubstituted hydroxamic acid . . . . .	119
7.9	Tilt dependence of work function-methyl hydroxamic acid . . . . .	120
7.10	Resonance structures of deprotonated hydroxamic acid . . . . .	120

8.1	Optical absorption spectrum of TPS-Tf . . . . .	125
8.2	Frontier orbitals of TPS-Tf . . . . .	126
8.3	Structure of poly(ferrocenylsilane) . . . . .	128
8.4	Structure of prototypical PFS monomer . . . . .	129
8.5	Bond dissociation energies of the ethyl-ferrocenylsilane monomer . . . . .	130
8.6	Bond dissociation energies of the dimethylamino-ferrocenylsilane monomer . . . .	130
8.7	Bond dissociation energies of the trimethylstannyl-ferrocenylsilane monomer . . .	131
8.8	Bond dissociation energies of the trimethylstannyl-ferrocenylsilane monomer . . .	132
8.9	Reaction profile of Cl <sup>-</sup> substitution . . . . .	134
8.10	Reaction profile of radical substitution . . . . .	135
8.11	Reaction profile of radical substitution . . . . .	137

## LIST OF TABLES

3.1	Photo-absorption cross-section of carbon, oxygen, hydrogen, and silicon at photon energies of 92 eV and 200 eV. . . . .	31
3.2	Absorption cross-sections of PHS and PMMA, as well as fractions of absorbed radiation by 30 nm film of these materials at photon energies of 92 eV and 200 eV.	31
5.1	Parameters for linear model between experiments and DFT for various functionals. The linear model is $Experiment = m \times E(DFT) + C$ . The coefficients of correlation and root mean square error are also included. . . . .	57
5.2	Energetics of independent mechanism . . . . .	73
5.3	Total reaction energy of the two rendezvous mechanisms . . . . .	77
5.4	Protonation energy of monomers . . . . .	78
5.5	Phenyl affinity and deprotonation energy in mediated deprotonation . . . . .	81
6.1	Homolysis energy of Sn-C bond Upon Ethyl Substitution . . . . .	99
6.2	Homolysis energy of Sn-C bond upon immersion in dielectric . . . . .	101
7.1	Hubbard parameters for DFT + U calculations . . . . .	113
7.2	Binding geometries of hydroxamic acid on a copper(I) oxide surface . . . . .	114
7.3	Binding geometries of dissociated hydroxamic acid on a copper(I) oxide surface . .	116

## CHAPTER 1

### Introduction

#### 1.1 Preface

The demand for higher computing throughput has been steadily rising for decades. That has put the semiconductor industry in the highest gear since its conception. The constant advancement in computing technology has in return enabled new applications that drive even higher demands. For example, without the exponential increase in computation power, recent emergence of artificial intelligence and big-data analytics would not have been possible.

The aforementioned exponential growth is not a figure of speech. The well-known “Moore’s Law” summarizes the observation that the number of transistors in computing circuits doubles every two years—indeed an exponential progression. In other words, to keep the physical size of chips reasonable, the circuit components have to shrink accordingly in an exponential manner. In this everlasting quest for miniaturization, technological challenges have emerged, and will emerge one after another. To overcome these hurdles, numerous ingenious solutions originated in basic research, such as high-k dielectric and fin-FET (Field Effect Transistor), have been commandeered.

At the present, Extreme Ultraviolet (EUV, 92 eV  $\sim$  13.5 nm) lithography is the state-of-the-art imaging process. Like its predecessors, it is an optical projection imaging technique, but the similarities end here. To go a step beyond Deep-UV (DUV, 193 nm  $\sim$  6.4 eV), ionizing radiation is inevitable. The introduction of EUV created a collections of obstacles, all at once. For example, new materials for optical elements had to be invented and special pulsing sequence is needed to make the light sources economical.

After years of hard work, EUV lithography has finally entered high volume manufacturing (HVM). At this very juncture, as a consensus in past few industry conferences, EUV photoresist is in the spotlight as the biggest challenge. The first chapter of this thesis would first provide a brief introduction to photoresist development and EUV lithography, providing a context for understanding why photoresist has become the new roadblock in EUV. Then, the author proceeds to explain how and why the problem has been narrowed down to its present scope.

## 1.2 Motivation and Context

### 1.2.1 Extreme Ultraviolet Lithography and photo resist

As feature size keeps shrinking, as long as a projection optics are used for imaging, source wavelength has to shrink accordingly. For a given wavelength, the resolution limit of single patterning is governed by the Rayleigh's equation (where  $\lambda$ , NA, R, and  $k_1$  are wavelength, numerical aperture, resolution and a process parameter)

$$R \leq k_1 \frac{\lambda}{NA} \quad (1.1)$$

With single patterning, for line-space patterns,  $k_1$  is lower bounded by the laws of physics at 0.5. Prior to the introduction of EUV, DUV photos (6.4 eV, 193 nm) were used. To circumvent this physical constrains, multiple patterning has been adopted. Such 'stop-gap' tactics did not exist in the transition from 254 nm (Kr-F excimer light source) to 193 nm (Ar-F excimer) and that hints on the enormity and multifaceted nature of the challenge of EUV.

To take a reasonable step up from 6.4 eV, the photon energy would very likely be above the ionization energies of almost all matters (8 ~ 10 eV) and that has brought in a multitude of problems. Plasma is produced, thus the use of transmission optics became impossible. Reflective optics are used and they are less flexible in terms of configuration and material choice. Also, an economical light source was not easy to identify. The combination of reflective optics and light source has left very few practical options and 92 eV was the best compromise. The stark increase in photon energy, coupled with the shrinking of features, also post novel challenges for photoresists.

### 1.2.2 New challenges facing EUV resists

In a nutshell, if the imaging system is a camera, photoresist is the 'negative' where it literally transforms information encoded in the aerial image into chemical changes which causes change in solubility. Therefore, once can eventually produce a mechanical mask by developing the exposed (and post-processed) resist film in solvents.

To print smaller features, a better understanding of microscopic and nano scale processes involved in the chemistry is needed to better control and engineer them. Moreover, the use of EUV radiation results in a few unique challenges. Firstly, the exposure chemistry is very different. In other words, how energy in the photons is transformed into a chemical image is different. In fact, the intermediate species and the their generation has been shown to differ a lot from DUV. More importantly, in DUV, dissolution switch is initiated by photochemistry. Together with subsequent processes, DUV photochemistry is well understood and optimized after decades of work. On the other hand, because of the ionizing nature of EUV, chemistry is not initiated by photo-excitation. Instead, ionization and electron attachment are responsible. Consequentially, there are still a lot of

unknowns in the EUV exposure chemistry, making rational design and engineering rather difficult.

Secondly, EUV photons are expensive and energy intensive. Subsequently, with the same optical power, for the same feature, the number of photons is reduced by a factor of 6. Since photons are quantized, stochastic effects become more prominent and would statistically result in failure. The stochastic problem can be alleviated by sacrificing resolution or increasing dose. Indeed, resolution, stochasticity (line edge roughness) and sensitivity (RLS) are shown to be in 3-way trade-off in photoresists [1, 2]. That presents a dilemma—increase in dose undermines the business case of EUV and letting go of resolution defeats the purpose of EUV.

Fortunately, incremental gains on this trade-off have been made on all fronts, and more in-depth investigations revealed EUV specific handles such as combating the trade-off with high quantum efficiency. As it would be explained in more details, quantum efficiency is part of the exposure chemistry and that reiterates the importance of understanding the novel exposure chemistry.

### 1.3 EUV resist chemistry and chemical activation

#### 1.3.1 Resist chemistry

To illustrate the challenges that EUV lithography posts on photoresists in context, we use Chemically Amplified Resists (CAR), the industry workhorse for the past three decades that is also currently in use in EUV, as a reference.

In essence, a CAR has at least two components, namely the photo acid generators (PAG) and the non-polar protection groups. In the simplest form, the chemistry of CARs can be summarized with the following sequence

- I Absorption of photon
- II The energy of the photon is converted into chemical changes. In CAR, that corresponds to the photo acid generator molecule reaching an unstable or excited state.
- III The unstable PAG molecule, with or without reacting with the matrix (in its immediate vicinity), produces a super-acid
- IV The resist film is baked. At elevated temperatures, the photo acids diffuse more rapidly.
- V Upon contact with a protection group, the photo acid reacts with it.
- VI As a result of the reaction, the non-polar protection group is converted into a polar group and the acid is released back to the matrix, making this reaction catalytic.
- VII The two previous steps happen persistently at baking temperature.

VIII Exposure leads to an increase in polarity. As a result, the resist can now be developed using polar solvents (most commonly Trimethylammonium hydroxide, TMAH)

The above sequence can be divided into two groups. Steps I to III belong to Chemical activation where a chemically reactive species is born. Steps IV to VI are parts of the subsequent Physio-chemical propagation. The sequence is divided into these two subsets because the introduction of EUV has very different implications on them.

### 1.3.2 EUV specific challenges on resist chemistry

**Chemical Activation in DUV and EUV are entirely different.** In DUV, since the photon is not ionizing, photochemistry is solely responsible for activation. Photochemistry is relatively well-known and specific, making rational design possible. The optical absorption spectrum of a compound is a function of the electronic structure of the molecule. A multitude of First-Principles computational chemistry techniques can predict the excited state energies and transition probabilities making identifying molecules with desirable optical properties a tractable problem (For example, Casida TDDFT is a well documented method [3]). Moreover, due to the non-ionizing nature of DUV, transparent materials still exist and again, can be identified and investigated with first-principles techniques. By using a PAG targeting DUV wavelength and a matrix made of polymers that are transparent to DUV, photons are absorbed specifically by PAG molecules. Moreover, the PAG can be engineered to be very unstable upon excitation to maximize the likelihood of chemical reactions [4].

With such formulation, a few goals are achieved. Firstly, it is possible to make the PAG the only DUV absorbing species (Note that sensitizers, which absorbs photons and transfers energy to the PAG, can be added to the polymer, providing a extra handle [4]. Such resonance transfer is intended to produce minimal loss (to the quantum efficiency), thus the photon to chemistry conversion still happens at the PAG.). With such clear division of labor, optimizing the quantum efficiency—number of acids generated from a photon absorption, is relatively straight forward. The author cautions that, although conceptually the quantum efficiency in DUV should be equal to or less than 1, in some cases it was observed to go above 1 (see table 1 in [5]). The ratio between acid and absorbed DUV photon can be computed by dividing forth column with the fifth. Amongst all polymers tested, poly(para-vinylanisole), PVA resembles the common backbone poly(hydroxylstyrene), PHS the most. The quantum efficiency was measured (inferring from table 1 in [5]) to be between 0.76 and 0.88). Secondly, the matrix can be made irrelevant in the discussion of chemical activation, reducing the complexity of the problem and more importantly, allowing greater freedom to optimize other aspects of the resist's performance, such as dissolution properties or etch resistance.

In EUV, as ionizing radiation is used, all molecular components contribute to photon absorption. Moreover, with details to be explained in chapter 2, photo-ionization and subsequent impact ionization take place, resulting in a cascade of slow electrons and ionized molecules as the end result. In the process, some molecules could be promoted into highly excited states. Such states, often results in self-ionization, are relatively short lived compared to chemical reaction time scales [6]. In the end, chemistry is likely to triggered by low lying excited states resulting from impact ionization or electron attachment. Indeed, in later chapters, it will be demonstrated that upon ionization or electron attachment, some molecules are capable of triggering chemistry even at the electronic ground state.

From photon absorption to chemical activation, there are two major differences between DUV and EUV. Firstly, while the entire process only involves the PAG molecule at DUV, at EUV the entire material matrix takes part in the process. Secondly, DUV chemical activation is localized at the PAG. At EUV, however, the slow electron cascade spreads over space and the process is less localized.

**The miniaturization of features also brings forth new demands for what happens after chemical activation.** While understanding chemical activation can lead to higher quantum efficiency, that is only part of the puzzle. There is a spatial component in the chemical activation of EUV. As of now, its length scale is understood to be less than the proceeding processes.

As feature size decrease, a few factors become more important. Firstly, as the number of photos per feature decreases, stochastic noise become a bigger problem. Secondly, as feature sizes approach the length scale of physio chemical processes, how these processes affect contrast and failure rate is under tighter scrutiny. The interplay between stochastics and these processes has been a frontier of research and creative solutions such as photo decomposable base [7] have been investigated to tackle this challenge.

### 1.3.3 Chemical Activation as the Subject of this study

Very different approaches are required for studying chemical activation and the following physio-chemical processes. For example, if one is to study chemical activation with computation chemistry, accurate descriptions of the electronic structures of the molecules are needed. For example, to study the effect of ionization or electron attachment on bond strength, first-principles methods are available and necessary. First principles approaches explicitly solve for the electronic structure of the molecule. Some first principle methods, such as the coupled cluster (CC) method, attempt to approximate the full many body wave function. There are also faster methods and uses only a single Slater determinant (instead of an expansion of Slater determinants as in CC or multi-reference methods) and they include Hartree-Fock (HF) and density functional theory (DFT). In any case,



single or multi determinant, these methods explicitly account for the interaction between all electrons and nuclei more or less from first principles, giving them reasonable predictive power [8]. However, even the best scaling variant of DFT computations still scale as the cube of the number of atoms so studying tens of thousands of atoms would not be efficient. This is acceptable for the investigation of chemical activation. While the slow electron cascade spreads across a range of nano-meters, all the sub-processes, including absorption, ionization, single electron scattering event, and electron attachment can be treated as molecular processes. For chemical activation investigations, what ultimately matters is the molecular changes that would initiate further reactions, such as the generation of acid in CARs. With that in mind, methods with accurate molecular descriptions is preferred over those which sacrifices molecular description in exchange for the ability to handle large systems.

On the other hand, to understand how the subsequent physio-chemical processes affect imaging outcome, one must cover a relatively huge volume (enclosing more than 100,000 atoms) to understand the collective behavior of these reactions and how they eventually impact imaging. The emergence of stochastics put a even higher demand on throughput as stochastic initial conditions are needed. To computationally understand these problems, results from single molecule studies are abstracted into parameters in more abstract molecular dynamics (MD) or even coarse graining (CG) methods to allow for higher throughput. In molecular dynamics simulations, electrons are not explicitly modeled and the interaction between atoms (inter-nuclei repulsion and electron mediated attraction alike) are modeled by force fields. The force fields are very specific to an atom's surroundings. The same bond in a different molecule can be parameterized differently. Prior knowledge or assumptions about the molecular structure is needed for parametrization. The abstract nature of MD force field implies limited extrapolation capacity. In other words, the accuracy of MD and CG is questionable if the system has atoms or features that don't exist in the pool of molecules used for the particular force field's parametrization. MD and CG are therefore not good for exploring chemical activation where molecules are expected to fracture into radicals or ions that are treated as unknowns. Further abstraction which replaces atomistic description with finite volume density field is possible and has provided valuable insight into the physio-chemical processes and their implications on the RLS trade-off [2, 7]

With the goals and methodologies in studying the two categories of reactions so vastly different, this thesis investigates on the former, which is the more molecular focused chemical activation in EUV resists.

The investigation of chemical activation, in a practical sense, would aid the improvement of quantum efficiency, which is a key driver in the RLS trade-off [1, 2].

## CHAPTER 2

### Electron Driven Radiation Chemistry in EUV

As the initiation of chemistry is the subject of this thesis, it would only be sensible to take a deep dive into the radiation chemistry in EUV materials. The relative novelty of EUV related physical processes presents numerous research opportunities. In some cases, the community is faced with ‘unknown unknowns’, a situation where even delineating and formulating a research problem is a challenge. The author would therefore go through the EUV radiation chemical processes with sufficient contextual information and describe the current status of relevant research. Not all research questions can be answered at once. To make the best use of time and effort, specific problems are selected for how viable it is to investigate them with existing techniques.

#### 2.1 Radiation Chemistry in EUV

A huge body of literature has been dedicated to understanding the radiation chemistry of EUV. From the absorption of EUV photons to the creation of acid (in Chemically Amplified Resists, CARs), there are roughly four stages.

##### 2.1.1 Primary photoionization

Firstly, an EUV photon is absorbed. Given the energy of a EUV photon (92 eV), photo ionization, where a primary electron is ejected, is considered to be the most likely outcome. Depending on the material, the energy and absorption cross-section have varying sensitivity to chemistry. For systems utilizing d electrons, such as halogen and metal containing resists, the d-orbitals responsible for EUV absorption are not hybridized. In that case, the chemistry does not affect the absorption cross-section and primary electron energy. In organic systems, as will be demonstrated in later chapters, the primary electrons are coming mostly from valence states, which are actively involved in chemical bonding. However, there has been no reports suggesting EUV absorption cross section can be manipulated by altering chemical bonding. Instead, fluorination has shown to be a driver of EUV absorption cross-section in organic resists. Moreover, the quantity of fluorine linearly predicts the EUV cross-sections. Since fluorine atoms are known to have a high EUV absorption, from

an empirical point of view, EUV absorption cross-section is known to be mostly atomic, agnostic of chemical bonding and coordination.

The kinetic energy of the electron, by the laws of energy conservation, is 92 eV minus the binding energy of the electron. In any given molecule, there are multiple orbitals and therefore multiple electrons that can absorb an EUV photon. The cross-sections of each electron are different and is proportional to the magnitude square of the dipole transition matrix element. Indeed orbital geometry and the delay onset of optical absorption of elements such as iodine is responsible for its high absorption[6].

None the less, due to the aforementioned atomic nature of EUV absorption, measurements and computations performed on different compounds can be compared directly. Therefore accurate and reliable atomic absorption cross-section data exists. The other piece of the puzzle is the kinetic energy of the primary electron. It has been demonstrated that the computation of binding energy would yield predictions with an accuracy of 2 eV [9].

When the electron is photoionized from a semi-core orbital such as the d orbitals of iodine and tin, or the  $2a_1$  orbital of water[10], the molecule possesses excess energy after ionization and is likely to relax by having a valence electron falling back into the semi-core orbital and ejecting another valence electron simultaneously, a process known as Auger emission, resulting in a double cation. The strong electrostatic energy in the doubly ionized molecule would result in fragmentation.

Theoretical models for Auger emission life time has been derived from time dependent perturbation theory [11, 12]. In another theoretical study, the Auger process is shown to overtake thermal cooling/dissociation when the photo electron is originally deeper than 20 eV. The evaluation of Auger life time requires the full description of the basis functions and canonical orbitals, which is not easily accessible when commercial packages such as Q-Chem or Gaussian are used.

In terms of exposure chemistry, the end result of photoionization and subsequent Auger emission are one or two ‘hole electron pair’. In other works, one or two hot electrons are ejected leaving behind the same number of positively charged species. Kozawa suggested that these species are responsible for creating the proton for the acid in CARs[13]. Since the EUV photon to acid conversion ratio was found to be around 5 [13, 14], with the exception of semi-core electron rich systems, the primary ionization event is not as important as the subsequent impact ionization events.

### 2.1.2 Secondary Electron Cascade

Secondly, there is an cascade of secondary electrons subsequent to the ejection of the primary electron.

With a kinetic energy less than 92 eV, the primary electron has a small scattering mean free path in any condensed phase materials and is likely to scatter with molecules in the thin film.

Upon a collision, the outcome is incident energy dependent. Above 20 eV, impact ionization is the most likely outcome [15, 16]. As a result, the incident electron loses energy and another electron is ejected, leaving behind another ionized molecule. Below 20 eV, other processes, such as dissociative electron attachment, plasmon trapping and vibrational excitation would come into play. Unlike predicting EUV absorption, investigating the scattering cross-section of electrons are more convoluted because of electron-molecule interactions are more complicated. In the context of EUV photoresists, there are two major questions.

1. Energetics—how much energy is deposited upon a scattering event? And where has that energy gone?
2. Electron blur—the electrons propagates between scattering events until they are trapped or absorbed. How far does it travel? Do the electrons scatter isotropically?

Conceptually, if one can obtain the energy resolved energy loss differential scattering cross-section at all incident electron energies, one can simulate the probabilistic scattering of electron with a Monte-Carlo trajectory model and answer all the above questions.

$$\sigma(E_{\text{ini}}; E_{\text{Loss}}, \Omega) = \int_0^{E_{\text{ini}}} dE_{\text{Loss}} \int d\Omega \underbrace{\frac{d\sigma}{dE_{\text{Loss}}d\Omega}(E_{\text{ini}}, E_{\text{Loss}}, \Omega)}_{E_{\text{ini}}, E_{\text{Loss}} \text{ resolved differential cross-section}} \quad (2.1)$$

where

$E_{\text{ini}}$  is the initial energy of incident electron

$E_{\text{Loss}}$  is the energy loss by the incident electron

$\Omega$  is the scattering angle (usually expressed in  $\theta$  and  $\phi$ )

Equation 2.1 does not address what happens to the molecule upon the scattering of an electron. In reality, there are multiple physical mechanisms, such as impact ionization and internal excitation, responsible for electron scattering. They all have different outcomes and distinctly different scattering cross-sections. Hypothetically, if one knows the differential cross sections for all the mechanisms, one can use the (angle and energy loss integrated) cross-sections to determine the likelihood of different outcomes.

The deduction of differential cross sections, and how they are incorporated into an electron model is rather technical and will be discussed in later chapters. The author will proceed to provide a qualitative overview of dominant scattering mechanisms and how they are being investigated

As mentioned, when an electron has more than 20 eV, the dominant energy loss mechanism is impact ionization, where part of the incident electron's energy is used to ionize the target molecule.

A secondary electron is created and the incident electron continues its journey. A positively charged molecule is left behind [17] and, upon proper formulation, is hypothesized to contribute to acid production [13].

Below 20 eV internal excitation, where the incident electron loses energy to promote the target molecule into an excited state, becomes more important [14]. Yet the absolute efficacy of internal excitation in EUV radiation chemistry is not a closed case and there will be more detailed discussion in later chapters.

When the electron energy falls to a few eV ‘scattering’ mechanisms that arrest the electron’s motion would come into play. These mechanisms include dissociative electron attachment, where a molecule absorbs a slow electron and becomes unstable and spontaneously breaks apart. The electron attachment of the cation in onium PAGs is hypothesized to result in acid generation [13].

Between inelastic events (where energy is lost) there is also elastic scattering, which would affect the electron blur.

The above electron-matter interactions are rather non-discriminative compared to DUV. For example, by avoiding conjugating monomers in the polymer matrix, almost no 193nm photons are absorbed by the polymer. In EUV, electron-matter interaction dominates. Even though some materials, such as fluorinated polymers are more likely to scatter electrons, their non-fluorinated siblings still have cross-sections at the same order of magnitude [18, 19]. Therefore, the strategy to single out a component by engineering an inert background, one that worked fabulously in DUV, is not applicable to electron scattering in EUV.

To further complicate the problem, unless the electron is absorbed, the post-scattering direction of the electron would ultimately affect the spread of the electron cascade, which is also known as the electron blur. In light of that, accurate understanding of the differential (angular) scattering cross-section mentioned is needed.

Experimentally the scattering cross-sections can be experimentally measured. Indeed, there is a plethora of measurements of the full differential scattering cross-section (with incident energy, energy loss, and scattering angle dependence), but most of these measurements are done in the gas phase on small molecules. For accurate measurement of scattering the cross-section of a condensed film, sample thickness should at most be comparable to the scattering mean free path to ensure that in most cases only a single scattering event takes place. That requires the use of free standing films with a thickness of a few nanometers or less. That however presents a catch-22 situation—the very thickness of these films, or lack thereof, make them inaccurate proxies for properties of their thicker ( $\sim 20$  nm) siblings. Besides, there hasn’t been any reports on electron scattering experiments on free standing polymeric material with such thicknesses. In reality, the scattering mean free paths are inferred indirectly from other experiments.

Theoretical prediction of energy resolved differential scattering cross-section has also proved

to be difficult, especially when the electron energies are below 80 eV [16]. Below 80 eV, electron scattering becomes more molecular in nature [20]. It has been reported that by subtracting the overlapping contributions of atomic electron scattering cross-sections, these cross-sections are reliable down to 40 eV (the independent-atom-model-screening-corrected additivity rule, IAM-SCAR, method [21, 22]). Below 40 eV, molecular resonances start coming into play, necessitating more explicit description of the electronic structure of the molecule. The IAM-SCAR has demonstrated considerable success with investigating the scattering of positron in liquid water[23]. In a broader context, such models, especially when applied to condensed phase systems, suffer from the lack of experimental verification due to the immense challenges facing the experimentalists.

First principles methods has been developed. In these schemes, the target molecule's electronic structures and excited states are computed using wave-function based methods such as configuration interactions (CI) and complete active space (CAS). In all cases, the goal is to create the many-body wave functions for the ground and excited states of the target molecule to enable the computation of electron scattering cross-section. Examples include R-matrix [24, 25] and a overview can be found in section 3 of [26]. While these methods have been verified by gas phase experiments, there are two major challenges. Firstly, then entire scheme is very computationally demanding. The computation time of wave-functions scales as  $N_{atom}^5 \sim N_{atom}^6$  [27] and the R matrix computations would add more. Secondly, computational artifacts, such as orthogonal discretized continuum (ODC) states, plague the computation of excited states [28] (The scattering target). As a result, while one can use these computations to interpret experiments, it's predictive power is weakened. For the specific problem of ODC states, basis function relaxation methods have been introduced and resulted in considerable success [28]. However, the density of ODC states increases with basis size, which increases with the number of atoms. In other words, the computation time would scale at least one order worse. Given the complexity of EUV materials, in terms of the variety and size of molecules, such methods currently do not posses the scalability and throughput needed for effective computational material engineering.

An alternative to a full first principles approach is the Binary-Encounter-Dipole (BED) model[11, 29]. This model focuses on the impact ionization cross-setion and is not capturing the physics for low energy electron capture and scattering. In its original form the differential scattering oscillator strength is obtained semi-empirically but it can also be computed from the first principles. The advantage of this model is that the most computationally demanding step is the evaluation of the differential scattering oscillator strength, which upon some assumptions (For example, the excitation is single particle in nature), is essentially a single particle dipole transition matrix element. The integration time appears to scale with the basis size (which scales with the number of atoms).

On the other hand, empirical approaches have been used to construct the differential scattering cross-section as well. For example, the dielectric model has proved its prowess at higher kinetic

energies. The premise is that one can compute the differential scattering cross-section from the momentum and energy resolved dielectric function, which is still difficult to measure. However some models, such as the Mermin Model can be used to obtain the momentum resolved dielectric function from the zero-momentum dielectric function[30, 31]. The zero-momentum dielectric function can be measured by electron energy loss (EELS) experiments, ultimately yielding the energy-loss and angle resolved scattering cross-sections as a function of incident energy. This framework captures impact ionization, internal excitation and plasmon excitation (which usually results in ionization eventually) but the incorporation of the Mermin model means that it is only applicable to periodic solid state system where the physics can be described by simple parabolic bands. In most resist materials, this is not the case.

For readers who intent to learn more about low energy electron interaction with matter, reference [32] provides an organized overview and reference [33] contains in-depth discussions about selected topics.

### 2.1.3 Generation of reactive species

As one can see, there are a few places where chemistry can be initiated. In other words, there are a few ways for reactive radicals and anions to be generated. For their role in the exposure chemistry, these species are expected to be unstable but by studying the end products one can still infer the identity of these intermediate species with spectroscopy experiments such as Fourier Transform Infrared (FTIR)[34, 35] and XPS[36, 37]

Although chemical activation happens in CARs and non-CARs alike, for the purpose of simplicity, the following discussion will be centered around CARs.

#### 2.1.3.1 Impact ionization

First of all, subsequent to impact ionization, the ionized molecule is in a meta-stable state and could relax by the means of fragmentation. It has been hypothesize that specific functional groups such as phenol can localize the hole and facilitate deprotonation which result in half an acid (the other half being the counter anion such as the commonly used nonaflate and triflate anions) [13, 38]. The primary ionization event as discussed in section 2.1.1, could result in similar outcomes.

Impact ionization can be studied with electron scattering experiments [39].

The modeling approaches mentioned in section 2.1.2 could be used to study impact ionization as well. The binary encounter dipole (BED) approach is in fact formulated for impact ionization [11, 29, 39]. One caveat of the BED model is the lack of discussion in identifying angle differential cross-sections needed for trajectory scattering simulations. The cross-sections are angle integrated at the very beginning in [29].

### 2.1.3.2 Internal excitation

A traveling electron can also promote a molecule into an excited state. This mechanism, colloquially known as internal excitation, is very similar to the photo chemical excitation in DUV. The biggest difference between EUV internal excitation and DUV photo excitation is the spectrum of the excitation radiation. DUV radiation has a very small bandwidth and as a result it will promote the PAG to a specific excited state. The specificity of excited state gives certainty in chemical outcome. In EUV, internal excitation is indeed driven by the wake field produced by a traveling electron. The wake field is essentially a localized broadband radiation. As a result, the PAG can be promoted to a range of different excited states.

Subsequent to the excitation, PAG would break apart. Although hypothetically how the PAG breaks apart could depend on which excited state it has been promoted to, the commonly used triphenyl sulfonium (TPS) PAG seems to always fragment by cleaving one of its sulfur-carbon bonds. All the reported photo products, regardless of exposure source (and as it turns out, irrespective of exposure source), can be trace back to this particular bond cleavage [40].

The DUV like nature of internal excitation means that upon a single internal excitation, an acid molecule is generated [13, 40, 4].

Experimentally, internal excitation in EUV materials has been studied with cathode luminescent experiments [41]. In that experiment, PAGs are replaced by fluorophores that would be internally excited by the electron cascade generated by the incident electron beam (instead of EUV) as PAGs would. The fluorophores do not break apart as PAGs would. Instead, they will fluoresce as an indicator of excitation. Note that there is no guarantee that the fluorophores have the same absorption or interaction cross-section as the PAGs so the results should be considered an order of magnitude estimate.

### 2.1.4 Electron capture

Electron capture takes place when a slow electron combines with a molecule. As a result, the molecule could become reactive immediately or it could fragment into reactive parts. How electron capture results in acid generation is still an open question. Take the example of the common TPS-triflate PAG, some suggested the role of electron capture is to neutralize the cation. Once the cation is neutralized, the Coulomb force binding the triflate anion to the TPS cation is gone, allowing the triflate anion to rendezvous with the proton created by ionization [13, 42]. What happens to the now neutralized TPS cat ion, does not matter in this picture. On the other hand, it has been demonstrated with cyclic voltametry experiments that the reduction of TPS triflate, in the absence of ionization, would produce acid [43], which appears to suggested that the neutralized PAG is responsible for the extraction of the proton. In that case, dissociative electron attachment (DEA)



of the PAG matters.

Experimentally, DEA can be characterized by ionic yield experiment. In such experiments, molecules are vaporized, exposed to electrons. The yield of anions are measured as a function of electron energy [17]. These experiments requires samples that can be vaporized, forbidding oniums. However, it was demonstrated that even for non-ionic PAG N-Hydroxynaphthalimide triflate, upon electron attachment, the dominant product is the triflate anion [17], consistent with the Kozawa hypothesis [13].

Theoretically, CI and CAS based wave function methods previously mentioned in section 2.1.2 has been used to investigate and predict DEA spectra [28]. Therefore, modeling of DEA is faced with the same problems. Attempts were made with density functional theory (DFT) methods, which could reduce the barrier for scaling up this computations [44].

### 2.1.5 The key challenges

Summarizing from the above overview, we realize a few key challenges for engineering the radiation chemistry or EUV.

The mechanism where reactive species are created in EUV is very different from DUV is a few distinctive ways.

Firstly, in DUV photochemistry, the division of labor is clear—the polymer matrix can be engineer out of the picture, making the PAG the only participant. (In some cases the polymer as a photo-sensitizer has been explored [4]). In EUV, all constituents partake in the electron cascade. Investigating how they affect the cascade is informative for understanding and eventually controlling the electron blur.

Secondly, the majority of processes mentioned above are novel—they did not exist in DUV. The role of DUV like photochemistry is still a subject of study, but impact ionization and electron attachment, neither of which exists in DUV, appear to play rather substantial roles in EUV. Understanding how they lead to reactive species would, as mentioned previously, lead to improvement of quantum efficiency.

Thirdly, the presence of the electron cascade implies that from photon absorption to generation of active species, there is a spatial spread. In contrast, in DUV, acid is generated by the PAG which is also responsible for photon absorption. The spatial spread has been estimated to be around 2 to 3 nm, which is still not a major concern at the present. However, as features keep shrinking, it will become a bigger hindrance to resolution improvement.

### 2.1.6 Relevance of e-beam resist

E-beam exposure is conceptually similar to EUV—both induce chemistry by creating a cascade of secondary electrons. In e-beam exposure though, the incident electrons often have keVs of kinetic energy while EUV ionized primary electrons have energies around 80 eV in polymers as shown in figure 3.3. A few differences should be noted.

Firstly, the more energetic primary electron can impact ionize from core levels [15]. However, electron energy loss spectroscopy (EELS) has demonstrated that plasmon excitation is still the most likely outcome should impact ionization happen in organic films [45, 46], and that most likely leads to ionization of valence electrons [15]. In other words, the ionization driven chemistry could be very similar to EUV (albeit the quantum efficiency is different).

Secondly, at high kinetic energy, where the dielectric model is valid (see section 4.4.2), inelastic scattering is mostly forward. That is also true for elastic scattering (see equation 3.8 in [47], where  $\alpha \propto E^{-1}$ , which has an angular dependence similar to equation 4.6). Thus the beam is not expected to diverge much through the thickness of the resist, as evident in simulation work [48], (which is an evolution of the formalism proposed by Joy [47]) and [49] as long as the resist is thinner than 50 nm.

Thirdly, the scattering cross-section is lower at keV energies so even though these electrons have more energy, they deposit a small fraction in the thin film [45]. Therefore, in an infinitely thick film, the interaction between e-beam and the film is similar to EUV-film interaction (what an 80 eV electron could initiate) plus everything else before the primary electron (and possibly some energetic secondaries) reaches 80 eV. A typical film used in EUV lithography is less than 100 nm thick. In such a distance, the primary electron is not likely to have decelerated to 80 eV [45].

An 80 eV electrons are more likely to scatter at higher angles. In a very simplistic view, there are two components of the total electron blur—the lateral footprint for the 80 eV electron to lose energy, and that of the secondary cascades generated by each impact ionization (which would result in a secondary electron with around 10 to 30 eV of kinetic energy, see EELS spectra in [46]). On the contrary, electrons with keVs of energy would not change direction much traveling through the film so the total lateral electron blur is mostly coming from the secondary electron blur.

## 2.2 Structure of the thesis

The breadth and depth of Radiation chemistry in EUV is as immense as it is complicated. In this thesis, the author will focus on a few specific questions in the radiation chemistry.

Firstly, the electron cascade will be discussed in detail.

In chapter 3, experimental efforts to characterize the electron cascade will be discussed in detail. The author conducted Photoemission (PES), total electron yield (TEY) and electron atten-

uation length (EAL) experiments. As previously mentioned, directly characterizing single scattering events are experimentally almost impossible. However, by combining the above experiments, one can extract information useful to the development of these materials. The descriptions and specifications of these experiments will be provided and much of the chapter will be built upon publications [50, 51, 52]

In chapter 4, a question arose from chapter 3 will be addressed with Monte Carlo simulations. While PES experiments measure the electron energy spectra upon EUV exposure, it is by definition providing information about the electrons that manage to escape. Since it is the electrons within the sample that are responsible for inducing chemistry, the discrepancy between the two has to be understood. Given the difficulty of characterizing electrons within a condensed film, Monte Carlo simulation is a more viable way of addressing this issue.

In chapter 5, the author will examine how sulfonium PAG, the industry workhorse, reacts differently to DUV and EUV using density functional methods. Computations of vertical attachment energy are compared against actual exposure sensitivity to identify exposure performance drivers and elucidate the relative importance of DUV like internal excitation in EUV materials.

In the later chapters, novel EUV material platforms are investigated and discussed.

In chapter 6, in light of the rise of metal oxide organo-tin resists platforms, the prototypical Sn-12 tin-oxo cluster  $[(R-Sn)_{12}O_{14}(OH)_6]^{2+}A_2^-$  will be investigated using first principles quantum chemistry methods. The chemical activation mechanism, and its relationship to the superior performance of this system, was investigated. Moreover, an ionization induced proton transfer pathway is identified. Upon ionization, the cation can donate a proton to an anion, resulting in a neutral conjugate acid observed experimentally.

In chapter 7, resist substrate engineering using self-assembled-monolayers (SAMs) will be discussed. SAMs have huge potential in the miniaturization of features. SAMs can be deposited with area selectivity, enabling self-alignment and mitigating placement errors. As EUV sensitivity in standalone SAM layers has been reported, the origin of such sensitivity would be of great interest. The interface will be studied with a combination of spectroscopy experiments and DFT computations using slab geometry.

Finally, the author will conclude by giving his impression on the prospects of EUV materials research. The role of computational techniques will be discussed.

## CHAPTER 3

### Experimental Investigation of Electron Processes

#### 3.1 Introduction

As previously mentioned, in EUV, chemistry is driven by the cascade of slow electrons and an array of physical processes that do not exist in DUV. These processes in the cascade are intertwined and they all could contribute to sensitivity and stochastics. To enable targeted engineering of EUV materials, experiments have been conceived to disentangle these processes with our best efforts. Given the difficulties in characterizing electron scattering, a more strategic approach is needed.

In lieu of directly aiming at the electron scattering cross-sections, we seek to utilize a suite of experiments which is applicable to condensed films. The separate pieces of information can be combined to infer parameters that are difficult to measure. An example would be the photo-to-electron conversion ratio, which is closely related to the quantum efficiency.

In this chapter, three experiments, namely Photoemission (PES), Total Electron Yield (TEY), and Electron Attenuation Length (EAL), will be discussed. A brief discussion would follow to explain how the latter two, in conjunction with EUV photo-absorption measurements, can shed light on the photon-to-electron conversion ratio of samples.

The discussion on condensed PES is largely based on the publication "*Investigating EUV radiochemistry with condensed phase photoemission*", *Proc. SPIE 10957, Extreme Ultraviolet (EUV) Lithography X, 109571Y (30 May 2019)* whereas the section about EAL is built upon the publication "*Determination of effective attenuation length of slow electrons in polymer films* *Journal of Applied Physics* 127, 245301 (2020)

#### 3.2 Condensed Phase Photoemission

##### 3.2.1 Background

Condensed phase photoemission spectroscopy is a technique to measure the properties of electrons escaping a sample, be it a resist, an underlayer or other materials of interest. An immediate application is measuring the energy of electrons escaping underlayers, the very same electrons that will

be fed into the photoresist in normal operation.

Condensed phase photoemission spectroscopy in conjunction with various light sources is a well established technique to study composition, bonding and chemistry of condensed materials[53] [54] using mostly information from primary electron signal. In addition, processes that can potentially be capitalized in EUV material engineering, such as Auger processes[53]and plasmon excitation[54], can be characterized with condensed phase photoemission spectroscopy as well.

On top of information about the primary electrons, a secondary electron background also shows up in condensed phase photoemission spectra. This background is representative of the physical reality that most electrons inside the resist have low kinetic energy. However, there is no guarantee that the energy distribution in the secondary background signal is identical to that inside the resist. As it is the electrons inside resists that drives radiochemistry, a reconstruction method is needed to bridge the internal and photoemission electron energy spectra.

To address this concern, we developed a technique to recover the actinic internal electron energy spectrum from the photoemission energy spectrum. In addition to the photoemission spectra measured with 92 eV light, our technique only requires the correlation adjusted energy resolved electron mean free path.

The experimental aspects of condensed phase photoemission in section 3.2.2. Preliminary results with actual resist and underlayers will be presented in sections 3.2.3.1 and 3.2.3.2. The theoretical background of the reconstruction technique will be discussed in section 4.1 and the results in 4.6.

### 3.2.2 Experimental Setup

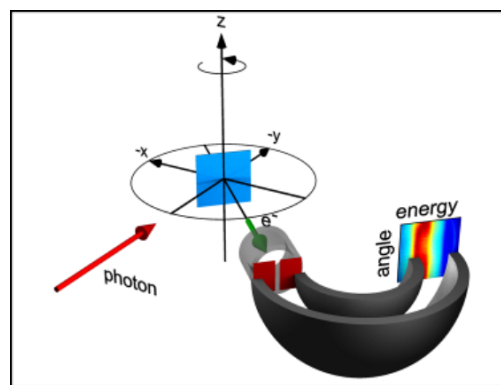


**Fig. 3.1** The schematic for photoemission spectroscopy. Adapted from Smith group at Boston University. (URL: [http://physics.bu.edu/~ksmith/index\\_files/Page934.htm](http://physics.bu.edu/~ksmith/index_files/Page934.htm))

Condensed phase photoemission is a photon-in electron-out technique. Sample is loaded into a

vacuum chamber and exposed to EUV radiation. Electrons are ejected in the process and some of the electrons are collected by an electron analyzer. Depending on the configuration of the system, two types of information, namely the kinetic energy and angle distributions, can be obtained.

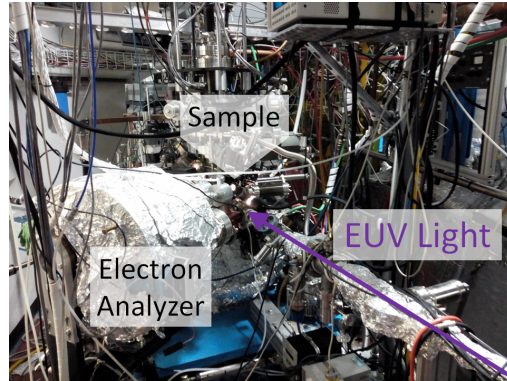


**Fig. 3.2** The experimental apparatus at the advanced light source. As in figure 3.1, the analyzer is placed horizontally

Our system is located at BL 12.0.0.1 of the Advanced Light Source at Lawrence Berkeley National Laboratory. Equipped with a Scienta R3000 hemispherical analyzer (Bottom left corner of figure 3.2), the energy distribution of ejected electrons can be measured with an resolution better than 50 meV. EUV radiation is produced by the synchrotron and 92 eV light is singled out by a grating monochromator.

Energy resolution is provided by the electrons lenses inside the analyzer. Upon entering the analyzer, electrons are deflected by lens elements before reaching a detector. As illustrated in figure 3.1 a electrons are registered by a camera, and their positions (in our case horizontal position) on the detector give information about their kinetic energies.

### 3.2.3 Photoemission measurements

#### 3.2.3.1 Photoresists

The photoemission spectrum of a commercial resists was measured. A wafer sputtered with 40 nm gold was coated with a commercial chemically amplified EUV resist. The 40 nm gold layer between the resist and the substrate are introduced to mitigate charging. The wafer was then diced into a  $5 \times 5 \text{ mm}^2$  piece. The sample is secured by tantalum strips spot welded onto a tantalum sample holder. The sample holder is needed for the sample to be transferred between vacuum chambers of the system. During the measurement, the exit slit size was varied to change flux. No energy shift was observed as a result, indicating that charging, if existed, was smaller than 50 meV.

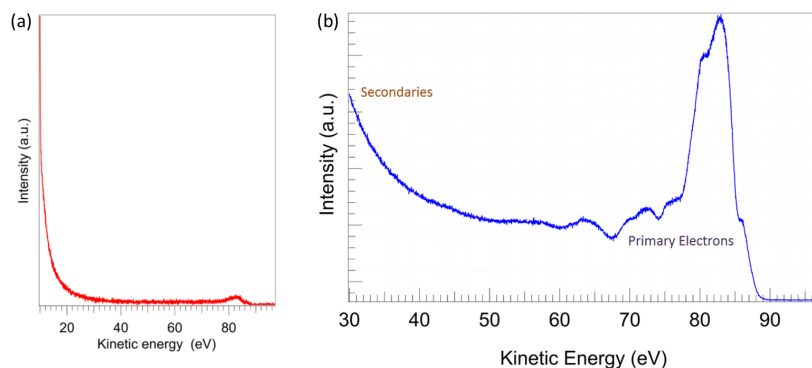


**Fig. 3.3** The photoemission spectrum of a commercial chemically amplified EUV resist at two energy ranges. (a) is the full spectrum from 10 to 100 eV and (b) magnifies the 30 to 100 eV subset of the spectrum.

The spectrum contains information about the primary electrons, those generated immediately after absorption of EUV photons, and a background of secondary and scattered electrons. Primary electrons have their energies determined by their composition and bonding. As a result, they are usually manifested in sharp peaks [53]. The sharp peaks around 79-88 eV are the primary electrons, corroborating with the common understanding that most primary electrons have a kinetic energy of roughly 10 eV. As these primary electrons scatter around, they lose energy and create a cascade of low energy secondary electrons in the process. As the ionization threshold of polymeric materials is in the order of 10 eV, electrons with a higher energy are capable of generating secondary electrons as well. Therefore, the lower the energy, larger is this scattering background. In fact, one primary electron spawns multiple secondary electrons and the energy of the primary electron is shared by its daughter electrons. Therefore the majority of electrons inside the resist have very low kinetic energy. As one can see in figure 3.3 (b), most of the spectral weight lies below 30 eV. The lower limit of the spectrum is currently limited by lensing settings. The detector needs to be reconfigured to go lower than 10 eV.

One of the advantages of photoemission on condensed resist is the possibility to measure the primary electron spectra as is. It is possible to breakdown the resist into its constituents and perform gas phase photoemission spectroscopy on the vaporized constituents [55]. However, molecular properties are known to shift in energy from gas phase to condensed phase[6]. Measuring the photoelectron spectra in condensed phase, one can observe the actually primary electron spectra in resists.

To extract the primary electron spectrum, we perform a simple least squares fitting procedure with a collection of peaks and two types of backgrounds. First, two exponential decays are assigned to the low energy scattering background. To further account for scattering features close to the

primary peak, a Tougaard convolution background[56] is used for each peak. In short, the model function is a collection of Gaussian distributions and their respective Tougaard background with two exponential functions and a constant as background. The same Tougaard parameters were applied to all peaks. Peaks are only added if there is a peak present in the residuals of the fit. To avoid convergence issues, the fit is split into phases where peak positions, and background parameters are fixed alternately.

$$T(E - E_0) = \begin{cases} -\frac{T_B(E-E_0)}{(T_C^2+(E-E_0)^2)^2} & E < E_0 \\ 0 & E \geq E_0 \end{cases} \quad (3.1)$$

**Fig. 3.4** The functional form of the Tougaard background

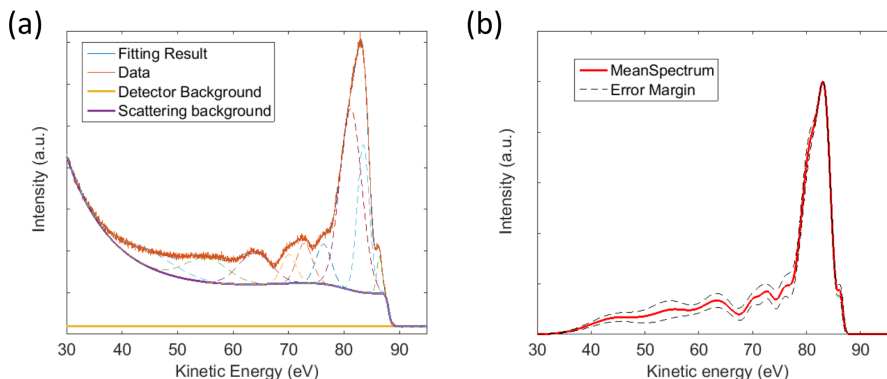


**Fig. 3.5** The curve fitting technique to recover the primary electron spectrum is illustrated in (a). Dashed lines are primary electron peaks extracted by the fitting technique. The mean and variance calculated using three spectra taken on the same sample as a measure of the reliability of this technique and shown in (b)

As one can see from the reconstruction results, within the error margins, a few conclusions can be drawn. First, the notion that the real primary signal is a sum of Gaussian distributions appears to be valid. We attempted using Lorentzians, they always resulted in worse fits in this case probably because the experiment was carried out at room temperature. We tried convolving the Lorentzian based model with a Gaussian to account for instrumental effects and no significant improvement was observed. Second, roughly half of the primary electrons come from the peak around 80 eV. In molecules, in terms of energy, valence states are much closer to each other than semi-core and core levels [55]. Therefore, at the band edge (the cut-off around 88 eV), the density of state is high, resulting in a strong primary signal. As one can see the background does not go to zero approaching the band edge. This imperfection could be due to the use to Togaard background, which is shown to be valid in XPS experiments where the photoelectrons usually have kinetic



energies of 100's of eV. Barring all these qualitative uncertainties, condensed phase photoemission spectroscopy is nonetheless the only know technique to extract the photoemission energy spectra of EUV materials in their native state.

### 3.2.3.2 Underlayers

Underlayers can possibly enhance the efficiency of resist by feeding photoelectrons and secondary electrons into the resist. As we are interested in the electrons escaping the underlayer through the top surface, photoemission spectroscopy is the right tool as it directly measure those electrons.

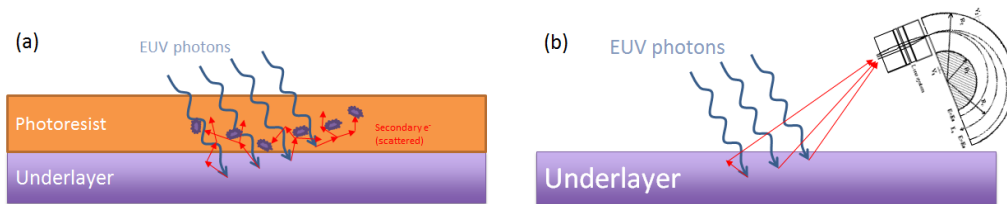


**Fig. 3.6** The proposed dose enhancement mechanism of underlayer (a) and a schematic for photoemission measurements for underlayers (b).

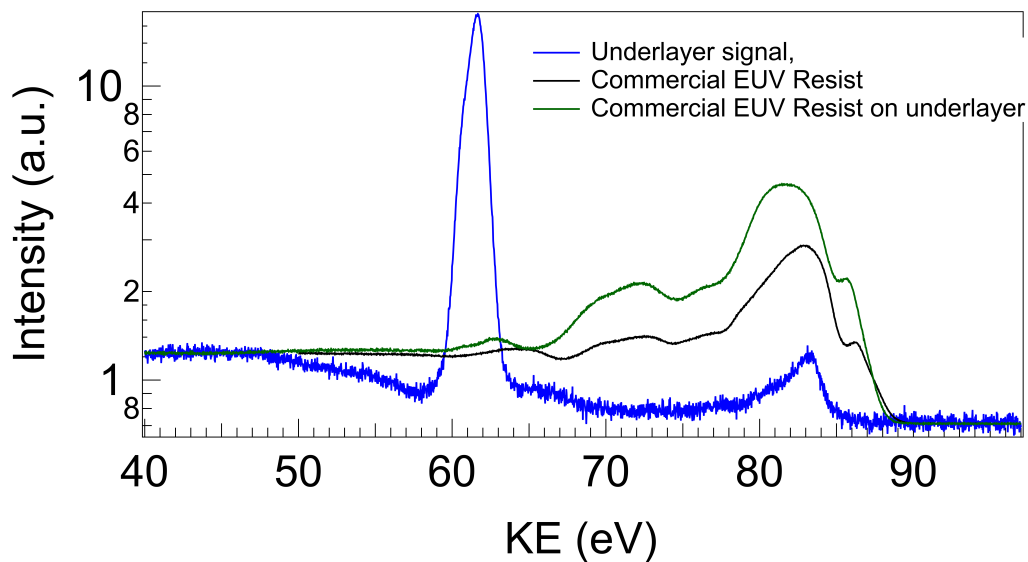


**Fig. 3.7** Photoemission spectra of three samples—underlayer, photoresist on underlayer and photoresist. Curves are scaled vertically for ease of comparison

As one can see in figure 3.7, the primary spectrum of the underlayer studied here is drastically different from that of conventional polymer photoresists. Albeit having a peak around the band edge as in the resist, most of the primary electrons have a kinetic energy of 61.5 eV. This is due to

the presence of d-orbital electrons in the material. The photoemission energy spectra of the resist on silicon wafer and on underlayer are qualitatively the same. On the resist-on-underlayer sample, there is a small peak around 63 eV not observed in the resist-on-silicon sample. Given the 1 eV resolution of our instrument, that peak is not that from the d-orbital electrons from the underlayer. The binding energy of that feature is  $92\text{eV} - 63\text{eV} = 29\text{eV}$ , indicating that it can be a oxygen 2s signal[57].

### 3.3 Total Electron Yield Experiment

#### 3.3.1 Experimental Setup

The total electron yield experiment measures the photonemission current upon EUV radiation. The experimental setup is rather simple. The sample is electrically connected to an ammeter which measures the drain current. Assuming charge conserves, the drain current and the photoemission current are equal. To drive a current through the sample, the surface can be slightly positively charged. To counter this problem, a 12 V bias electrode is added to drain slow electrons away from the surface. The experiments took place at the reflectometer at beam line 6.3.2 at the Advanced Light Source.

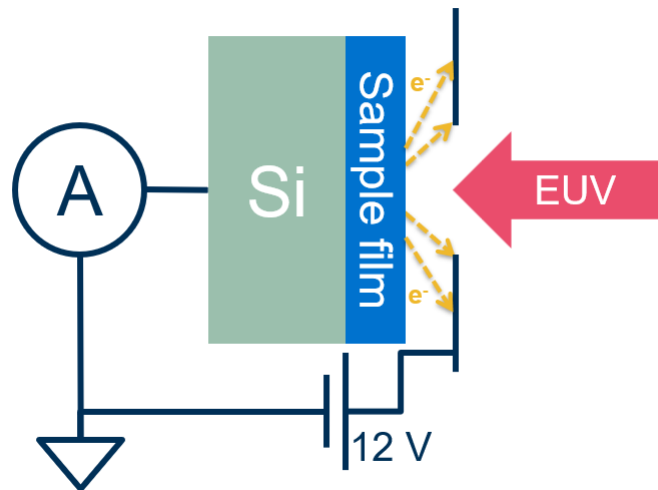


**Fig. 3.8** Experimental setup of total electron yield (TEY) experiment

#### 3.3.2 Data processing

Since the ejected electrons are products of EUV exposure, the drain current is an increasing function of EUV dose. To make comparisons between different materials, one should compare the ratio

of drain current to EUV photon flux. The undulator at beamline 6.3 at the Advanced Light Source was the source of EUV photons. To record photon flux, the “direct current” is measured prior to each experiment. While the photon flux is not directly measured, the direct current is in fact the photo current of a known linear silicon diode, allowing for conversion to photon flux. The photon flux is a function of x-ray optics configuration at the beam line, filters used, and also the storage ring current. While the direct current measurement can capture most of these factors, it cannot compensate any real time variation in photon flux. To eliminate storage ring current fluctuations, both the drain and direct current (time dependent measurements) are divided by the storage ring current (measured concurrently), data point by data point.

The electrical setup itself has a dark current which is dependent on electrical interference. To accurately remove the dark current, a dark current scan is taken when the sample has been translated by more than 3 mm.

To assess uncertainties, for each flux/sample combination, at least two measurements are taken and their standard deviation is taken as the measurement error bar.

### 3.3.3 Charging

Given that EUV absorption events are scarce, the amount of low kinetic energy electrons should be proportional to EUV flux. If not, it is likely that sample is significantly charged during the experiment. To preempt this peril, two photon fluxes will be used. The flux is simply regulated by a filter. The process of record is to make measurement with two filters separately—silicon (Si) and beryllium (Be) filters. The transmission of Si filter is roughly 5 times of Be. The exact flux ratio is measured with the aforementioned silicon diode. Ideally, the drain to direct current ratio should be the same with either filters. Under charging, the magnitude of surface positive charge would be an increasing function of flux, thus lowering the drain to direct ratio (effectively the TEY) of the high flux (Si) data.

In the ideal situation where charging does not occur, the drain to direct ratio is flux independent. That however, does not imply that the time evolution will be the same. In fact, with a higher flux, the speed of chemistry increases proportionately, scaling the time evolution accordingly as well. Therefore, to compare time dependent TEY between two samples, the flux scaled time, which is proportional to dose, is a better choice for x-axis.

### 3.3.4 Data interpretation

As the measurement has a finite time span, at the end of a scan, the sample is likely chemically altered from its pristine form. While the evolution of drain current, as will be discussed shortly, could shed light on the exposure chemistry, it is the electron yield at  $t=0$ , when the sample is

still pristine, that is intrinsic. There is only one data point at  $t=0$ , making it rather susceptible to measurement errors. To reduce error by leveraging the rest of the time series, the (normalized) drain current is fit against an empirical model.

### 3.3.5 Time dependence of TEY and Fitting model

In neat polymer samples, an asymptotic decay is often observed. The origin of this decay is still unclear. Charging could be at play. However, the drain to current ratio does not recover when exposure is blocked for 2 minutes (a typical measurement lasts for 1 to 2 minutes) at high flux, suggesting if this is indeed charging, it has to be static. The time dependence fits the data fairly well with an exponential decay (with an offset), indicating that the decay is some form of bleaching.

In some materials, there is also a rise in TEY at the beginning. Without any assumptions of the origin, it appears that it can be accounted for using a rising exponential function. The three component model (equation 3.2) can capture the time dependence of TEY in most samples encountered.

$$I(t) = C_c + C_d e^{-t/t_d} + C_r (1 - e^{-t/t_r}) \quad (3.2)$$

$C_c$ : Constant component

$C_d$ : Decay component

$C_r$ : Rise component

$t_d$ : Decay time constant

$t_r$ : Rise time constant

(3.3)

Since the current at  $t=0$  is of great interest, making it a fitting parameter would make error analysis more straight forward. Noting that at  $t=0$ , the intensity is just  $C_c + C_d$ , one can rewrite equation 3.2 into 3.4. Eventually one can express the rising and decaying components as fractions of the initial intensity as shown in equation 3.5, The author would like to stress that it is possible to linearly transform the uncertainties in equation 3.2 into that of  $I_0$  and the transformation is done purely for easy book keeping.

$$\begin{aligned}
I(t) &= C_c + C_d e^{-t/t_d} + C_r (1 - e^{-t/t_r}) \\
&= C_c + C_d - C_d + C_d e^{-t/t_d} + C_r (1 - e^{-t/t_r}) \\
&= C_c + C_d + C_d (e^{-t/t_d} - 1) + C_r (1 - e^{-t/t_r}) \\
&= I_0 + C_d (e^{-t/t_d} - 1) + C_r (1 - e^{-t/t_r}) \\
&= I_0 \times [1 + r_d (e^{-t/t_d} - 1) + r_r (1 - e^{-t/t_r})]
\end{aligned}
\tag{3.4}$$

$$\tag{3.5}$$

where

$$I_0 = C_c + C_d$$

$$r_r = C_r / I_0$$

$$r_d = C_d / I_0$$

### 3.3.6 The rising component, electron capture, and implications for EUV molecular engineering

The sporadic presence of the rising component is rather intriguing. By comparing the TEY traces of multiple polymers it is apparent that the presence of electron withdrawing groups (which usually results higher electron affinity) coincides with the rising component as shown in figure 3.9.

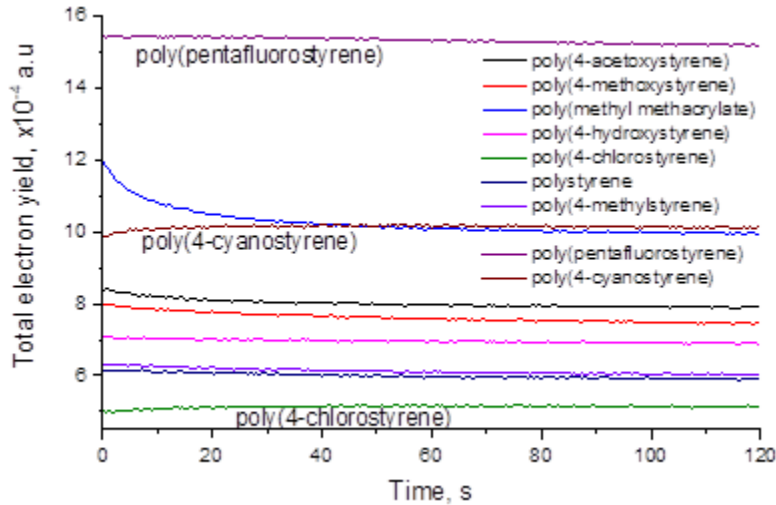


**Fig. 3.9** TEY traces of a collection of polymers. Most follow an exponential decay. Yet, polymers with cyano-, fluoro-, and chloro- moieties show an initial decay.

It has been demonstrated that cyano- (nitriles) [58] and halo-[55, 59] groups are susceptible to dissociative electron attachment (DEA). In other words, once they manage to capture an electron from the cascade, they fragment, making the reaction irreversible. Thus the electron is less likely to be released back into the resist. Each of such reaction would reduce the volumetric

electron scattering cross-section. Such saturation would gradually increase the mean free path of electrons, allowing more of them to escape, explaining the rise. The observation that the rise in poly(4-chlorostyrene) is stronger than poly(perfluorostyrene) is consistent with the observation that conjugated-carbon-halogen DEA is more potent further down the periodic table.

### 3.4 Electron Attenuation Length Experiment

#### 3.4.1 Background

As mentioned in previous chapters, low kinetic energy electrons play an important role in dissolution chemistry. Various techniques have been explored to determine the role of low KE electrons in electron induced chemistry in EUV lithography, as well as subsequent electron induced blur. For example interaction of 80 eV electrons generated by an electron gun with a resist film and subsequent film thickness loss provides information on the distance at which electrons cause solubility changing reactions in a resist film [60].

Numerous parameters, such as acid diffusion, secondary electron blur, and optical aberrations contribute to image blur, making it hard to extract blur length caused only by secondary electrons. Using modelling to analyze experimental results at 22 nm half pitch node it was determined that total blur length is 4 nm. That value is dominated by acid blur and indicates that secondary electron blur should be well below that number.[61]

For determination of the distances that electrons can travel, various direct experimental techniques (such as low energy electron transmission or photo-injection)[62] or Monte Carlo simulations[63] can be used. One of the direct ways to determine the effective attenuation length (EAL) in organic films is the photo-injection (also known as overlayer) technique[64, 65]. The overlayer technique is based on generation of electrons in a substrate, which is coated by an organic film. The current, proportional to the number of escaped electrons, is monitored as a function of the film thickness. This allows for determination of the film thickness at which the number of electrons is attenuated by a factor of  $1/e$ , also known as EAL, to be determined. Many of these investigations use visible or UV light to emit valence electrons from a substrate[64, 65, 66]. The same technique was applied to core-shell nanoparticles, where the inorganic core was used to emit electrons that penetrate through the organic shell[67].

A similar concept, the inelastic mean free path (IMFP) – the average distance electrons travel between inelastic collisions is very important in surface science in general and in X-ray photoelectron spectroscopy in particular. These parameters define surface sensitivity of the technique. Hence comprehensive research of electron IMFP in different materials has been performed[68, 69, 70, 71]. Initially it was found that most materials, possess similar IMFP for the same electron kinetic energy (KE). Because of this similarity, the curve that outlines the dependence of IMFP as a function

of electron KE is sometimes regarded as a “universal” curve[72]. The curve displays the minimal IMFP around 0.7 nm for 20-50 eV electrons. However, its universality becomes more debatable at low energies. Slow electrons are reported to have smaller IMFP values than what the “universal” curve suggests and those values are material dependent[73, 74, 75, 76, 77].

A major distinction between EAL and IMFP–IMFP does not account for the effect of impact ionization events that take place along the cascade. In other words, the presence of impact ionization, which increases the electron flux would increase EAL but not IMFP. Furthermore EAL is more applicable when both inelastic and elastic scattering processes are present, making it independent of initial and final trajectory of the electrons. EAL might be similar to IMFP if elastic scattering is weak, but for low KE electrons, elastic scattering, capable of changing electron trajectory, is prominent so EAL could be significantly smaller than IMFP[77, 78]. In that sense, EAL is more empirical thus more representative of what drives EUV chemistry. As a corollary of its empirical nature, it can be inferred directly from experiments.

To further elucidate the behavior of slow electrons, we decided to measure EAL, which defines the attenuation of the electron flux as they travel in a resist. Methods designed with scientific purposes, albeit accurate, are not very applicable to resists materials. To measure resists in an environment that resembles a lithographic scanner the most, samples have to be spun-cast on to silicon wafers. That immediately rules out gas phase deposition in high vacuum, which suffers from low throughput and is only applicable to low molecular weight formulations.

### 3.4.2 Experimental Setup

A modified version of the aforementioned overlayer technique [64, 65], utilizing X-ray radiation to determine EAL in polymer films is shown in Fig. 3.10. X-ray radiation can be tuned to maximize absorption in a silicon substrate, minimizing any exposure induced changes in the sample. Most of the electrons inside the film are injected from the silicon wafer substrate. In the absence of the resist film, electrons, generated near the surface, can freely escape to vacuum. In the presence of a resist film, the same amount of electrons will be injected into the polymer film. The injected electrons can scatter via different inelastic processes described above, leading to reduction of the number of escaped electrons. As the resist layer thickness increases, the number of electrons able to escape into vacuum decreases.

The simple cartoon in figure 3.10 demonstrates that the number of electrons transmitted through a polymer film decreases as the distance from the substrate-polymer interface increases. The rate of decrease is defined by electron EAL, the distance at which the original number of electrons is attenuated by a factor of  $1/e$ .

This version of the technique is based on attenuation of substrate’s soft X-ray photoelectron peaks by polymer films and leads to determination of EAL at a particular electron KE. Such ex-

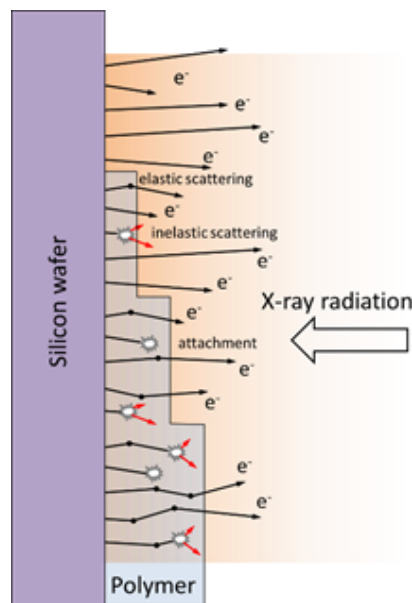


**Fig. 3.10** Scheme of the substrate-overlayer technique used to determine EAL. Absorption of X-ray photons by a silicon wafer (polymer is transparent for X-rays in this scheme) leads to electron emission from the substrate. With increase of polymer layer thickness, fewer electrons can reach the surface and escape from the polymer layer. Electrons injected in the polymer can scatter elastically, generate secondary electrons after inelastic scattering, or attach to a molecule.

periments were conducted to determine the attenuation length of photoelectrons in self-assembled monolayers of n-alkanethiols.[79, 80] The hydrocarbon films of different thickness, defined by the number of monolayers, were grown on a gold substrate and attenuation of gold photoelectron peaks emitted from the substrate allowed for determination of EAL. The obtained EAL varied from 0.7 nm for KE = 50 eV up to 4.2 nm for KE = 1402 eV[79, 80]. Another study looked at how the attenuation length changes as a result of fluorination[81]. Despite the higher scattering cross-section of fluorine atoms the segmentally fluorinated alkanethiolate films had EALs identical to that of non-fluorinated hydrocarbon film. This was rationalized by the fact that the fluorinated segments of the film are less densely packed, therefore the net scattering properties of the fluorinated film is equal to that of hydrocarbon film with higher packing density of weaker scattering atoms. A similar approach with a film deposited on a gold substrate was used to characterize EAL in other hydrocarbons, including PMMA or in graphene films grown on SiC substrate[82]. While most of the previous research was performed using high KE electrons, for EUV lithography it would be important to investigate EAL of low KE (KE < 80 eV) electrons.

Although the method does not provide the KE dependence of the EAL, it does present an easy way to determine realistic EAL in different materials, which enables prompt resist characterization. The technique was tested using poly (hydroxy styrene) (PHS) and poly (methyl metacrylate) (PMMA), materials commonly used as the polymer matrix for resists.



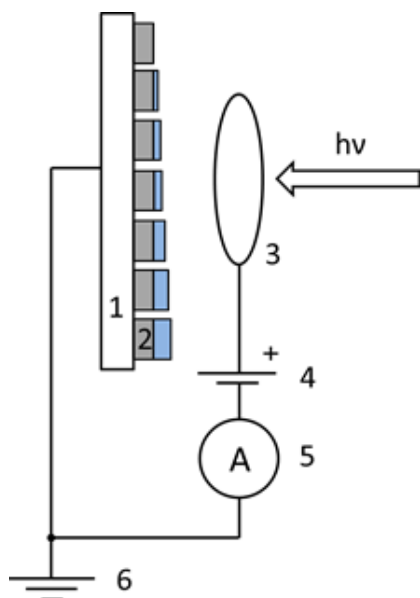


**Fig. 3.11** Electrical scheme of the experiment. (1) Metal sample holder with seven silicon wafer chips (2) coated by polymer films of various thickness. (3) Ring electrode collecting emitted electrons. (4) Positive bias between the ring and ammeter (5). (6) Ground.  $h\nu$  denotes X-ray beam.

The electrical scheme of the experiment is shown in Fig. 3.11. Polymer films of different thickness are coated on Si substrates (2 in Fig. 3.11) and attached to a metal sample holder (1). The sample is illuminated by 200 eV photons from the Advanced Light Source (ALS) at Berkeley Lab. As will be discussed below, the photons almost entirely transmit through the thin (1 – 30 nm) films and are absorbed by the Si substrate. The substrate emits electrons with a continuous distribution dominated by low KE electrons. The electrons penetrate through the film and are collected by the positively-biased ring electrode, which is parallel to the sample surface (3). The current generated by the escaped electrons is detected by an ammeter (5). To reduce sample damage and rate of surface charging interfering with the results, the sample stage (1) is moving during the measurement. The current values are measured continuously during the sample movement, allowing for current collection from a fresh, unexposed sample area. The experimental setup is located inside of a vacuum chamber, kept at pressure below  $10^{-6}$  Torr during measurement. The chamber is directly connected to a beamline which delivers X-ray radiation.

Thin film samples of PHS and PMMA of different thickness are prepared by spin coating polymer solutions in propylene glycol methyl ether acetate on 100 mm silicon wafers. For each thickness, a different wafer is used. The spin coated wafers are baked for 60 s at 130 C and then cleaved into 10 by 15 mm chips, used for measurement. Thickness of so prepared films is determined by a J.A. Woollam Co. M-2000 spectroscopic ellipsometer.

Element	Cross-section at 92 eV (Mb)	Cross-section at 200 eV (Mb)
Carbon	0.58	0.10
Hydrogen	0.02	0.002
Silicon	0.34	3.13

**Table 3.1** Photo-absorption cross-section of carbon, oxygen, hydrogen, and silicon at photon energies of 92 eV and 200 eV.

Polymer	Cross-section at 92 eV (Mb)	Cross-section at 200 eV (Mb)	Absorbed radiation at 92 eV (%)	Absorbed radiation at 200 eV (%)
PHS	7.02	1.21	11.5	2.1
PMMA	7.37	1.29	14.6	2.7

**Table 3.2** Absorption cross-sections of PHS and PMMA, as well as fractions of absorbed radiation by 30 nm film of these materials at photon energies of 92 eV and 200 eV.

### 3.4.3 Experimental Results

We hypothesize that the experimental technique is sensitive to the electrons emitted from the substrate. To achieve that, the energy of X-ray radiation was chosen so that polymers (usually consisting of carbon, hydrogen, and oxygen) are mostly transparent, whereas the substrate efficiently absorbs the X-ray photons. EUV resists may absorb a significant fraction of EUV photons, making EUV photon energy not optimal for this measurement. Indeed, the photoabsorption cross-section of carbon at the EUV energy is about two times higher than that of silicon (see Table 1),[83] meaning that a significant fraction of EUV radiation will be absorbed in the polymer film, significantly complicating the analysis. The situation is drastically different at photon energy of 200 eV. The photo-absorption cross-sections of hydrocarbon materials are small, whereas the cross-section of silicon is large (Table 1) because the photon energy is above Si 2p edge. In this case most of the 200 eV photons will pass through the thin polymer film and will be promptly absorbed by the silicon substrate. Half of the photons reaching the surface of silicon will be absorbed in the first 44 nm of the substrate.

To demonstrate the applicability of the technique, PHS ( $C_8H_8O$ ) and PMMA ( $C_5H_8O_2$ ) were chosen as polymer samples. Their properties at 92 eV and 200 eV are summarized in Table 3.2. The amount of photons absorbed by a 30 nm film is drastically different at those energies. Thus, at 92 eV both PHS and PMMA films absorb 11.5-14.6 % of EUV photons, while at 200 eV they absorb only 2.1-2.7 % of photons, depending on the material. The remaining 97 % of 200 eV radiation is absorbed by the silicon substrate.

After absorption of the 200 eV photon, most of the electrons emitted by the substrate are low KE secondary electrons. This is a known experimental fact observed in a range of different mate-

rials. [84, 85, 86, 87] To demonstrate that this assumption is valid for the experimental conditions used in the EAL measurement, we measured photoelectron spectra of bare silicon substrate using a retarding field photoelectron spectrometer. The spectra measured at photon energy of 200 eV and 92 eV are shown in Fig. 3.12a and b, correspondingly. Both spectra illustrate that most of the electrons emitted by the silicon wafer have a continuous distribution dominated by low KE electrons, peaking around KE of 2 eV. A similar distribution was observed by Henke et al. for different semiconductors and insulators[85]. The origin of the observed electron distribution is explained as follows: the absorption of a photon leads to emission of a photo- and, plausibly, an Auger electron. These electrons may scatter inelastically (via electron impact ionization process), loose part of their initial KE and generate additional low KE electrons. Several of such inelastic scattering events will decrease the initial KE of photoelectrons to a minimum, observed in the experimental spectra. Henke et al. developed a model, characterizing the shape of the SE distribution:

$$I(E_K) = k \frac{E_K}{(E_K + E_A)^3} \quad (3.6)$$

where  $I$  is the energy dependent intensity,  $k$  is a fitting coefficient,  $E_K$  is electron kinetic energy, and  $E_A$  is the electron affinity. The experimental spectra are fit to the model and the results are shown in figure 3.12 by red lines. While the fit is not perfect, the model works well to predict that majority of emitted electrons will be the slow secondary electrons.

Figure 3.12 also contains a weak signal generated by high KE electrons. While Si valence electrons (3s and 3p) are not resolved at 200 eV (Fig. 3.12a) they are slightly visible at 92 eV (Fig. 3.12b) [88, 89]. Photoelectron spectrum measured at photon energy of 200 eV also demonstrates a Si 2p photoelectron peak around KE of 90 eV. The Si 2p peak is relatively sharp because the electrons originate from a core level of Si. It is instructive to compare the number of low KE electrons to that of high KE electrons. At photon energy of 200 eV, the low KE electrons (with  $KE \leq 20$  eV) comprise 71 % of all emitted electrons, whereas at 92 eV they comprise 81 %. Similar distribution of electrons will be observed in a polymer film after absorption of EUV photons and it represents a typical electron energy distribution after several inelastic collisions. Therefore, the continuous electron distribution of low KE electrons, emitted by Si substrate after absorption of 200 eV photons can be used to characterize EAL of polymer films.

Example of the data collected using the designed experimental scheme 3.11: is shown in Fig. 3.13a. The data, collected for PHS films of six different thicknesses and a bare Si substrate, have a step-like structure, where regions of constant signal intensity correspond to electron emission from samples. Current spikes between samples are due to electron emission from the metal sample holder. It is apparent that the current emitted by a clean Si substrate has the largest value among

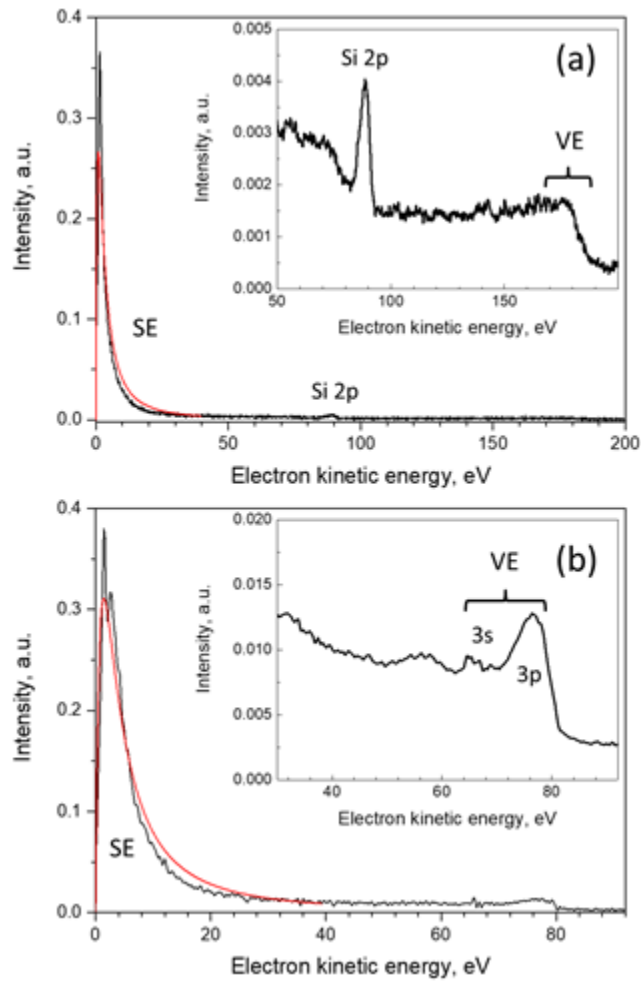


**Fig. 3.12** X-ray photoelectron spectra of silicon wafer collected at photon energy of (a) 200 eV and (b) 92 eV. Insets demonstrate the scaled up high KE electron signal. Red lines depict fit of low KE secondary electron signal with equation (3.6). SE: secondary electrons, VE: valence electrons.

all data points. This happens because PHS film of any thickness will attenuate the number of electrons emitted by a Si substrate. As the thickness of the film increases, the number of transmitted electrons becomes smaller. That is apparent in Fig. 3.13a: the 3.3 nm thick film significantly attenuates number of electrons emitted by a Si wafer; after transmission through the film, the current diminishes from 4.9 to 2.3. An increase in PHS film thickness to 5.1 nm further diminishes the current to 1.1. PHS film thickness above 7.7 nm does not cause significant change, with the current converging to the value of 0.6.

Analysis of the electron yield determined as demonstrated in Fig. 3.13a is presented in Fig. 3.13b (black symbols and line). The normalized values of the collected current are plotted as a function of polymer thickness. The obtained experimental data are fit with the exponential decay function:

$$I(h) = I_0 \exp(-h/EAL) \quad (3.7)$$

#### 3.4.4 Relevance EUV Lithography

where  $I_0$  is electron current collected from a bare Si substrate,  $h$  is the thickness of a film and  $EAL$  is effective attenuation length. The fit of the experimental data presented in Fig. 3.13b results in a value of  $EAL$  for PHS of  $2.66 \pm 0.31$  nm. This value corresponds to the thickness of PHS film that reduces the initial number of emitted slow electrons by a factor of  $1/e$  (to about 37% of initial number). The corresponding data for PMMA is shown in Fig. 4b by red squares and line. Corresponding  $EAL$  for PMMA is  $1.45 \pm 0.16$  nm.

In the context of lithography, it is important to know the thermalization distances of electrons – the distance which an electron can travel until it loses most of its energy. For PHS, the thermalization distance of  $3.2 \pm 0.6$  nm was determined by fitting results of Monte Carlo simulation into the experimental quantum efficiency data [87, 90]. The  $EAL$  value obtained in the current study for PHS of  $2.66 \pm 0.31$  nm is close to the semi-empirical thermalization distance value of  $3.2 \pm 0.6$  nm. While the  $EAL$  value defines the distance at which the population of electrons decreases to 37% ( $1/e$ ) of the initial distance injected population, the thermalization distance can be a bit larger, because extra travel might be needed to decrease energy of electrons to the thermal level. The same authors assumed that the thermalization distance in PMMA is  $6 \pm 1$  nm solely based on the fact that the thermalization distance in many alkane solutions ranges from 5 to 7 nm [88, 89, 90, 91]. Whereas the experimental study of thickness loss caused by interaction with 80 eV electrons suggests that the electron blur for PMMA is  $1.8 \pm 0.2$  nm. The latter value has similar meaning to the attenuation length and lies within error bars of determined in this study  $EAL$  value of  $1.45 \pm 0.16$  nm.

From formula (3.7), the  $EAL$  value extracted from the measurements strongly depends on

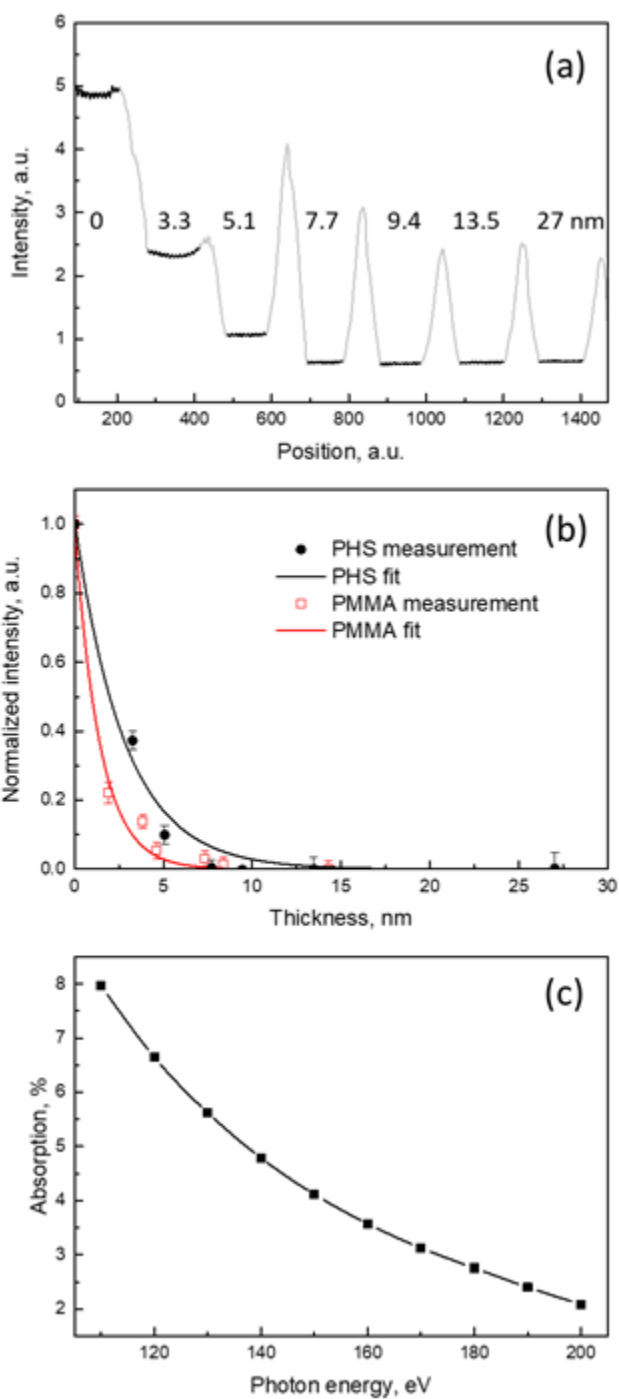


**Fig. 3.13** (a) Electron yield measurement as a function of sample position. Signal, originated from PHS films of different thickness (shown in black), is labeled with the corresponding thickness. Current spikes (shown in gray) between samples are due to electron emission from the metal sample holder. (b) Electron yield for PHS and PMMA (black and red symbols) fit with exponential decay functions (black and red lines). Error bars are determined from intensity variations between five consecutive measurements. (c) Fraction of X-ray radiation absorbed by a 30 nm film of PHS

knowledge of film thickness. Systematic overestimation (or underestimation) of film thickness will lead to correspondingly larger (or smaller) values of EAL. Incorrect thickness measurement of thin ( $h \leq 3$  EAL) films might lead to significant error in EAL analysis.

Because of the choice of X-ray photon energy described above, the absorption of photons by a film is negligible and might be neglected in the analysis (in the case of PHS consideration of photon absorption decreases the EAL value by less than 0.5%). Nevertheless, the more explicit analysis, which is only possible if the composition of the polymer is known, is presented below. To account for the fraction of photons absorbed in a polymer layer, the right hand side of equation (3.7) should be multiplied by  $(2 - \exp(-\sigma\rho h))$ , where the exponential part accounts for the Beer-Lambert law (attenuation of light in the material), where  $\sigma$  is absorption cross-section of polymer units and  $\rho$  is number density of the polymer units. The absorption cross-section can be calculated using tabulated values of elemental cross-sections[82, 83].

### 3.4.5 Direction for Development—Energy Resolution

While the technique described above provides general information on behavior of slow electrons, a more detailed analysis is required sometimes, such as EAL for electrons of a particular KE. A small modification of the proposed experiment allows for determination of KE dependence of EAL. Using tunable X-ray radiation one can selectively change KE of emitted photoelectrons. In particular, change of X-ray photon energy will lead to emission of Si 2p electrons (narrow peak in Fig. 3.12a) at different KE. Thus, at photon energy of 200 eV, the KE of Si 2p is 90 eV. Decrease of photon energy to 150 eV will lead to decrease of KE of emitted Si 2p electrons to 40 eV. Framing it differently, tuning the photon energy from 110 eV to 200 eV will generate Si 2p electrons with KE from 0 to 90 eV. It is worth noting that as the photon energy is decreased from 200 eV, the higher fraction of X-ray radiation will be absorbed by a polymer film. Thus, 30 nm film of PHS will absorb 4.1% of 150 eV photons and absorption reaches 8.0% at photon energy of 110 eV (Fig. 3.12c). This number needs to be accounted for during the data analysis as described above, because only the photons, reaching the surface of silicon can lead to emission of Si 2p electrons. A similar type of measurement as performed above, but in this case evaluating attenuation of Si 2p peak intensity as a function of polymer film thickness, can provide information on EAL of electrons with selected KE. An electron energy analyzer is needed to perform this measurement. Because high energy resolution is not required, a simple energy analyzer, such as a retarding field analyzer, can be utilized. As a result of such measurements, an EAL dependence on electron KE can be determined. The dependence will provide more information on EAL of low KE electrons and their correlation with the “universal curve”, possibly clarifying one more puzzle.

### 3.5 Combining TEY, EAL and EUV absorption measurements

The whole is greater than the sum of its parts—By combining the last two experimental techniques and the EUV absorption measurement, one could plausibly estimate the photon to electron conversion efficiency. Improvement in this conversion, as mentioned in chapter 2 would enhance quantum efficiency, putting us into a better position against the RLS trade-off.

By denoting the photon to electron conversion (number of electrons generated per an absorbed EUV photon) as  $\eta$ , the total number of electrons per unit incident EUV dose per volume is the product of  $\eta$  and  $\mu$ , the volumetric EUV absorption coefficient.

The amount of escaped electrons is a function of energy. It is proportional to the density of electrons at a given energy. The chance of escape depends on the electron attenuation length (EAL) (which is a function of kinetic energy) and the distance of the electron from the surface. The energy resolved electron yield is then given by the integral in equation 3.8.

$$EY(E) = \int_0^{\infty} dz \rho_e(E) e^{-z/EAL(E)} \quad (3.8)$$

TEY can naturally be obtained by integrating 3.8 over energy

$$TEY = \int_0^{92} dE \int_0^{\infty} dz \rho_e(E) e^{-z/EAL(E)} \quad (3.9)$$

As illustrated in figures 3.3 and 3.12, most of the electrons have low kinetic energy. That has two implications. First, the EAL measurement is effectively measuring the low energy EAL. Secondly, the integral in equation 3.9 is dominated by the low energy contribution. In that case, assuming that  $EAL(E)$  is a smooth function, we can ignore the energy dependence and replace  $EAL(E)$  with  $EAL$ , the experimentally measured value.

$$TEY = \left[ \int_0^{\infty} e^{-z/EAL} dz \right] \int_0^{92} dE \rho_e(E)$$

$$TEY \propto EAL \times \eta \times \mu \quad (3.10)$$

In essence, if one divides TEY with  $\mu$  and  $EAL$ , and do so with multiple samples, one can compare their photon to electron efficiency, at least in relative terms. Such analysis has been attempted on a series of prototypical polymers [92]. For the polymers tested (PMMA and PHS derivatives), TEY was plotted as a function of  $EAL \times \eta\mu$  in figure 7 in [92]. Most of the data points fall on the same line, indicating a very similar  $\eta$ . Even though the poly(pentafluorostyrene) has the highest EUV absorption and the highest TEY, it is not the most efficient as it appears to have a smaller *eta*. That is consistent with previous report [93] where an improvement of absorption and



TEY did not result in dose reduction. The stability of perfluorinated benzene ring upon electron attachment [94] (particularly those with near zero incident energy) could partially explain that.

## CHAPTER 4

# Inferring Internal Electron Energy Spectrum with Monte Carlo Electron Trajectory Simulation

### 4.1 Background

As mentioned, it is the internal electron energy spectrum that is representative the the electrons that drive radiochemistry in photoresists. Photo spectroscopy is by definition measuring the electrons escaped from the material and the resulting energy spectrum is not necessarily the same as the internal spectrum. Drawing a connection between the two is vital for photoemission spectroscopy to be a useful technique for studying electron induced chemistry in resists. However, the internal spectrum of electrons inside a condensed phase sample is impossible to measure directly. Therefore, theoretical endeavours have been made to address this problem.

It has been shown that the internal electron spectrum and the photoemission spectrum has a kinetic energy dependent correction factor which is a function of scattering mean free path and the material work function ( $E_A$ ) [84][85] as shown in equation 4.1. Dividing the photoemission energy spectrum by this factor, a spectrum that is proportional the internal electron energy spectrum can be obtained. The factor should depend only on the kinetic energy (KE) of the electron but ref. 8 suggested that an additional prefactor is needed for secondary electrons.

$$\text{Emission} = \underbrace{X(E)}_{\text{Internal Spectrum}} \lambda(E) \left( \frac{E - E_A}{E} \right) \pi \quad (4.1)$$

As the electron energy spectrum inside resists are impossible to measure, to examine these above relationships, we used a Monte Carlo electron trajectory simulator where we can “measure” the internal electron energy spectrum of the system.

### 4.2 Monte Carlo Electron Trajectory Simulation—An Overview

Monte Carlo Electron trajectory simulation is an extensively studied subject and its implementations have be documented elsewhere [16, 95]. The author would elect to give an overview of such

simulations with an aim to provide enough context with a few purposes in mind. Given the breadth and depth of research work put into such simulations, it would be helpful to quickly identify the strengths, and weakness of this technique in the context of EUV. The following discussion is also intended to provide a road map for systematically improving such models.

### 4.3 The Monte Carlo Scheme

*Casino de Monte-Carlo* is located in Monaco, one of the smallest sovereign states on Earth. Nobody talks about the odds of ‘playing Monte Carlo’ because Monte Carlo is not a game, it is a casino (technically an administrative region of Monaco where the casino is located) and your odds really depend on which game you’re playing (although to be fair, the author suspects that the Casino must have hired actuaries good enough to make sure that the house is winning roughly the same margins in all games). This nuance sounds like a nitpick but it’s actually spot on about Monte Carlo electron trajectory models in general. It’s a framework and a workflow with very few underlying assumptions. The framework itself has almost no physics in it, and the accuracy of a Monte Carlo model depends on the scattering cross-sections used and that’s where the commonality of all Monte Carlo electron simulators ends.

The Monte Carlo scheme assumes that an electron’s trajectory can be broken down into stretches of free propagation (the “propagation” box where the electron goes from  $\vec{x}_i$  to  $\vec{x}_{i+1}$ ), separated by discrete scattering events (where energy and momentum change) as shown in figure 4.1. The probability distribution of the ‘outcomes’ (with quotations here as the dimensionality of the output distribution can vary) is governed by the scattering cross-sections which can be regarded as ‘parameters’ of such models. The total cross-section is an amalgamation of multiple physical phenomena so in practice, there are different ‘models’ that describe, or more often, approximate some of the physical phenomena, or ‘mechanisms’ involved in electron scattering. Naturally, all ‘mechanisms’ are to a certain degree at play, so a typical model employs multiple scattering cross-sections. From a logical standpoint all ‘mechanisms’ considered have to be mutually exclusive but inquiries into this matter are surprisingly scant in the literature.

More specifically, the distance of propagation is determined by the total mean free path of all existing mechanisms. The scattering mean free path, which is generally a function of electron kinetic energy, is requested from each participating mechanism and their inverses are summed into the inverse of the total scattering cross-section (equation 4.2). The probability of having  $k$  scattering event(s) within the distance  $x$  is given by the Poisson distribution (equation 4.3). Notice that the expression is only realistic for  $k=0$  because kinetic energy changes upon scattering, resulting in an altered scattering cross-section. By passing a uniformly distributed random variable through the inverse cumulative distribution function, one can obtain a random variable with the

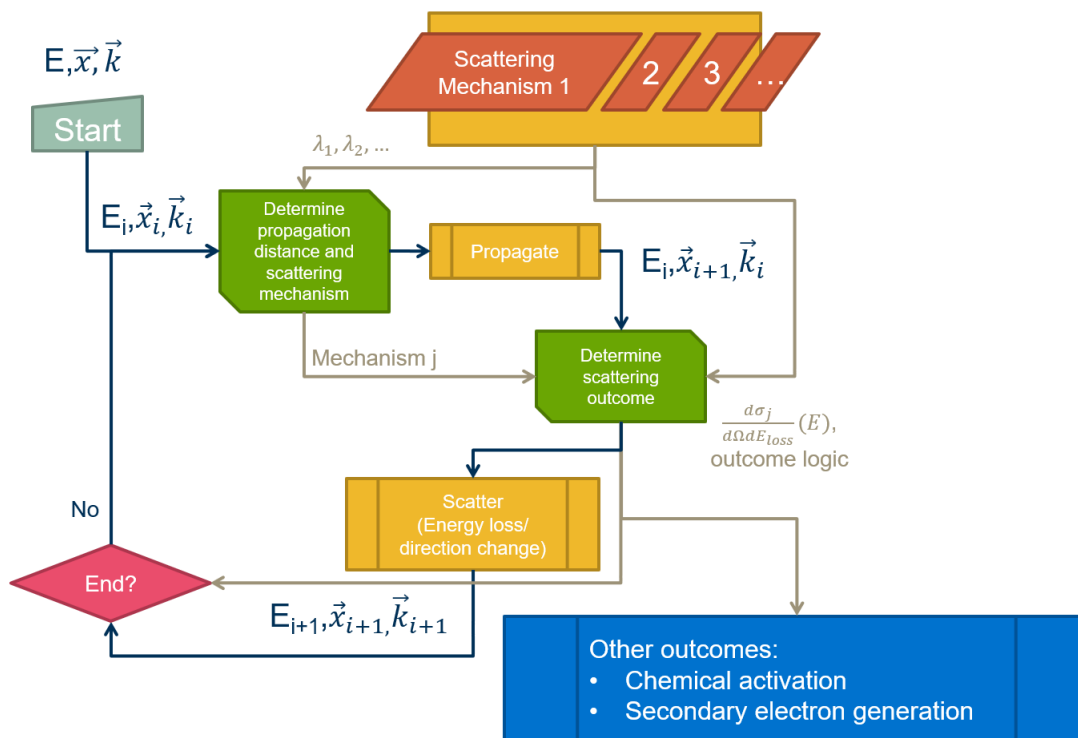


**Fig. 4.1** A schematic of the Monte-Carlo framework. Dark blue lines represent the electron and gray lines additional information flow.

target probability distribution (The derivative of the CDF used) (equation 4.4).

$$\frac{1}{\lambda} = \sum_{i=0}^N \frac{1}{\lambda_i} \quad (4.2)$$

$$\begin{aligned} P(x; k) &= \frac{x e^{-x/\lambda}}{\lambda k!} \\ P(x, 0) &= e^{-x/\lambda} \\ CDF(x) &= 1 - e^{-x/\lambda} \end{aligned} \quad (4.3)$$

$$x = CDF^{-1}(y) = \lambda \ln \left[ \frac{1}{1-y} \right] \Big| P(y) = \begin{cases} 1, & y \in [0, 1] \\ 0, & \text{otherwise} \end{cases} \quad (4.4)$$

After the partial scattering mean free paths are requested, the scattering mechanism, which is a random categorical variable, can also be determined. The likelihood of mechanism  $j$  is given by  $\frac{1/\lambda_j}{\sum_{i=0}^N 1/\lambda_i}$ . The differential scattering cross-section of the mechanism involved would be obtained to generated the energy loss and momentum change.

Worth mentioning are the implication of “outcomes”. Figure 4.1 only shows the flow chart following a single electron. If a secondary electron is generated, a new simulation, or “flow chart” will be initiated. For other outcomes such as chemical activation, additional data structures are needed to register them.

The current implementation assumes that the scattering cross-sections are not time dependent. In other words, the cross-sections are not altered by previous scattering events.

## 4.4 Scattering Mechanisms

In this section multiple scattering mechanisms will be discussed with their features, strengths and limitations briefly mentioned with appropriate references. More attention will be paid to the dielectric model owed to its presence in numerous implementations [16, 45, 14].

### 4.4.1 Electron-nuclei elastic scattering

Electron-nuclei scattering is almost lossless as atomic nuclei are much heavier than electrons. Since elastic scattering was not used in this study, its details are documented in chapter 4 of [16] are not elaborated in this thesis. The simplest form of electron-nuclei scattering is Rutherford scattering, which has a the well known scattering cross-section (equation 4.5).

$$\frac{d\sigma_{Ruth}}{d\Omega} = \frac{Z^2 e^4}{4E^2} \frac{1}{(1 - \cos \theta)^2} = \frac{Z^2 e^4}{16E^2} \frac{1}{(\sin^2(\theta/2))^2} \quad (4.5)$$

$$\frac{d\sigma_{RS}}{d\Omega} = \frac{Z^2 e^4}{16E^2} \frac{1}{(\sin^2[\theta/2] + \alpha)^2} \quad (4.6)$$

$$\alpha = \frac{m_e e^4 \pi^2 Z^{2/3}}{h^2 E}$$

$Z$  atomic number

$E$  kinetic energy of incident electron

$m_e$  mass of electron

$h$  Planck's constant

The Rutherford cross-section is less accurate for high- $Z$  atoms because of inner electron scattering. To account for this effect, the Coulomb electro static potential is “softened” with an exponential decay (For details please refer to equation 4.4 in [16]) and the resultant cross-section falls off less rapidly with  $\theta$ , as shown in equation 4.6. It is known as the screened Rutherford cross-section.

Still, the screened Rutherford cross-section becomes less accurate when the kinetic energy of electrons are lower than 5 keV or when the atomic number is high. According to [16], for Rutherford cross-section to be valid, equation 4.7 has to be satisfied.

$$E \gg \frac{e^2}{2a_0} Z^2 \quad (4.7)$$

When assumption 4.7 breaks down, Mott scattering cross-sections have to be considered for better agreements with experiment (see figure 4.5 of [16]). The formalism of Mott scattering is outlined in Appendix A in [16]

#### 4.4.2 Dielectric model

The dielectric model is one of the most prevalent [15, 45, 16]. It assumes that if the momentum resolved dielectric function of a material, and its energy dependence, is known, then the total inelastic scattering cross-section. It is closer to the reality when the kinetic energy of the electron is much higher than possible energy loss. The commonly used equation is only valid when this condition is fulfilled, one that is very dubious below 100 eV. Given that EUV photoelectrons have kinetic energy of around 80 eV, the author advises the use of caution.

The dielectric model, in optimal circumstances, is accurate as the dielectric function used. Therefore, much attention has been paid in identifying a functional description of the dielectric

model.

To understand this model in depth, the author would briefly go through the derivation used in frequently cite reference by Ergerton. Notice that this textbook is meant to be a scanning transmission electron microscopy (STEM) reference, where incident energies are usually measured in keV.

In the literature [45, 15, 16], the momentum transfer resolved scattering cross-section (which is different from the scattering angle cross section) is often given in the form.

$$[h]d\frac{d\sigma}{d\omega} \sim dE_{ini} \frac{1}{\rho E_{ini}} \mathbf{Im} \frac{-1}{\epsilon} \frac{1}{q^2} \tilde{q} dq \quad (4.8)$$

To avoid confusion, the variables are defined as follows

$$\begin{aligned} E_{loss} &= \hbar\omega && \text{Electron energy loss in a scattering event} \\ \vec{q} &&& \text{The momentum transfer wave vector,} \\ &&& \hbar\vec{q} \text{ is the momentum transfer} \\ E_{ini} &&& \text{Kinetic energy of the incident electron} \\ E_{fin} &&& \text{The energy of the electron post scattering} \\ \vec{k}_{ini} &&& \text{momentum of the incident electron} \\ &&& (|\vec{k}_{ini}|^2 = 2 \times m_e \times E_{ini}) \\ \vec{k}_{fin} &&& \text{momentum of the incident electron} \\ &&& (|\vec{k}_{fin}|^2 = 2 \times m_e \times E_{fin}) \end{aligned} \quad (4.9)$$

Also, it is assumed that momentum and energy conserve

$$E_{Loss} + E_{fin} = E_{ini} \quad (4.10)$$

$$\vec{q} + \vec{k}_{ini} = \vec{k}_{fin} \quad (4.11)$$

To begin with, the electric displacement D and electric field E are related by

$$\epsilon_0(1 + \chi)E = \epsilon_0\epsilon E = D \quad (4.12)$$

In Fourier space, by setting  $\epsilon_0$  to 1

$$E(x, \omega) = \frac{1}{\epsilon(\omega)} D(x, \omega) \quad (4.13)$$

For a non-relativistic moving charge traveling along the x axis, as shown in [96] the electric displacement potential in Fourier space is given by

$$\Phi_D(\vec{q}, t) = -8\pi^2 e \frac{\delta(q_x \times v + \omega)}{q^2} \quad (4.14)$$

which implies an electric potential

$$\Phi_E(\vec{q}, t) = -\frac{8\pi^2 e}{\epsilon(\vec{q}, \omega)} \frac{\delta(q_x \times v + \omega)}{q^2} \quad (4.15)$$

Taking the gradient along x (multiply by  $q_x$ ) and using the condition that  $q_x = \omega/v$  (which turn  $q_x$  into an extra  $\omega/v$  factor), one arrives at equation 7 in [96].  $\frac{dW}{dx} = \int d\omega \omega dq_x dq_y dq_z P(\vec{q}, \omega) \delta(q_x - \omega/v) = \int d\omega \omega dq_y dq_z P(\vec{q}, \omega)$  leads to equation 8 in [96].

Realizing that  $\int P(\vec{q}_\perp, \omega) d^2 q_\perp$  is actually  $d\lambda^{-1} = \rho d\sigma$ ,

$$d \frac{d\sigma}{d\omega} = \frac{e^2 m_e}{\rho \pi^2 \hbar m_e v^2} \mathbf{Im}^{-1} \frac{1}{\epsilon q_y^2 + q_z^2 + (\omega/v)^2} dq_y dq_z = \frac{e^2 m_e}{\rho 2\pi^2 \hbar E_{ini}} \mathbf{Im}^{-1} \frac{1}{\epsilon q_y^2 + q_z^2 + (\omega/v)^2} dq_y dq_z \quad (4.16)$$

Leveraging the azimuthal symmetry in the system,

$$\begin{aligned} d \frac{d\sigma}{d\omega} &= \frac{e^2 m_e}{2\pi^2 \hbar \rho E_{ini}} \mathbf{Im}^{-1} \frac{1}{\epsilon q_\perp^2 + (\omega/v)^2} 2\pi q_\perp dq_\perp \\ &\sim \frac{1}{\rho E_{ini}} \mathbf{Im}^{-1} \frac{1}{\epsilon q_\perp^2 + (\omega/v)^2} q_\perp dq_\perp \end{aligned} \quad (4.17)$$

With the substitution  $\tilde{q}^2 = q_\perp^2 + (\omega/v)^2$ ,

$$d \frac{d\sigma}{d\omega} \sim \frac{1}{\rho E_{ini}} \mathbf{Im}^{-1} \frac{1}{\epsilon \tilde{q}^2} \tilde{q} d\tilde{q} \quad (4.18)$$

equation 4.18 looks identical to equation 5.2 in [45]. The difference is that if equation 4.18 is used, the integration is actually over the modulus of the radial component (in the y-z plane) of the momentum transfer which is different from an integration over the modulus of the momentum transfer. This difference would manifest in integration limits. Yet, when the incident energy is huge relative to the energy loss, and when  $q$  is small, the momentum transfer is almost radial and this detail becomes unimportant. The fact that there is a  $1/q$  (or  $1/\tilde{q}$ ) in the integration diminishes the contributions from large  $q$ .

At this point, one can follow equation 5.2 through 5.6 in [45] to obtain the expression for angle



resolved differential scattering cross-sections ( $\frac{d\sigma}{d\omega d\Omega}$ ).

Before moving on to discussing the dielectric functions, the author would like to point out the energy does not seem to be conserved in this formalism.

$$\begin{aligned}
E_{Loss} + E_{fin} &= E_{ini} \\
\frac{2m_e E_{Loss}}{\hbar^2} + k_{fin}^2 &= k_{ini}^2 \\
2m_e E_{Loss} + (k_{ini} - (\omega/v))^2 + q_{\perp}^2 &= k_{ini}^2 \\
q_{\perp}^2 &= k_{ini}^2 - 2\frac{m_e E_{Loss}}{\hbar^2} - \left(k_{ini} - \left(\frac{E_{Loss}}{\hbar v}\right)\right)^2 \\
&= k_{ini}^2 - 2\frac{m_e E_{Loss}}{\hbar^2} - \left(k_{ini} - \left(\frac{E_{Loss} m_e}{\hbar^2 k_i}\right)\right)^2 \quad (4.19)
\end{aligned}$$

At this point if one looks at the equation,  $q_{\perp}$  has to be imaginary, which does not look realistic. In other words, in the entire integration, the integrand is never physical.

In reference [15], the entire problem is not discussed probably because so many approximations were made in the derivation.

Given the empirical success of this formalism in the TEM literature, the author would stop short of questioning its credibility. However, with much of its prowess resting on empirical success at high incident energy, one should not assume that it will work at low kinetic energy.

With this matter aside, as previously mentioned, this model's accuracy depends on the dielectric function ( $\epsilon$ ) used. To experimentally measure the momentum AND energy resolved dielectric function is very difficult because in most EELS or TEM experiments, there is only access to a very small  $q$ -range. On the flip side, it also means that the energy loss function ( $-\text{Im}[1/\epsilon(\omega, q)]$ ) at the small  $q$  limit can be experimentally acquired.

Analytic models of the dielectric function have therefore been developed. The parameters for such models can be obtained by fitting the  $q = 0$  energy loss function and the  $q$  dependence can be recovered, or extrapolated using the analytic model. Two examples of dielectric functions used in this approach are Lindhard and Mermin models and the latter is especially common.

#### 4.4.2.1 Lindhard Model

The Lindhard dielectric model [31] has the following form

$$\begin{aligned}
 z &= \frac{q}{2q_F} \\
 u &= \frac{\omega}{q \times v_F} \\
 f &= \frac{1}{2} + \frac{1}{8z} [1 - (z - u)^2] \log \left[ \frac{z - u + 1}{z - u - 1} \right] \\
 &\quad + \frac{1}{8z} [1 - (z + u)^2] \log \left[ \frac{z + u + 1}{z + u - 1} \right] \\
 \epsilon_L(\omega, q; \omega_p) &= 1 + 3 \frac{\omega_p^2}{q^2 v_F^2} \times f(\omega, q)
 \end{aligned} \tag{4.20}$$

Notice that there are a few extra parameters in the model. They include the plasmon frequency ( $\omega_p$ ), the Fermi velocity ( $v_F$ ) or momentum ( $q_F = v_F \frac{m_e}{\hbar}$ ). They can be treated as input/assumptions or, as will be illustrated using the Mermin Model, be empirically acquired by fitting. The Lindhard model could capture plasmon scattering and single electron excitation. The derivation of Lindhard model relies explicitly on parabolic band assumption, which is not likely to be true in amorphous films such as resists

It is notable that since the model is derived in the context of a single parabolic band and one associated mode, a linear combination of Linhard ‘modes’ is needed if there is more than one band or one plasmon mode participating in electron scattering.

As previously mentioned, the parameters for a Lindhard mode can be obtained by fitting the zero  $q$  energy loss function with experimental data such as EELS spectra.

#### 4.4.2.2 Mermin Model

The Mermin Model [97] is an conceptual evolution of the Lindhard Model. It accounts for the fact that plasmon modes have finite life times and thus an imaginary frequency component [15].

The Mermin dielectric model for a plasmon mode takes the form

$$\epsilon_M(q, \omega + i\gamma; \omega_p) = 1 + \frac{1 + i\frac{\gamma}{\omega} [\epsilon_L(q, \omega + i\gamma; \omega_p) - 1]}{1 + i\frac{\gamma}{\omega} \frac{\epsilon_L(q, \omega + i\gamma; \omega_p) - 1}{\epsilon_L(q, 0; \omega_p) - 1}} \tag{4.21}$$

It has been shown to yield results consistent with experiments [30, 16, 15]. Again, tracing back to its origin, a parabolic band is assumed so it shares the Achilles heel with the Lindhard Model. Similar to the Lindhard model, multiple Mermin modes are needed when there is clearly multiple plasmon modes.

#### 4.4.3 Phonon/vibrational scattering

The thermal vibrational motion of nuclei can interact with a traveling electron and result in scattering.

In a periodic system, the vibrations between different unit cells interact and form collective modes known as phonons. The biggest difference between vibrations of isolated molecules and phonons is that the latter can ideally be represented by a spatial periodic function, giving it a rather definite momentum and more specific scattering rules, requiring a different treatment.

For isolated molecules vibrational scattering cross-sections can be measured experimentally [98, 20] but computing them from first principles or predicting them with only the molecular structure as input is not a trivial problem as mentioned in chapter 2

For crystalline solids, the phonon dispersion plays an important role in the scattering cross-section. An example of such is the Frölich formalism [16].

In an amorphous film like a photoresist, unlike crystalline systems, the electronic structures of neighboring molecules don't interact nearly as much as neighboring unit cells. Therefore, the isolated molecule picture is conceivably more realistic. Yet, since vibrational modes are often measured in meV, the dispersion (van der Waal's and London) interaction between neighbors could be significant in relative terms.

#### 4.4.4 Electron capture

Electrons can be captured. That terminates the trajectory of the electron. At least two types of electron capture has been discussed in the literature.

Dissociative electron attachment (DEA) is hypothesized to take place in EUV resists. Such cross-sections for small molecules can be measured in gas phase incident energy resolved ionic mass spectroscopy. In practice, it is often represented by a 'wall'—when an electron falls below a threshold, the electron would be captured.

Also, polaron trapping has been reported in Hafnium systems. Such polaron traps occurs in minor imperfection of the crystal and the trapped electron would amplify the defect. This mechanism is surprisingly similar to the imaging hypothesis of silver bromide films [99, 100]

#### 4.4.5 Scattering mechanisms used in this study

Three mechanisms are included in this study.

1. Dielectric scattering. The energy loss function is modeled with the Mermin formalism. Parameters of the Mermin modes are extracted from low- $q$  EELS measurement as detailed in chapter 5.5 to 5.6 of [45]

2. Vibrational scattering. Vibrational scattering cross-section of tetrahydrofuran was taken from [98] and scaled by the atomic density of carbon
3. Electron capture. Electron capture is modeled by a simple cutoff at 5 eV as suggested in [14]

#### 4.5 Model setup and results

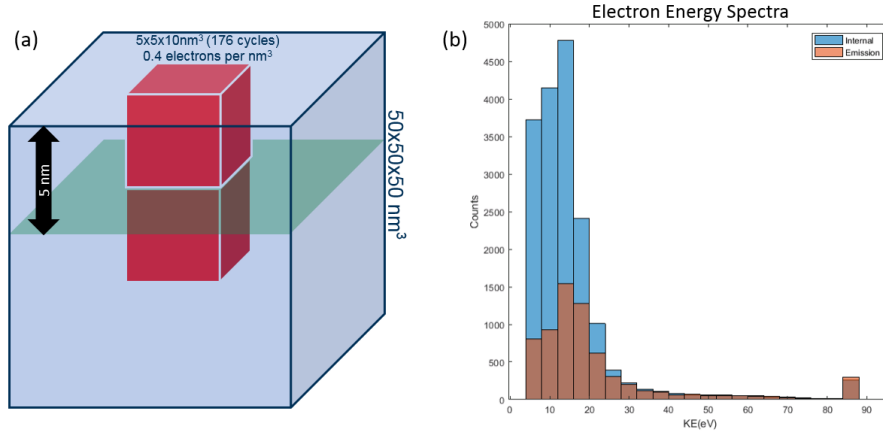


**Fig. 4.2** (a) is the schematic of the electron Monte Carlo simulation. Volume within which electron trajectories are generated is highlighted in red. (b) is the electron spectra measure at the surface and 5 nm below the surface at the middle of the trajectory initiation region

As illustrated in figure 4.2, on average, 0.4 electrons per  $\text{nm}^3$  are seeded in a  $5 \times 5 \times 10 \text{nm}^3$  volume extending from the top surface of a big resist matrix and the simulation is repeated for 176 cycles for statistics. All primary electrons are assumed to have a kinetic energy (KE) of 85 eV.

The flux and energy of electron through the top surface and the upward flux of electron through the depth of 5nm were measured and shown in (b). As one can see, the internal energy spectrum is roughly proportional to the photoemission spectrum above 30 eV of KE. Below that, the photoemission spectrum has proportionately less electrons than the internal spectra.

Ionization[45], plasmon scattering[45][30], low energy vibrational scattering and low energy absorption-activation[14] are included in the discrete-energy-loss model. For simplicity, the difference in work function between the resist and vacuum is set to zero.

A first attempt to address the issue is to divide the photoemission spectrum by the scattering mean free path as mentioned in section 4.1.

Ideally, one wants the correction to produce a spectrum that is proportional to the internal electron energy distribution. In other words, the energy resolved ratio between the internal energy spectrum  $S_{\text{int}}$  and the post-correction experimental spectrum  $S_{\text{corr}}$  should be energy independent.

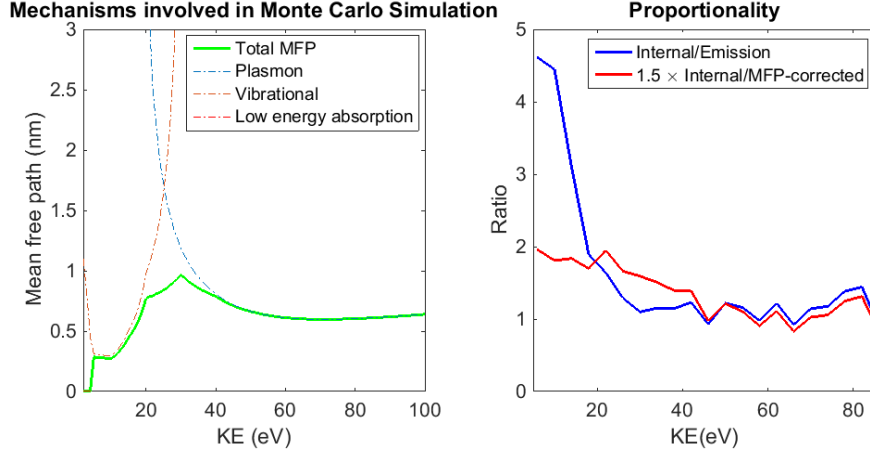


**Fig. 4.3** Left: the energy resolved electron mean free path and scattering components used in the Monte Carlo Simulation. Right: The ratio between internal and emission energy spectra before and after MFP-division correction.

Therefore, if  $R(E) = \frac{S_{\text{int}}}{S_{\text{corr}}}$ , as plotted in the right panel of figures 4.3, is a flat line,  $S_{\text{corr}}$  is essentially a scaled version of  $S_{\text{int}}$  and contains information about the relative intensities at different energies.

As shown in 4.3, dividing the photoemission energy spectrum  $S_{\text{exp}}$  with the scattering mean free path does not suffice to proportionately recover the low energy electron spectral weight. After correcting the photoemission spectrum by dividing it with the scattering mean free path, the ratio  $R(E) = \frac{S_{\text{int}}}{S_{\text{corr}}} = \frac{S_{\text{int}}}{S_{\text{exp}}/\lambda}$  (red) is still energy dependent as a downward slope can be observed from 5 to 60 eV.

## 4.6 Correlation Adjusted Mean Free Path Approach

We attribute the discrepancy to the fact that the scattering mean free path does not account for the effective correlation of scattering steps. If a scattering mechanism is more likely to result in a small scattering angle (more correlated), the electron is more likely to retain its direction of travel. Compared to another electron with the same scattering mean free path but a higher probability to make a sharp turn, it would take a longer distance for the more correlated electron to lose its memory of its original direction of travel. In other words, given the same physical scattering mean free path, a more forward scattering mechanism results in a longer effective mean free path.

To account for correlation, we perform similar Monte-Carlo simulation except that in this simulation there is no energy loss. For each given energy, multiple trajectories of 2 to 300 scattering steps are initiated and their statistics are measured. By assuming that the energy conserving scattering is a random walk with an effective mean free path, which is different from the scattering mean free path due to correlation effects. The effective mean free path is assumed to be related to the displacement of the trajectory  $\sqrt{\langle R^2 \rangle}$  and the number of scattering steps  $N$  by the following

equation

$$\sqrt{\langle R^2 \rangle} = \lambda_{\text{eff}}(E) N^{1/2} \quad (4.22)$$

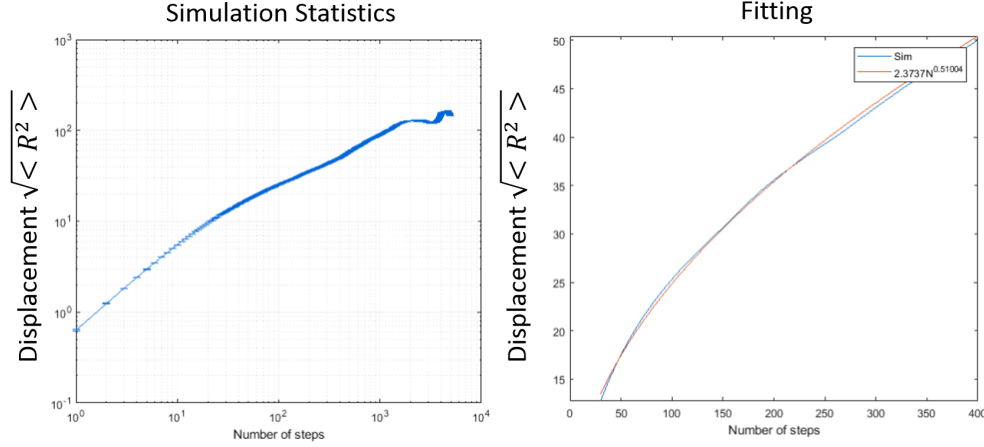


**Fig. 4.4** Left: The simulated root-mean-squared displacement of a collections of trajectories taken at 80 eV. Right: fit to recover the pre-factor  $\lambda_{\text{eff}}$  using the function  $\sqrt{\langle R^2 \rangle} = \lambda_{\text{eff}}(E) N^{1/2}$  at 80 eV

For each energy and each  $N$ ,  $\sqrt{\langle R^2 \rangle}$  for can be calculated for the corresponding ensemble of trajectories and  $\lambda_{\text{eff}}(E)$  can be extracted by curve fitting, as shown in figure 4.4

## 4.7 Results

The correlation-adjusted mean free path is extracted for  $5 < \text{KE} < 90$  (figure 4.5). The correlation adjusted mean free path is much higher than the scattering mean free path for energies above 25 eV. Above 25 eV, plasmon scattering becomes prominent. The Mermin formalism[30] is used to generate the plasmon scattering cross-sections in the Monte-Carlo simulation resulting in very forward scattering cross-sections.

We proceeded to divide the photoemission by the correlation adjusted mean free path. The ratio between this correlation adjusted photoemission energy spectrum and the internal spectrum (magenta curve in figure 4.5) is the flattest compared with the uncorrected ratio (blue) and MFP-corrected ratio (red).

As previously mentioned, ideally one wants the correction to produce a spectrum that is proportional to the internal electron energy distribution. In other words,  $R(E) = \frac{S_{\text{int}}}{S_{\text{corr}}}$ , as plotted in the right panel of figures 4.3 and 4.5, should be a flat line so that  $S_{\text{corr}}$  is essentially a scaled version of  $S_{\text{int}}$ .

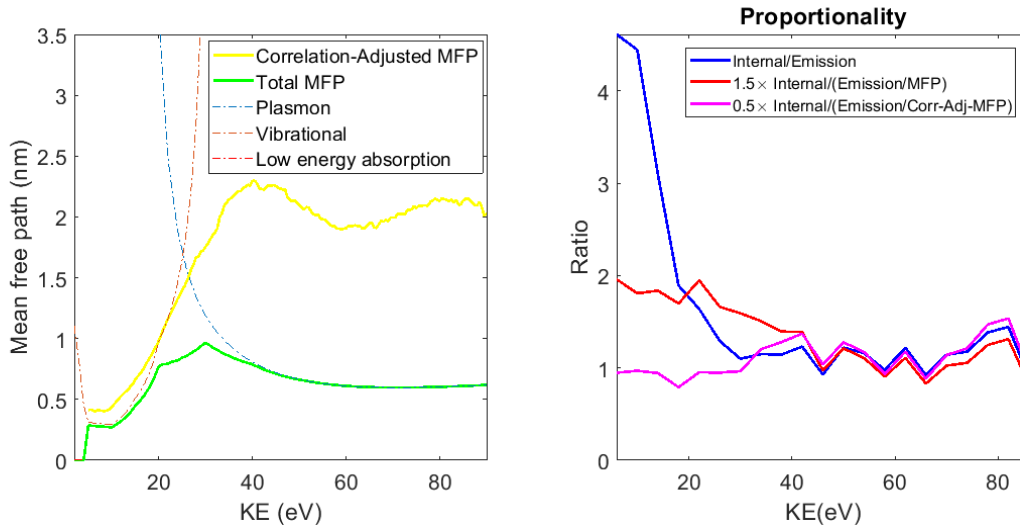


**Fig. 4.5** Left: the correlation adjusted electron mean free path. Right: comparison between different correction methods. In an ideal case, the proportionality should be a flat horizontal line

If one corrects the photo-emission spectrum with equation 4.1, as shown in figure 4.3 on the right,  $R(E)$  is less energy dependent as the red curve has a smaller vertical variance than the blue one. However, if one substitutes the scattering mean free path  $\lambda$  with its correlation adjusted sibling  $\lambda_{\text{eff}}$  as defined in equation 4.22, the ratio becomes significantly less energy dependent as shown in figure 4.5 on the right. The magenta curve (division by  $\lambda_{\text{eff}}(E)$ ) is a significant improvement over the red (division by  $\lambda(E)$ ) and is almost flat, indicating  $R(E)$  is almost energy independent. Therefore, if one divides the photoemission spectrum with  $\lambda_{\text{eff}}(E)$ , the resulting corrected spectrum will have the same shape as the internal electron energy distribution. While this technique is useful, the author cautions that acquiring  $\lambda_{\text{eff}}(E)$  in practice is not straight forward.

## CHAPTER 5

### Photo Acid Generators in EUV

#### 5.1 Introduction

Chemically amplified resists (CAR) has been the industry workhorse in the Deep Ultraviolet (EUV) era. For its flexibility in formulation and well proven efficacy, extending its use into EUV is a logical step forward. Dissolution switching in CARs is initiated by the photon initiated acid generation, a process that involves the photo acid generator (PAG).

To provide a context, an acid is a compound that very readily gives up a proton. Upon deprotonation, the anionic remainder is called the conjugate base. The propensity to deprotonate depends on the intrinsic acidity of the acid molecule and the dielectric background. Within a dielectric medium, the conjugate base and proton are stabilized so deprotonation is more common than in vacuum. In the archetypal triphenyl sulfonium triflate (TPS-triflate) PAG, the triflate anion is in fact the conjugate base of a very strong acid (one that is very ready to deprotonate). Ultimately, the strategy therefore is to eliminate the ionic attraction between the TPS cation and the triflate anion, and produce a proton to pair with the triflate anion. The proton-triflate product is by definition a triflic acid. In DUV, it is understood that the TPS cation is “neutralized” by photo chemistry. The photo-excited TPS cation fragments (as will be illustrated in section 5.3) reacts with each other or with a C-H bond on the polymer to produce a proton, which also takes away the positive charge. The proton then combines with the triflate anion to form an acid.

With the introduction of EUV, electron driven processes in photoresists become relevant. In DUV, resists operate with photochemistry [101]. Photochemistry is specific and relatively well studied [101, 40], making function specific engineering possible. For example, it is understood that photon absorption is only useful if it happens at the PAG. As a result, polymers are engineered to be transparent and the UV absorption cross-sections are to be optimized in order to maximize quantum efficiency.

In EUV, as illustrated in chapter 2, acid is generated as a result of a different collection of processes that involves a cascade of secondary electrons. Understanding how these electron processes result in acid generation is vital for several reasons. Since more than one secondary electron is



generated, the quantum efficiency (absorbed photon to acid conversion ratio) of EUV resists can be larger than unity and is currently known to be around 2 to 3 [102]. Leveraging our knowledge in EUV radiation chemistry processes allows us to further improve the quantum yield, which comes with the obvious benefit of reducing dose to clear. On top of that, optimizing the quantum yield is shown to bring us closer to the photon shot noise limit of stochastics [103]. Last but not the least, the extra efficiency provided by increased quantum efficiency enables more flexible use of contrast enhancing mechanisms such as photo-decomposable quencher [7].

In this chapter, the author investigates whether first principles quantum chemistry calculations can provide insights to electron triggered acid production or even predict yield. To accurately describe the chemistry of a material, an accurate description of the electronic structure is needed as previously mentioned in chapter 2, leaving us with Density Functional Theory [104] or Wave Function methods such as CCSD [105]. Density Functional Theory based first principle calculations have a few advantages. Compared to wave function-based methods such as CCSD, it has a better resource scaling ( $N^3$  to  $N^4$  of DFT/hybrid-DFT vs  $N^5$  to  $N^6$  of CCSD [27]), thus making it a more viable method for studying large molecules and systems.

A few processes are investigated. The yield intuitively depends on how likely an electron attaches to the PAG cation, which would electrostatically release the triflate anion. To that end, we report that electron attachment calculations can be applied to predict reduction potential and dose to clear.

To characterize the likelihood of the PAG breaking apart, ab-initio molecular dynamics calculations, which tracks the forces acting on each individual atom at room temperature, were carried out to study and compare the two activation mechanisms. The dynamics calculations address the questions regarding the outcome provided an extra electron is attached.

A long standing question in EUV PAG chemistry is the relative important of internal excitation and electron attachment. By comparing our computational results with published experimental data, we can infer that internal excitation do not play a dominant role.

As mentioned, how an acid is produced after the PAG has reacted is a complicated problem. In the last section of this chapter, different hypotheses will be discussed and examined.

## 5.2 Electron Attachment

Electron affinity and its effect on PAG performance has been studied [43, 106, 107] showing that if a PAG can be reduced more easily in a cyclic voltammetry, resists consisting of that PAG have a lower dose to clear [43].

To estimate the electron affinity computationally, we compute the lowest unoccupied molecular orbital (LUMO) energy of the four onium PAGs used in [43] and use it as a proxy for electron

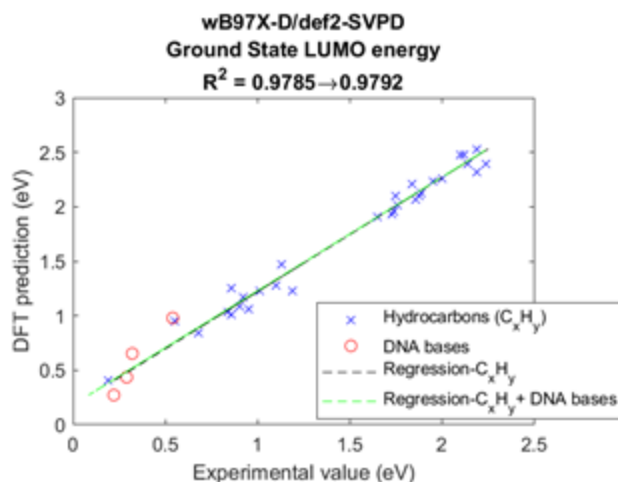


**Fig. 5.1** Example of assessment of predictive power of a single functional/basis combination. Each of the blue crosses and red circles represents a molecule. Linear regression is performed with (green dotted line) and without (black dotted line) DNA bases to infer the robust of the combination.  $R^2$ , which is identical to correlation coefficient squared in linear regression, is 0.9785 (hydrocarbons only) and 0.9792 (hydrocarbons and DNA bases).

attachment affinity. In [43] the reduction potential is measured with the PAGs dissolved in acetonitrile while in condensed phase, the PAGs are tightly bound to their nonaflate counter anion.

Vertical electron affinity computations are inherently unstable for neutral species due to the presence of orthogonal discretized continuum (ODC) states [108]. Since onium PAGs in polymer resists are tightly bound to their counter anion, a method suitable for neutral species should be used. The aforementioned issues with ODC states can be systematically mitigated but doing so is computationally costly. Instead, we seek to empirically identify the most predictive functional/basis combinations that are the least susceptible to ODC states.

$\Delta$ -SCF method was attempted as well.  $\Delta$ -SCF is a procedure where the total energy of the molecule is evaluated with and without the extra electron. The difference in energy (hence  $\Delta$ ) is the electron affinity. Conceptually this method should perform better but it showed a poorer correlation with experiments compared to LUMO energy. Anecdotally,  $\Delta$ -SCF method is more prone to ODC problems and LUMO energy is used in this study purely because of its empirically better performance.

The predictive power of our method is studied empirically, as illustrated in Figure 5 and Figure 6. The first vertical electron affinities of 30 hydrocarbons [108] and 4 DNA nucleobases [109] have been reported. A total of 34 molecules are included. Their molecular geometries are optimized with the PBE0[110] functional and def2-SVPD basis[111]. The LUMO energies of the molecules are then calculated using various combinations of functionals and basis sets. Two metrics are used to assess the predictive power. First, correlation between experimental values and the LUMO

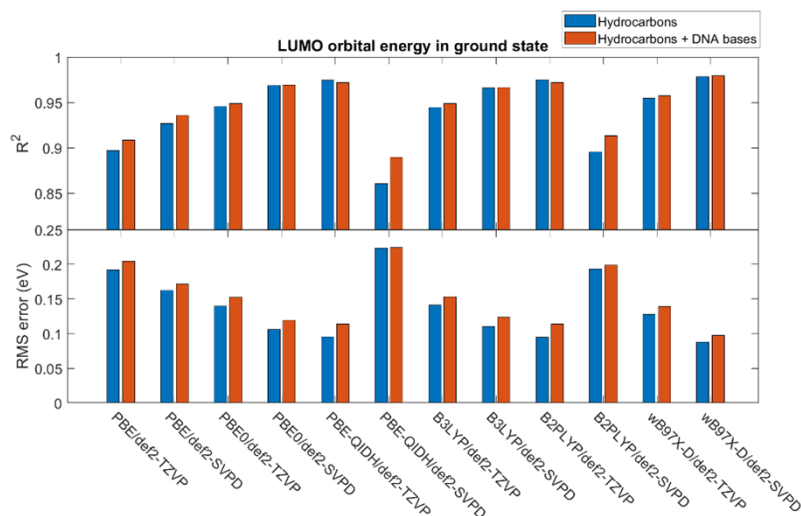


**Fig. 5.2** Predictive powers of different functional/basis combinations. Coefficient of correlation between experimental data and predictions are shown on the upper panel. Slopes of best linear fit Root mean square error (regression slope) is shown in the lower panel. Two colors represent two different datasets used for regression.

energies are compared for each combination is used. Second, the experimental values are fitted against the predictions made by each basis/functional combination and the regression slope is obtained the root mean square error (RMSE) is report for each method. The same procedure is repeated with the DNA nucleobases removed (Figure 5.2) to understand the robustness of the methods. The change in regression slope upon such perturbation indicates the stability of the method—the less the slope changes, more robust is the method.

The functionals PBE, PBE0, B3LYP, B2PLYP, PBE-QIDH,  $\omega$ B97X-D were tested. PBE0, B3LYP and  $\omega$ B97X-D are found to be the best compromise perform the best. Three functionals are selected altogether to ensure there is a qualitative agreement between them. As shown in Figure 6 and Table 1, Tthe improvements in statistical correlation from PBE to PBE0 indicates that inclusion of exact exchange [110] improves prediction. Double hybrids (B2PLYP/PBE-QIDH) incorporate MP2 electronic dynamic correlation, which does not improve performance significantly. Yet the computational time scaling is increased by an order of magnitude (from  $N_{\text{basis}}^4$  of B3LYP/PBE0 to  $N_{\text{basis}}^5$  of B2PLYP/PBE-QIDH [27]. Moreover, as shown in Figure 5.2 and Table 5.1, double hybrid functionals are very basis sensitive in terms of their performance.

All electron affinity calculations are carried out at the Nano or Etna cluster at LBL-LRC using the package Q-Chem 5.1. A single Etna node (with 2 12-core Xeon E5-2670 v3 processors and 64 GB of memory) or three nano nodes (each with 2 4-core Xeon X5550 processors and 24 GB of memory) were used for functional assessment. For PAG molecules, given their sizes, either two Etna nodes or four Vulcan nodes (each with 2 4-core XEON E5530 processors and 24 GB of

Functional/Basis	Slope (m)	Intercept (C)	r <sup>2</sup>	RMSE (eV)
wB97X-D/def2-SVPD	0.9589	-0.1774	0.9792	0.0975
B2PLYP/def2-TZVP	0.9944	0.0990	0.9718	0.1137
PBE-QIDH/def2-TZVP	0.9504	-0.4156	0.9717	0.1139
PBE0/def2-SVPD	0.9803	1.5328	0.9689	0.1192
B3LYP/def2-SVPD	1.0187	1.7800	0.9665	0.1239
wB97X-D/def2-TZVP	0.9268	-0.1837	0.9576	0.1393
PBE0/def2-TZVP	0.9703	1.4788	0.9490	0.1528
B3LYP/def2-TZVP	0.9967	1.7139	0.9488	0.1531
PBE/def2-SVPD	1.0162	2.5272	0.9360	0.1711
B2PLYP/def2-SVPD	1.1811	0.0900	0.9136	0.1989
PBE/def2-TZVP	1.0022	2.4603	0.9084	0.2048
PBE-QIDH/def2-SVPD	1.1865	-0.5701	0.8898	0.2245

**Table 5.1** Parameters for linear model between experiments and DFT for various functionals. The linear model is  $Experiment = m \times E(DFT) + C$ . The coefficients of correlation and root mean square error are also included.

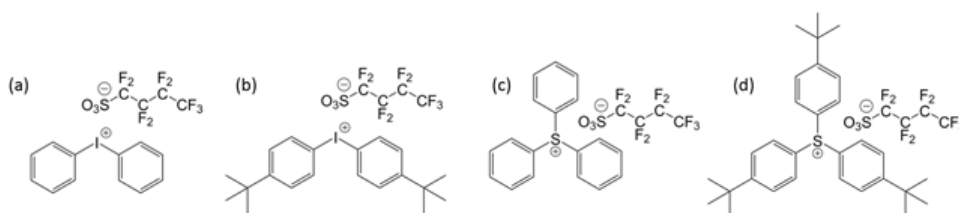


**Fig. 5.3** The four onium PAGs investigated. (a) Diphenyl-iodonium (DPI)-nonaflate, (b) Bis(4-tert-butylphenyl)-iodonium (BTBPI)-nonaflate, (c) Triphenyl-sulfonium (TPS)-nonaflate, (d) Tris(4-tert-butylphenyl)-sulfonium (TTBPS)-nonaflate.

memory) are used.

For the three selected functionals, it is consistent that def2-SVPD is more robust than def2-TZVP. The latter is supposedly a bigger basis set that provides better descriptions of molecules. The superiority of the former indicates the importance of diffuse functions in such calculations. Although def2-TZVP is larger than def2-SVPD thus supposedly more computationally demanding, significant speed disadvantage was not observed and the author speculates that the linear dependence arisen from the diffuse function offsets the relative compactness of the def2-SVPD basis.

In [43], the reduction potential and dose to clear of four onium PAGs were reported. In the reduction potential measurement, the PAG is dissolved in acetonitrile, resulting in ionic dissociation. In actual resist, the PAG is likely to be bound to its counter anion. The two cases need to be treated separately.

To make accurate predictions about onium PAGs in acetonitrile, two factors have to be accounted for. First, as a result of ionic dissociation, the counter anion is no longer in the vicinity

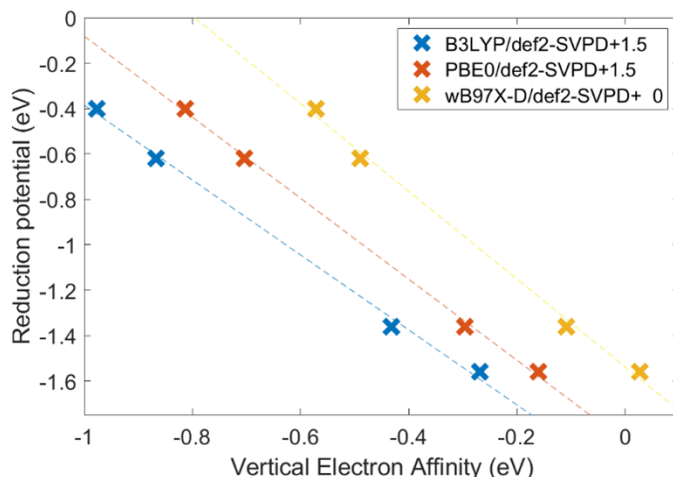


**Fig. 5.4** Computational vertical electron affinity of four onium PAG cations calculated in conjunction with pcm versus experimentally measured reduction potential reported in [43]. Dashed lines are linear fits.

of chemically active onium ion. Second, the presence of acetonitrile has to be accounted for. The vertical electron affinity of the onium ions are calculated in conjunction with polarizable continuum model (pcm), which captures the physics of polar solvents [112] and is implemented in the Q-Chem package.

In all three hybrid functionals, the experimental reduction potential and the computational vertical electron affinities, calculated from the molecular LUMO energies, form a linear relationship (Figure 5.4). Additionally, all three functionals give qualitatively similar results, meaning that the correlation between the two is not theory dependent and thus we expect the calculations to be robust. As the data points lie closely to the line of best linear fit, the regression line can be used to predict the experimental reduction potential from computational vertical attachment energies with reasonable confidence.

We move on to calculate the vertical electron affinities of the onium triflates, which is representative of their behavior in condensed phase. As indicated in Figure 5.5, the vertical attachment energies correlate well with the experimental dose to clear. In this case, however, a quadratic function is a better fit

It has been reported that using another computational approach, the AM-1 semi-empirical method, the correlation between vertical electron affinity and dose to clear was not identified [107]. In [107], the effect of electron affinity was studied with a different series of molecules. The most notable difference is that in the engineered electron grabbing species are hetero-cyclic—they have two of the three phenyl rings connected. As the efficiency of dissociative electron attachment depends on both the attachment of the electron and the likelihood of dissociation, having the im-

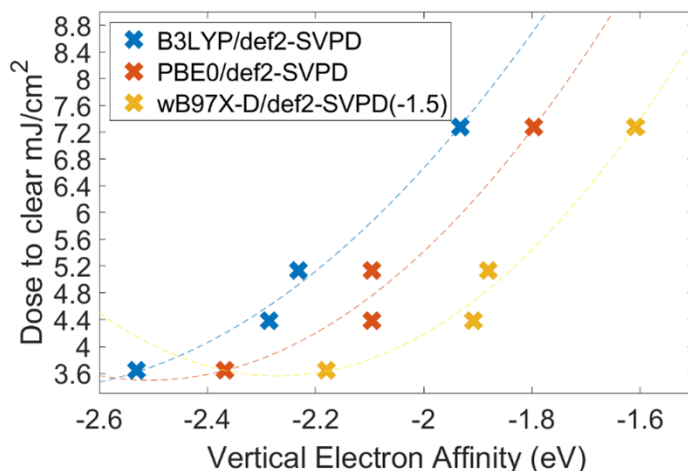


**Fig. 5.5** Computational vertical electron affinities of four onium PAGs versus dose to clear reported in [43]. Dashed lines are quadratic fits.

mobilized aryl groups could impede dissociation, offsetting the benefits of lower vertical electron affinity.

Subsequent molecular dynamics study is being explored to investigate the effect heterocyclic aryl groups in TPS like onium PAGs to understand the trade-off between attachment affinity and dissociation impedance.

## 5.3 Ab-Initio Molecular Dynamics of Photo Acid Generators

### 5.3.1 Internal Excitation

Internal excitation as a PAG activation mechanism has been shown to be present in EUV resists [41]. As [41] suggested however, the quantum efficiency is only on the order of 0.1. Understanding internal excitation at a fundamental level could allow us to identify strategies to improve the quantum efficiency of this process in EUV materials.

Internal excitation is a process through which a molecule (in the context of CARs, a PAG), is promoted to an excited state by an electron that propagates nearby. The propagating electron generates a time varying electric field as observed by a stationary PAG. The PAG is essentially subjected to broadband electromagnetic radiation. If the spectrum of the radiation overlaps with the absorption spectrum of the PAG, the PAG can be excited optically. The PAG is not ionized nor is the electron captured by the PAG in the process. In an excited state, the PAG molecule becomes unstable and becomes susceptible to breaking apart.

To study this process, Time dependent Density Functional Theory (TDDFT) calculations [3, 113] are used. The forces acting on each atom in a molecule can be evaluated for each excited

state, thus the motion of the molecule can be calculated. Such calculations are implemented with the Ab-Initio Molecular Dynamics (AIMD) module of Q-Chem. In an excited state, a molecule has a finite chance of transitioning into another excited state [114]. To account for such transitions, Fewest Switches Surface Hopping (FSSH) coupling is included in the dynamics calculations. All calculations are carried out using a single node the Vulcan cluster (each with 2 4-core XEON E5530 processors and 24 GB of memory) at LBL-LRC.

We hope to achieve two goals with our excited state dynamics calculations. Firstly, to reproduce certain known chemistry to validate our dynamics calculations. Secondly, because measurements of yield are seldom direct [3] [20], such calculations can provide a clean way of characterizing the propensity of a PAG to break apart upon excitation.

Triphenyl sulfonium (TPS) triflate (-OTf) is well studied and has very well-understood chemistry at DUV [2] [20] [21]. Upon optical excitation, cleavage of a sulfur-carbon bond was demonstrated to be the immediate outcome [3] [22]. As demonstrated in [4], internal excitation is very similar to optical excitation. We therefore anticipate that sulfur-carbon bond cleavage as a direct result of internal excitation as well.

AIMD-FSSH calculations with excited states are extremely expensive. With the presence of light atoms like hydrogen, the largest achievable time-step was 241 atto-second, requiring around 1000 steps to study bond breaking processes which typically takes hundreds of femto-seconds [23]. To keep computation time reasonable, the anion is ignored as chemistry is driven by the TPS cation. On top of that, we use a smaller basis set—the double zeta cc-pVDZ basis set in conjunction with the functional PBE0. Mechanical properties such as geometry was demonstrated to be less sensitive to basis size [24]. Moreover, with the absence of the anion, the subject is a cation with tightly bound orbitals, rendering diffuse functions unnecessary.

At room temperature, the molecule is subjected to thermal perturbations. That has to be factored into the initial geometry and velocity of the simulation. Also, as the reaction continues, such perturbation has to be included in the evolution of the molecule. To acquire an ensemble of realistic initial conditions, the molecule is first allowed to evolve at room temperature. 50 geometries/velocity were then taken from that evolution and used as initial conditions for the dynamics calculation. We promote the molecule to its 1st and 11th excited states to understand its evolution upon excitation. And in all cases the TPS PAG is simulated for 241 fs.

Our simulations indicate that there are two possible outcomes. Either the TPS PAG remains intact, or a sulfur-carbon bond is cleaved, and a phenyl ring is ejected. With this knowledge, we can characterize the reaction with the sulfur-carbon (of the phenyl ring that ends up the furthest away from the Sulphur) bond length.

The bond length is around 1.7 to 1.8 Angstrom in all initial configurations and its distribution is represented with blue bars in Figure 5.6. We use 2 Angstrom as a cut-off for bond cleavage.

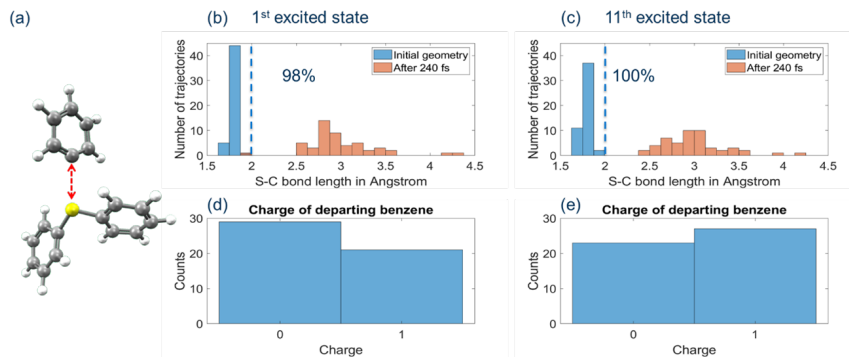


**Fig. 5.6** Results for internal excitation AIMD calculations. The cleavage of carbon-sulfur bond is shown in (a) with the red dashed arrow indicating the bond-length. The distributions of bond lengths before and after evolutions initiated in the 1st and the 11th excited states are shown in (b) and (c). The charge carried by the departing benzene in the two initial conditions are shown in (d) and (e).

After the evolution, the distribution of sulfur carbon bond length is shown with orange bars. In 49 out of 50 initial conditions, cleavage occurs if the PAG is promoted to its first excited state. By promoting the PAG into its 11th excited state, the outcome is qualitatively the same—sulfur-carbon bond cleavage is found to be the only chemical outcome and the yield is nominally 100

The charge carried by the ejected phenyl ring was also calculated using Mulliken population analysis [25]. By exciting a TPS PAG to a higher excited state, the benzene ring is more likely to be positively charged. While this is consistent with previous experimental work [20], the difference is too small to be conclusive with 50 trajectories.

### 5.3.2 Electron Attachment

The main driver of EUV chemistry is low kinetic energy electron attachment [26]. The efficiency of this process could depend on the likelihood of the PAG to break apart after electron attachment (relevant mechanisms will be discussed in detail in section 5.6). AIMD calculations can be used to understand the dynamics of the PAG subsequent to electron attachment as well.

As in internal excitation, 50 realistic initial geometries and velocities were prepared for the TPS cation. For each of these conditions, an extra electron is added. Assuming the incident electron is almost thermalized, the molecule is assumed to be in ground state. With ground state as a starting point, FSSH coupling is not needed. AIMD calculations are again made with PBE0 functional and def2-SVP basis.

Similar to internal excitation, there are only two possible outcomes—the PAG either remains intact or ejects a phenyl ring by carbon-sulfur bond cleavage. The outcome is characterized similarly. In Figure 4 are the initial and final distributions of carbon-sulfur bond length. After 240 fs of evolution, with a 2 Angstrom cut-off, a sulfur-carbon bond breaks in 47 out of the 50 initial con-



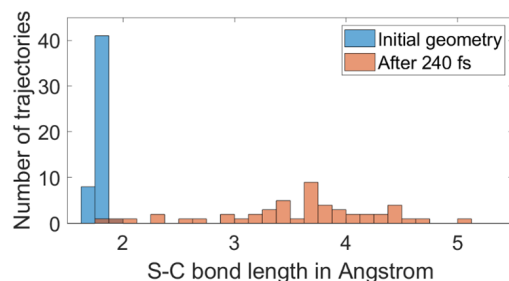


**Fig. 5.7** The distributions of bond lengths before and after AIMD simulations initiated with electron attachment at ground state.

ditions, indicating that the yield is around 94%. Compared to internal excitation, the distribution of final carbon-sulfur bond length in post-attachment dissociation is broader yet the expectation value of the bond-length is larger. The charge carried by the ejected phenyl ring is found to be zero in all initial conditions. Although this result suggest that electron attachment does not lead to heterolysis, we would like to point out that the simulations takes place in vacuum. Real resists are likely dielectric media. Therefore, a logical extension of this study will be incorporating dielectric medium into molecular dynamics calculations.

### 5.3.3 Reactions after S-C bond cleavage

In the broader context of TPS PAG chemistry, the cleavage of S-C bond, the subject of the study, is merely the beginning a series of chemical reactions. Due to the volatile nature of the immediate products of S-C bond cleavage, they react readily. The in-cage or cage escaped products previously reported [40, 115] are understood to be results of the fragments reacting with each other or the substrate, suggesting that S-C bond cleavage initiates the entire process [40, 116, 115]. This work demonstrates that the cleavage of the S-C bond can be predicted with ab-initio molecular dynamics calculations, products further downstream, such as in cage products where the phenyl fragments recombine, are subject to environment dependent reactions. For example, the lifetime of the ejected phenyl depends on the density and moiety of the surrounding. To accurately predict the outcome, of these reactions, an accurate description of the environment is needed. The size of the system would therefore have to be increased dramatically. Further investigations into methods specialized for large systems is required for scalable investigations of the interaction of the active species their surroundings.

## 5.4 Relative Importance between Internal Excitation and Electron Attachment

### 5.4.1 Existing Experimental Investigations

One of the leading questions in CAR chemistry is the relative importance of internal excitation and electron attachment. Due to the complexity of the thermal chemistry subsequent to acid generation, and the fact that both would lead to dissolution switch, studying this problem using exposed resists presents huge difficulties. Pulse radiolysis (Time resolved optical spectroscopy with electron pump) appears to have confirmed the prevalence of electron induced chemistry [13]. Furthermore, cathode-luminescence experiment appeared to have put a upper limit of 0.5 internal excitation per incident EUV photon [41]. While both provided valuable information for the subject matter, they have their limitations.

On the one hand, the pulse radiolysis works reported in [13] were performed in solution phase using molecules that in some way resembles a PAG. On the other hand the cathode-luminescence work delineated in [41] were performed on condensed film instead of liquid phase solutions. However, since PAG molecules fragments upon excitation, they by definition do not fluoresce (fluorescence is a process through which an electronically excited molecule relaxes to ground state by releasing a photon). As a result, fluorescence dyes were used in place of PAGs. Given the highly conjugated nature of such dyes, their optical absorption cross-sections are expected to be comparable to or higher than PAGs. As such, this experiment can still provide an upper bound. Another noteworthy aspect of this experiment is the incident electron energy. While some data was taken with 80 eV electrons, which are representative of primary photoelectrons (see chapter 2), most of the measurements were made with way more energetic electrons.

Given the immensity of this challenge, notwithstanding the aforementioned limitations, such attempts were respectable. However, given the indirect nature of such measurements, it is worth the while to revisit this subject from a different perspective. While it is extremely difficult, if not impossible to compute electron capturing cross-section in absolute terms for PAG molecules, it is possible to compare quantum chemistry computations, and DUV/EUV dose to draw indirect conclusion regarding the relative importance of internal excitation and electron attachment.

### 5.4.2 Reports on DUV insensitive EUV PAGs

Such opportunity was brought to light in a study involving engineered PAG molecules [107]. In this work the authors attempted to engineer the electron affinity of PAGs by altering the chemical structure of the PAG molecule. They reported that (see figure 7 of [107]) the engineered heterocyclic PAGs have similar performance as triphenyl sulfonium (TPS), the reference PAG, when exposed to EUV. However, when exposed to DUV, the heterocyclic PAGs are 10 times less sen-

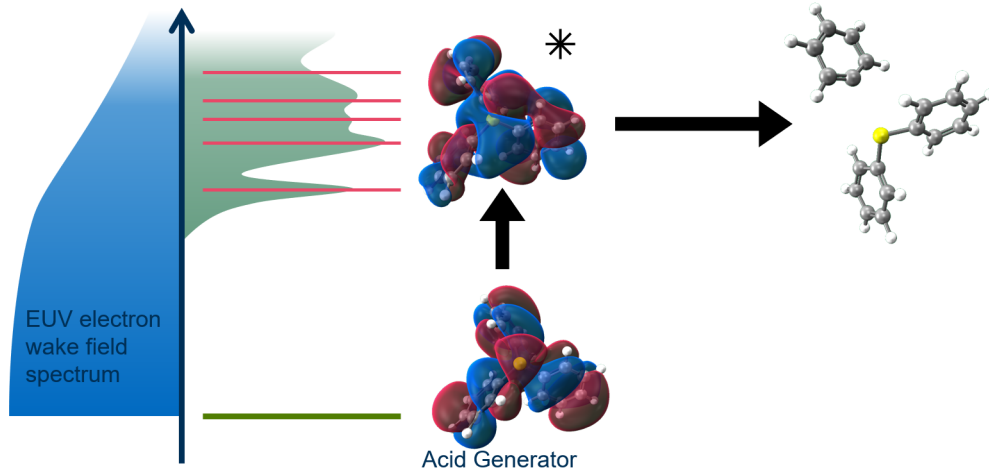


**Fig. 5.8** A schematic illustration of the difference between EUV internal excitation and DUV excitation. In DUV the radiation has a very narrow band while the wave radiation in EUV has a very broad spectrum

sitive than TPS. It appears that the low sensitivity to DUV does not spell disaster to their EUV performance.

This result appears to imply that internal excitation, which is conceptually similar to DUV optical excitation, does not contribute much to EUV sensitivity. In reality, there is a small but important difference between EUV internal excitation and DUV optical excitation.

#### 5.4.3 Possible Causes for Low DUV sensitivity

One of the difference between EUV and DUV excitation is the energy spectrum. In DUV, it is narrow band real photons (can be modeled as plane waves) that are responsible for the electronic transition. In EUV however the *de facto* radiation is the wake field of a traveling electron as observed by a stationary PAG molecule. The spatial extent of the wake field is much smaller than EUV wavelength, making it a virtual photon process. Also, the wake filed is actually a broad band radiation and the on-axis component is shown in equation 5.1 and illustrated in figure 5.8.

$$E_x = A_0 \omega \frac{1}{v^2 \gamma^2} K_0(\lambda \rho) = \frac{1}{v \gamma} \left[ A_0 \frac{\omega}{v \gamma} K_0(\lambda \rho) \right] \quad (5.1)$$

$$\lambda^2 = \omega^2 \left( \frac{1}{v^2} - \frac{\epsilon(\omega)}{c^2} \right) \quad (5.2)$$

Two failure modes could explain the loss in DUV sensitivity

1. The excited state energies are elevated above 248 nm

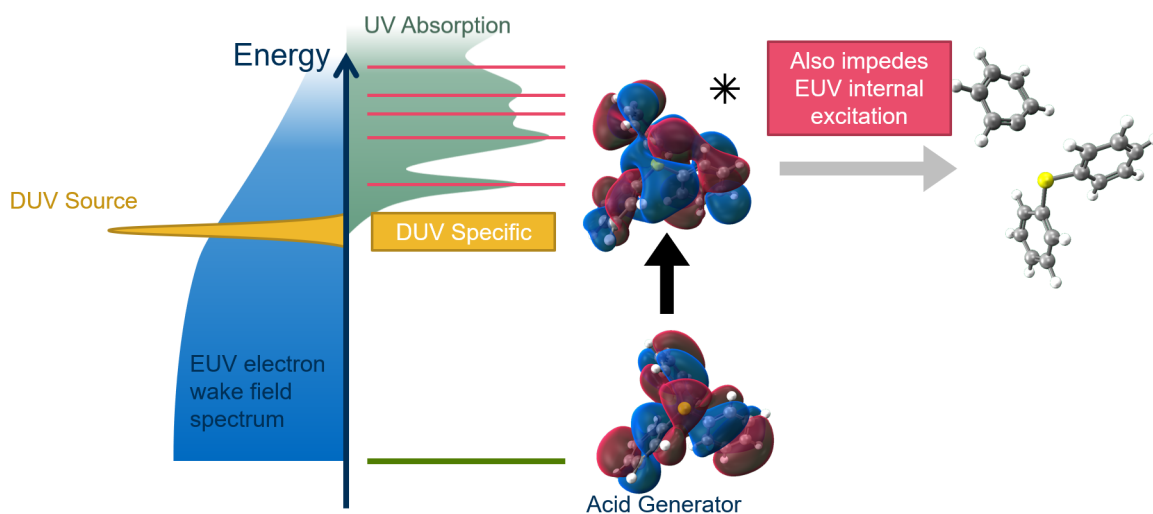


**Fig. 5.9** Illustration of failure modes. DUV specific mode 1 is highlighted in yellow and mode 2 in red

## 2. The molecules do not fragment favorably after excitation

Failure mode 1 would have limited effect on EUV internal excitation but is detrimental to DUV excitations. Failure mode 2 however would hinder both EUV and DUV pathways equally.

### 5.4.4 Failure mode 1—Optical Absorption

To understand if failure mode 1 is at play, one can theoretically evaluate the optical absorption spectrum using linear response time dependent density functional theory (TDDFT) as shown in figure 5.10a. With the use of Gaussian basis and a reasonable number of virtual orbitals included, the Casida formalism[3] is selected and implemented in Q-chem with the Tamm Dancoff Approximation[113]. The PBE0 hybrid functional was used in conjunction with the def2-TZVPD basis set. Molecular geometries were relaxed with the same functional and the def2-SVP basis set.

The optical absorption spectra of the PAGs 0, 1, 2, 4, and 5 are obtained by broadening the TDDFT transition lines by 0.2 eV as shown in figure 5.10a. As one can see the optical absorption edge of all PAGs are much lower than 5 eV, indicating that all of them are capable of absorbing 5 eV (248 nm) photons. It is also noticeable that the optical absorption of PAGs 1, 2, 4 and 5 at 5 eV is either comparable with or better than PAG-0 (TPS) at 5 eV. In fact, their integrated absorption up to 5 eV (a proxy of excited states accessible with 248 nm photons) is consistently larger than TPS (figure 5.10b). Apparently, the lack of DUV sensitivity is not originated in optical absorption and that appears to suggest that the lack of DUV sensitivity is a result of non-ideal post excitation molecular dynamics.

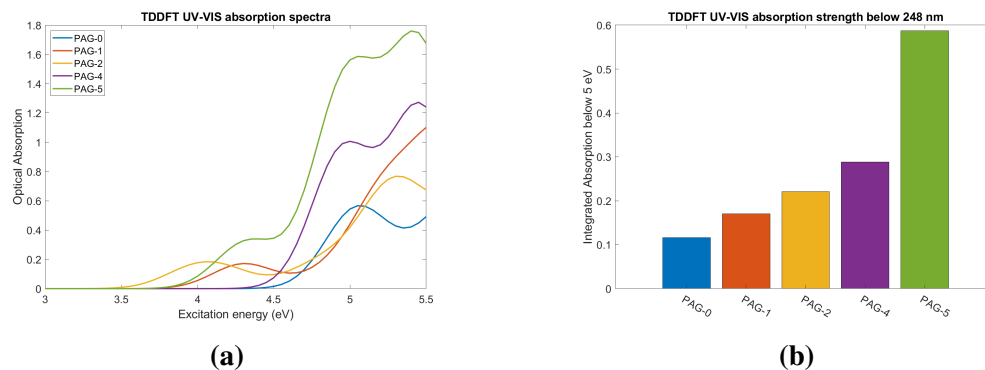


**Fig. 5.10** (5.10a) The optical absorption spectra computed with TDDFT. Absorption lines are broadened by 0.2 eV. (5.10b) The integrated optical absorption up to 5 eV

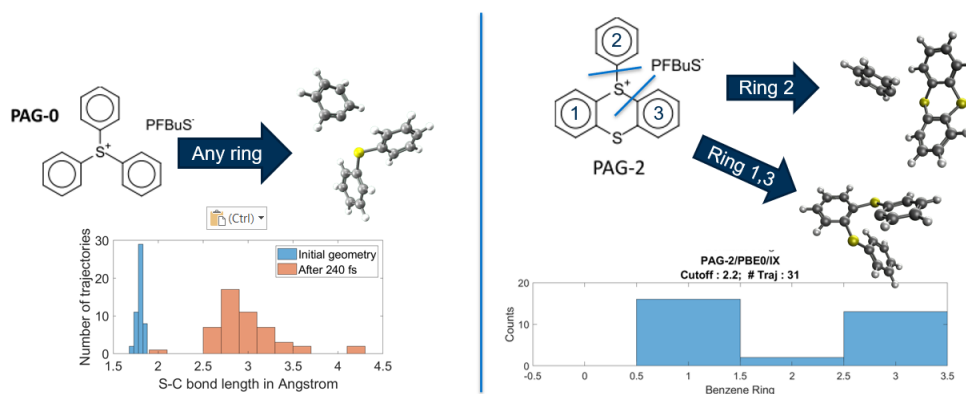


**Fig. 5.11** The fragmentation yield of PAG-0 and PAG-2 at the first excited state. For PAG-2, benzene ring 0 indicates no fragmentation.

#### 5.4.5 Failure mode 2—Fragmentation Dynamics

Logically, mechanisms 1 and 2 are exhaustive. In other words, if optical absorption is not responsible for the DUV performance problem, undesirable post absorption dynamics must be. None the less, to be through we seek to explicitly investigate 2 with *ab-initio molecular dynamics* (AIMD) computations as describe in section 5.3. PAG-0 and PAG-2 are compared as shown in

Upon optical excitation to the first excited state, PAG-0 (TPS) as previously mentioned, is very likely to eject a phenyl radical or cation with an expected yield (The likelihood that the S-C bond length is longer than the 2.2 Å cutoff) of 94%. On the contrary, PAG has multiple fragmentation outcomes. Only 3 our of the 31 initial conditions resulted in the ejection of ring-2, indicating likelihood above 94% of sulfur-carbon cleavage at the first or third ring, resulting in a shuttlecock shaped product which is presumably less mobile than a benzene radical/cation.

Such inability to reliably produce benzene radical/cation appears to impede PAG-2's performance upon DUV excitation and would supposedly hinder EUV internal excitation as well. The

fact that a huge increase in EUV dose was not reported in [107] for PAG-2 indicates that internal excitation probably does not play a huge role in EUV sensitivity. The author would caution against interpreting the chemical yield from AIMD computations quantitatively because these calculations were after all made in vacuum with no representation of the environment. However, given the stark contrast shown in these calculations, it is unlikely that internal excitation would play a huge role. This investigation, together with pulse radiolysis [13] and cathode-luminescence work conducted previously, might not have been perfect given the difficulty of the problem. Yet, since all three of them point towards the same answer, the prevalence of electron attachment driven processes over internal excitation is the most reasonable interpretation.

#### 5.4.6 Limitations of the Current Molecular Dynamics Computation Scheme

There are few obvious shortfalls of this methodology. Firstly, density functional base methods are known not to be accurate for describing homolytic cleavage especially in the regime where there is singlet-triplet degeneracy. Secondly, there is no representation of the environment. Thirdly, since electrons carry spin, it is possible that total spin angular momentum don't conserve upon EUV internal excitation (through angular momentum exchange with the incident electron), yielding a triplet excited state.

The first issue is mitigated by the fact that DUV bond cleavage was reproduced with our excited state AIMD computations. To account for the multi-reference (two or more Slater determinants with comparable importance) nature some point in the bond breaking process, explicitly multi-reference methods such as complete active space self consistent field (CASSCF) or more recent "spin-flip" methods, which could provide accurate results by using a high spin reference for a low spin system, are needed. Due to the enormous computation demand or scarcity of stable implementations, such methods are not practical for investigating collections of PAG molecule. Moreover, multi-reference computation time scales worse than  $N_{basis}^6$ , in contrast to  $N_{basis}^4$  of hybrid density functional methods. Therefore, for molecules as big as these PAGs, computation time could be intractable.

However, one can qualitatively assess the bond fragmentation process by investigating the potential energy surface (PES) in place of a full off random-sampled molecular dynamics ensemble simulation, as described in the next section

The second issue can be addressed by solvent model such as the polarizable continuum model (PCM)[112]. Such models are known describe the dielectric nature of the background well and which is important cations. The author does caution that solvent model would increase the chance of non-convergence.

The third issue can be addressed by repeating the the above computations with a triplet excited state. In the process of addressing the first issue, spin flip methods were used. In other worlds,

triplet PES were computed and their implication on the relevance of triplet excited states will be discussed as well.

## 5.5 Assessing the Accuracy of Molecular Dynamics Simulation Using Spin Flip Methods

Density functional theory, even in the most ideal situation, is only accurate if the ground state charge density is unique. Along the course of homolytic bond breaking, the singlet and triplet states would approach near degeneracy and the premise of unique ground state charge density becomes questionable. To understand how this issue would impact our conclusions, we sought compare our computations with spin-flip TDDFT methods [117], which has been demonstrated to cope with the multi-reference nature of the bond breaking process better.

Stable implementations of SF-TDDFT that is also compatible with the Tully FSSH algorithm do not exist in Q-chem, making this comparison difficult. However, it is understood that reaction dynamics can be inferred from the potential energy surface (PES) of the reaction. In this case, to study the PES is to compute the energy of the ground state and the excited states as one rigidly pull the phenyl ring away from the sulfur center.

As one can see, when it comes to the first excited state, TDDFT (figure 5.12) and SF-TDDFT (figure 5.13a) are very consistent—both showing a slightly dissociative profile near the equilibrium position. The TDDFT computations near equilibrium also provides another valuable piece of information. Since a triplet reference is needed for spin flip calculations, one automatically obtains the energy of the first triplet state, which appears to be around 3.5 eV above the spin flipped singlet ground state in SF-TDDFT and 4.1 eV above the singlet ground state using a non spin-flip singlet reference. Since a singlet reference is better in describing the singlet ground state, 4.1 eV would be a better estimate of the actual triplet excitation energy, which put it rather close to the singlet excitation energy of around 4.9 eV. In other words, the energetic of triplet excitation does not appear to be significantly more favorable than singlet excitation.

The SF-TDDFT formalism used is observed to be quite susceptible to spin contamination. In other words, some excited states are evaluated to not have a definite spin angular momentum—an unphysical solution. To remedy this problem, the same PES is evaluated with Spin adapted spin-flipped TDDFT (SASF-TDDFT). As one can see in figure (figure 5.13b), qualitatively, TDDFT, SF-TDDFT, and SASF-TDDFT all predict a slightly dissociative PES for the first excited state. As such, one anticipates the AIMD computations, which are essentially TDDFT, to qualitative reproduce the behavior of the actual molecule.

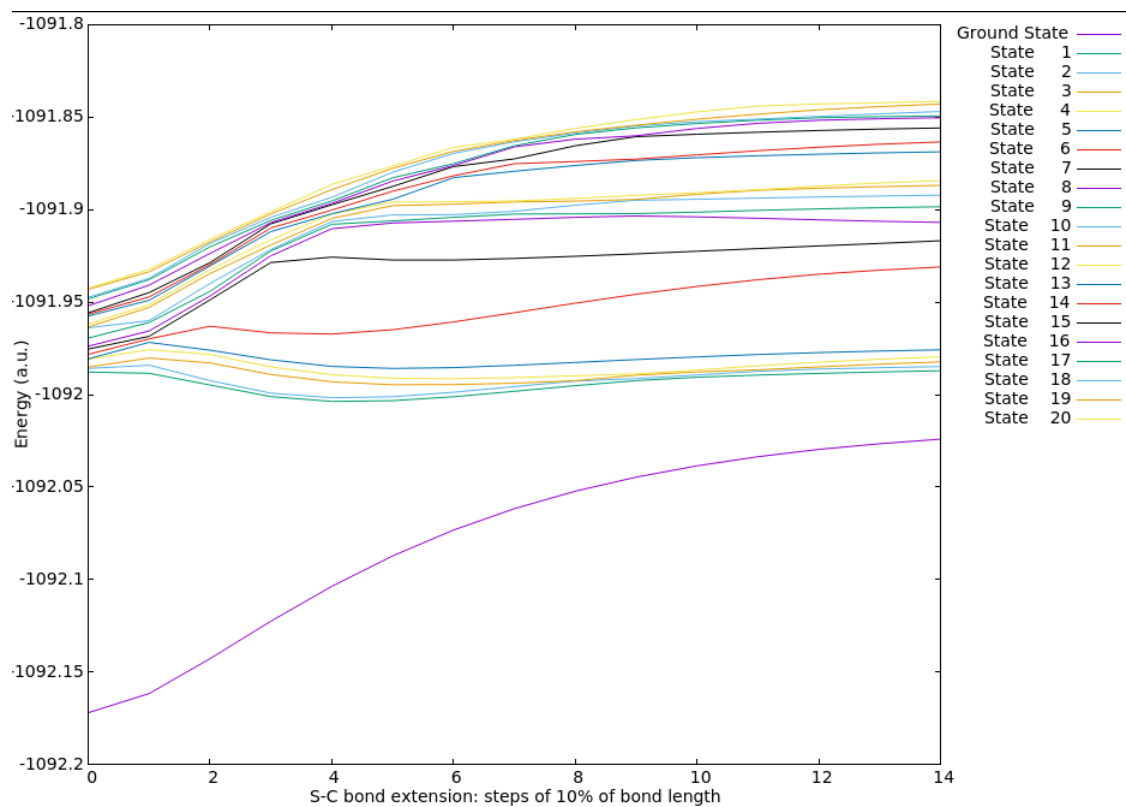
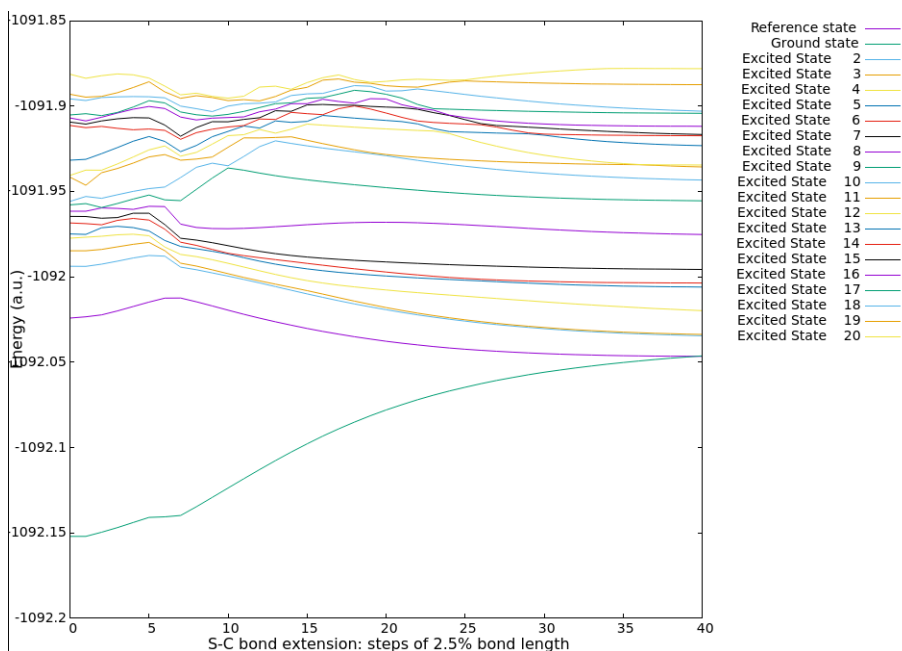
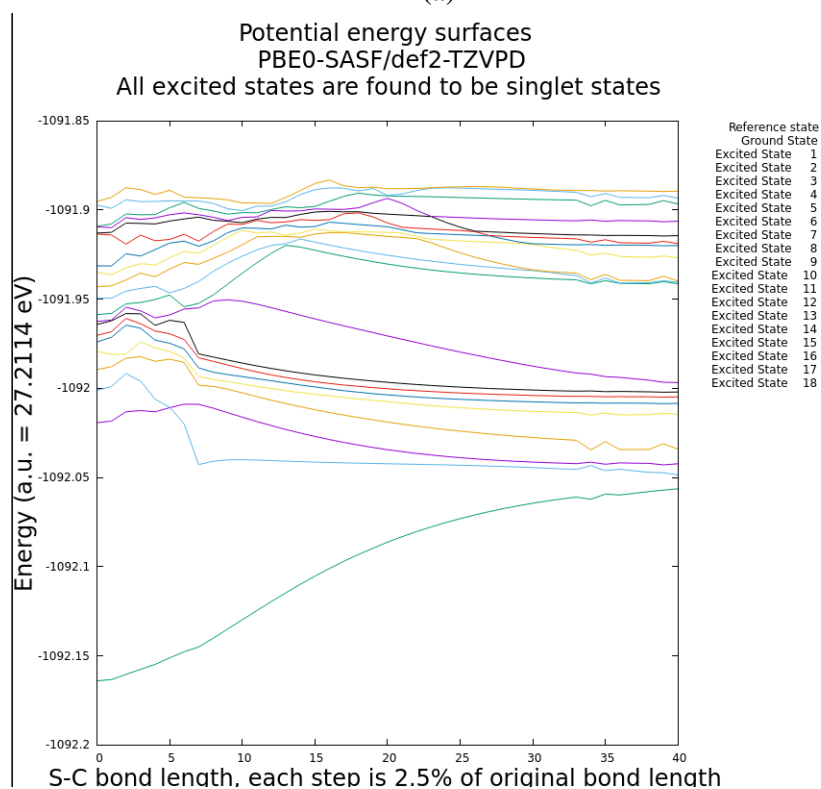


**Fig. 5.12** The potential energy surfaces of the phenyl ejection reaction (sulfur-carbon bond cleavage) evaluated by TDDFT





(a)



(b)

**Fig. 5.13** The potential energy surfaces of the phenyl ejection reaction (sulfur-carbon bond cleavage) evaluated by SF-TDDFT(a) and SASF-TDDFT(b)

## 5.6 Between PAG activation and acid generation

In DUV, acid generation only involves the photo acid generator. If one follows the reaction closely, the charge neutrality is ensured across the entire process. In EUV however, if we focus only on the PAG, we notice there is a net increase of negative charge. In the case of the archetypal TPS triflate, a very unstable neutral TPS radical and a triflate anion are produced. In the end, it's the triflate acid who's responsible for acid catalytic deprotection, and identifying how the proton is extracted to enable acid production would provide useful information. Moreover, as ionization takes place in the polymer, radical cations are left behind. Intuitively, they would play a part in acid generation for a few reasons. Firstly, they are unstable and for any given electron there is a radical cation left behind. It would be inconceivable if none of them partake in acid generation. Secondly, they possess a positive charge, getting rid of which could prove energetically favorable. Deprotonation upon ionization has been proposed as a relaxation pathway of this sort. In light of such development, the author would further investigate the role of polymer radical cation in acid generation.

There are two competing concepts on the role of radical cation. In the first one, the independent mechanism, electron attachment chemistry and ionization chemistry can separately generate acid (similar to the tin-oxo systems in chapter 6 where the almost exact same scission can be initiated by either ionization or electron attachment). In the second hypothesis, namely the rendezvous mechanism(s), the intermediates generated through ionization have to recombine with those from electron attachment to form an acid.

The proponents of the independent mechanism, such as Dr. Robert Brainard from SUNY, Albany, believe that rendezvous mechanisms are impractical because of their second order nature—the products of two reactions have to find each other, significantly reducing the likelihood of reaction. The biggest issue with the independent mechanism is that reactions involved are not identified or even proposed as of yet. When TPS-triflate is used, triflic acid would be the target product. For the ionization only chemistry to be convincing, a mechanism which the ionized polymer deprotonates and recombines with the triflate anion must be present. Similarly upon electron attachment, even though it is evident that a phenyl radical is generated, how a proton can be extracted from the interaction between a neutral radical and the surrounding polymer is not trivial. As of now, one of the biggest inconsistencies between the independent mechanisms and experiment is the fact that one can experimentally reduce acid generation by a factor of 1/20 by altering the polymer [38]. That either implies that the electron attachment part of the chemistry is not contributing much, or the two processes have to come together at some point.

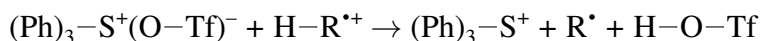
On the other hand, there are more comprehensive mechanistic propositions for the rendezvous mechanisms. Kozawa concluded in the most likely scenario, the radical cation would deprotonate

spontaneously upon ionization [13]. Meanwhile, the TPS cation is neutralized to release the triflate anion. The two rendezvous with each other to form a triflate acid. This mechanism is supported by experiments (Please refer to references in [13]). A slightly different hypothesis suggests that deprotonation and neutralization of the TPS cation are not independent. Instead, the phenyl radical generated from electron attachment is responsible for triggering the deprotonation [4]. The statistical correlation between the two events would make the proton-triflate rendezvous more likely than a simple second order reaction, partially addressing questions raised by the proponents of the independent mechanism.

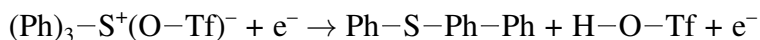
As mentioned in section 5.3.2, the complexity of the problem cannot be underestimated. The interaction between involved molecules and the surroundings cannot be ignored, as a results, the number of possible reactions can potentially be very huge. In lieu of attempting to exhaustively decimate this problem, one seeks to limit possibilities by identifying simple constraints. In other words simple energy computations of initial reactants, products, and transition geometries have been carried out to at their respective electronic ground states to understand whether any of these mechanisms make sense at all.

### 5.6.1 The independent mechanism

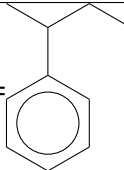
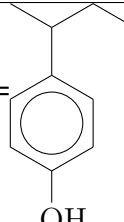
The most simplistic approach to tackle the independent mechanism is to look at the energy difference the initial reactants and the final products. On the ionization side, it is assume the independent hole reaction leaves the TPS cation a spectator.



On the electron attachment side, it is assumed that polymer is not involved and the electron is a spectator. In essence, this reaction is equivalent to a isomerization of TPS-triflate.



To imitate the effect of the polymer backbone, the SMD solvent model [118] was used. Since ions are involved, the biggest correction comes from polarization. Therefore, imitating the dielectric response would be vital. As poly(hydroxystyrene) (PHS) and polystyrene (PS) have been commonly used for acid generation studies such as [38], benzene and benzylalcohol were chosen to represent the two respectively. Benzylalcohol were chosen in place of phenol because phenol is a solid in atmospheric conditions, there no solvent particularization exists. PS is represented by a methyl terminated saturated monomer 2-phenylbutane for simplicity and PHS is represented 4-(1-Methylpropyl)phenol for similar reasons. Calculations were perform at the level wB97X-D/def2-TZVP//wB97X-D/def2-SVP (High precision energy evaluated at wB97X-D/def2-TZVP and geometries optimized at wB97X-D/def2-SVP).

	 PS/R= (Benzene)	 PHS/R= (Benzylalcohol)
Ionization only	0.73 eV	0.67 eV
Electron only	-0.50 eV	-0.23 eV

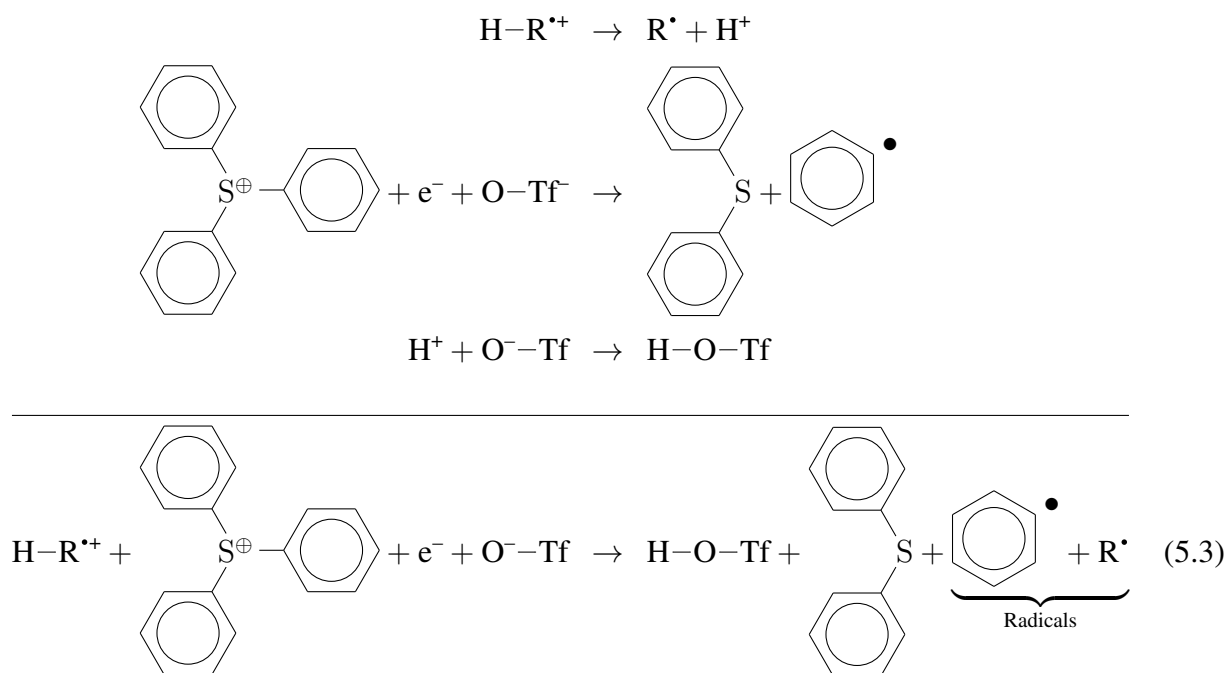
**Table 5.2** The reaction energies if the ionization and electron attachment reactions are fully independent

As one can see from table 5.2, the ionization pathway is endothermic. Yet the ionization process (not included) takes around 6 to 10 eV and could put the polymer into an excited state so overcoming a barrier of around 0.7 eV is not inconceivable. The polymer radical cation is assumed not to interact with the TPS cation due to Coulomb repulsion. The electron process is strictly exothermic. However, as previously shown, the electron attachment process is exothermic (0.3 eV as a conservative estimation. Combining figure 5.4 and table 5.1, 0.3 eV is a rough estimate for TPS acetonitrile, which is more polar than either PS or PHS. The extra polarity of acetonitrile results in underestimation of electron affinity) and the subsequent cleavage of sulfur-carbon bond would further release 0.3 eV. In other words, take the more optimistic case of PS, upon electron attachment the intermediate state  $\text{Ph}_2\text{-S} + \text{PH}^* + \text{O-Tf}^-$  is already 0.6 eV below the initial reactants and slightly below the proposed final products. Even if the two are comparable energetically (which is a reasonable statement given the computations are rather rudimentary, the two could be indistinguishable), it takes some creativity to propose a proton transfer mechanism in the absence of a positively charged specie that also has a low reaction barrier (since the energy difference between the intermediate and final states doesn't suffice to drive the reaction).

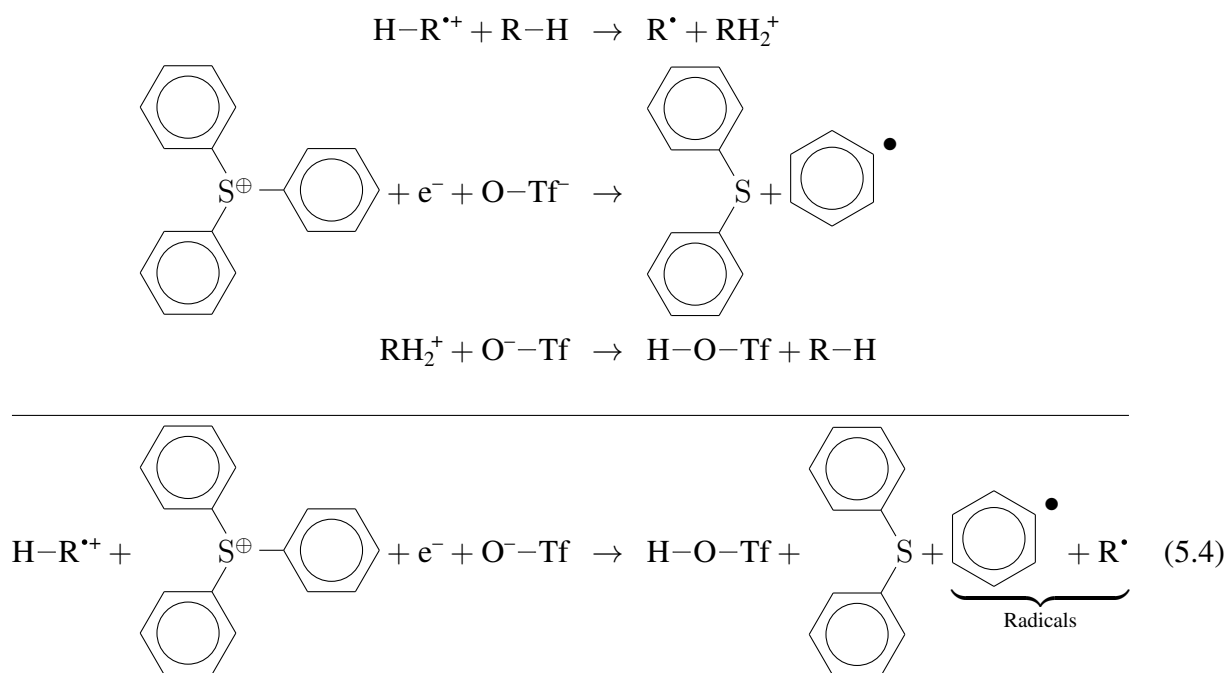
## 5.6.2 Rendezvous Mechanisms

### 5.6.2.1 Last Minute Rendezvous

The first rendezvous mechanism assumes that the ionization generated deprotonation and the electron induced PAG fragmentation happen independently [13] (The first two reactions in schemes 5.3 and 5.4 can happen in any order). However, the products of the two have to combine at the very last moment for acid generation. equation 5.3 provides a simplistic view of deprotonation as proton solvation is ignored entirely.



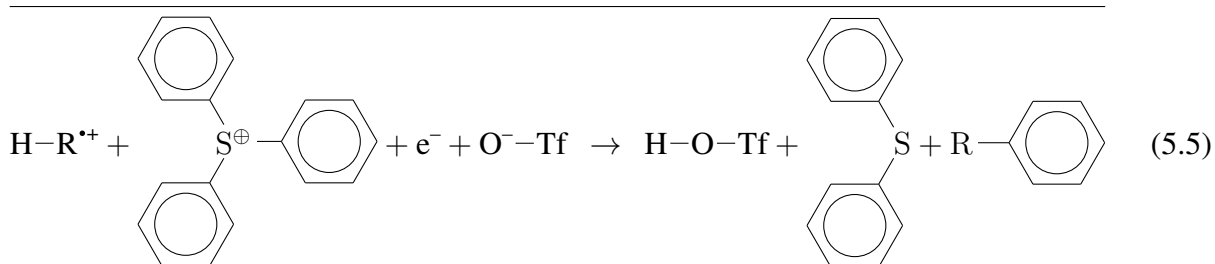
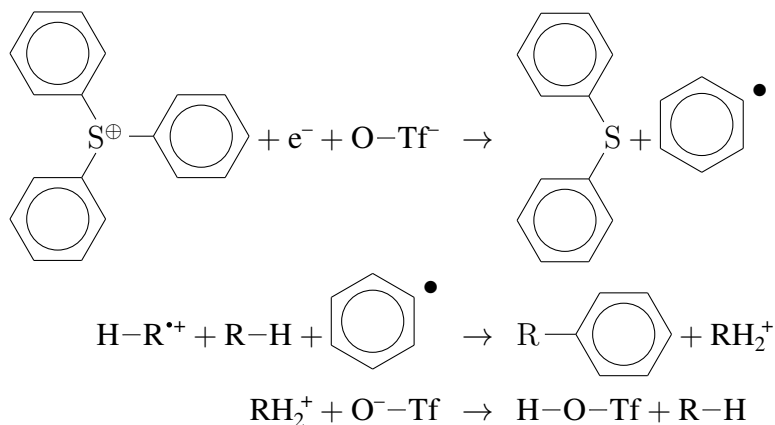
It is however noted in [13] that as deprotonate happens, the proton is more likely “dissolving” itself into neighboring neutral polymer molecules to form a metastable complex. However, even if the intermediate steps differ from scheme 5.3, the net initial reactants and final products turn out to be the same as shown in scheme 5.4. The polymer acting as a proton solvent is ultimately a spectator.



### 5.6.2.2 Rendezvous-Relay Mechanism

The second mechanism summarized by Hinsberg and Wallraff [4] suggests that deprotonation is prompted by a radical attack. In other words, deprotonation always happen after dissociative

electron attachment of the TPS cation.

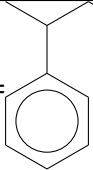
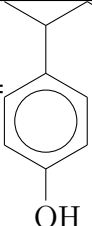


If one only considers the initial reactants and final products, schemes 5.3, 5.4, and 5.4 are very similar. Indeed the only difference lies in the final product. In the Last Minute proposition [13], the radicals can be left free. In the Rendezvous-Relay mechanism, the radicals would have already recombined. Rather obviously, due to the exothermic nature of bi-radical recombination, the Rendezvous-Relay mechanism is expected to be more energetically favorable.

### 5.6.3 The Two Rendezvous Mechanisms

The energy difference between the reactants and products are tabulated in table 5.3. Again, the energies are evaluated at the level  $\omega\text{B97X-D/def2-TZVP//}\omega\text{B97X-D/def2-SVP}$ .

There are few interesting observations. First of all, not so surprisingly, the Rendezvous-Relay Mechanism is more favorable energetically because of the net bi-radical recombination. The author would caution that such simple reactant-product comparison ignores the intermediaries which determines energy barrier and reaction order, factors which in the end could be limiting. Given the how exothermic the reactions are, one can none the less conclude that these schemes cannot be eliminated. Secondly, it has been reported that more acid is generated by PHS (by a factor of 20 compared to PS) [38], an observation that these simple computations cannot explain. Alluring to the first observation, one needs too look closer into the details. While the release of the anion is similar in both rendezvous mechanisms, the way that the proton is generated is very different. In

	 PS/R= (Benzene)	 PHS/R= (Benzylalcohol)
Last Minute Rendezvous	-2.65	-2.04
Rendezvous-Relay	-7.79	-5.90

**Table 5.3** The energy difference between the final products and initial reactants of the rendezvous mechanisms in eV

the Last Minute pathway, the proton is generated uncorrelated to the neutralization of TPS cation [13], possibly with excess energy from the impact ionization process. In the Rendezvous-Relay mechanism, deprotonation occurs upon phenyl radical attack. A more detailed investigation of the deprotonation process could help identify the dominant pathway.

#### 5.6.4 Unmediated Deprotonation in Last Minute Rendezvous

When deprotonation takes place in a dense environment (liquid or condensed) phase, the proton dissolves itself into neighboring molecules to form metastable complexes [13, 119]. The stability of these complexes relative to the radical cation determines the mobility of the proton.

The stability of the radical cation can largely explain the relationship between the polymers and acid generation in [38]. Indeed, by including electron withdrawing group at the *para*- position, the polymers become better conjugate bases upon deprotonation and these modifications coincide with an increase in acid yield. Conversely, when the most favorable deprotonation site—the alpha carbon (because of radical resonance structures that extends to the phenyl ring) has the only hydrogen replaced by methyl, the deprotonation cost increases, reducing acid yield. These arguments apply very well in vacuum as they are in polar solvents

However, as the vacuum deprotonation energies are computed for PHS and PS monomers, the vacuum deprotonation energy is more confusing. The cost to deprotonate in vacuum is actually lower for a PS monomer. The Coulomb interaction between the proton and the remaining radical makes deprotonation energy very sensitive to the dielectric background. Moreover, neighboring molecule would accept the proton and form a metastable state. This process would also alter the deprotonation likelihood.

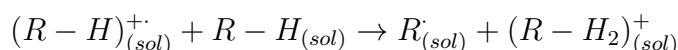
To fully account for the the surroundings, two measures are taken. First, all reactions are evaluated in solvents that reasonably represent the molecules (benzene for PS and benzylalcohol for PHS. The SMD solvent model was used). Secondly, proton dissolution is taken into account as



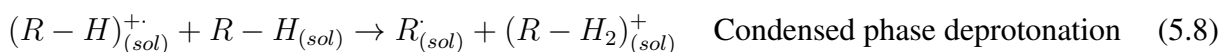
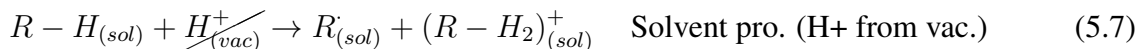
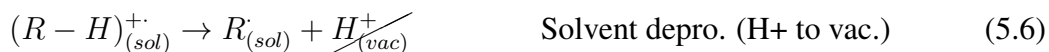
	Protonation site	Protonation energy (eV)
PHS monomer	OH	-10.685
	meta-	-10.945
	ortho-	-10.570
PS monomer	para-	-9.709
	meta-	-9.474
	ortho-	-9.665

**Table 5.4** Protonation energy (see equation 5.7) of PHS and PS monomers at different sites on the phenyl ring

described in literature [13, 119]. Essentially, the following reaction is considered



For a monomer with  $N$  hydrogen atoms and  $M$  protonation sites, there are  $M \times N$  proton shift combinations. However, the deprotonation-proton solvation reaction can be broken into two separate reactions. The total energy of the reaction is the sum of the two.



The protonation energy (equation 5.7) depends on the site. Not surprisingly PHS (represented by 4-(1-Methylpropyl)phenol) has a much higher proton affinity than PS (represented by 2-phenylbutane). However, contrary to what [13] proposed, the meta position is the best protonation site. Given that the different positions on the PS phenyl ring show a smaller spread (of around 0.24 eV, compared to 0.37 eV of PHS), the effect of hydroxyl group is not only systematic—it also alters the relative reactivity of the rest of the ring.

With proton solvation accounted for, the total deprotonation energy can explain the trends observed in [38]. As one can see in figure 5.14, in vacuum, the resonance protected alpha carbon on the PS monomer is the most favorable deprotonation site with a cost of 9.17 eV. The optimal deprotonation site shifts to the hydroxy group in the PHS monomer but the deprotonation cost is still around 0.7 eV higher than PS.

Upon immersion in respective solvents and accounting for proton solvation (at the most favorable site listed in table 5.4), deprotonation is easier for PHS by a margin of 0.67 eV (0.70 eV at

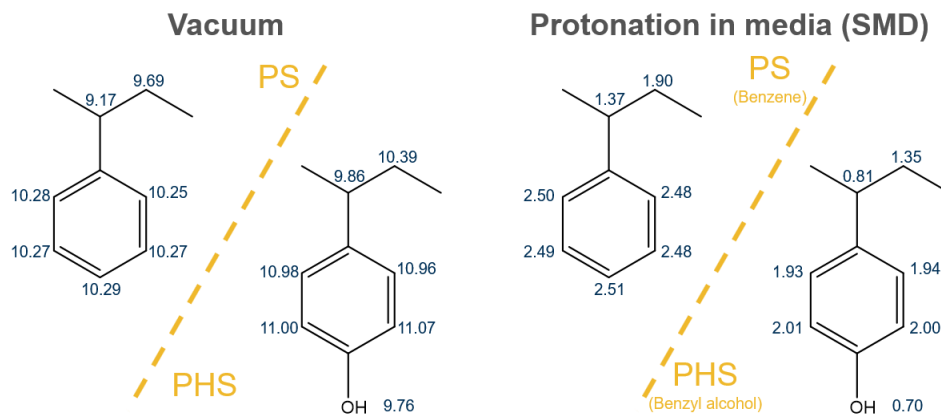
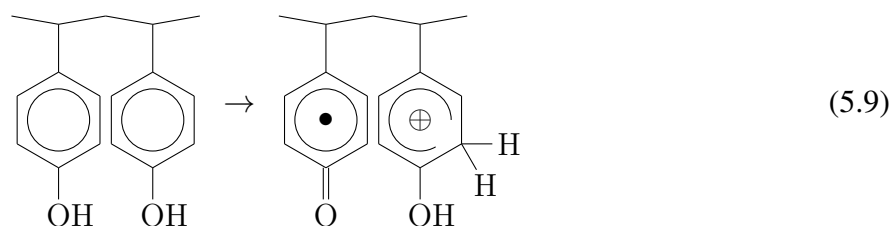


**Fig. 5.14** The deprotonation energy in vacuum (left) and in respective media with proton solvation accounted for (right). Energies are measure in eV

the OH on the PHS vs 1.37 eV at the alpha carbon on the PS). In the protonation computation, two separate molecules are used as the source and destination of the proton. To have a rough idea of the robustness of the deprotonation energy, the computation is repeated for analogous proton shift in a dimer as shown in scheme 5.9. The cost is 0.8 eV, which, given the 0.2 to 0.5 eV accuracy of DFT computations (with the current configuration the accuracy is assumed to be worse), is indistinguishable from inter-molecule deprotonation.

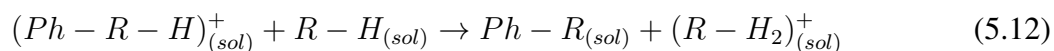
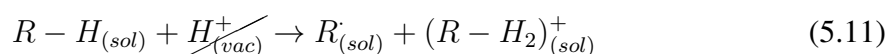
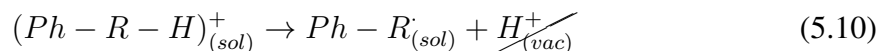


With the in-media deprotonation-protonation energy consistent with [38], it appears that not only is the polymer providing a proton for the acid, its ability to solvate protons also matters. Higher proton solubility increases the likelihood of deprotonation and eventually rendezvous with the conjugate base. The above computations suggest that proton solubility contributed significantly to the advantage that PHS holds over PS. Since the OH group is changing the proton affinity of the phenyl ring from a distance, we assume alkyloxy groups (such as methoxy group) would have similar effects to a different extent. Our computation also reveals that the advantage of eliminating a proton from the OH group upon ionization is optimal but by only a small margin over the  $\alpha$ -carbon (the carbon on the chain that branches out to the phenyl ring). In other words, if one replaces the hydroxyl group with methoxy group, we anticipate that deprotonation upon ionization would probably be less likely than PHS but still significantly more likely than PS. It has been

proposed that by replacing the hydroxyl group with methoxy group, ionization driven deprotonation will be eliminated [120] (In that reference, ionization driven deprotonation is referred to as “Kozawa mechanism”). The above mechanistic computations suggests that the reality could be a bit more nuanced. Therefore, it is not immediately clear that one can ascribe acid generation in poly(methoxystyrene) entirely to electron only processes, or processes where ionization induced deprotonation do not play a role, without further investigation.

### 5.6.5 Mediated Deprotonation–Rendezvous-Relay Mechanism

The intermediaries of this pathway has been proposed in [4] and illustrated in scheme 5.5. The proton elimination is a two step process in this hypothesis. Firstly, the phenyl radical attack, and secondly elimination of proton. Similar to unmediated deprotonation, the proton is dissolved into another polymer molecule upon deprotonation following a scheme very similar to equation 5.8 except that the proton source is now a full-shell phenylized polymer ion as shown in equation 5.12.

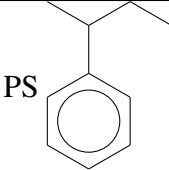
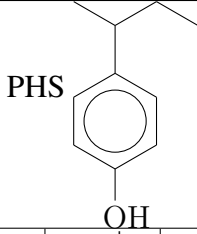


For steric and electronic structure reasons, the radical attack is most likely to happen on the conjugate ring. The phenyl radical attachment energy on the same representative monomers have therefore been evaluated in same respective solvents and so is the subsequent deprotonation. The ortho- meta- and para- positions are expected to have different reactivity so computations were carried out for substitution at all three positions as shown in table 5.5.

It appears that phenyl radical will more readily attach onto PS radical cation (-3.323) than PHS (-2.983) but deprotonation is more favorable in the PHS complex. The total energy of the substitution reaction favors PS over PHS. That appears to contradict the observed acid yield of PHS [38]. Energetically speaking, the second step is limiting but the fact that phenyl addition is a bi-molecular reaction in condensed phase means that the overall reaction is probably kinematically limited by the first.

### 5.6.6 Summary and Prospects on Deprotonation

To sum up, the Last Minute Rendezvous mechanism is more consistent with acid yield measurements [38] on face value. Other factors could be at play. The localization of hole and hole mobility

	 PS			 PHS		
	+ Ph·	-H <sup>+</sup>	Total	+ Ph·	-H <sup>+</sup>	Total
ortho-	-3.318	-0.139	-3.457	-2.558	-0.565	-3.123
meta-	-3.102	-0.417	-3.519	-2.983	-0.128	-3.111
para-/OH	-3.323	-0.197	-3.520	-2.241	-0.356	-2.597

**Table 5.5** The phenyl affinity and deprotonation energy (subsequent proton elimination from the same site) of PS and PHS monomers at different positions on the phenyl ring

in the presence of radical or anion has not been studied extensively. If the radical anion can be localized by neighboring radicals or anion, such statistical correlation implies that phenyl radical attack is no longer a second order reaction, thus less kinematically limiting. More over, homogeneity affects reaction kinematic in condensed phase critically. Homogeneity improves the likelihood of different reactants encountering each other. Polarity induced by oxy bridges could improve homogeneity of sulfonium PAG blended polymer resists [5]. PHS would therefore be better at uniformly dissolving TPS triflate PAG. If that is the case, the advantage of PHS over PS would be purely kinematic and the focus for improving proton generation should be on uniformity. As of now, there isn't sufficient information to prove or disprove the uniformity argument. Binding the PAG onto the polymer at specific sequence can eliminate the difference in film uniformity, thus elucidating the reaction mechanism.

None the less in all conceivable mechanisms, enhancing impact ionization induced deprotonation is beneficial. Therefore, materials with good proton affinity (equation 5.7) could boost acid generation.

Nitrogen atoms in organic compounds are usually good proton acceptors. Including them in a polymer backbone could improve proton solubility. Nitrogen based polymers are not rear—Nylon is a widely used example. Most nitrogen containing polymers have a amide moiety on the backbone, which coincidentally provide multiple protonation sites. The proton solvation energy (equation 5.7) of a prototypical amide polymer is evaluated at the level  $\omega$ B97X-D/def2-TZVP// $\omega$ B97X-D/def2-SVP in conjunction with SMD solvent model. N,N-dimethylacetamide was chose to simulate the environment because it contains the amide functional group.

As illustrated in figure 5.15, proton solvation on the backbone is more exothermic than on the phenyl rings. With the exception of the terminal amine group (which is not next to a electron withdrawing carbonyl group) the carbonyl oxygen and carbon are the most likely solvation sites. The protonation energy is also more exothermic than PHS or PS shown in table 5.4. The prototypical

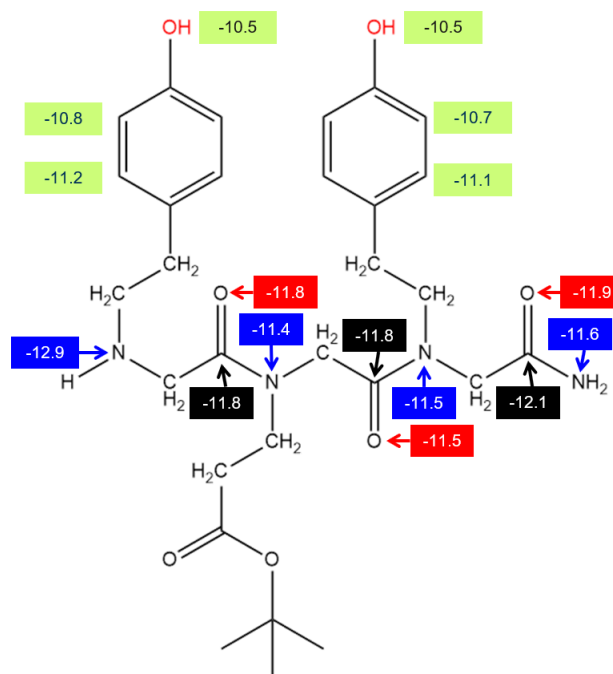


**Fig. 5.15** Proton solvation energy (equation 5.7) of a prototypical amide trimer in eV. Red, blue, and black sites are backbone oxygen, nitrogen and carbon sites.

amide has two PHS like units and the protonation energy on those phenyl rings are consistent with those in table 5.4, suggesting that the amide backbone would indeed promote proton solvation more so than the phenyl rings, hydroxylated or not. Such properties are not relevant in DUV and could have been overlooked in the development of EUV CAR resists.

## CHAPTER 6

### Mechanistic Advantages of Organometallic Resists

#### 6.1 Introduction

The introduction of EUV lithography gave rise to new demands and performance criteria for photoresists. Organotin resists have shown potential for a few reasons. Firstly, tin atoms have a high EUV absorption cross-section[121, 6], thus facilitating a better sensitivity. Secondly, the carbon-tin bond is chemically stable in comparison with alkyl bonds to more conventional transition metals. Such bond strength allows for more stable manufacturing processes. On the other hand, commercial metal oxide resists on the market are in some respect superior to conventional chemically amplified resists (CARs). On the practical front, metal containing systems have several well-known advantages[122]. High etch selectivity has been reported [122]. The combination of high EUV absorption and etch selectivity effectively reduces the thickness of tin-oxo resists and the likelihood of pattern collapse. In addition, compared to conventional polymer resists, molecular resists are more homogeneous in the sense that there are fewer molecular components with all functionalities packed into one molecule. Such uniformity could eliminate material stochasticity. Since every single molecule can hypothetically perform all of the chemical functions, electrons or holes do not need to spatially propagate to active species (such as PAGs or quenchers in CARs) to trigger chemistry, potentially reducing loss in quantum efficiency.

The rise of new activation mechanisms, as previously discussed in chapter 2, has encouraged the exploration of new materials. Organometallic systems also appear to have an efficient mechanism that is very compatible with EUV and is suggested to have good quantum efficiency [123]. Therefore, to understand the origin of its superior performance and fully exploit the potential of these compounds for EUV applications, the exposure chemistry should be closely examined. To that end, we use density functional theory to more thoroughly examine the thermal chemistry subsequent to EUV exposure.

To gain insights, we employ the prototypical “football”  $[(R-Sn)_{12}O_{14}(OH)_6](A)_2$  compound (which will be referred to as  $Sn_{12}R_{12}(A)_2$ ), which has been the center of mechanistic studies for organotin resist[124, 125, 126, 127, 37]. With proper process conditions, this compound is capable

of achieving sensitivity comparable with commercial systems, indicating its potential for practical applications. Given that the chemistry is based upon tin-carbon bond cleavage taking place in a tin-oxo framework, insights gained from studying this system could be useful for understanding similar systems under investigation for application in EUV lithography, such as tin Keggin ions[128, 129, 130].

As shown in figure 6.1,  $\text{Sn}_{12}\text{R}_{12}(\text{A})_2$  consists of twelve tin atoms connected by oxo-bridges, consistent with X-ray crystallography[131]. Six of the tin atoms sit on the “belt” and the other six reside on the “caps”—three for each cap. The tin atoms on the belt are five-coordinate and the ones on the caps are six-coordinate. Each tin atom is connected to an organic side group (R-). Similar molecular frameworks have been reported with different metals such as titanium  $[(\text{EtO}-\text{Ti})_{12}\text{O}_{14}(\text{OEt})_4(\text{O})_2](\text{A})_2$ [132] and vanadium  $[(\text{O}-\text{V})_{12}\text{O}_{12}\text{F}_2(\text{OH})_6]^{6-}$ [133].

The tin cage has a charge of 2+, thus it is normally accompanied by two anions with charge 1-. Through substitution techniques, cages with various anions have been successfully separated and their properties have been investigated[134, 135]. While the anion has been shown to have an effect on exposure sensitivity[124, 135], the anion is believed to play a secondary role to tin-carbon bond chemistry[125, 37]. As we will demonstrate, the tin-carbon bond strength changes by less than 0.1 eV upon the removal of both anions. To simplify calculations, the hydroxide ion is used in this work. Multiple organic side groups have been synthesized and assessed in previous experimental endeavors[136, 137]. To focus our attention on the radiation chemistry of the system, which centers around the tin-carbon bond, we start our investigation with methyl ligands

The biggest difference between EUV and UV lithography is the ionizing nature of EUV radiation excitation source. Due to its high energy, a single EUV photon leaves behind multiple pairs of ionized molecules and low energy electrons[4, 13]. The prevalence of impact ionization and low energy electrons led to the understanding that these events, instead of UV-induced optical transitions, are responsible for initiating exposure chemistry that ultimately results in solubility switching.

Most previous studies used the  $\text{Sn}_{12}\text{R}_{12}(\text{A})_2$  “football” cluster as a “molecular resist” where all functionalities are packed into a single molecule[124, 125, 126, 127, 37] (x-ray crystallography has revealed residual solvent molecules[131]). In that case, both ionization and electron attachment occur in the cluster and the effects of these phenomena on bond strengths and stability have been sporadically explored [127] but are yet to be understood in a comprehensive manner. While experimental endeavors have resulted in a rather comprehensive qualitative understanding of the exposure chemistry, they can be complemented by quantitative investigation which interrogates the details of ionization- and attachment-induced processes.

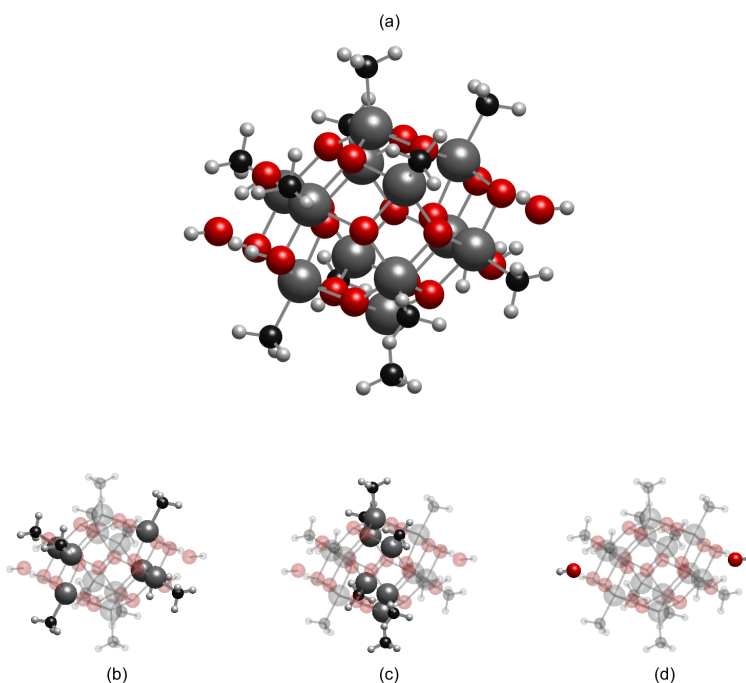


**Fig. 6.1** The structure of  $\text{Sn}_{12}\text{Me}_{12}(\text{OH})_2$  is shown in (a). Red, gray, black and white atoms are oxygen, tin, carbon and hydrogen, respectively. The cap and belt tin-carbon bonds are highlighted in (b) and (c) and the counter anions, in this case  $\text{OH}^-$ , are highlighted in (d)

## 6.2 Computation Methodology

We therefore investigate the network of relevant reactions with quantum chemistry investigations. Radiation processes, in particular ionization, would often excite a molecule to an electronic excited state. However, to fully understand how chemistry is driven by electronic excited states in this context, multi-reference or wave-function methods are needed. Excited-state chemistry often leverages the potentially dissociative potential energy surface (PES). In a bond-breaking process the single determinant description of the electronic structure often breaks down, rendering multi-reference methods such as complete active space self consistent field (CASSCF) necessary for computing the excited state PES[138]. Such methods, albeit accurate, are impractical for  $\text{Sn}_{12}\text{R}_{12}(\text{A})_2$ . A state-of-the-art CASSCF algorithm can efficiently compress the determinant space to enable an active space of (50,50)[139]. However, in the simplest variant ( $\text{R} = \text{methyl}$  and  $\text{A} = \text{none}$ ),  $\text{Sn}_{12}\text{R}_{12}(\text{A})_2$  comprises 86 atoms, which results in a frontier manifold of 88 occupied canonical orbitals. Such computations could still be possible after careful selection of the active space but they are not practical as we set out to elucidate a network of reactions. We would therefore limit our investigation to the electronic ground state, which if unstable, is strong evidence for ionization-driven chemistry.



Due to the size of the system, balance between computational accuracy and speed is necessary, thus the PBE0-D3(BJ) hybrid functional was chosen. Considering that the system is ionic and the radical nature of ionized and electron-attached species, mitigating self-interaction error (SIE) is a priority in the choice of functional. The PBE family has been parameterized to minimize SIE[110] and was shown to perform well with radicals among common hybrid functionals[8].

To incorporate dispersion interaction, D3 corrections[140] with BJ damping[141] is used. Non-local dispersion correction has been considered but the lack of analytic Hessian makes such implementations impractical.

Structures are relaxed with Ahlrich's def2-SVP basis set. The same basis was used in Hessian calculations to extract vibrational modes and thermochemistry at room temperature. Those same Hessian calculations were used to confirm that imaginary modes (with the exception of methyl rotor modes) do not exist. To compute the electronic energy, we performed high accuracy single point calculations with the def2-TZVP basis set. In all calculations, the effective core potential def2-ECP was used for Sn atoms. All calculations were carried out with Q-Chem[142].

We will first have an overview of the thermochemical reaction network of a the prototypical tin-oxo cage upon single-electron attachment or ionization, and in the presence of two, one, and zero counter anions. By examining the network of reactions, we report a few intriguing phenomena.

## 6.3 Origin of Sensitivity

### 6.3.1 Overview

The cage can be accompanied by zero, one, or two hydroxide ions. We first focus on the charge-neutral variant with both hydroxides,  $\text{Sn}_{12}\text{Me}_{12}(\text{OH})_2$  as shown in figure 6.1(a). As one can see there are two categories of tin atoms (and corresponding tin-carbon bonds). In figure 6.1(b), the ones near the cap are 6-coordinate and those on the belt are 5-coordinate. The counter anions are located at the caps in figure 6.1(d).

Prior to ionization or electron attachment, as shown in figure 6.2 the bond dissociation free energies (BDFE) are 2.47 and 2.43 eV for belt and cap methyl groups, which is consistent with thermal programmed desorption (TPD) measurements on a similar system (2.4 to 3.0 eV)[143]. Our calculations were performed in gas phase. Compared to the condensed film used in the experiment, we anticipate the entropy gain from dissociation to be larger in vacuum, resulting in an underestimation of the BDFE. The slight preference for belt homolysis is consistent with previous computational study. The inclusion of entropy and dispersion energy reduces the difference from 0.1 eV to 0.04 eV.

Rather unsurprisingly, homolysis is significantly more favorable than heterolysis (removal of  $\text{CH}_3^+$ )—heterolysis BDFE are 8.7 and 9.5 for belt and cap methyl groups. The difference between

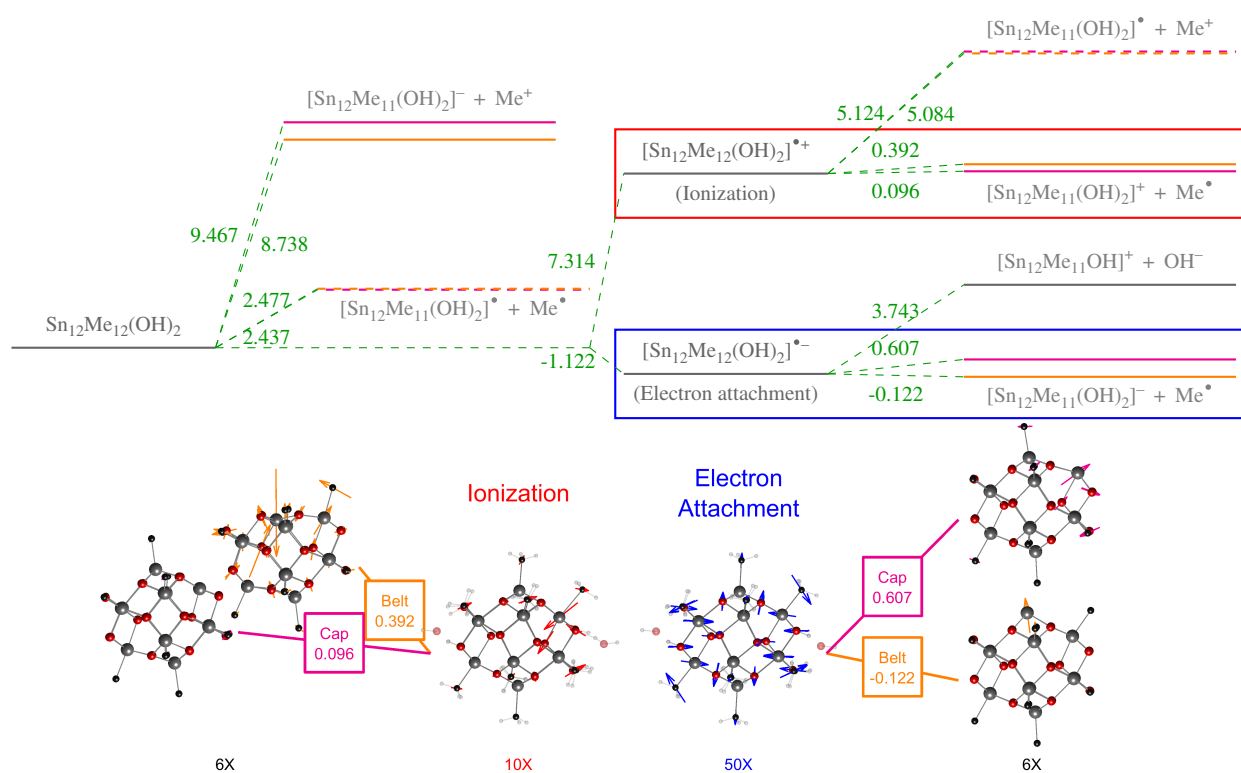


**Fig. 6.2** A graphical representation of reaction free energies for  $\text{Sn}_{12}\text{Me}_{12}(\text{OH})_2$ . Ionization, electron-attachment, and bond-dissociation reactions are included. Energy levels are drawn to scale. Numbers are reaction free energies in eV. Belt/cap methyl dissociation levels are in orange/magenta, respectively. The post-ionization and electron attachment demethylation reactions are expanded in the bottom left and right panels. Red/blue arrows in the insets indicates scaled atomic displacement from neutral equilibrium geometry upon ionization/electron attachment. Orange/magenta arrows indicate tin-oxo cage atomic displacement upon removal of belt/cap methyl groups from respective their perturbed (ionized or electron attached) geometries. Numbers at the bottom are magnifications for atomic displacements.

the two is related to the geometry of the frontier orbitals. Heterolysis, in context, is homolysis followed by ionization of  $\text{CH}_3^\bullet$  and electron addition to the de-methylated cage. As shown in figure 6.3, the highest occupied molecular orbital (HOMO) and the near degenerate HOMO-1 is mostly a bonding orbital localized around the cap tin-carbon bonds. On the other hand, the lowest unoccupied molecular orbital (LUMO) is localized around the belt tin atoms. As a result of heterolysis, the methyl-deficient cage has one electron more than it has after homolysis. No matter if this extra electron enters either the LUMO (SOMO without this extra electron) or the HOMO, it will preferentially stabilize the cap tin-carbon bonds.

### 6.3.2 One electron redox

As previously mentioned, chemistry is expected to be generated by ionization[127] and electron attachment upon EUV exposure[125] in this system and in EUV in general[13]. The low-energy electrons are known to result in dissociative electron attachment in certain systems. To investigate this possibility, we began with determining whether the electron affinity is positive. Our computation indicates that the adiabatic electron affinity is 1.1 eV, suggesting that electron attachment is favorable.

Upon one-electron ionization, the tin-carbon bonds are also destabilized. In this scenario, the cap tin-carbon bonds are weakened preferably. Although cleavage is not spontaneous after including the entropy gain at room temperature, the BDFE is on the order of 0.1 eV, which is surprisingly lower than previously reported. We attribute the difference to the inclusion of entropy, enthalpy, and dispersion interaction. The reaction entropy contribution ( $T\Delta S$ ) is 0.45 eV for the cap methyl group and 0.67 eV for the belt methyl group. Inclusion of counter anions, as we will demonstrate later on, does not explain the difference. There is an apparent discrepancy between our BDFE and multi-reference bond strength[138] (0.09 vs 0.96 eV) but they are not directly comparable as the multi-reference calculation only provides the electronic contribution. By ignoring the vibrational (zero point and finite temperature) and entropic contributions to the BDFE, the PBE0-D3(BJ) contribution to this reaction is 0.67 eV.

We also report notable changes in cage geometry upon ionization. Consistent with previous calculations, a particular cap tin-carbon bond is weakened spontaneously and the associated methyl group relaxes into an  $sp^2$  geometry as shown in figure 6.2. The drastic reduction of bond energy and change in methyl geometry is consistent with multi-reference calculations performed on ionized  $\text{Sn}(\text{CH}_3)_3\text{OH}$ [138]. Atomic displacements subsequent to ionization are magnified by 10 times and shown with red arrows in the bottom left panel of figure 6.2. The tin atom moves towards the center and is co-planar with the surrounding oxygen atoms. On the far left of the lower left panel of figure 6.2, we report the absence of significant atomic displacements upon removal of a cap methyl from an ionized cage. However, if a belt methyl group is removed from an ionized cage,

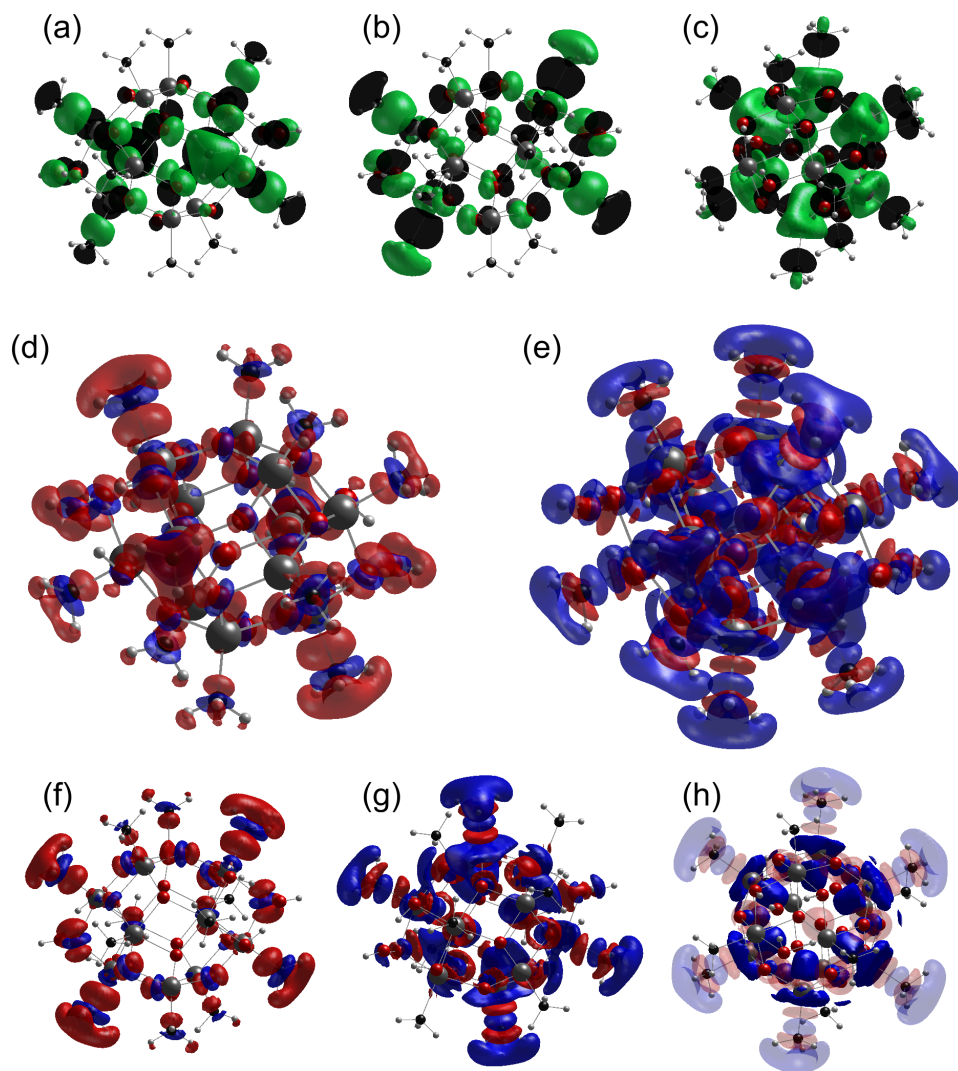


**Fig. 6.3** (a-c) HOMO-1, HOMO, and LUMO densities. Color indicates sign. (c,d) The change in electron density when  $\text{Sn}_{12}\text{Me}_{12}(\text{OH})_2$  is ionized (c) and upon electron attachment (d). Red indicates a reduction in electron density and blue indicates an increase. (f) Clipped electron density change upon ionization for clarity. (g,h) Clipped electron attachment density. Notice the difference between belt and cap tin atoms (g) and the attachment density near the 5-coordinate belt tin atoms that resembles the Sn  $5d_{z^2}$  orbital (h).

the now 4-coordinate tin atom moves towards the center as the internal axial oxygen atom is drawn to this tin atom, indicating that a coordination number of 5 is significantly more stable than 4 in this system when it is ionized. This rearrangement appears to paint a picture where the hole migrates to the 4-coordinate tin atom, prompting it to relax by finding a fifth bonding neighbor.

Upon electron attachment, the bond strengths are reduced to 0.61 eV for cap and -0.12 eV for belt methyl groups as shown in figure 6.2. On top of the previously reported preferential destabilization of the belt tin-carbon bonds[51], we discovered that the entropic contribution suffices to reduce the reaction free energy, resulting in a spontaneous entropy driven homolytic bond cleavage. Interestingly, compared to results using PBE0 functional at 0 K, our method and conditions (revPBE0-D3BJ/293K) actually result in a less exothermic reaction *enthalpy* (free energy minus entropy) of 0.115 eV. This could be attributed to the attractive dispersion interaction between the two fragments.

Also as a result of electron attachment, the tin-oxo cage “bloats” slightly as shown in the lower right panel in figure 6.2. Given the molecule size and abundance of electrons, atomic displacements are expected to be small. By amplifying them by 50 times, as illustrated in the bottom right panel of figure 6.2, we reveal that the oxygen atoms between the belt and cap tin atoms are moving radially outward, opening up what appears to be the “sixth coordination site” and bringing the belt tin atoms closer to a “half octahedron” coordination. The cap tin and oxygen atoms are drawn simultaneously closer to the center. Such geometric changes seem to suggest that the extra electron resides, as shown in later discussions, around the belt tin atoms opposite to the methyl carbon.

Subsequent to tin-carbon bond cleavage, as shown in the far right column in 6.2, the involved tin atom moves away from the cage, indicating that the lone pair of the now full-shell cage is localized at the tin atom.

Another possible result of electron attachment is the ionic dissociation of the hydroxide anion. However, the dissociation free energy of the counter anion is 3.743 eV which is still on the order of a few eVs. In comparison, tin-carbon bond cleavage is a more likely outcome. The high counter anion dissociation energy barrier does not explain the correlation between resist performance and anion mass reported[124]. As we will discuss later on, there is a proton transfer mechanism involved to account for the presence of diffusing conjugate acid of the anions.

Heterolysis energy cost upon ionization is still much higher than homolysis. Cap heterolysis is only 0.04 eV more favorable than belt. Again, it appears that heterolysis has a tendency to favor belt-methyl group removal, which is consistent with computations for an un-ionized cage.

As mentioned, ionization and electron attachment selectively destabilize different tin-carbon bonds. This selectivity can be elucidated with the change in electron density subsequent to ionization or electron attachment. The electron-density difference upon ionization and electron attachment is shown in figure 6.3(d) and (e). The vertical density changes, where atomic movements

upon ionization or electron attachment are neglected, are shown.

Upon ionization, electron density mainly withdraws from between the tin and carbon atoms surrounding the cap. For clarity, figure 6.3(d) is clipped to emphasize the cap methyl groups (6.3(f)). Apparently, electron density is withdrawn from the bond into associated carbon atoms. Since the withdrawn density is located near the mid point of the tin-carbon bonds, it is bonding in nature. The diminished bonding density in cap tin-carbon bonds thus explains why it is preferentially destabilized. The withdrawal of density also explains the geometrical change previously shown in figure 6.2. The change in electron density correlates very well with the HOMO density (figure 6.3(b)).

Upon electron attachment, the overall change in electron density (figure 6.3(e)) is more nuanced. Regardless of the location, the electron density increases and decreases alternately along the length of the bond. The magnitude of modulation is very similar between cap and belt methyl groups. Interestingly, the carbon atom is actually located at a node between positive and negative electron density change. We produce a clipped cutout of figure 6.3(e) to closely examine the differences between cap and belt tin-carbon bonds in figure 6.3(g). Near the vertical center line are two belt tin-carbon bonds (enclosed by electron density iso-surfaces). Approximately 60 degrees counter clockwise from the them are two cap tin-carbon bonds. As one can see, there is extra electron density in the shape of a plug on the inside of the belt tin atoms. Such density, as shown in another cutout containing only belt tin atoms (figure 6.3(h)), is present underneath all belt Sn atoms, increasing electrostatic repulsion along the bond. The absence of such density in cap Sn atoms explains the relative destabilization of belt tin-carbon bonds and the geometrical change upon electron attachment shown in the bottom right panel of figure 6.2. Such “in-cage” density is also present in the LUMO orbital.

The plug like shape of the “in-cage” density partially resembles the  $5dz^2$  orbitals of the tin atom, suggesting that their availability is key to its susceptibility to electron attachment. The tin atoms on the cap are 6-coordinate and the  $5dz^2$  orbital is involved in bonding. The belt tin atoms are 5-coordinate and that explains the availability of empty  $5dz^2$  orbitals. With this observation, we can generalize that in a complex tin-oxo system where tin atoms with different coordinate numbers co-exist, electron attachment density would concentrate around the lowest-coordinate tin atom. From the observed locality of this phenomenon, whether the tin-oxo cage arranges itself into a cage is not expected to play a big role, suggesting that it would occur in similar clusters or even amorphous organic tin-oxo networks.

### 6.3.3 Tin-Carbon Thermal Chemistry

From the trends observed in BDFEs under various circumstances, the geometries of frontier orbitals appear to explain much of the thermal-chemistry, including the excitation selectivity and

the tilt in bond cleavage preference in heterolysis. This is consistent with previous reports. Our investigation revealed that either impact ionization or electron alone can result in cleavage and the two processes need not converge. In other words, one ionization-electron pair could lead to two useful chemical events. This gives organotin system an edge over chemically amplified systems where one ionization-electron pair can generate only one acid as, according to the leading hypothesis, ionization and electron attachment induced chemistry need to rendezvous for acid generation[13]

The belt (5-coordinate) and cap (6-coordinate) tin atoms are sensitive to different chemical triggers, a behavior largely explained by frontier-orbital geometries and charge-density distribution. As the orbitals are non-local in nature, it begs the question whether juxtaposing two type of tin atoms contributed to the sensitivity. In other words, if one is to make a hypothetical tin cluster consisting of only 5- or 6-coordinate tin, would the reactivity or sensitivity decrease? Recent experiments indicate that sensitivity, albeit to a lesser extent, can be achieved by the  $\text{Sn}_6$  “drum” cluster, which is comprised of only 6-coordinate tin [144], suggesting that such juxtaposition is not necessary for lithographic sensitivity. However, the “football” cluster is still faster than the “drum” in e-beam lithography. Sharps et al. [144] suggested that two factors are competing when it comes to sensitivity, namely the binding energies of counter anions and the preexistence of tin-oxo frameworks in the molecule. Our calculations, on the other hand, suggest that tin-carbon cleavage plays a much bigger role in chemistry than counter anion dissociation. Indeed, qualitatively, the acetic acid out-gassing of the “football” cluster is similar to that of the “drum” after normalizing for the tin-to-acetate ratio. The “drum” cluster has one tin atom per acetate whereas the “football” has six. However, the acetic acid yield of the “drum” is around 4 to 8 times that of the “football” cluster. This observation suggests that the elimination of anion conjugate acid is not the only sensitivity mechanism. However, up to this point, our computations have yet to provide explanation for the very existence of conjugate acids previously reported. On top of that, there is an indisputably clear link between counter anion mass and sensitivity [124]. The reported benefits with respect to post exposure bake are also consistent with the notion that diffusion is an integral part of the exposure chemistry. In light of those results, it is almost certain that there exists a pathway for protons to recombine with the anions, resulting in the conjugate acid. Given that ionization-induced deprotonation is a widely studied subject in chemically amplified resists, we investigated whether a similar phenomenon takes place in the  $[(\text{R-Sn})_{12}\text{O}_{14}(\text{OH})_6](\text{A})_2$  family.

#### 6.3.4 Proton transfer

Upon ionization, hole transfer and eventual deprotonation has been investigated and reported to play an integral role in acid generation in EUV chemically amplified resists [13, 38]. In  $\text{Sn}_{12}\text{Me}_{12}(\text{OH})_x$ , surprisingly, we report the auto de-protonation of terminal hydroxyl groups at-

tached cap tin atoms in the presence of one or two hydroxide counter anions. In the process of geometric relaxation, a hydrogen atom detaches from the cap of the cage and combines with a hydroxide counter anion, essentially neutralizing the hydroxide base.

Deprotonation is slightly different depending on the number of counter anions. With two hydroxide anions, deprotonation occurs as a result of ionization. In the presence of a single anion, ionization does not result in deprotonation. However, a combination of ionization and de-alkylation of the belt or cap-2 alkyl groups does trigger deprotonation.

Deprotonation does not occur in the absence of counter anions. We anticipate similar behavior when the anion is a strong base and, by definition, has a weak conjugate acid, which is the case in a previous study [124]. In that study, a larger counter anion is shown to reduce dose-to-clear, hinting at the role of diffusion of the counter anions. However, the anions are bonded by Coulomb interaction to the cap of the cages, making diffusion inherently difficult at room temperature. Our observation presents a channel for the conjugate base to be neutralized, providing an explanation for the linearity between anion size and dose-to-clear.

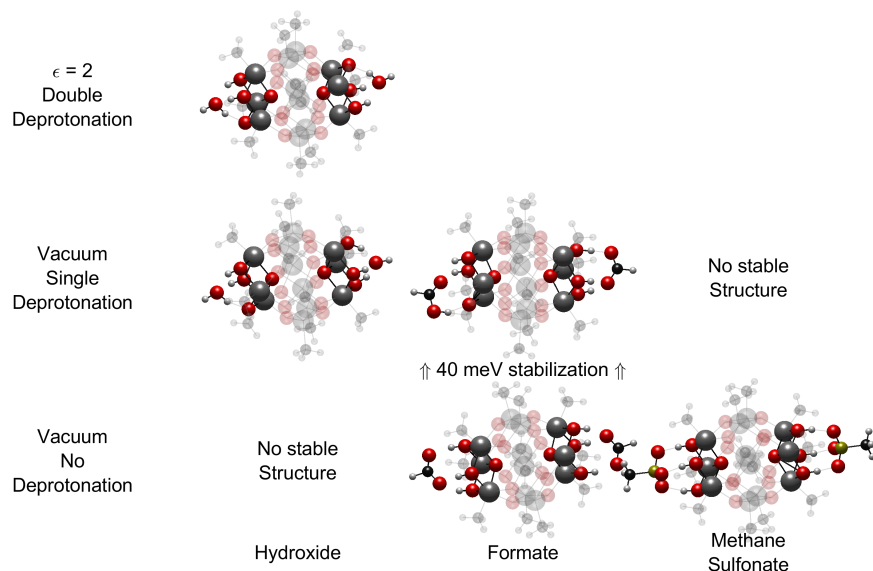


**Fig. 6.4** The structures of  $\text{Sn}_{12}\text{Me}_{12}\text{A}_2$  clusters at various degrees of cage deprotonation. Red, gray, black, white, and yellow atoms are oxygen, tin, carbon, hydrogen, and sulfur, respectively. The anions ( $\text{A}^-$ ) hydroxide ( $\text{OH}^-$ ), formate ( $\text{CHO}_2^-$ ), and methanesulfonate ( $\text{CH}_3\text{SO}_3^-$ ) are considered. The crown-like structure at the caps and the anions are highlighted for clarity

To examine this hypothesis, we compared the energetics of a few different bases, including the aforementioned hydroxide ( $\text{A}^- = \text{OH}^-$  pKa  $\sim 14$  in water[145, 146]), formate ( $\text{A}^- = \text{CHO}_2^-$  pKa



$\sim 4$  in water), and methanesulfonate ( $A^- = \text{CH}_3\text{SO}_3^-$  pKa  $\sim -1$  in water). These are common counter anions for this system. Sulfonate and hydroxide are the weakest and strongest conjugate bases. Most counter anions are carboxylates for which formate is an archetypal representative. Given the size of the methanesulfonate group, Hessian calculations were omitted and energy differences reported are electronic self-consistent energy evaluated at revPBE0-D3BJ/def2-TZVP on geometries optimized at revPBE0-D3BJ/def2-SVP.

The relaxed structures are shown in figure 6.4. In the presence of hydroxide anion, deprotonation occurs spontaneously upon ionization—a stable geometry with two hydroxide anions does not exist. We started the geometric minimization with a two anions but deprotonation proceeds spontaneously in geometric relaxation. With the formate anion (center column in figure 6.4), stable geometries exist with or without deprotonation and the deprotonated geometry is around 40 meV more stable than its bi-anion counterpart. In other words, at room temperature, even with the precision of our calculations accounted for, a significant portion of ionized formate cluster would deprotonate and produce formic acid molecules. Moreover, the existence of stable geometries for both deprotonated and protonated  $[\text{Sn}_{12}\text{Me}_{12}(\text{CHO}_2^-)_2]^+$  indicates the presence of an energy barrier for deprotonation. Whether this is a correlation between the barrier height and basicity could be an interesting question. Noticeably, formic acid is a rather acidic member of the carboxylic acid family, the common choice for counter anion for  $[\text{Sn}_{12}\text{Me}_{12}]^{2+}(A^-)_2$  systems [135, 124]. Thus, the propensity of formate anion to deprotonate the cage suggests that it would be a common occurrence in most carboxylic acids, providing an explanation for the anion mass dependence of resist sensitivity. Lastly, we could not observe any stable deprotonated geometry when methanesulfonate ( $A^- = \text{CH}_3\text{SO}_3^-$ ) is used as the counter anion—even when a deprotonated initial geometry is used, the methanesulfonic acid spontaneously dissociates and re-protonates the cage.

We anticipate ionization-induced deprotonation to be more prevalent in condensed phase resist, as the dielectric background is likely to substantially affect proton-transfer energy. By raising the dielectric constant from 1 (vacuum) to 2 both hydroxide ions in  $[\text{Sn}_{12}\text{Me}_{12}]^{2+}(\text{OH}^-)_2$  are predicted to be neutralized by cage deprotonation (Top left of figure 6.4). This suggests that vacuum computations are underestimating the likelihood of deprotonation and thus providing a conservative estimate of the degree of proton transfer from cage to anions.

The presented ionization-driven acid generation has a few implications on our understanding of these materials, as an EUV resist and beyond. Spatial propagation of chemistry in these materials has been assumed to be minimal, at least in modeling studies [123]. Our computations, consistent with experiments [124], suggest the presence of thermally-mobile acid upon ionization. Without initiating any reaction, the diffusion of acid away from the exposed volumes would facilitate condensation (or formation of chemical bonds), resulting in lower dose. It has been reported that lighter counter anions and higher post-exposure bake temperatures result in higher sensitivity[135].

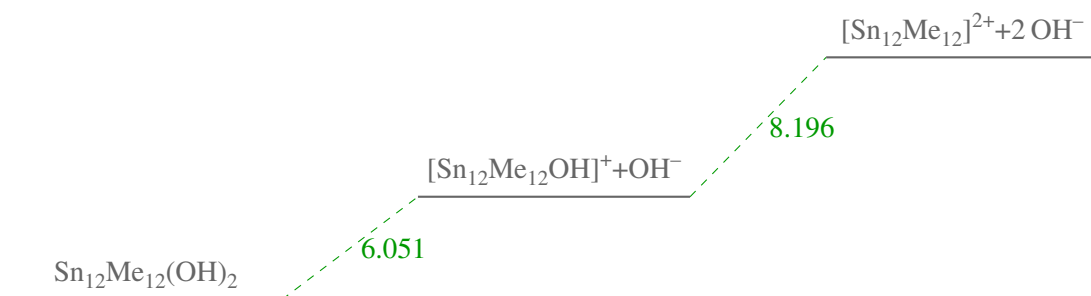


**Fig. 6.5** First and second ionic dissociation energies of the cluster with the hydroxide anion.

Our computations have provided another piece of evidence along this line of reasoning. Such diffusion is likely to have an impact on the line-edge-roughness (LER) of the resist as in chemically amplified resists[2].

Utilizing the acid as a reagent of the exposure chemistry would however be challenging. In existing synthetic schemes, the conjugate acids of the counter anions are used as a reagent [134, 135]. In the process,  $[\text{Sn}_{12}\text{Me}_{12}]^{2+}(\text{A}^-)_2$  is exposed to its conjugate acid, suggesting that the cage and tin-carbon bonds are inert to the conjugate acid. However, since  $[\text{Sn}_{12}\text{Me}_{12}]^{2+}(\text{A}^-)_2$  can be separated into solid powders, it is conceivable to include acid-labile components into the formulation.

## 6.4 Tin-Carbon Chemistry—Complex Environments and Formulation Considerations

Up to this point, computations on tin-carbon chemistry were performed in gas phase with one type of R group. Consequently, how well the results translate to thin film is still uncertain. In light of that, the robustness of the ionization and electron attachment chemistry will be investigated. Computation of Gibb's Free Energy of bond dissociation (Electronic energy + vibrational enthalpy correction - entropy ( $T\Delta S$ )) are repeated over a few variables. They include the number of anions, the length of the R group and the dielectric constant of the background.

### 6.4.1 Ionic dissociation

Photoresists are condensed films and the environment can affect the coordination between the anions and the cage. The extent of these effects depends on how much the chemistry is affected by the anions.

To proceed, we investigate the consequences of removing the counter anion. We begin with the scenario where both anions are removed. In this case the inversion symmetry of the molecules is preserved so all belt and cap methyl groups are geometrically equivalent. The total ionic dissociation energy in vacuum is found to be 14.27 eV See figure 6.5.

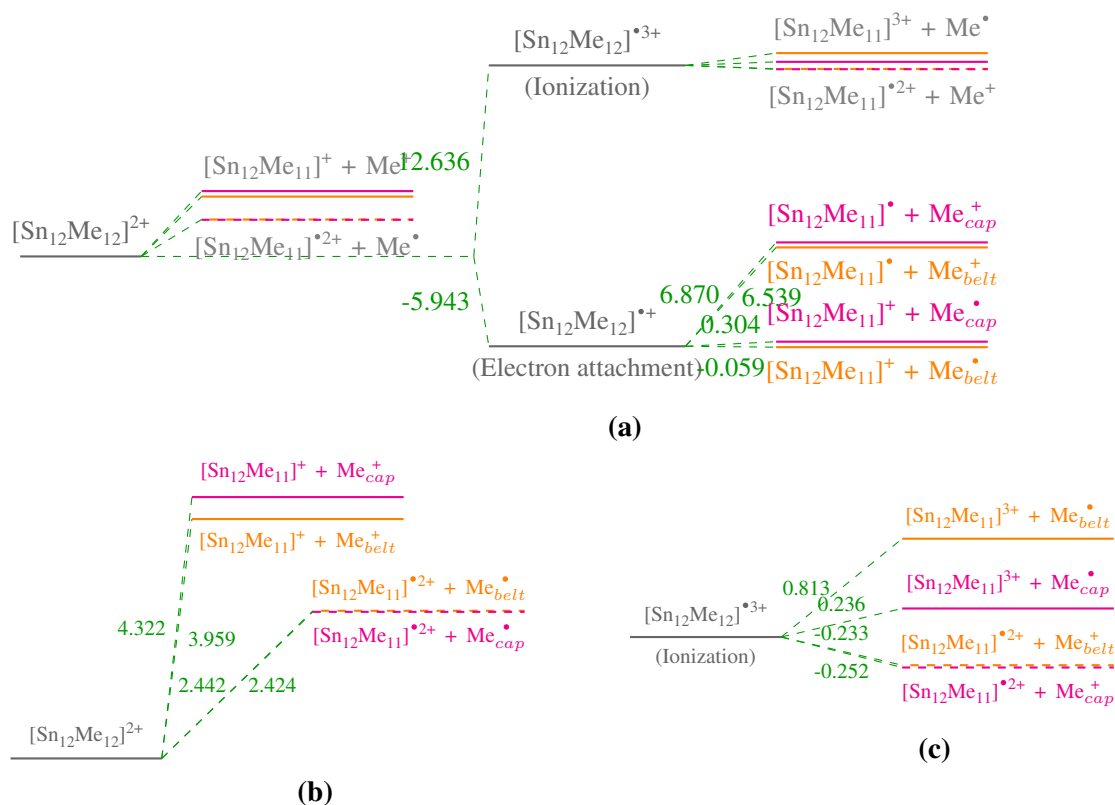


**Fig. 6.6** A graphical representation of reaction free energies for [Sn<sub>12</sub>Me<sub>12</sub>]<sup>2+</sup>. Energy levels are drawn to scale and numbers are reaction free energies in eV. (a) is an overview juxtaposing all relevant reactions. (b) and (c) show the BDFE of [Sn<sub>12</sub>Me<sub>12</sub>]<sup>2+</sup> and [Sn<sub>12</sub>Me<sub>12</sub>]<sup>3+</sup> on expanded energy scales.

Comparing bond energies in figures 6.2 and 6.6b, prior to electron addition and removal, the elimination of counter anions changes the homolytic BDFE of the tin carbon bond by less than 0.1 eV. However, the absence of counter anions significantly increases the electrostatic energy of the system. As a result, the heterolytic BDFE sees a significant reduction of around 5 eV (figure 6.6b).

The bare cage (as illustrated in figure 6.6a) with a charge of 2+, has a much higher ionization potential of 12.6 eV and that agrees with experimentally measured fragmentation yield onset [127]. Subsequent to ionization, the cap homolytic BDFE is reduced by 2 eV to 0.24 eV. The process is not spontaneous. Yet the small barrier size implies that if the molecule is promoted to a low lying excited state, the process would likely be spontaneous. From experimental data, we see a steep rise less than a eV above the onset. Heterolysis, which is sensitive to Coulomb interaction, is exothermic once the bare cage is ionized to a charge of 3+. The presence of de-alkylated cage with charge 3+ reported is therefore intriguing [127]. Multi-reference calculations suggested the presence of multiple dissociative homolytic excited state potential energy surfaces [138], which could explain the observation.

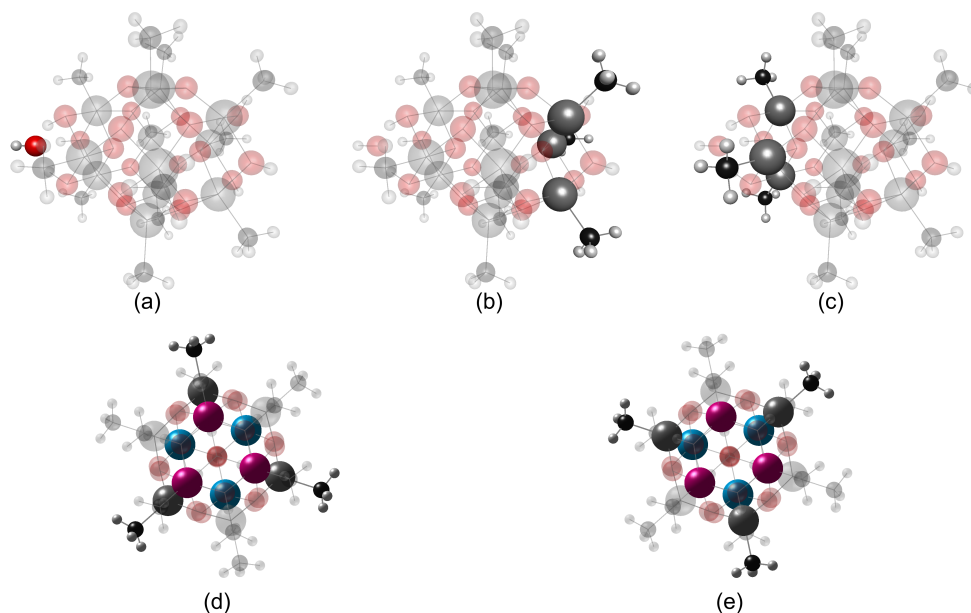


**Fig. 6.7** The locations of the remaining counter anion (a), cap-1 tin-carbon bonds (b), and cap-2 tin-carbon bonds. The belt-1 and belt-2 tin-carbon bonds are highlighted in (d) and (e), with cap-1 (magenta) and cap-2 (cyan) tin atoms colored for reference.

With an extra electron, homolytic cleavage becomes spontaneous, just as when both the anions are present. The electron affinity is much higher in the absence of anions, which is presumably a result of electrostatic interaction.

For homolysis alone, the bond energies and excitation selectivity are similar with or without the anions. Noticeably though, the post-ionization bias towards cap methyl groups increases in the absence of anions. On the other hand, the post-attachment bias towards belt methyl groups decreases. Moreover, regardless of the absolute heterolysis energies, post-ionization heterolysis is more belt-biased compared to post-ionization homolysis, consistent with what is observed in the presence of both anions. It indicates that the orbital geometry arguments appears to be true regardless of the presence of counter anions.

Upon the removal of a single hydroxide counter anion, the inversion symmetry of the molecule is broken and there are two geometrically nonequivalent types of belt and cap groups as shown in figure 6.7. Cap-1 are those next to the empty anion site and the cap-2 are next to the remaining hydroxide anion, as illustrated in figure 6.7b and 6.7c. To understand the symmetry of belt groups, we take an axial view through which the two anion sites align. The cap-1 and cap-2 tin atoms (magenta and cyan) form two equilateral triangles that are a 60 degree azimuthal rotation apart. Belt tin-carbon bonds that azimuthally align with cap-1 groups are belt-1 groups (figure 6.7d). Similarly, belt tin-carbon bonds that share “longitudes” with cap-2 groups are belt-2 groups (figure 6.7e).

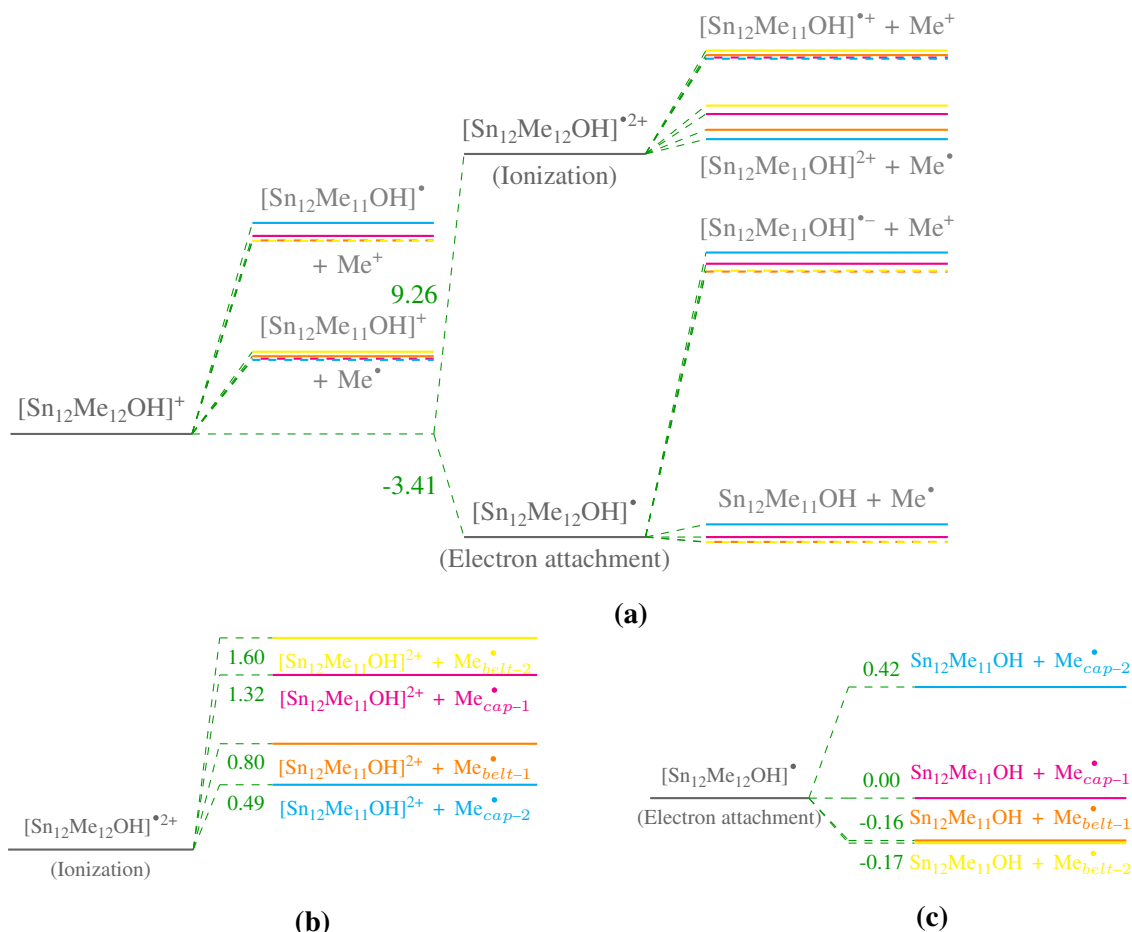


**Fig. 6.8** Reaction free energies for  $[\text{Sn}_{12}\text{Me}_{12}\text{OH}]^+$ . A accurately scaled graphical representation of ionization, electron attachment, and bond dissociation energies is shown in (a) with numbers representing free energy change in eV. Magenta, cyan, orange and yellow represent cap-1, cap-2, belt-1, and belt-2 groups, respectively. The homolysis energies upon ionization and electron attachment are shown in (b) and (c), respectively

The homolytic BDFEs, as shown in figure 6.8, are similar to that with none or both of the hydroxide ions. Homolysis is still more likely to happen than heterolysis upon ionization or electron attachment.

Noticeably cap-1 and cap-2 react very differently to ionization (figure 6.8b). Cap-2 tin-carbon bonds are weakened more than their cap-1 counterparts. Still, their BDFE (0.49 eV) is higher than when the cage has both (0.236 eV) or none (0.096 eV) of the hydroxide anions. To understand this behavior, we examine the canonical orbitals and we observe that the spin density is not coming from the frontier orbitals. In fact, it is concentrated on the remaining hydroxide group (specifically in an oxygen *p* orbital) even though the near-degenerate HOMO and HOMO-1 are rather delocalized, as they are in the presence of both anions (figure 6.3). This unexpected location of the spin density points to strong non-Aufbau behavior which has been reported in complex systems as a possible radical-stabilization mechanism[147, 148, 149]. With inversion symmetry broken, electron density moves towards the remaining hydroxide as a reaction to the localized hole, in the process shielding the alkyl groups from the hole and stabilizing the cap-2 tin-carbon bonds. As a result, although cap-2 bonds are still the most vulnerable, their bond strength is stronger compared with their center-symmetric relatives (with two or zero anions).

Moreover, upon electron attachment all tin-carbon bonds, with the exception of those close to the remaining hydroxide group (cap-2), are prone to spontaneous cleavage.

#### 6.4.2 Ethyl substitution

Molecule	Site	R=Methyl				R=Ethyl			
		$\Delta E_{\text{ele}}(\text{Me})$		$\Delta G(\text{Me})$		$\Delta E_{\text{ele}}(\text{Et})$		$\Delta G(\text{Me})$ + $[\Delta E_{\text{ele}}(\text{Et})$ - $\Delta E_{\text{ele}}(\text{Me})]$	
		BE	$\Delta$ BE	BE	$\Delta$ BE	BE	$\Delta$ BE	BE	$\Delta$ BE
Unperturbed	Belt	3.084		2.477		2.974		2.367	
	Cap	3.024		2.437		2.810		2.223	
Ionization	Belt	1.067	-2.017	0.392	-2.085	1.330	-1.644	0.655	-1.712
	Cap	0.668	-2.356	0.096	-2.341	0.823	-1.987	0.251	-1.972
Electron Attachment	Belt	0.115	-2.969	-0.122	-2.599	0.004	-2.970	-0.233	-2.600
	Cap	0.953	-2.071	0.607	-1.830	0.590	-2.220	0.244	-1.979

**Table 6.1** The homolysis free energy of tin-carbon bonds in  $[(\text{Me}-\text{Sn})_{12}\text{O}_{14}(\text{OH})_6](\text{OH})_2$  and  $[(\text{Et}-\text{Sn})_{12}\text{O}_{14}(\text{OH})_6](\text{OH})_2$ . BE columns give the bond energy with the corresponding energy or free energy.  $\Delta$ BE columns refer to the change in bond free energy induced by ionization or electron attachment. All numbers are in eV.

Cages using various ligands have been synthesized [127] and aliphatic chains ( $\text{C}_n\text{H}_{2n+1}$ ) are commonly used. As a rule of thumb, longer aliphatic chains are more electron donating, and would

presumably affect the bond strengths. To investigate this effect, computations are repeated on the ethylated sibling  $[(\text{Et}-\text{Sn})_{12}\text{O}_{14}(\text{OH})_6](\text{OH})_2$ . Given the size of the ethylated cluster, coupled-perturbed self-consistent-field (CPSCF) computations are not possible. As a result, the vibrational contribution to enthalpy, entropy and eventually free energy is not accessible, so the electronic energy ( $E_{\text{ele}}$ ) evaluated on revPBE0/def2-TZVP level will be compared instead. To further remedy this shortfall, we seek to approximate the bond free energy by adding the electronic energy correction ( $[\Delta E_{\text{ele}}(\text{Et}) - \Delta E_{\text{ele}}(\text{Me})]$ ) to the bond free energy of the methyl cage ( $\Delta G(\text{Me}) + [\Delta E_{\text{ele}}(\text{Et}) - \Delta E_{\text{ele}}(\text{Me})]$ ), which is tabulated in the last two columns in table 6.1.

Noticeably, by replacing methyl with ethyl, the tin-carbon bonds are weakened by around 0.1 eV.

With this substitution, one can see that ionization destabilizes the molecule less while the electron attachment induced destabilization does not vary by much. As shown in table 6.1, the bond electronic energy  $\Delta E_{\text{ele}}$  of belt/cap tin-carbon bonds after ionization are 1.067 and 0.668 eV, respectively, for methyl. With ethyls in place of methyls, the energies become 1.330 and 0.823 eV, respectively. The same pattern exists in the (approximated) free energies. The bond free energy upon ionization for belt and cap are 0.392 and 0.096 eV, respectively, for methyl. For ethyl, they increase to 0.655 and 0.251, respectively, effectively making ionization induced cleavage not spontaneous.

One can draw similar conclusions by looking at the change in bond energy induced by ionization. Comparing the electronic ( $\Delta E_{\text{ele}}$ )  $\Delta\text{BE}$  columns of the two R-groups shows that the changes induced by electron attachment (bottom two rows) are similar. However, upon ionization (the third and fourth rows), the bond strength is not reduced as much when an ethylated cluster is used. Similar trends can be observed in the free energy ( $\Delta G$ )  $\Delta\text{BE}$ .

Although electron attachment does not destabilize the molecule more upon ethyl substitution, the general decrease in bond strength prior to excitation implies that the bond energies are lower upon electron attachment, increasing sensitivity to this pathway

The selectivity (the difference in bond energy between belt and cap) is augmented by this substitution upon ionization but reduced by this substitution upon electron attachment. Since ethyl is more electron donating, it could effectively be adding part of an electron to the cage (presumably localized more at the belt) before the actual electron attachment, reducing the localization of the extra electron.

The substitution of R groups is shown to change the radiation chemistry. By substituting methyl with ethyl, the practical implication is that the ionization pathway is slowed down but the electron attachment activity is expected to be enhanced. This is an example where it is possible to trade resolution for dose—low energy electrons are more mobile than radical cations so reactions can be triggered further away from where the EUV photon is absorbed. Increasing electron attachment

sensitivity potentially implies an improved EUV dose yet the increased spread of tin-carbon bond cleavage would be a peril to resolution in future nodes.

### 6.4.3 Dielectric medium

Molecule	Site	Vacuum ( $\epsilon=1$ )				Dielectric ( $\epsilon=2$ )			
		2 Anions Homolysis		No Anion Heterolysis		2 Anions Homolysis		No Anion Heterolysis	
		BE	$\Delta$ BE	BE	$\Delta$ BE	BE	$\Delta$ BE	BE	$\Delta$ BE
Unperturbed	Belt	2.477				2.433			
	Cap	2.437				2.303			
Ionization	Belt	0.392	-2.085	-0.234	-2.676	0.455	-1.978	1.020	-1.413
	Cap	0.096	-2.341	-0.252	-2.676	0.266	-2.037	0.887	-1.316
Electron Attachment	Belt	-0.122	-2.599			-0.340	-2.773		
	Cap	0.607	-1.830			0.132	-2.171		

**Table 6.2** The homolysis free energy of tin-carbon bonds in  $[(\text{Me-Sn})_{12}\text{O}_{14}(\text{OH})_6](\text{OH})_2$  and  $[(\text{Et-Sn})_{12}\text{O}_{14}(\text{OH})_6](\text{OH})_2$ . BE columns give the bond energy with the corresponding energy or free energy.  $\Delta$ BE columns refer to the change in bond free energy induced by ionization or electron attachment. All numbers are in eV.

When clusters are situated in a condensed film, one of the biggest influences on their bond energies would be the dielectric polarization in the matrix. Such interaction usually reduces electrostatic interaction, so neutral species become more likely to dissociate into ion pairs and highly charged species are stabilized and less prone to fragmentation.

To estimate the correction from a dielectric background, the polarizable continuum model (C-PCM, implemented in Q-Chem) is used[150, 112]. The dielectric constant of the background is needed as an input to C-PCM. Remaining isopropyl solvent has been reported in these systems[131] (4 molecules in  $9.971 \text{ nm}^3$ ), and can be used to estimate the lower bound of dielectric constant. The dielectric constant of isopropyl is 19.92 (implying a polarizability of 18.92). Scaling that with the molecular density  $\chi = 18.92 \times \frac{4/(9.791 \text{ nm}^3)}{7.876/( \text{nm}^3)} = 0.9814$ , gives a dielectric constant ( $\epsilon = 1 + \chi$ ) of around 2. In comparison, the dielectric constant of water is around 78. We notice that although the cage itself has a huge dynamic polarizability (which contributes to  $\chi$ ), the huge volume of the molecule means that the cage contributes only around 0.1 to 0.2 to the total polarizability.

The results of the computations are tabulated in table 6.2. At the first glance, qualitatively, the division of labor still exists—ionization promotes tin-carbon cleavage at the caps while cleavage is spontaneous at the belt upon electron attachment. The dielectric background induces a similar effect as ethyl substitution, albeit to a lesser extent. We report a reduction in homolysis bond energy prior to excitation. The tin-carbon bonds are less destabilized upon ionization and more destabilized upon electron attachment (see columns  $\Delta$ BE under **Homolysis** in table 6.2). As a



result, the radiation chemistry is again biased towards electron attachment.

Moreover, as anticipated, in the presence of background polarization, heterolysis bond energy increases from around -0.24 eV to 0.9 eV (See the **Heterolysis** columns in table 6.2), implying that in real systems the chemistry is probably homolysis driven.

## 6.5 Conclusion

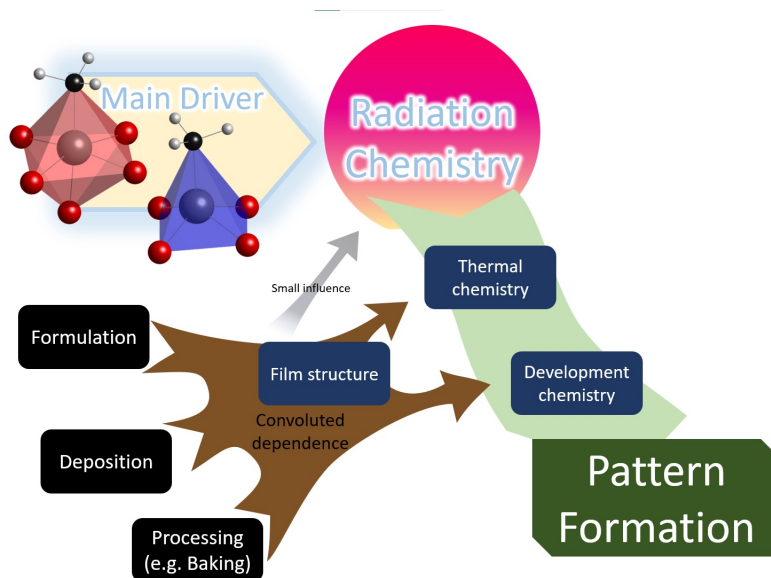


**Fig. 6.9** Summary—The radiation chemistry can be largely explained by electron density changes localized to the tin atoms. As a result, radiation chemistry can be decoupled from other factors such as formulation and processing, eventually simplifying the material identification problem.

With our systematic study of the  $[\text{Sn}_{12}\text{Me}_{12}]^{2+}(\text{A}^-)_2$  system, we have further upheld the understanding that cleavage of tin-carbon bonds dominates the chemistry of this system. Our computations has provided a molecular-level understanding of the sensitization mechanism, illustrating that either ionization and electron attachment can trigger tin-carbon bond cleavage. This full utilization of the electron-hole pair generated by each impact ionization event could explain the superiority of tin-oxo resists for EUV applications. The ability to initiate chemistry with both impact ionization and electron attachment is a stark contrast to chemically amplified systems (CAR). In CARs, impact ionization and electron attachment induced chemistry is understood to converge in order to produce an acid [13]. As a result, an electron-ionization pair can at most create one acid in CARs. In contrast, an electron-ionization pair can create two active sites in the resist film, practically doubling the quantum efficiency, which is vital in combating the RLS tradeoff [2].

On top of predicting an excitation selectivity as previously reported, we have demonstrated that selectivity is generally not affected by the presence of anions. Such robustness in this selec-

tivity would set the stage for possible selectivity engineering in the future—by placing different side chains on tin atoms on the belt and the cap, one can generate different chemical outcomes subsequent to ionization and electron attachment.

A further investigation into the origin of such selectivity also suggests that the large “in-cage” LUMO and vertical attachment density located at 5-coordinate (belt) tin atoms contributes to this selectivity. Such density is rather localized and resembles a  $dz^2$  orbital, suggesting that the chemical environment beyond the coordinating oxygen and carbon would do little to its electron affinity. Similarly, the HOMO is localized to the tin-carbon bonds at the caps, thus explaining their sensitivity to impact ionization. This observation could therefore be valid for other tin-oxo system regardless of the exact geometry, or in other words, the arrangements of tin tetrahedrons.

In the broader context, this discovery can speed up EUV material development. Resist chemistry has generally been very convoluted. As shown in figure 6.9, the radiation chemistry only initiates the pattern formation and there are various processes lie between. Generally speaking, these processes, together with radiation chemistry, have complicated dependence with tuning parameters such as formulation, deposition, and additional processing such as baking. Such interdependence increases the difficulty in targeted material design as one can hardly independently. In our study, we demonstrated that the radiation chemistry efficiency is related to the immediate coordination of the tin-carbon bond. As a result, as long as the local coordination is preserved, one can expect the efficacy of radiation chemistry to remain similar upon changes in formulation, processing, or even macro-molecular structure as illustrated previous studies[144].

We went further to investigate how a condensed phase environment could affect such division of labor and selectivity. We noticed that they are both robust upon ionic dissociation and immersion into dielectric media. By substituting the methyl group with ethyl, we demonstrated that the sensitivity and selectivity could be modulated. It is worth mentioning that the employment of various R groups can be achieved by using different precursors, making such molecular changes practically viable.

On top of tin-carbon cleavage, the relevance of anion conjugate acid has been reported [124, 144]. Our computation has illustrated that ionization–deprotonation is a possible explanation of such acids, providing a starting point for creating formulations around this reaction route. Its propensity can be modulated by the basicity of counter anion. Since this deprotonation has been shown to be favorable with carboxylate ions common in  $[\text{Sn}_{12}\text{Me}_{12}]^{2+}(\text{A}^-)_2$  systems, we propose that such exposure-induced acid can be factored into resist formulation.

## CHAPTER 7

# Recording Materials Interface EUV Sensitivity Engineering with Self Assembled Monolayers

### 7.1 Introduction

Generally speaking, as feature sizes shrink, the thickness of photoresists has to be reduced accordingly to avoid pattern collapse. The reduction in thickness inevitable makes the interfaces more important. Near an interface, polymer materials for example, exhibit new properties such as change in glass transition temperature. Even prior to the introduction of EUV, interface specific phenomena in photo resists have been reported. Depletion of photo acid generator (PAG) has been observed with secondary-ion mass spectrometry (SIMS). Such ‘poisoning’ is reported to extent 10 nm above the resist-substrate interface.[151] To compensate for such acid loss, an interface specific delivery vehicle is needed. Self Assembled Monolayers (SAMs) have been explored to serve this purpose [152]. SAMs are a distinct class of organic materials that self-assemble into well-ordered crystalline monolayers. The monolayer constituent is composed of three distinct moieties: a head group that interacts with the substrate, a tail group that presents a chemical functional group at the monolayer surface and the side-chain, the region between the monolayer surface and the substrate-anchoring head group. Under the right conditions, SAMs would form a 2-dimensional lattice on a substrate. Its growth is self limiting—it does not grow vertically beyond a single layer and stops growing after a mono-layer coverage is reached. PAGs can be attached to such SAM molecules, turning SAMs into the solution to the acid poisoning problem. This exemplifies the utility of SAMs in the context of lithography and how they can be used as a tool to address interface specific challenges.

In the context of EUV lithography, on top of the reduction in thickness, a few additional challenges arise. As mentioned in previous chapters (see chapters 1 and 2), in EUV, resists, the RLS trade-off is a bigger concern than ever. In other words, every photon counts. Yet, by aggressively increasing the EUV absorption cross-section, there would be a vertical anisotropy of absorption density. In a negative tone resist, it results in undercutting at the bottom. Conversely for positive tone resists, the shortage of photons near the boundary gives rise to tree rooting. Imaging

performance is degraded in either case. Directional etching has been reported as a remedy for negative tone metal oxide system. Effective in this specific system, this approach is not applicable to positive tone resists. The silver lining is that, as previously mentioned in chapter 2, the chemical activation in EUV is delocalized, it is possible to utilize the photoelectrons generated in the substrate near the resist.

Such interface induced sensitivity may sound far fetching. However, EUV sensitivity in SAMs attributed to secondary electrons traversing across the interface has been reported. On top of extra sensitivity, self assembled monolayers can provide additional leverages for pattern and edge placement error (EPE) mitigation. Edge placement error is the combination of overlay error (Whether two layers overlap correctly) and critical dimension uniformity (Whether the features are in right sizes)—both of which can result in missed connections or accidental shorts.

EPE reduction potential comes from the area selectivity of SAMs. Area selective deposition (ASD) is a method to deposit materials on a specific portion of a pre-patterned surface composed of dissimilar materials. This technology is increasingly garnering attention for its ability to streamline process flow and address overlay errors in the near term, and will enable further applications in the future [153, 154, 155, 156]. While there are several tools to achieve ASD, organic monolayers, which act as inhibitors of surface deposition, exhibit some of the highest levels of selectivity. [157, 158, 159, 160, 161, 162, 163] Once the inhibitor is deposited, the undesired surface is fully deactivated and the deposition only occurs on the desired portion (See figure 1 in [164]). This method would then, at most, produce surface topography from a starting coplanar surface.

The EUV sensitivity in SAMs enables an evolution of ASD—Additive lithography process. Additive lithography describes a process that combines the exposure of a photosensitive self-assembled monolayer (SAM) with ASD. During a pattern-wise exposure the monolayer undergoes a chemical transformation to either crosslink or oxidize the SAM material and either deactivate or activate a selected region toward deposition. The pattern development is then achieved by an ASD process using atomic layer deposition (ALD) (see figure 1 in [164]). While the chemical response to irradiation was linear (e.g., irradiation does not trigger a catalytic reaction), the response to ALD inhibition was non-linear providing an effective image development method to build contrast and amplify the exposure induced chemical response. As an example, a pilot system was achieved with hydroxamic acid SAMs which, as a monolayer, produce a positive tone behavior after ALD development and as a multi multi-layer a negative tone. Furthermore, substituents at the hydroxamic acid headgroup were found to provide control over dose sensitivity and therefore development contrast [164].

Since EUV sensitivity in SAMs has the potential to address absorption anisotropy and enable additive lithography, understanding the sensitivity mechanism is vital.

The head group dependent sensitivity in [164] could shed light on the sensitization mechanism

and understanding what is happening and that is the focus of this chapter. Since the head group substitution is not expected to change the attachment chemistry, they should all work on the same substrates.

## 7.2 Origin of Head Group Sensitivity—the Hypothesis

### 7.2.1 The Elusive Head Group Dependence

The most obvious hypothesis for the sensitivity dependence in head group comes from the packing density. However, as shown in [164], this would not suffice to explain the dramatic difference between the methyl substituted and unsubstituted hydroxamic acids. Also, near edge x ray absorption fine structure (NEXAFS) could also provide a hint on the exposure chemistry. NEXAFS prior and after EUV exposure indicates a loss in ordering of the carbon tail and the increase of C=C double bond, suggesting a cross-linking based sensitization mechanism as detailed in figure 4 in reference [164]. This deepens the mystery—if the tail, instead of the head, is mostly responsible for the blocking selectivity, why would the head group modify the sensitivity by a factor larger than 2?

The reality appears to be more nuanced so in order to identify a competing narrative, one needs to understand the origin of EUV sensitivity. It is straight forward to assume that the entire electron cascade (chapter 2) happens within the monolayer. However, while it has been reported that the electron attenuation length is in the order of a few nanometers (chapter 3), the thickness of such octadecyl hydroxamic acid layers is smaller than 2 nm. In essence, the electrons originated in the substrate should not be discarded. In fact, since the SAM is made mostly of carbon atoms, its optical  $\beta$  is rather mediocre at EUV compared to oxygen, which is rather abundant on the silicon oxide surface. Not only did other researchers share the same understanding [165], upon simple algebra, it appears that EUV absorption at the monolayer is too sparse to conceivably initiate cross-linking that results in the negative tone behavior reported in [164, 165]. In fact, only 0.2 photons are absorbed per nanometer squared, implying that only 1 in 30 hydroxamic SAM is expected to absorb an EUV photon.

The scarcity of photons, as previously mentioned, suggests that secondary electrons originated in the substrate could play a vital role in sensitivity. Along this line of thinking, the head groups can potentially throttle the amount of electrons passing through the interface, modulating the effective dose even though they don't participate in the cross-linking chemistry. The question is how.

### 7.2.2 Interface Dipole Moment, Work Function and Electron Transmission

The work function of a given solid state or condensed material is the difference between its (electron) Fermi energy and (having an electron at) infinity. Along this line, if the interface has a normal

	EUV absorption cross-section of a carbon atom	$5.8 \times 10^{-5} \text{nm}^2$
×	Number of hydroxamic acid per $\text{nm}^2$	$6 \text{nm}^{-2}$
×	number of carbon atoms per hydroxamic acid	18
<hr/>		
	EUV Absorption probability	0.0065
×	Observed dose	$50 \text{mJ}/\text{cm}^2$
×	$\frac{1}{92 \text{eV}} \times 10^{-14} \frac{\text{cm}^2}{\text{nm}^2}$	$0.678/\text{nm}^2 \left( \frac{\text{mJ}}{\text{cm}^2} \right)^{-1}$
<hr/>		
	Photons absorbed per area	$0.2/\text{nm}^2$

**Fig. 7.1** Estimation of photon absorption density in a self assembled monolayers and assumptions used

dipole moment by any means, the work function would change. The surface dipole would act like a brief parallel plate accelerator/retarder for escaping electrons, effectively changing the energy barrier.

Surface dipole driven work function modification has been extensively studied [166, 167, 168]. While SAMs can be a reliable means of engineering interface work function, other factors such as cleavage plane and surface roughness can also play a role.

In particular, the use of SAM to tune interface work function has been reported with a multitude of SAMs [167]. All these studies point to the conclusion that work function change can be largely explained by the normal component of the SAM's permanent dipole moment. On top of providing good reference for this subject, such investigations also provide a road map to tackle similar research problems. It has been demonstrated that

1. Density functional theory (DFT) calculations in slab geometry is accurate in predicting the work function of a given interface measured in experiment. The work function can be computed by taking the different between the Fermi energy and the local potential at the center of vacuum portion [167, 168].
2. The orientation of a SAM molecule affects the pointing of its dipole moment, thus the work function. and the orientation has been successfully extracted by NEXAFS experiments [168].

As a preliminary precaution, the dipole moment of a few SAMs were compared and shown in figure 7.2. In figure 3 of [164], the high dipole moment hydroxamic acid is sensitive to EUV

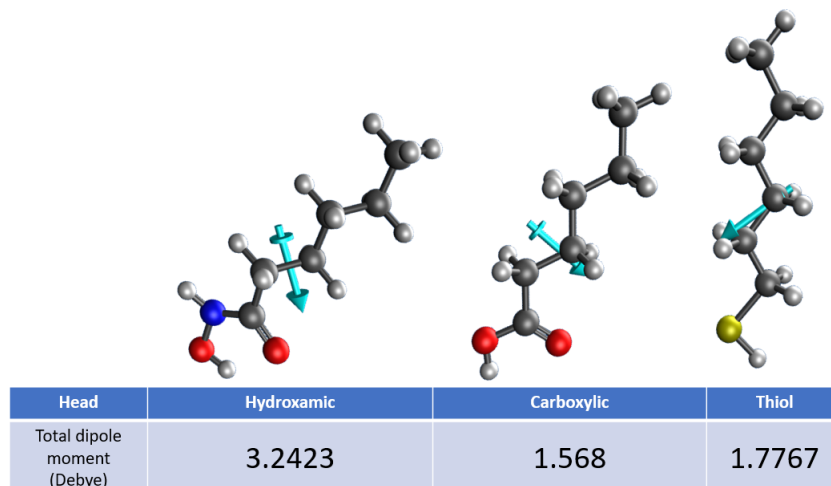


**Fig. 7.2** Permanent dipole moments of hydroxamic acid, carboxylic acid, and thiol estimated at the level PBE0/def2-TZVP//PBE0/def2-SVP. The molecules are angled in the most likely orientation when adsorbed. Arrows indicate the direction of dipole moment

while the low dipole moment thiol did not have any EUV sensitivity and this observations warrants further investigation of this hypothesis on interface work function.

### 7.3 Divide and Conquer

Due to the complexity of the octadecyl SAM molecules, a full geometry relaxation is prone to local minima. In previous studies of hexadecyl amine monolayers, multiple initial conditions were used to ensure that the global minima is identified. However, the fact that the author is not able to reproduce the exact bond length even with the input files provided by the author of ref. [169] (an older version of VASP was used in the reference) indicates how much of a minimization quagmire this problem is.

To make the problem more tractable, we exploit the fact that the tilt or orientation of SAMs are dominated by the inter tail interaction. This is evident in the NEXAFS measurements of the unsubstituted octadecyl hydroxamic acid on ZnO and TiO<sub>2</sub> substrates. As shown in figure 7.3, their angle dependencies of the C-H  $\sigma^*$  (around 287 eV) and C-C  $\sigma^*$  (around 292 eV) are almost identical suggesting that these bonds are pointing in the same direction regardless of the metal oxide surface. To provide a direct comparison, the differences in intensity between incident angles 20 and 80 degrees for both substrates were shown in figure 7.3 (a). As one can see, the two curves are very similar.

Raw spectra have been normalized for direct comparison. a linear background is extracting by tiffing the pre-edge signal (around 270 to 277 eV) and the background subtracted intensities are

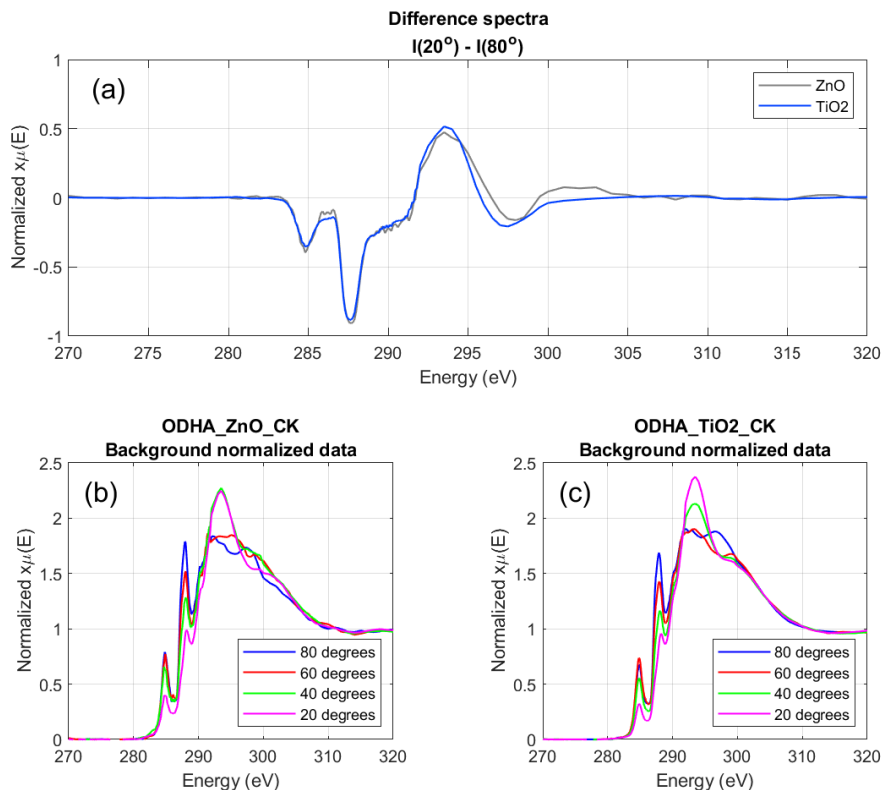


**Fig. 7.3** (a) the difference in normalized NEXAFS spectra between 80(oblique) and 20 (near grazing) degrees. (b) and (c) are the angle resolved NEXAFS spectra of octadecyl hydroxamic acid on zinc(II) oxide and titanium(IV) oxide

normalized by the integrated spectral weight between above edge (around 300 to 320 eV).

Meanwhile, the tilt angle dependence of the head group is computed with constrained geometry optimization of an interface slab. The complete methodology is rather complicated and will be detailed in a dedicated section.

## 7.4 SAM-SAM interaction

To identify the tilt angle of the SAM, which is likely dependent on SAM-SAM interaction. The strategy would be to relax a layer of octadecyl hydroxamic acid (ODHA) in vacuum and identify the optimal packing density and geometry.

DFT calculations were carried out with the Vienna Ab-initio Simulation Package[170, 171, 172, 173] (VASP 5.4.4) using the PBE functional [174]in conjunction with projector augmented-wave method [175]. Van der Wall's interactions were accounted for using Grimme's D3 dispersion correction [140]. Due to its packing efficiency and the underlying hexagonal lattice structure of



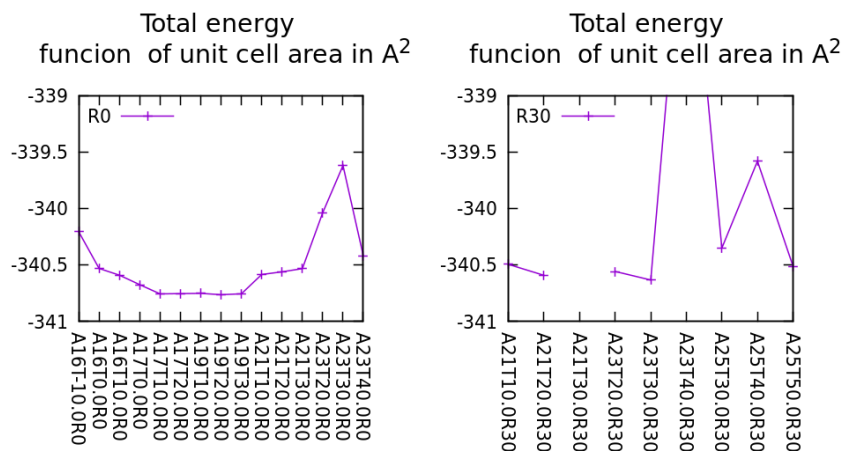


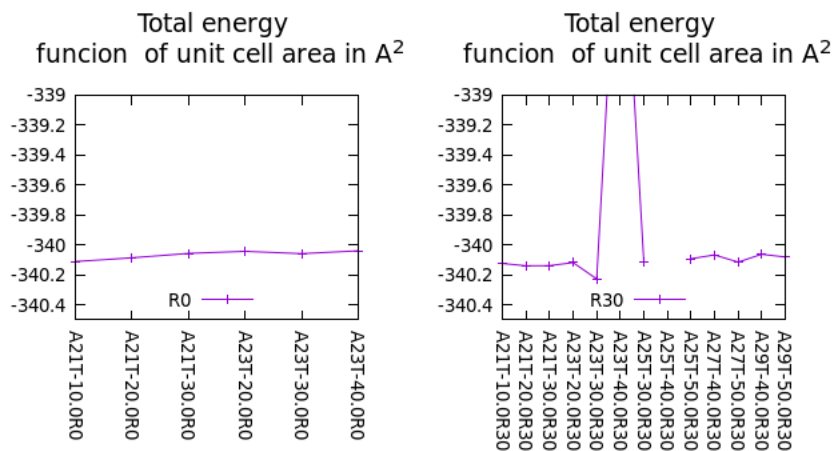
**Fig. 7.4** High precision free energy of free standing unsubstituted hydroxamic acid as a function of cell area (number after A), initial tilt angle (number after T), and initial azimuthal angle (number after R, zero denotes point towards nearest neighbor)

Copper(I) oxide, the SAMs are assumed to pack in hexagonal order. In similar systems it has also been demonstrated that for on the 111 surface of copper, which also has hexagonal symmetry, hexadecyl amine SAM prefer to pack in hexagonal order [169].

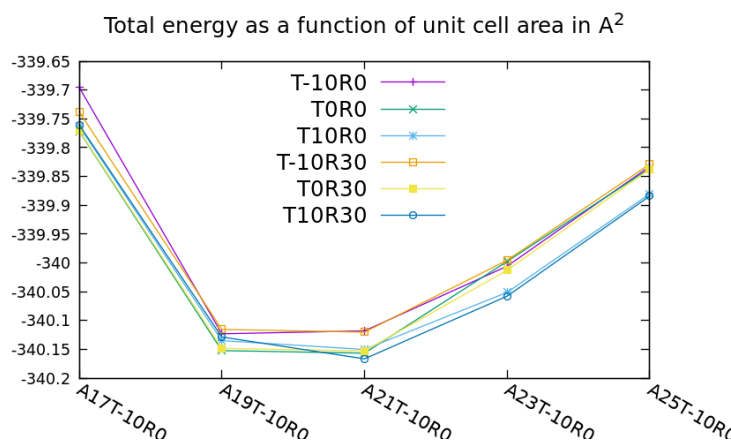
Hexagonal slabs with cell area between  $16 \text{ \AA}^2$  and  $31 \text{ \AA}^2$  were relaxed until residual forces are smaller than  $0.01 \text{ eV/\AA}$ . Relaxation calculations were carried out with an energy cutoff of  $300 \text{ eV}$  and a  $(4 \times 4 \times 1)$  Monkhorst-Pack k-point mesh. The height of the slab is kept at  $40 \text{ \AA}$ , leaving more than  $23 \text{ \AA}$  between monolayers to mitigate vertical interactions. Using the relaxed geometry, a high precision single point calculation, with an energy cutoff of  $420 \text{ eV}$  and a  $(6 \times 6 \times 1)$  Monkhorst-Pack k-point mesh, was carried out to calculate the total energy for a subset of initial conditions. The optimal packing area is identified where the total energy is the lowest.

A huge number of initial conditions were used especially for the methyl substituted variant. For the unsubstituted variant, as shown in figure 7.4, the optimal packing density is around  $1/19 \text{ \AA}^{-2}$ , which corresponds to SAMs with almost zero tilt (vertical), consistent with NEXAFS results in figure 7.3. For the methyl substituted variant, upon searching through various initial conditions the optimal packing density is around  $1 \text{ per } 23 \text{ \AA}^{-2}$  as shown in fig 7.5. The final tilt angle is around 20 to 25 degrees and the uncertainty comes from the fact that the tail is not entirely straight.

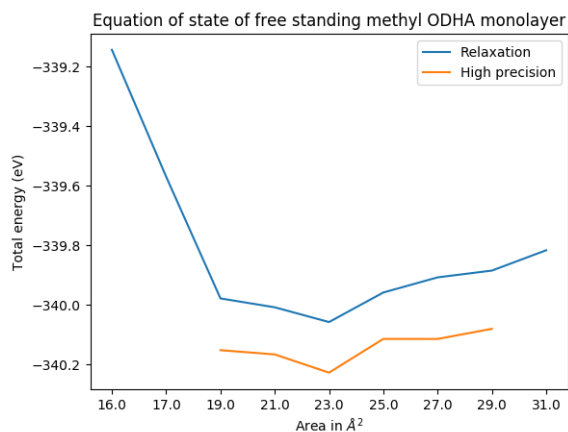
It is noticeable that the equation of state is rather anharmonic—the energy rises much more quickly with compression than extension. It turns out that as the layer becomes sparse, the molecules tilt more to recover some van der Waal’s attraction.



(a) High precision free energy of free standing methylsubstituted hydroxamic acids with tilted initial conditions



(b) High precision free energy of free standing methylsubstituted hydroxamic acids with straight initial conditions. The tilt (T) and azimuthal (R) information on the bottom should be disregarded.



(c) The equation of state for free standing methyl substituted hydroxamic acid SAM. For each cell size, the most stable final geometry (out of many initial conditions) is taken.

**Fig. 7.5** High precision free energy of free standing unsubstituted hydroxamic acid as a function of cell area (number after A), initial tilt angle (number after T), and initial azimuthal angle (number after R, zero denotes point towards nearest neighbor)

## 7.5 Tilt Dependence of Interface Work function

### 7.5.1 Substrates and Computational Method

The substrate could have a number of effects on the interface work function. Even though the packing and overall tilt of the SAM is not likely to be affected by the head group-substrate interaction, such interactions can still strain the SAM in particular ways. In the context of this work, there is a more urgent concern. The hydroxamic acid is an acid of very low pKa. Yet, if the substrate is an oxide, it is more likely than not basic. One can estimate whether acid-base neutralization would happen or just consider both possibilities in the head group computations. The lattice orientation of the substrate also matters—it is a known fact that different cleavage planes have different reactivity and surface energy.

In [164], copper sputtered on  $\text{Al}_2\text{O}_3(111)$  was used. However, prior to coating, the surface was cleaned by oxygen plasma. X-ray scattering of similarly treated surfaces reveals a signature of  $\text{Cu}_2\text{O}(111)$ , suggesting that the SAM is deposited on copper(I) oxide [176].

Before proceeding, the correct orientation of  $\text{Cu}_2\text{O}$  has to be confirmed. DFT+U computations seem to corroborate that surface aligns with the (111) direction [177, 178, 179]. However, the exact cleavage plane matters. Multiple DFT+U studies point to cleavage at the oxygen plane [177, 178, 179, 180]. More in depth investigation on this cleavage plane reveals that the unsaturated copper site is probably vacant [178, 179] but then in a set  $\text{CO}_2$  adsorption computations, it appears that the surface without unsaturated copper vacancies is more capable of adsorption [180]. Also, as will be mention later on, surface acid base reaction appears to be favorable in the presence of two unsaturated sites (on oxygen and one copper). For simplicity, and the fact that the goal of this study is to understand the surface dipole moment induced by the head group, a phenomenon dominated by the orientation of the head group, the presence of the vacancies should not affect the results too much.

It has been reported that the high symmetry geometry of the  $\text{Cu}_2\text{O}(111)$  slab (with oxygen cleavage plane) is a stationary point (It is a local maximum) [178, 180]. The author made a similar observation. By perturbing the initial surface geometry randomly, the relaxed slab always has the same symmetry breaking as figure 3 in [178].

Again, DFT calculations were carried out with the Vienna Ab-initio Simulation Package [170, 171, 172, 173] (VASP 5.4.4). However, with the substrate involved, the computation method is adjusted. Copper(I) oxide is a Mott insulator. In other words, its insulating behavior cannot be explained by the single particle Hamiltonian. Mean field theory such as Hartree Fock is known not to capture the dynamic electron-electron correlation in Mott insulators properly. In fact the inclusion of Fock exchange has been shown to degrade a functional's performance in multi-reference problems where dynamic correlation is prominent [8]. Following examples in [177, 178, 179, 180],

	U (eV)	J	<i>l</i>
Cu	6	0	2
C,O,H,N	0	0	0

**Table 7.1** The Hubbard parameters used for interface DFT + U computations

the same DFT+U approach is adopted. Hubbard model, specifically the formalism introduced by Dudarev [181] (LDAUTYPE = 4), is employed and the Hubbard's parameters are as shown in table 7.1. The Hubbard-U for copper was identified by matching both band gap and magnetic moment. Since both constraints can be reasonably satisfied by setting  $U \sim 6$  to  $7$  eV [177, 178], Hubbard's model appears to capture the physics of copper(I) oxide reasonably well. Again, the PBE functional with generalized gradient approximation [174] was used in conjunction with projector augmented-wave method [175]. Dispersion interactions were accounted for using Grimme's D3 correction [140].

Furthermore, to ensure that the substrate slab itself does not create a permanent dipole moment, the cleavage planes are the same on both sides of the slab. In the following discussions regarding the interaction between the head group and the surface, the substrate slab has 5 copper layers and the bottom two layers are fixed during relaxation.

The slab unit cells is orthorhombic with an angle of 60 degrees, sides 6.038 Angstrom long and a height of 35 Angstroms and a (4x4x1) Monkhorst-Pack k-point mesh was used. The unit cell in plane dimensions are determined by the reported  $\text{Cu}_2\text{O}$  lattice constants [178, 180, 177, 176]

### 7.5.2 Binding Site and Acid Base Reaction

Common wisdom is that metal oxides are rather basic. Even though hydroxamic acid is a weak acid, upon contact with a strong base, neutralization is still conceivable. In a previous study, it was shown that hydroxamic acid dissociates (or equivalently deprotonate) upon interacting with titanium (IV) oxide[182]. In light of that, geometries where dissociation happened or not have been investigated.

To avoid complications in geometry relaxation, the alkyl chain has been shortened. The minimal length where the frontier orbitals become identical to that of the octadexyl chain is 6.

On the surface, it is apparent that reactivity would likely come from the unsaturated copper and the un saturated oxygen sites. On the other hand, the polarity and abundance of lone pairs in the H-N, O=C and HO-N moieties on the hydroxamic acid make them plausible binding anchors.

	Total energy (eV)	H-O	H-N	O=C	
1	-228.439	\ O <sub>u</sub>		↓↓ Cu <sub>s</sub>	
2	-228.445	\ O <sub>u</sub>		↓↓ Cu <sub>s</sub>	
3	-229.034	↓ Cu <sub>u</sub>	\ O <sub>s</sub>		
4	-229.173	↓ Cu <sub>u</sub>	\ O <sub>u</sub>	↓↓ Cu <sub>s</sub>	
5	-229.199	↓ Cu <sub>u</sub>	\ O <sub>u</sub>	↓↓ Cu <sub>s</sub>	
6	-229.216	↓ Cu <sub>u</sub>	\ O <sub>u</sub>	↓↓ Cu <sub>s</sub>	
7	-229.271	\ O <sub>u</sub>		↓ Cu <sub>u</sub>	
8	-229.468	\ O <sub>u</sub>		↓ Cu <sub>u</sub>	
9	-229.470	\ O <sub>u</sub>	↗ O <sub>s</sub>	↓ Cu <sub>u</sub>	

**Table 7.2** A summary of final binding geometries of 9 initial conditions. ↓ indicates that the functional group is sitting right above a site on the surface, (↓↓—more than 2 Å above) \ indicates that the moiety is pointing at a site, and ↗ indicates that the in plane bond projection is pointing at a site but the out of plane component is pointing away from the surface.

#### 7.5.2.1 Binding with no dissociation

Nine initial conditions were used and the corresponding final geometries are summarized in table 7.2. It is noticeable that with the exception of the three least stable configurations, the binding is bi-dentate. In other words, there are two binding sites. On top of that, in those geometries, there is a N-H-O<sub>u</sub> or O-H-O<sub>u</sub> hydrogen bonding involved. Among the six, there are two groups of three. The O-H-O<sub>u</sub>/C=O-Cu<sub>u</sub> configurations are systematically more stable than the complimentary O-H-Cu<sub>u</sub>/C=O-O<sub>u</sub> configurations, suggesting that hydrogen bonding is shaping the interaction. The carbonyl group is not observed to bind onto the unsaturated oxygen site. Instead, it prefers to bind with the unsaturated copper atom, hinting at a redox reaction where by the lone pairs in the oxygen donate electrons to the copper atom.

With the exception of geometries 2-4, the OH group was initiated above a saturated copper atom. The relaxation process moves the OH group towards unsaturated sites, indicating its affinity is not a product of initialization bias, but a true physical phenomenon.

#### 7.5.2.2 Binding upon dissociation

Upon dissociation, the hydroxyl group on the hydroxamic acid dissociates into -O<sup>-</sup> and H<sup>+</sup>. We charge conservation, the proton is assumed to remain on the surface. There are two unsaturated sites per unit cell, one copper and one oxygen. Given the reactivity of these sites, the reasonable configurations are N-O<sup>(-)</sup>-Cu<sub>u</sub>/H<sup>(+)</sup>-O<sub>u</sub> and N-O<sup>(-)</sup>-O<sub>u</sub>/H<sup>(+)</sup>-Cu<sub>u</sub>. Four initial conditions are used for geometry relaxation—three in the former and one in the latter configuration. The results are summarized in table 7.3. It appears that the former is more favorable. Geometries 3-4 are almost identical. 2 and 3 differ by the (C<sub>18</sub>H<sub>37</sub>)-C torsional angle. Although the energy difference between

1 and 4 (around 0.23) eV is above room temperature by an order of magnitude, it's comparable to weak interactions such as dispersion energy. In other words, one cannot definitively rule out 1. However, the copper-oxygen affinity is rather apparent regardless of initialization. It is also noticeable that all final configurations are tautomers-they are one proton transfer and a rotation along the O-N bond from each other. It is known that hydroxamic acid has quasi-degenerate tautomers so there is no surprise such ambiguity manifests in surface binding. The head group is assumed to be a Z-keto conformer (As shown in figure 7.2 where both oxygen on the same side of the C-N bond), which, prior to dissociation, appears to be the most stable [183] or one of the most stable [184].

In fact, [184] suggests that deprotonation is most likely to take place at the H-N bond while maintaining the Z-keto conformation. Admittedly, the inclusion of this geometry could improve the validity of this study. However, it would be demonstrated that should this geometry be incorporated, it will make this particular variant less sensitive and would not qualitatively affect the conclusion

### 7.5.3 Tilt dependence

Given that dissociated hydroxamic acid is marginally more stable, it will be the system of interest in the tilt dependence computations.

Attempting to explicitly hold the tilt angle of the short chain is not straight forward, especially in Cartesian coordinates. To fix the tilt angle without explicitly constraining the azimuthal angle and translational motion, the mathematical form of the constraints might not be linear at all, hindering actual implementation. Such physical constraints could be implemented more easily in internal coordinates but that is not supported in VASP.

In lieu of enforcing the angle constraint, the altitude of the highest carbon is fixed. At a different height constraint, different final geometries and tilt angles would be resulted. Subsequently, the tilt angle dependence of work function and other properties can be backed out indirectly. Again, given the complexity of the problem, for each given altitude (or tilt angle), a series of azimuthal angles would be used as initial conditions to identify the most stable configuration of a given height, and equivalently, angle. As evident from figure 7.6, regardless of initial azimuthal angle, the final energy and tilt angles cluster when the same constraint is applied. Under this optimization scheme the hydroxamic acid is free to rotate during relaxation, increasing the odds of identifying the global minimum.

The final tilt angle is identified by considering the position covariance matrix of the final positions of the carbon atoms on the chain. By denoting the position vector of the  $i$ -th carbon atom as  $\vec{r}_i = [x_i, y_i, z_i]$ , one can construct the centered covariant matrix  $C$  (equation 7.2) from the centered position matrix  $A$  (equation 7.1).

#	Final energy (eV)	Initial configuration	Final configuration			
			O <sup>(-)</sup>	H-N	O=C	H <sup>(+)</sup>
1	-229.30	N-O <sup>(-)</sup> -O <sub>u</sub> /H <sup>(+)</sup> -Cu <sub>u</sub>	↓ Cu <sub>u</sub>	↘ O <sub>u</sub>		
2	-229.42	N-O <sup>(-)</sup> -Cu <sub>u</sub> /H <sup>(+)</sup> -O <sub>u</sub>	↓ Cu <sub>u</sub>			
3	-229.53					
4	-229.53					

**Table 7.3** A summary of final binding geometries of 4 initial conditions. Arrows have the same definitions as in table 7.2.

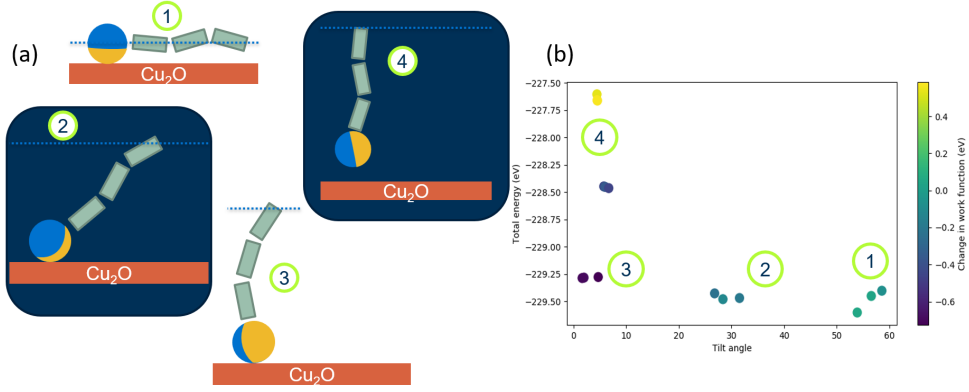


**Fig. 7.6** A schematic of the tilt dependence geometry computation. The system and constraints (blue dotted line) are shown in (a). (b) shows how energy varies with final tilt angle with color indicating the work function shift. Numbers in circles indicate the correspondence between configurations in (a) and clusters in (b).

$$\vec{R} = \frac{1}{6} \sum_{i=1}^6 \vec{r}_i$$

$$\vec{r}' = \vec{r} - \vec{R}$$

$$A = \begin{bmatrix} \vec{r}'_1 \\ \vec{r}'_2 \\ \vdots \\ \vec{r}'_6 \end{bmatrix} = \begin{bmatrix} x'_1 & y'_1 & z'_1 \\ x'_2 & y'_2 & z'_2 \\ \vdots & \vdots & \vdots \\ x'_6 & y'_6 & z'_6 \end{bmatrix} \quad (7.1)$$

$$C = A^T A = \begin{bmatrix} \sum_{i=1}^6 x_i'^2 & \sum_{i=1}^6 x'_i y'_i & \sum_{i=1}^6 x'_i z'_i \\ \sum_{i=1}^6 y'_i x'_i & \sum_{i=1}^6 y_i'^2 & \sum_{i=1}^6 y'_i z'_i \\ \sum_{i=1}^6 z'_i x'_i & \sum_{i=1}^6 z'_i y'_i & \sum_{i=1}^6 z_i'^2 \end{bmatrix} \quad (7.2)$$

The largest eigenvector of  $C$  is the direction along which most of the positional variance is coming from, thus the tilt vector. This process is equivalent to a principle component analysis of  $A$ .

#### 7.5.4 Evaluating work function shift

The work function of a material can be identified with a slab calculation. The work function is difference between the local potential (the Hartree potential) at the middle of the vacuum of the slab and the Fermi energy. For this method to be valid, one must allow for normal permanent dipole moment and leave enough space for the vacuum so that the local potential is flat in the middle of



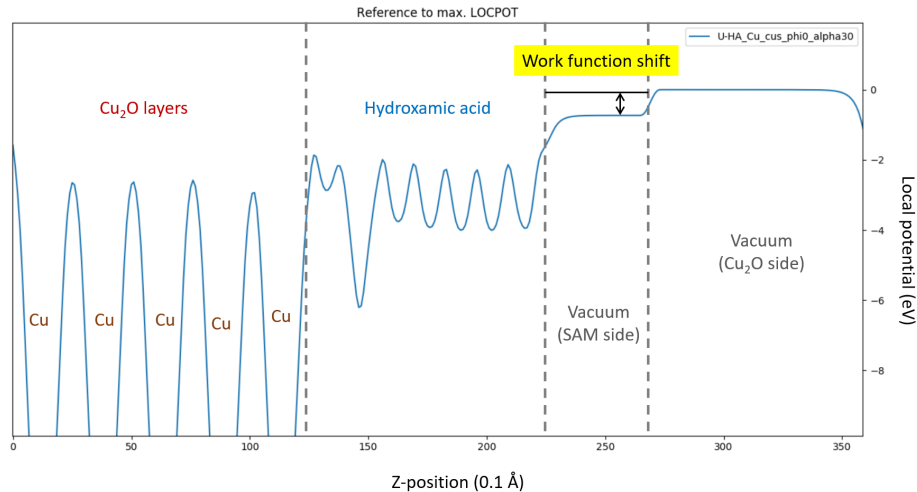


**Fig. 7.7** Extracting work function shift from the z-dependence of local potential. Notice the step between the vacuum potentials on the two sides

the vacuum portion.

Since the slab used does not have permanent dipole moment, the work function on both sides of the slab is the same. Therefore, as illustrated in figure 7.7, upon the addition of hydroxamic acid on one side, one can take the difference in work function between both sides as the shift induced by the additive.

Given the negligible additional cost for evaluating the local potential, it is evaluated for all interface computations.

## 7.6 Results

### 7.6.1 Unsubstituted Hydroxamic Acid

As shown in figure 7.8, one can locate the most stable geometry for each cluster and identify the corresponding work function shift. A green “guide to the eye” is added to show how the work function trends with tile angle. Given the extra 1 or two eV of potential energy, the two higher energy clusters correspond to configurations where the head group is not fully attached onto the surface.

As one can see, the trend is monotonic. The work function shift is the most negative when the hydroxamic acid is near vertical, the geometry observed in NEXAFS experiments. Therefore the estimated work function reduction for unsubstituted hydroxamic acid is around 0.7 eV

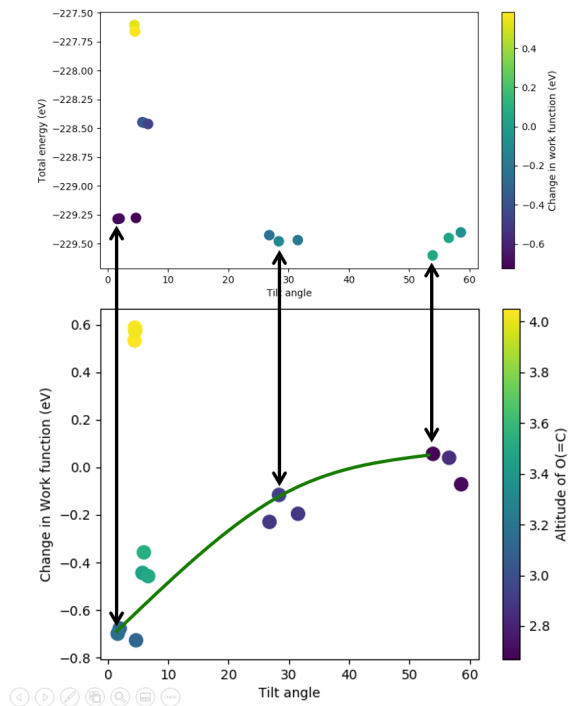


**Fig. 7.8** The tilt dependence of unsubstituted hydroxamic acid. Upper–Total energy of the interface as a function of tilt angle. Lower–Work function shift at different tilt angles. Arrows–the most stable geometries of each cluster (of initial conditions) in angle space

### 7.6.2 Methyl Hydroxamic Acid

Since methyl hydroxamic acid is more complicated, more initial conditions are used. As a result, in the angle dependence of energy, there are no clear clusters. Given that most data points appear to fall on the same line, outliers can be identified.

There is subjectivity when it comes to eliminating outliers. On the left panels in figure 7.8, data points are removed if they are more than approximately 0.1 eV from the energy-tilt trends line (panel a). The resulting work function-tilt trend is shown in panel (c). If one only excludes data point more than 0.2 eV away, as shown in figure 7.8, the work-function-tilt trend is rather different as shown in panel 7.9(d). Given that the tilt angle is estimated to be around 20 to 30 degrees from the packing computations, the reduction of work function is expected to be between 0.8 (More data points excluded) to 1.0 eV (Only one data point excluded). In both cases, there is a bigger work function reduction in the methyl substituted hydroxamic acid.

The H-N dissociation mentioned near the end of section 7.5.2.2 could come into play. Upon dissociation, according to [184], upon the H-N deprotonation, there are two resonance structures as shown in figure 7.10.

The structure on the left points the polar C=O bond towards the surface, reducing the surface dipole moment thus further increasing the work function barrier. The structure on the right is

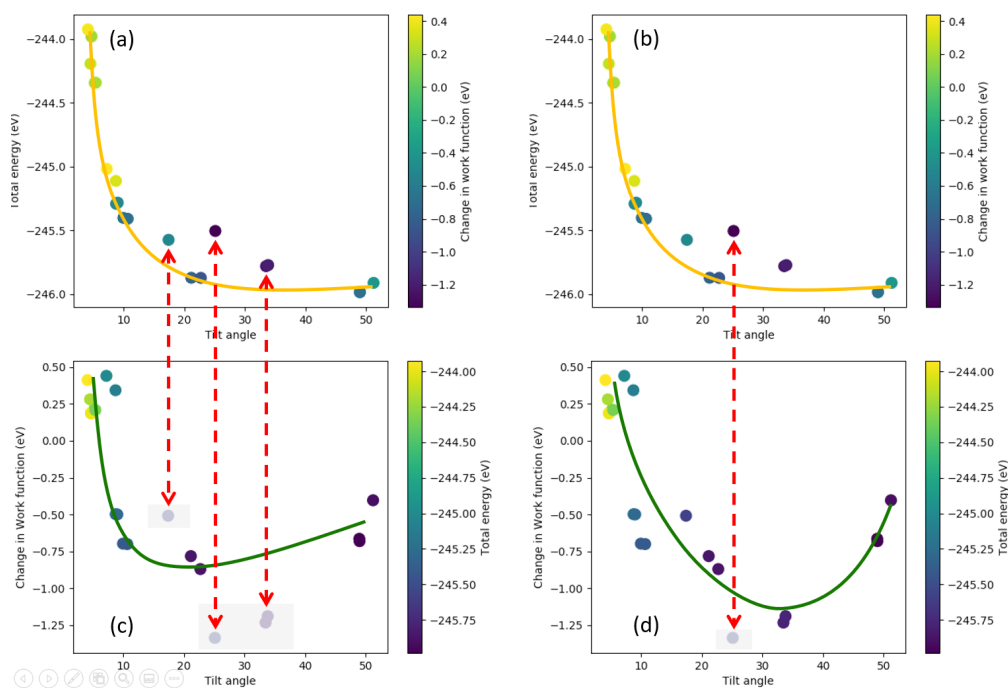


**Fig. 7.9** The tilt dependence of methyl hydroxamic acid. (a),(c)—Total energy of the interface as a function of tilt angle. (b),(d)—Work function shift at different tilt angles. Arrows—geometries identified as outliers. The left and right panels are identical except that fewer outliers are removed on the right.

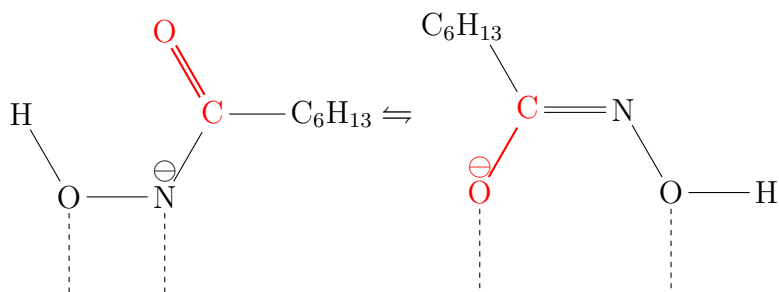


**Fig. 7.10** Resonance structures of deprotonated hydroxamic acid reported in [184].

geometrically similar to structures 2-4 in table 7.3 suggesting a similar change in work function. In either case, the work function reduction is not likely to be larger than those shown in figure 7.8, thus not undermining the conclusion that the methyl substituted hydroxamic acid provides a bigger reduction in work function.

As a closing note, our computations indicate that larger SAM induced work function reduction correlates with lower dose, which is consistent with the hypothesis that a lower work function would allow more electrons to be injected into the SAM layer from the substrate.

## 7.7 Additional Discussion

The substrate plays a role in the interface work function. The chemical composition, coordination, and even cleavage plane of the surface can affect the work function. As a matter of fact, at the same orientation, surface roughness alone can reduce the work function barrier. These factors should be taken into account in interface engineering.

### 7.7.1 Substrate Matters—Comparison with Copper Substrate

Similar interface computations have been carried out on a copper substrate. They predated the ones described earlier on in this chapter and was part of the effort to identify the proper workflow. Therefore, the copper substrate computations are by no means representative and have no experimental reference.

The copper substrate computations were performed with full sized chains. The geometric minimization often result questionable geometries. For example, rare torsion angle appears near the head group. The geometric minimization algorithm does not mimic the natural relaxation process. Physically unlikely configurations can be accessed (theoretically, as an intermediate step on its way to global minima) and sometimes these configurations could be a local minimum. The fact that some computations manage to further relax in the order of eV is casting doubts on the full chain minimization approach.

However, regardless of how unreasonable the head group was bent, these set of calculations yielded a variety of head group configuration, all with different work function modifications. In those computations, the largest reduction recorded is 2.2 eV, which is significantly lower than any of the configurations that have a copper(I) oxide surface. The biggest reduction of 1.3 eV was computed with a local minima geometry of the methylated hydroxamic acid as shown in figure 7.9. This result does not indicate that attaching octadecyl hydroxamic acid to a copper surface would improve EUV dose as it did not identify the proper packing geometry. Instead, it highlights that the substrate has a substantial effect.

### 7.7.2 Additional Knobs

It is rather intuitive that chemically different copper and copper(I) oxide would interact with adsorbed molecules differently. However, in the absence of adsorption, different cleavage planes of the same material do not have the same work function. In compounds where different cleavage planes or orientations reveals different active sites, such changes are relatively intuitive [185]. However, the same is true even for solid metals such as tungsten [186, 187].

The roughness of the surface can also play a role. By manipulating step density, surface roughness can be controlled and subsequent studies suggests that high step density results in a lower work function [188, 189] (For interested readers, <http://venables.asu.edu/qmms/PROJ/metal1a.html> provides a very concise introduction to the matter). The mechanism proposed by [188, 189] hints that rougher surfaces are expected to have lower work function.

While monolayer adsorption such as SAM deposition is one way to manipulate the interface work function, the parameter space is huge. So is the potential applications. The above study was conducted to assess the impact of interface modification on recording material sensitivity but similar techniques can be used to induce near-interface doping and other phenomena useful to nano-electronics.

## CHAPTER 8

### Ongoing Endeavors—Ferrocene Based Resists

In this chapter, an ongoing endeavors of mechanistic investigations into a potential EUV resist material platform will be presented. As explained later in this chapter, EUV induced chemical changes have been reported in this system. While our collaborators are spearheading the synthetic efforts, the author seeks to complement them by identifying feasible radiation chemistry pathways and narrow down possibilities with computational techniques. Ultimately, such investigations would facilitate and speed up rational design and engineering on this material platform. The wealth of existing experimental reports provides valuable references for computational investigation. The combination of literature reports and computational investigations can shed light on potentially useful chemistry such as chain scission.

Ferrocene and its polymeric form has lots of interesting properties and is being used as a redox agent. Its potential utility upon one electron oxidation has been thoroughly investigated [190, 191]. It has been explored as the electron donor for a charge transfer resist [192]. The basic concept of such a resist is simple. Upon excitation, an electron is transferred from Ferrocene to a nearby electron acceptor. Given that the lowest unoccupied molecular orbital (LUMO) has a positive orbital energy, upon excitation the electron is likely to depart from the ferrocene and combine with a supposedly nearby electron acceptor, facilitating charge transfer. Such charge separation upon excitation makes the exposed area more polar, thus creating dissolution contrast. Upon one-electron oxidation, the color of ferrocene changes from pale orange to dark blue [192].

#### 8.1 Charge transfer nature

Such charge transfer has successfully been introduced by UV [192], e-beam [193], EUV[192] and even X-ray [194]. Preliminary studies have been conducted to explore using ferrocene as a X-ray resist. In EUV, e-beam and X-ray, due to the presence of ionizing radiation, the electron is likely ejected from the ferrocene molecule by impact ionization. After dissipating its energy over a distance, it becomes trapped by an electron acceptor (See chapter 2 for more details). Unlike other system such as chemically amplified resists (CAR), in both UV (optical) and ionizing radiation,

charge transfer is involved and similar chemical changes happen to the ferrocene center and the electron acceptor.

Although there is a correlation between EUV and DUV dose in this particular class of materials [192], one should not expect the its dose relative to CARs be the same in DUV and EUV. The reasoning lies in the radiation chemistry CARs have very different mechanisms in DUV and EUV while ferrocene based systems are expected to have very similar ones. In other words, if there are two types ferrocene resist A and B, if A works better than B in DUV, one expects A to do better in EUV as well. However, this correlation is not relevant to how their performances compare to, say chemically amplified resist. In other words, given this correlation, both A and B can both under-perform CARs in DUV but beat CARs in EUV.

The charge transfer nature in both EUV and DUV would undoubtedly make material research easier. Yet they are similar but not identical and the devil is in the details. As mentioned, in either EUV or DUV, chemistry is initiated when an ion pair is created. In DUV, this is triggered by optical absorption. Intuitively, because the target transition has a charge transfer nature, this process is inefficient in DUV. In optical transition, at the weak field limit (where Fermi's golden rule applies), the transition rate is proportional to the dipole matrix element magnitude squared.

$$M \propto |\langle \Psi_f(\{r_j\}) | \sum_j \vec{r}_j | \Psi_i(\{r_j\}) \rangle|^2 \quad (8.1)$$

$$(8.2)$$

In the simplest case where the excitation is essentially a single electron transition (For interested readers, the section on configuration interaction singles, CIS, in Q-Chem manual would be a good starting point) or a linear combinations of those, the transition probability is essentially the orbital dipole transition matrix element

$$\begin{aligned} M &\propto \left| \sum_{i,f} c_{i,f} \langle \phi_f | \vec{r} | \phi_i \rangle \right|^2 \\ &= \left| \sum_{i,f} c_{i,f} \int d^3r \phi_f(\vec{r}) \vec{r} \phi_i(\vec{r}) \right|^2 \end{aligned} \quad (8.3)$$

where

$c_{i,f}$  the coefficient of the  $i$  to  $f$  single excitation contribution to this excited state

$\phi_i$  the initial orbital

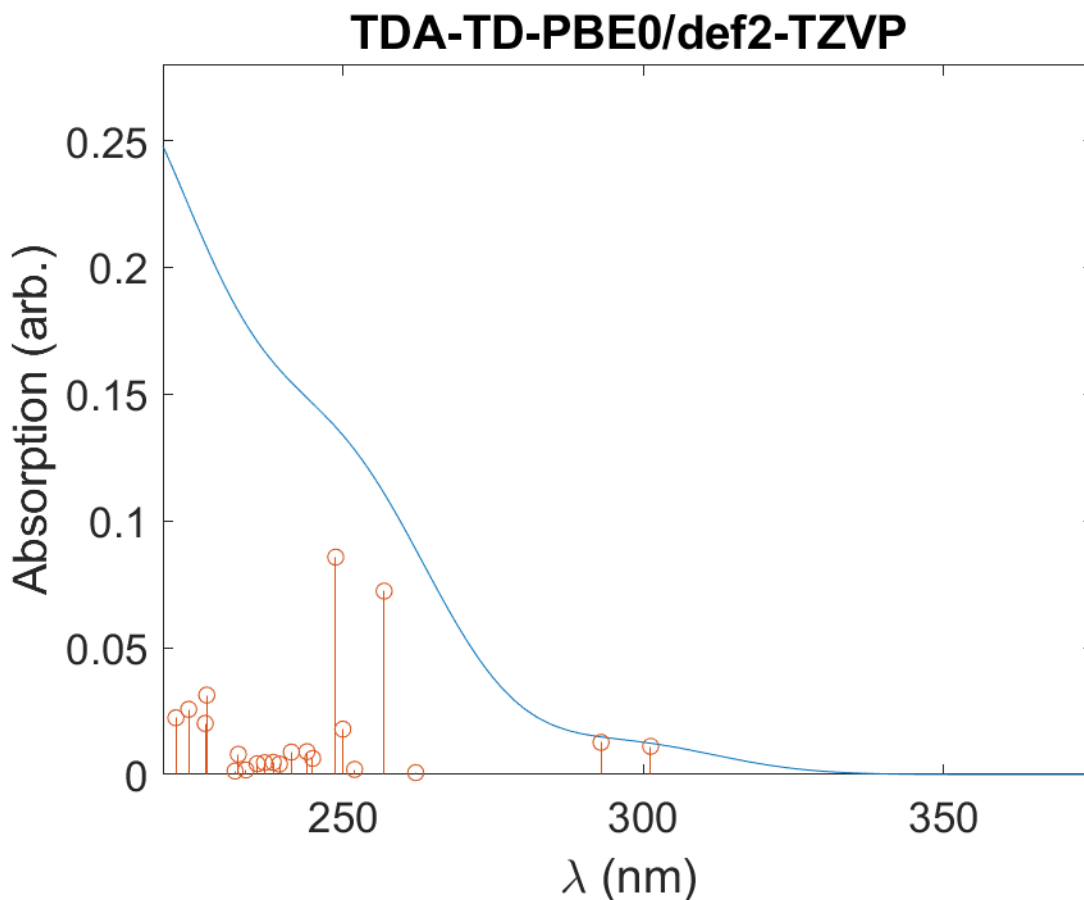


**Fig. 8.1** The optical absorption spectrum of triphenyl sulfonium triflate (TPS-TF). Spikes represent the energies of excited states and optical transition oscillator strength (excitation probability) and blue line is obtained by convolving the spikes with a 15 nm Gaussian kernel.

$\phi_f$  the final orbital

In most common cases,  $M$  is dominated by only a few leading contributors. For example, if the optical excitation is from HOMO to LUMO, then  $M = |\langle \phi_{LUMO} | \vec{r} | \phi_{HOMO} \rangle|^2$ . In any case, one can see that if  $\phi_f$  has little spatial overlap with  $\phi_i$  in terms where  $c_{i,f}$  is non zero (when they are far apart spatially) then  $M$  is going to be small. This is exactly the case for charge transfer excitation.

In fact, if one looks at the optical absorption spectrum of triphenyl sulfonium (TPS) triflate or nonaflate, one sees a low energy shoulder with very negligible contribution around 300 nm as shown in figure 8.1. That feature is coming from a charge transfer excitation where an electron is drawn from the anion (where the HOMO is localized) to the LUMO and LUMO+1 of the sulfonium cation ( $\phi_{106} \rightarrow \phi_{107}$  and  $\phi_{106} \rightarrow \phi_{108}$ ). On the other hand, the spectral weight of the optical transitions WITHIN the TPS cation completely dwarfs the charge transfer contribution, hinting at the importance of the transition matrix element. For example, the two tall spikes near 250 nm corresponds to transitions  $(0.63\phi_{104} + 0.74\phi_{105}) \rightarrow \phi_{107}$  and  $(0.54\phi_{104} + 0.79\phi_{105}) \rightarrow \phi_{108}$ . As



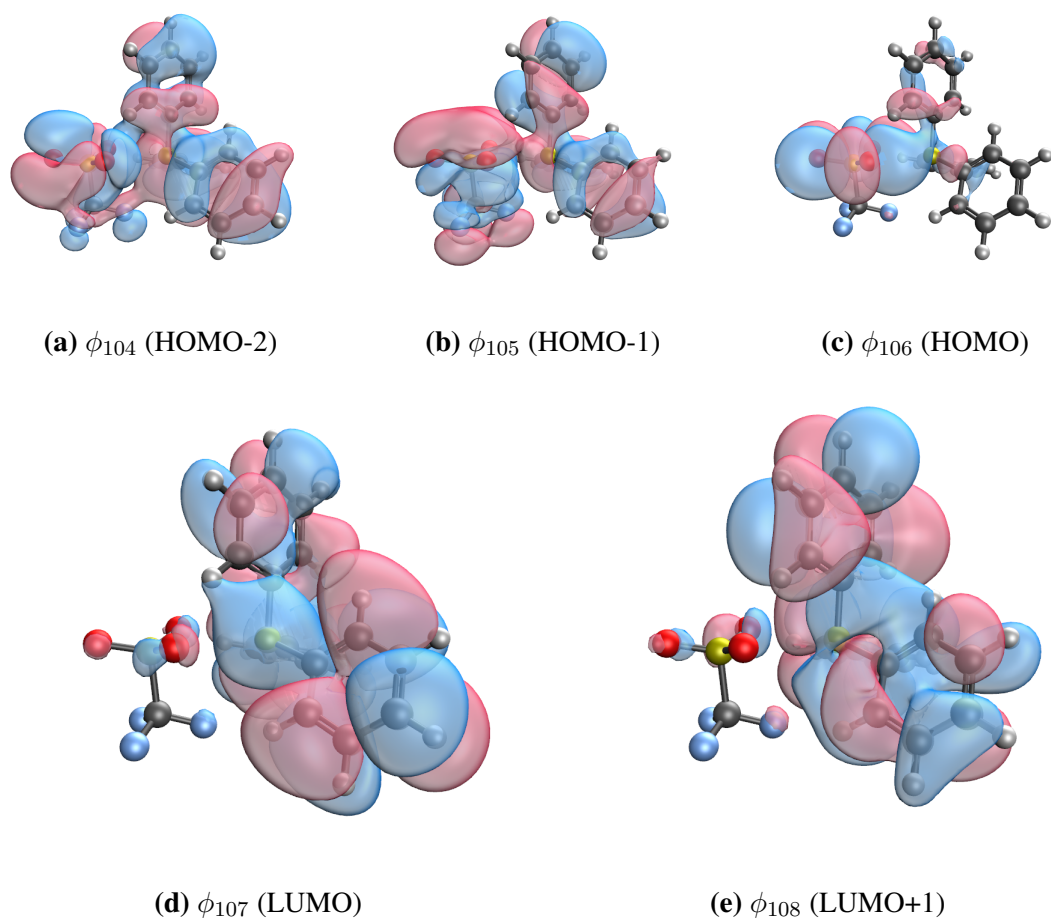


**Fig. 8.2** Frontier orbitals of TPS-Tf from HOMO-2(104) to LUMO+1(108). Colors indicate sign.

shown in figure 8.2, if one sum up orbitals 104 and 105, they qualitatively cancel each other out at the triflate anion (on the left). In other words, due to this interference, the electron in these strong transitions is actually coming from the TPS cation (on the right).

DUV photo-chemistry is limited by the optical transition matrix element. In a single step charge transfer process, the spatial overlap between the initial and final orbitals would be the limiting factor.

In some molecules, optical excitation and charge transfer don't happen simultaneously. In such scenario, the molecule is optically promoted to a higher excited state before decaying to charge transfer state. For example, optical excitation at an anthracene followed by charge transfer from the anthracene to the  $\text{Cu}_2^+$  ion trapped in thiacyclam (1,4,8,11-tetrathiacyclotetradecane) connected to the anthracene [195]. Such excite-transfer processes involving ferrocene can be found in reference [196]

So how about ferrocene (with no extra sensitizing group such as anthracene)? Should a single step process be responsible, the spatial separation between the ferrocene and the electron acceptor implies very small matrix element. Should the excite-transfer process involved, the limitation would be the matrix element for exciting the ferrocene within itself. It is known that the first few excited states of ferrocene is not optically accessible due to symmetry reasons [197]. The matrix element becomes non-zero when the molecule vibrates [197]. (thus the faint orange color at room temperature). Such limitations do not occur at higher excited states but that restricts the use of UV wavelengths such as 365 nm.

None the less in both scenarios, DUV driven charge transfer depends on the an optical transition matrix element. EUV radiation chemistry on the other hand does not. Upon ionization, the ejected electron is energetic and more importantly, would exist as a "free agent" for a limited amount of time before cooling down and falling into the most favorable electron trap or acceptor.

So, in summary, both DUV photo chemistry and EUV radiation chemistry would create the very same immediate active species (which is not the case in CARs). So the chemistry that follows would be similar, and one would expect EUV and DUV performance to correlate. Yet the way that DUV creates these species is inherently different.

## 8.2 Polyferrocene

From the above description, it appears that ANY ferrocene compound doped with a decent electron acceptor would act as a good EUV resist. That is the case if you can make a film. Ferrocene forms a crystalline solid at atmospheric conditions. To ensure uniform mixing, a polymer carrier or solvent is needed. That introduces an additional component which could prove unpredictable in the ensuing chemistry. Moreover, the content of the solvent is determined by film formation

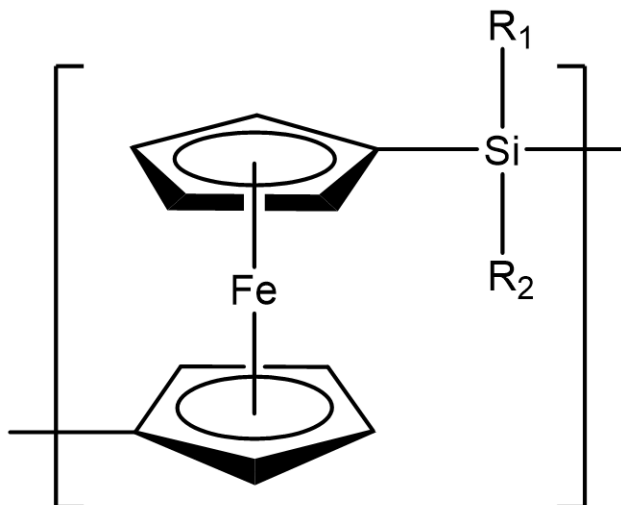


**Fig. 8.3** Molecular structure of poly(ferrocenylsilane, for more details on conformation of oligomers, please refer to [190]

requirements and might potentially limit the concentration of active components. However, if one can polymerize ferrocene, there would be no (potentially) inert component. At the same time, physical phases and thermal properties can be manipulated through the polymerization process.

Fortunately, scalable polymerization processes have been identified for polyferrocylsilane (PFS) [198] and similar processes for its germane (PFG) and stannane (PFSn) cousins. On top of the new “knob” provided by polymerization, the monomer structure also allows for additional functional. Instead of connecting ferrocene groups directly onto each other, there is a silane bridge between ferrocene groups and the functionalization of the silane bridge could act as an additional “knob”.

### 8.3 Additional Contrast Handles

The “default” contrast mechanism of generating ion pairs with charge transfer is simple enough but it is also very linear. In polyferrocene systems chain scission has been reported[199, 191], providing potential non-linear mechanisms. The scission mechanism has to be understood for it to be manipulated. Poly(ferrocenylsilane) is a complex system. In other words, there are many possibilities. Given the charge transfer is what initiates chemistry, what happens on the ferrocene chain is very likely ionization driven. At a glimpse, there are two very different possibilities at the highest level. The chain could scission spontaneously upon ionization, or the scission could be mediated by other species.

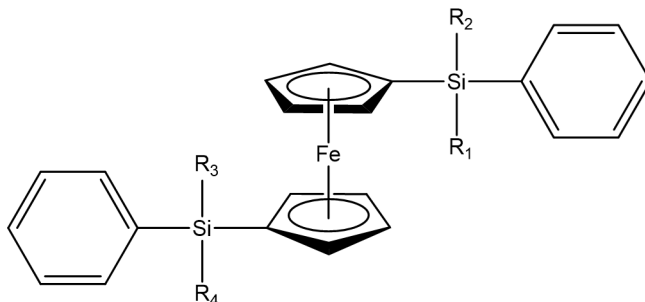


**Fig. 8.4** Molecular structure of the prototypical poly(ferrocenylsilane) monomer used in spontaneous scission assessment

## 8.4 Spontaneous scission

To decide whether scission is spontaneous, the bond strengths of a few prototypical monomers are computed. To avoid artifacts from the end group, phenyl rings are placed at the end (figure 8.4).

Four configurations of R groups are used. Ethyl group serves as a reference. Iodoform and dimethylamino groups are used to assess the effects of electron withdrawing groups and electron donating groups on the main chain. The trimethylstannyl group is included to see if having such a trivial EUV absorbing pendent group would affect main chain stability.

All computations were carried out at  $\omega$ B97X-D/def2-TZVP// $\omega$ B97X-D/def2-SVP [200, 111] in vacuum using Q-Chem [142].

Rather unsurprisingly, only one substitution, the iodoform variant, has a positive electron affinity. The rest have self ionizing lowest unoccupied molecular orbitals in vacuum.

As one can see in figure 8.5, in the reference monomer, the bond strength on the main chain is in the order of 4 to 5 eV before ionization. Upon ionization, even with the more stable silyl cationic fragment, the bond strength on the main chain is still between 3 to 4 eV in vacuum, which is comparable to a typical C-C single bond. The presence of electron donating group does not seem to weaken the main chain before or after ionization as indicated in figure 8.6. The presence of the ad-hoc trimethylstannyl group appears to weaken the main chain before ionization but the susceptibility of Sn-Si and Sn-C bonds appears to be protecting the main chain in the event of ionization as shown in figure 8.7. The Sn-C and Sn-Si bonds become much weaker upon ionization compared to the main chain.

When iodoform is incorporated into the monomer, as in figure 8.8, its low lying orbitals give it a positive electron affinity and the C-I bonds are prone to dissociative electron attachment but that is a property of the functional group itself.

In any case, spontaneous scission is not likely. It appears that the full shell ferrocene silylium ion provides some form of stabilization. As one can see in figure 8.8c, singlet products are more

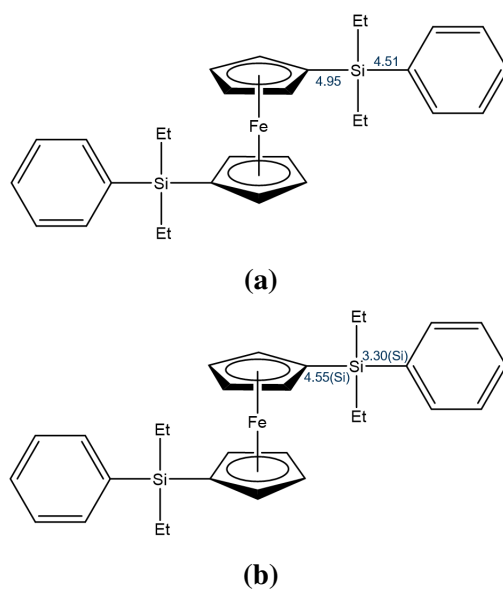


**Fig. 8.5** The bond dissociation energies (in eV) of the ethyl-ferrocenylsilane monomer before (8.5a) and after (8.5b) ionization. The cationic fragment of the more energetically favourable pathway is indicated in the parenthesis.

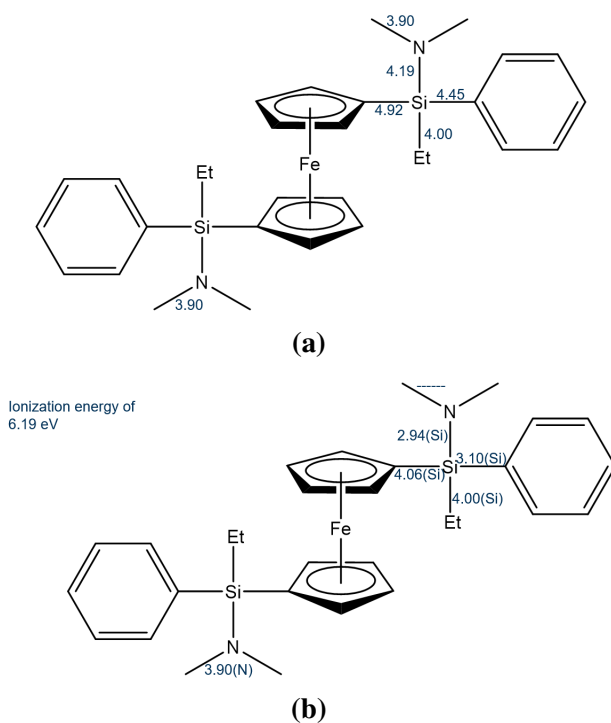


**Fig. 8.6** The bond dissociation energies (in eV) of the dimethylamino-ferrocenylsilane monomer before (8.6a) and after (8.6b) ionization. The cationic fragment of the more energetically favourable pathway is indicated in the parenthesis.

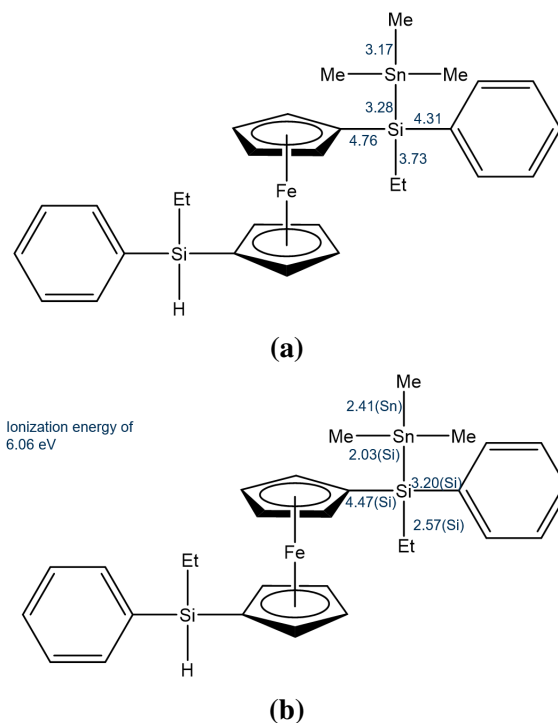


**Fig. 8.7** The bond dissociation energies (in eV) of the trimethylstannyl-ferrocenylsilane monomer before (8.7a) and after (8.7b) ionization. The cationic fragment of the more energetically favourable pathway is indicated in the parenthesis.

stable. In those configurations, the silyl group is drawn closer to the iron center, consistent with previous report [201]. This geometry is very similar to other full shell metastable intermediates in electrophilic attack on neutral ferrocene. Although this ultimately does not make spontaneous scission viable, this geometry is a recurring motif in ferrocene chemistry and will be shown to play a role in mediated scission.

In any case, the bond strength of the main chain is surprisingly insensitive to substitution on the silicon atom. The trimethylstannyl variant does stand out as shown in figure 8.7. Ionization does not destabilize the main chain as much as the other variants. The author speculates that the tin center provides more orbitals to hybridize with the cyclopentadiene rings, shifting the HOMO towards the tin atom, protecting the main chain. The reasoning behind this behaviour, if understood, can be used as a handle for chain scission as it moves the labile site away from the main chain, making attack on main chain (that will be discussed in following sections) less likely.

## 8.5 Mediated Scission

While spontaneous scission is unlikely, mediated scission becomes the prime suspect. In fact, it has been shown that the degree of chain scission can be manipulated by anions in the solution

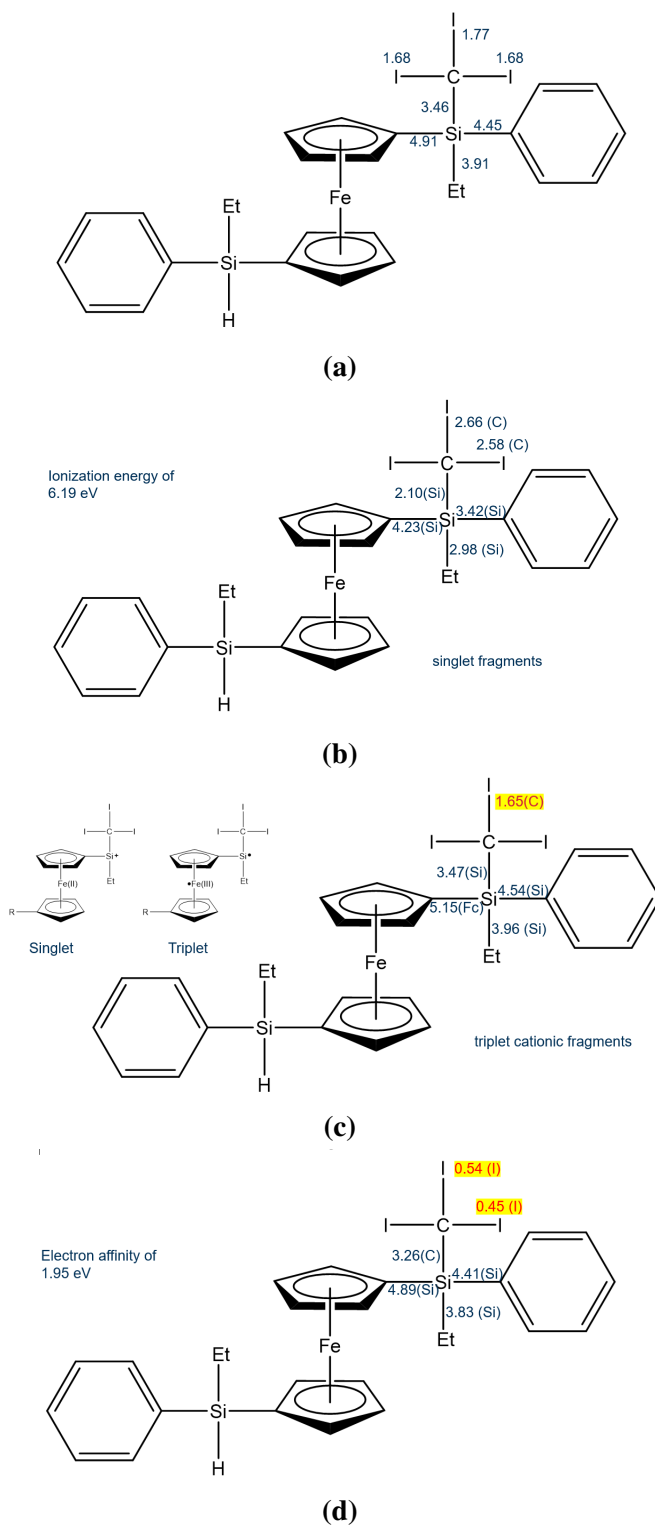


**Fig. 8.8** The bond dissociation energies (in eV) of the trimethylstannyl-ferrocenylsilane monomer before (8.8a) and after ionization with singlet cationic fragments (8.8b) and triplet cationic fragments (8.8c). The cationic (or anionic) fragment of the more energetically favourable pathway is indicated in the parenthesis. Bond dissociation energies upon electron attachment is shown in 8.8d.

Oxidant	DEA reaction	Initial chain Mn	Final chain Mn	Remarks
I <sub>2</sub> without immediate precipitation	$I_2 \rightarrow I^\bullet + I^-$ ( $2I_2 \rightarrow I^\bullet + I_3^-$ )	5e5	1e4 (50x)	Apparent slow reaction
I <sub>2</sub> with immediate precipitation with PF <sub>6</sub>	$I_2 \rightarrow I^\bullet + I^-$ ( $2I_2 \rightarrow I^\bullet + I_3^-$ )	1e5	4e4 (2.5x)	Only non-self precipitating combo
[NO <sup>+</sup> ][PF <sub>6</sub> <sup>-</sup> ] (PF <sub>6</sub> also act as the precipitating agent)	$[NO^+][PF_6^-] \rightarrow [NO^\bullet] + [PF_6^-]$	5e5	6e3 (83x)	most scission
[(p-BrC <sub>6</sub> H <sub>4</sub> ) <sub>3</sub> N <sup>+</sup> ][PF <sub>6</sub> <sup>-</sup> ] (PF <sub>6</sub> also act as the precipitating agent)	$[(p-BrC_6H_4)_3N^+][PF_6^-] \rightarrow [(p-BrC_6H_4)_3N] + [PF_6^-]$	5e5	4e4 (12.5x)	

[199]. That complicates the problem. A lot of good electron acceptors (which are essentially good one electron oxidizers) dissociate upon capturing an electron. This phenomenon is known as dissociative electron attachment (DEA). With some exceptions (for shelf stable molecules), the electron acceptors are full shell charge neutral molecules. Upon DEA, very likely a full shell anion and a charge neutral radical are produced. It's unclear which one is responsible for initiating the scission. Further more, there is a possibility that both take part in the scission at different stages.

Therefore, a couple of possible mechanisms are investigated and hopefully by elimination, the actual mechanism can be narrowed down.

Existing experimental results can provide some references for computational investigations. In reference [199] There are a few takeaways. Firstly, we know a few agents capable of triggering scission, they include Cl<sub>2</sub>, I<sub>2</sub>, [NO<sup>+</sup>][PF<sub>6</sub><sup>-</sup>], and [(p-BrC<sub>6</sub>H<sub>4</sub>)<sub>3</sub>N<sup>+</sup>][PF<sub>6</sub><sup>-</sup>]. The relative chain scission rates of 4 of them (with Cl<sub>2</sub> excluded) are discussed in detail in reference [199].

### 8.5.1 Anion Attack

The most intuitive possibility is the full shell anion attacking the radical polyferrocylsilane cation. The first question to address is whether the substitution happens at the ferrocene or at the silane moieties. However, when methyl groups were replaced with phenyl rings, which are much more bulky, chain scission wasn't reduced detrimentally suggesting that steric hindrance is not the limiting factor, which is usually the case for similar mechanisms such as bi-molecular nucleophilic substitution [191].

That brings us to the ferrocene itself. The chemistry of ferrocenium radical cation is not that



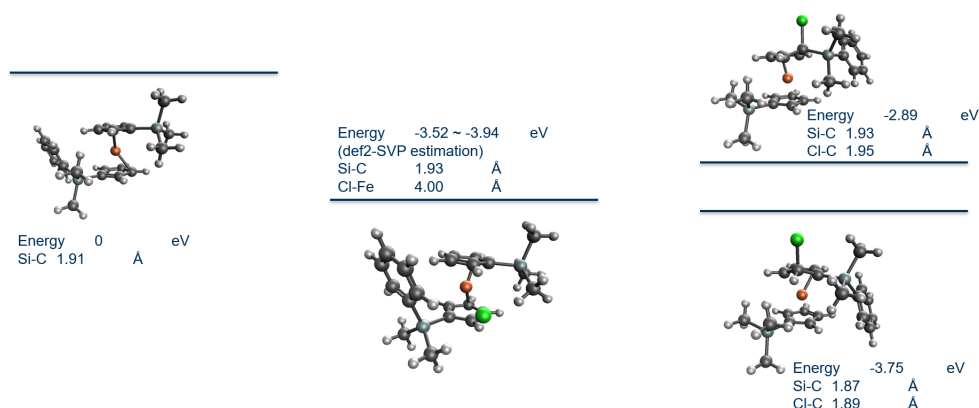


**Fig. 8.9** The intermediate state energy upon a  $\text{Cl}^-$  attack. At the middle, pathway 3. On the right, pathways 1 (above) and 2 (below)

well understood. Still one can use ferrocene as a reference. Apparently, (prior to ionization of course) the aromatic ring is as usual electron rich, making the ring susceptible to electrophilic attack. In fact, electrophilic substitution is a common way of producing ferrocene derivatives. There are a few possible avenues of ingress

1. Direct displacement—the attacking anion make the Si-Cp carbon tetravalent, eventually severing the Si-C bond.
2. Indirect displacement—the attacking anion make a H-Cp carbon tetravalent. The hydrogen (whose charge is actually ambiguous) atom is shifted to a neighboring Cp carbon, making it tetravalent. The process continues until the main chain carbon becomes tetravalent and expels the silane main chain.[202]
3. Outer sphere docking—the attacking anion somehow finds a stable position on the “equator” of the ferrocenium. How that evolves into substitution is unclear but such intermediate state could set the stage for the above Cp-based pathways.

For direct and indirect displacement pathways, stable intermediates are identified when the attacking anion is chloride as shown in figure 8.9. When the same anion is used, a docking geometry is also identified. Energetically, docking geometry could promote the displacement pathways.

Note that indirect displacement is essentially direct displacement with extra steps. So if direct displacement is not favourable, so would be indirect displacement.

However, this excursion in to anionic attack is short lived because the author could not identify a transition geometry for pathways 1,2, or 3 when iodide ion (which would conceivably be the responsible reagent when  $\text{I}_2$  is reported to induce scission [199])) is used.

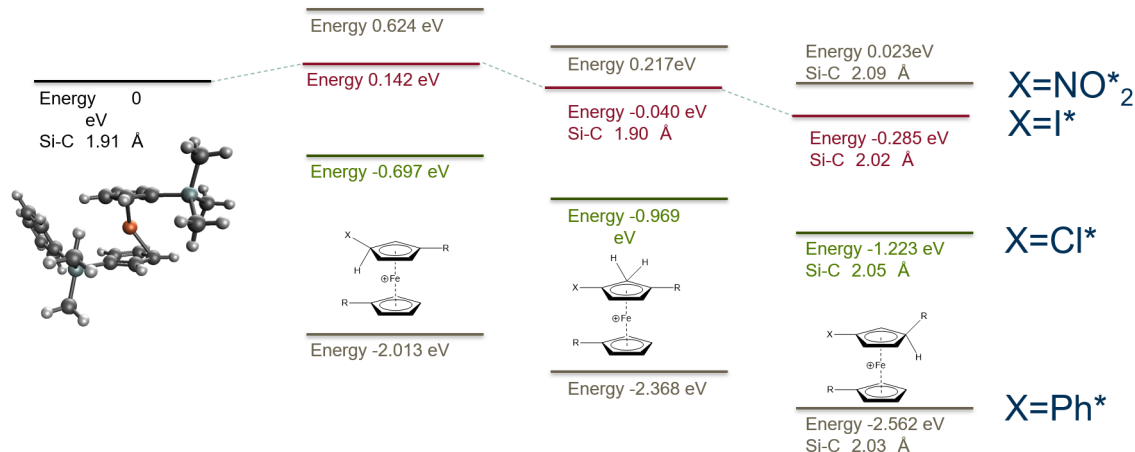


**Fig. 8.10** The intermediate state energy of different incoming radical

### 8.5.2 Radical Attack

In a very procedural manner, one can replicate what have been attempted with anions with radicals. Before diving into the details, the author would like to point out that the intermediate states of a radical attack on ferrocenium is the same as a ferrocene under the attack of full shell cation of the radical. This class of intermediate species have a few notable feature. Until something is eliminated, there would be a tetravalent carbon on one of the cyclopentadiene rings. It has been reported that the (or one of the) hydrogen atom would be drawn towards the iron center. This interaction might stabilize the intermediate geometry but the fact remains that this intermediate geometry plays an integral role of ferrocene (not ferrocenium) chemistry and now it appears to be accessible through radical attack on a ferrocenium ion.

The author attempted to identify the intermediate geometries involved in this pathway using I<sup>\*</sup>, Cl<sup>\*</sup>, and NO<sup>\*</sup> at the beginning. It appears the NO<sup>\*</sup> addition is very endothermic. However, NO<sub>2</sub><sup>\*</sup> addition seems more viable. The author notes that NO<sub>2</sub><sup>\*</sup> can technically occur but could not estimate the likelihood of this process.

Regardless of the incoming radical, as long as it is attached to one of the cyclopentadiene rings, every step towards main chain scission is exothermic. In other words, as long as the incoming radical combines with the ferrocenium and form an intermediate geometry, it will arrive at the transition geometry where the Si-Cp carbon is tetravalent for energetic reason. And in that particular geometry, the Si-Cp bond is lengthened in all cases

The computations on radical attack demonstrates the viability of this mechanism. It is consistent with the fact that [NO<sup>+</sup>][PF<sub>6</sub><sup>-</sup>] is more capable of scission than [(p-BrC<sub>6</sub>H<sub>4</sub>)<sub>3</sub>N<sup>+</sup>][PF<sub>6</sub><sup>-</sup>] as no radical is generated in the DEA of the latter.

However the same calculations also suggest that I<sub>2</sub> should result in more scission than [NO<sup>+</sup>][PF<sub>6</sub><sup>-</sup>]

but experimentally it wasn't the case. With some low level DFT computations (at B3LYP/def2-SVPD//B3LYP/def2-SVPD), the author realized that the bond strength upon electron attachment is around 1.9 eV. Alternatively, at the level of  $\omega$ B97X-D/def2-TZVP// $\omega$ B97X-D/def2-SVP, the bond strength is around 1.3 eV. In both cases the reaction is still very far above room temperature, which is 0.026 eV. However, the reaction  $I_2^- + I_2 \rightarrow I_3^- + I^\cdot$  is much less endothermic in vacuum and its energy, evaluated at  $\omega$ B97X-D/def2-TZVP// $\omega$ B97X-D/def2-SVP (the energy of  $I_2$  is estimated by that of  $I_2^-$  plus the electron affinity on the NIST database. The average value of 2.5 eV is used), is 0.13 eV. While it is more energetically viable, it is bi-molecular in nature, making it slower. These results on iodine dissociation, combining with the energy of intermediate species in the radical attack pathway could explain the experimental observation that scission is slow when  $I_2$  is used as the oxidizer. To make this argument complete, the dissociation energies of other oxidizers have to be computed for comparison as well.

This set of computation none the less suggests that if one can produce a phenyl radical (which can be generated by a sulfonium (TPS) cation upon exposure to EUV), one can speed up chain scission. The author however cautions that in DUV, the interaction between TPS and ferrocene would complicate the simple picture presented in the discussion on DUV excitation in chapter 5. When both TPS cation and ferrocene are present, not only is the ferrocene backbone actively competing for photons with the TPS cation, there could also be resonant energy transfer between the two as they are both conjugated compounds. Since subsequent acid generation is not necessary, TPS salt with anions such as  $PF_6^-$  or  $SbF_6^-$ , which are rather strong precipitating agents (in organic solvent), can be used to enhance solubility contrast. On the other hand, the opposite might be more preferable but in any case, the anion is another knob for material tuning and is now not constrained by the acidity of its conjugate acid.

Even though the main chain Si-Cp bond is weakened, that is still a stable geometry. It does not imply that scission is not spontaneous—scission can be an exothermic process with an energy barrier. To investigate whether this is the case is straight forward. Only additional calculations about scission products are needed. Another possibility is anion mediated scission. None the less, at this point the ferrocene monomer is still positively charged.

### 8.5.3 Anion Attack after radical attack

The anion attack on the last intermediate geometry shown in figure 8.10 is surprisingly potent. By placing a iodide anion on the opposite side of the silane group, as shown in figure 8.11 on the left, instead of being repelled like in typical  $S_N2$  reactions (that happens because the transition geometry is a local energy maximum in typical  $S_N2$  reactions) the iodide ion is drawn towards the back side, prompting the silane into a *sp*<sup>2</sup> geometry as in typical  $S_N2$  transition states, as shown in figure 8.11 at the middle. However, unlike  $S_N2$  reactions, this geometry (since it is not a local

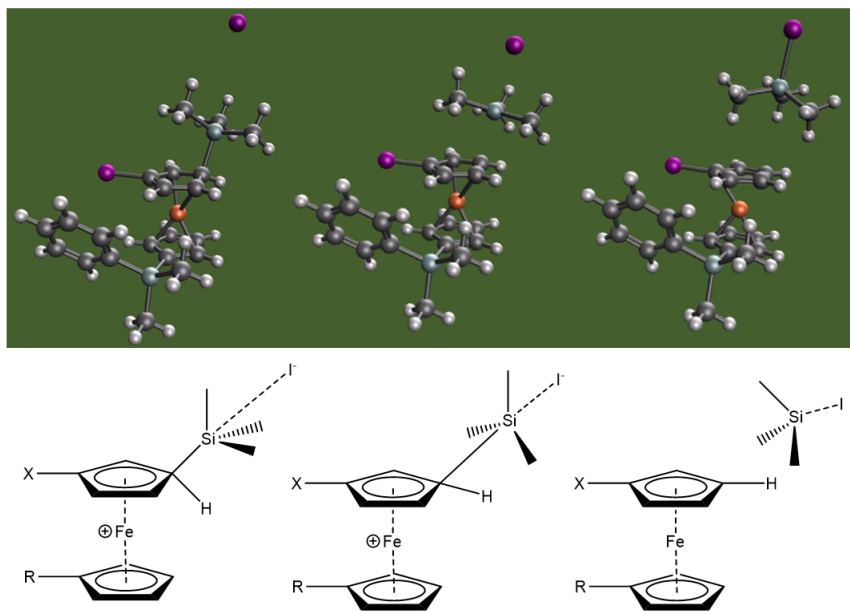


**Fig. 8.11** The spontaneous anion attack after radical substitution.

extremum, it does not qualify to be a transition or intermediate geometry) is on an energy gradient and process continues until an iodosilane is formed (figure 8.11, on the right). The entire process happens in geometric minimization, strongly hinting at its spontaneity.

This mechanism is reasonable when the incoming anion is coordinating. That is—it is clear how it would bond with the silane. If less coordinating anions are used this back side substitution process might not be as spontaneous, which is somewhat consistent with experiments [191].

## 8.6 Lingering Questions

The above investigations paint a picture with the following implications.

1. The polyferrocene monomer is incapable of capturing electrons. To facilitate electron transfer, electron acceptors need to be included by blending or functionalization of the main chain.
2. Scission has to be mediated.

While the above statements appears to be true, they are as valid as the computational methods used

### 8.6.1 Can Polyferrocene be an Electron Acceptor

As a by product of the computations in section 8.4, given the positive binding energy of the LUMO in all but one monomers, we expect them to have negative electron affinity. In other words, they

do not prefer to capture an extra electron. However, these computations are carried out in vacuum, and polar media are known to stabilize charged species. It is conceivable that the surrounding polymer molecules could act as a dielectric and stabilize the polyferrocene anion, thus making polyferrocene an electron trap. The author does not rule out this possibility but he would also like to point out that such stabilization occurs to all anions so other charge neutral electron acceptor such as iodoform will also have stronger electron affinity in a dielectric background. However, for ionic pair electron acceptors (where the cation is carrying out the function), the cation becomes less polar upon capturing an electron, rendering a more complicated picture.

#### 8.6.2 Where does Spontaneous Scission Stand?

Again, the computations in section 8.5 were all carried out in vacuum and the stability of the silylium cation can be underestimated. Even though the post ionization bond strength in the order of typical C-C bonds, the dielectric stabilization of cations can be in the order of eVs, making repeating these computations in dielectric media a sensible next step.

### 8.7 Summary

Combining previous endeavour in understanding ferrocene containing systems as a resist [192], existing experimental characterization of poly(ferrocenylsilane) [199, 191], and computational investigations presented in this chapter, the author believes that the exposure chemistry is likely charge transfer driven. Also, electron acceptors are likely to play a role in enhancing, if not enabling such chemistry. The experimentally reported electron acceptor dependence, combined with the intermediates identified in section 8.5 suggests that a systematic study on electron acceptor and silane functionalization could help elucidate mechanism further and identify performance driver.

## CHAPTER 9

### Prospects

The content of this thesis can simply be summarized by a few concise statements. Firstly, EUV radiation chemistry specific experiments were developed and characterized. Secondly, chemical activation in EUV is a performance driver that can be investigated and manipulated with existing know-hows. Thirdly, computational chemistry methods with reasonable scalability can be applied to aid the engineering of chemical activation. To illustrate the point molecular level process that drive EUV chemical activation were studied and presented.

As the individual chapters are rather self-contained, in lieu of repeating the conclusions from each individual chapters, the author attempts to build upon what he has learned in the process of his work to identify feasible material research opportunities.

As detailed in chapters 1 and 2, EUV radiation chemistry is novel. With underlying principles so drastically different from DUV, a material revolution, instead of a evolution as in the past decades, is necessary. The commercialization of tin based metal oxide resists, and the mushrooming of material path-finding presentations in recent conferences are testimonies of this ongoing tectonic change. Such reaction from the industry highlights the scale of this challenge. On the flip side, because the immensity of such challenge, bold and innovative solutions are needed, making this subject matter a breeding ground of opportunities. At a higher level, the urgency to move out of the pure trial-and-error evolutionary approach opens the door for other avenues.

The abrupt entrance of novel radiation chemistry makes rational material design—creating materials from the bottom up, in place of pure trial-and-error sound all reasonable again. After all shooting in the dark has its Achilles' heel—it's slow and chances are you don't end up very far from where you started. Still, everything that works has to be tried and tested so trial-and-error has to stay so the question is about how to rationally decide what to try.

In chapters 6 and 7, novel technologies that are original to EUV were discussed. In those discussions, the materials and technologies have their potentials explored by exposure experiments before mechanistic studies entered to investigate how it they function. By having exposures before mechanistic investigations, the identification of new chemistry is not “first principles based”. In reality chemical intuition is involved in identifying potential chemistry but then intuition would

be the only gate keeper. In fact, the two existing organotin-oxo resists were born out of chemical intuition. One can however, hypothetically, turn the table around—by identifying potentially useful chemistry, narrowing down options and eventually engineering them into patterning materials. Is that practical?

The appeal of “following first principles” is its potential to identify candidates that had once been unimaginable. That strikes the weakness of the trial-and-error, make-it-then-expose-it approach at its heart. To create a prototypical material platform capable of producing exposure contrast, selection and screening of solvent, developer, and other processes are necessary. For every new concept, this entire process has to be repeated again.

More than often researcher have to go through lots of material combinations and are thus rather resource intensive. By bring mechanistic studies earlier into the picture, there are a few benefits. First of all, if there is any show-stopper issues in the proposed mechanism, it would more likely be identified before the full-on trial-and-error formulation process. This is especially important for EUV. In DUV, given the dominance of chemically amplified resist (CARs), most material advances were about improving the acid catalytic chemistry. Armed with decades of research, the mechanism of CAR has been rather well understood in DUV. So material improvements are often optimizations and process specific modification where the risk of complete failure is low. In EUV, given a different radiation-material interaction paradigm, EUV specific chemistry that is not derived from DUV (The metal oxide system in chapter 6 to a large extent qualifies for that. Using organotin-oxo systems as a DUV resist has been considered [126] but the true advantage of that material platform lies in EUV) is needed. The task on hand is not the evolutionary optimization of DUV CAR anymore so, should one repeat the pure trial-and-error approach, the chance of absolute failure is significantly higher and the parameter space to explore is much bigger.

Moving away from pure trial-and-error paradigm to a more rational approach has been an on going evolution and is in fact happening. It is one thing to have a photo-active system, its another to manipulate subsequent dissolution contrast—imaging performance and contrast curve depend on all of the chemical and physical processes involved, making isolating the contribution of acid complicated. So experimental mechanistic studies alongside material development is not a novelty. For example, Coumarin-6 (C6) has been widely used to measure acid concentration in films[4, 13, 38]. The optical absorption spectrum of C6 changes upon protonation. By observing the optical spectra of C6 doped films between different process steps, the production of acid can be studied directly. That is a great improvement from having only patterning or contrast curve measurements because C-6 acid yield experiments do not require development so identification of a developer is not needed for every new formulation, bypassing the aforementioned complications, thus speeding up investigations.

The example of Coumarin-6 shows that rational design is desirable. Going back to compu-

tational chemistry, can it be a practical tool for rational design? At this point the greater chemistry/chemical engineering community have a rather reasonable understanding of the strength and weaknesses of various computational methods. As the author illustrated, in the myriad events subsequent to EUV photon absorption, computational chemistry is good for investigating some reactions, or even predicting outcome. For some other processes, computational approaches just do not fare well.

The holy grail is to use computational method (Not necessarily computational chemistry) to identify possible mechanism. Yet for a mechanism to work, the stars have to align everything from the radiation chemistry all the way to dissolution and the complexity make it a very ambitious goal. A more realistic target, as a good starting point, is to use computational methods to optimize a proposed or existing platform. Mechanistic investigations would help elucidate the mechanism and once the roles of the reagents are understood, their requirements become clear and the problem is more tractable. Everything in chapters 5,6, and 7 fit well into this rational.

The success of computational material research for batteries can shed light on how computational methods can be inserted into EUV material research. The example [203] is highly illustrative.

First of all, the task on hand is well defined. This is an inherent advantage of solar fuel cell (batteries as well)—the role and function of the electrodes are always the same so it is rather clear what properties are desirable and what computations are to be executed

Secondly, there is a very strategic use of different methods. At the very beginning, PBE+U computations are used. These computations are known to underestimate bandgap but they are fast and scale well (to  $N_{\text{atoms}}^3$ ) making them good for extreme throughput screening. Even if it can't reliably predict the exact band gap, it is still capable of ruling out candidates. As the number of candidates go down, more sophisticated and demanding methods, such as HSE (a hybrid GGA method) and PBE+U slab computations (similar to those in chapter 7) can be used.

Thirdly, computations and experimentation came together seamlessly. At some point experimental criteria take over to further narrow down the funnel. Some of the measurements such as XRD, provide information, in this case purity, that is not accessible with computations. Some experimental criteria, such as optical band gap, serve as verification. This transition signifies the point where it becomes more economical to experimentally test a set of compounds than developing a computational method that could predict the outcome or create a similarly useful screening criterion.

Identifying the computation-experimentation transition is critical. At some point, it would be more efficient to do experiment and attempting to introduce computational methods at that stage would be a fool's errand in a strategic sense. Realizing whether a problem has crossed that threshold is more an art than it appears. For example, if one wants to identify a photo acid



generator for, say 254 nm lithography, in principle, one can break down the functionalities of a PAG into tractable computations and make recommendations. In reality though, 254 nm is a mature technology where significant changes that could impact upstream or downstream material processing would not be welcomed. That put a huge constraints on possible molecular variations. Combining that with tightening EPA regulations, the number of feasible molecules could be so small that experimentation could just be way easier. Having said so, should computational material discovery been as developed as they are in the dawn of CARs, the conclusion could have been completely different. This illustrates the importance to have industry experts in the loop so that the development of such projects could be nimble enough to stay relevant and cutting edge at the same time.

At this point, once the material platform and mechanism is more less known, the same recipe (Constructing the problem, funnel down, and transition to experiment) can be used should the material space for any of the reactions is large enough that computational screening has an advantage.

Yet, as mentioned, that does not bring us the holy grail—picking a possible new chemistry is still a human intuition based process. Identifying a new platform or paradigm could be difficult because in every platform, the number of reactions and the relationships between reagents are conceivably very different. That adds extra dimensions to the parameter space and uncertainties of what questions to ask or what to compute. In contrast, when one attempts to identify an electrode, in any battery system, the properties of interest are always the same, allowing for a clearer road map.

The challenge is enormous and at this point it is rather intractable. What's on the horizon are incremental improvements that enhance the current approach. Computational methods which aids the instincts of material scientists and engineers are in an indirect sense a computational material method. Artificial intelligence has its sight set to mimic human intelligence but that should not and does not pit humans and machines against each other. A new computational paradigm does not necessarily displaces a human process.

The human chemical intuitive comes from the knowledge and understanding of physical principles accumulated over decades and generations. To make this body of knowledge and experience as accessible as possible would undoubtedly enhances the intuition of domain experts.

Speaking from experience, the author often build his knowledge from “citation networks”. He starts from a publication and branches out to publications that cite or are cited by the starting publication and so on. However, relevant subjects don't necessarily share the same network. A very tangible example is the fact, according to experts fluent in both subjects, that EUV ionization/electron-attachment driven chemistry is similar to battery chemistry yet the similarity is often neglected. Although the goals might not be the same, the convergence of the two implies there are opportunities for collaboration. So is there a way for the community to leverage the knowledge, experience,

and expertise of people whom we do not realize they are relevant?

Natural Language Processing (NLP) has proven its worth in multiple disciplines and could offer a few applications. It can provide quick summary, possibly analyze the relationships and hierarchies between different research work, providing researchers a landscape of existing investigations, putting them at a better vantage point to start of them intuitive search.

NLP is a class of methods. While some of them overlaps with machine learning or artificial intelligence, NLP is not a subset of either. However, it does require a huge amount of data. Scouring the material science literature is a routine task in industry research and development. The potential of NLP has been illustrated in a study aimed at in identifying thermoelectric materials[204]. In that work, keywords were abstracted into embedding, which are high dimensional vectors whose basis is identified using machine learning algorithms with relevant scientific abstracts as inputs. In essence, the user gives the algorithm a body of literature to provide a context to create a high dimensional representation of words. This new representation of keywords, as it turned out, allows one to estimate relevance of concepts by simply looking at the cosine distance between two keywords in this hyperspace (apparently the vectors are not normalized so cosine distances are used instead of dot product).

There are tow noticeable takeaway from [204]. Firstly, their method is capable of beating density functional theory (which is the generalized gradient functional PBE[174] in [204]) in predicting the rank of thermal power. Secondly, it is capable of suggesting new materials to try. For example,  $\text{Li}_2\text{CuSb}$ , in this hyperspace of words, is very close to ‘thermoelectric’. However, ‘thermoelectricity’ and related keywords never coexisted with  $\text{Li}_2\text{CuSb}$  in any abstract (alluding to the aforementioned problem about disconnected knowledge networks). With abstracts dating back to 1922, the predictive power of this criterion was back tested. For each given year, there are materials that scored high but had never been linked with thermoelectricity. On average, if one picks the top 50 predictions, around 20 of them would turn out to be accurate in 19 years. Thirdly, unlike a lot of well known machine learning models such as alpha-fold[205, 206], the method in [204] is not (or to a much lesser extent) a black box. The model provided enough information to explain why such predictions were missed by unearthing existing but neglected connections. In the example of  $\text{Li}_2\text{CuSb}$ , it was found to be closely related to the concepts ‘Heusler compound’, ‘indirect band [gap]’, ‘ $\text{BaCu}_2\text{S}_2$ ’, and ‘optoelectronics’—all of which are related to ‘thermoelectric’. While these connections are new, they are not counter-intuitive. In fact, these connections exists because they are closely related in existing abstracts, hardly counter-intuitive.

The fact that such NLP method beats DFT is surprising to the authors of [204]. However, upon a quick glimpse at their methodology for computing the Seebeck coefficient from DFT, one realizes that they assume the relaxation time, which is related to scattering, is constant across all materials. This is a big assumption as myriad factors such as lattice dislocation and grain boundaries all affect

relaxation time. While it is relatively straightforward to compute the effective mass, Fermi velocity and other parameters related to the dispersion with DFT, accounting for all the phenomena that affect the relaxation time with DFT is a lot more convoluted. For example, one can start an odyssey to understand the thermodynamics of lattice dislocation. However, this would take a lot more resource than simply computing the dispersion with DFT so doing it over 48,000 compounds mentioned in [204] would be a challenge at another level. This complication mirrors what faces EUV material research. We know roughly what computations can predict which processes, but should we put all our eggs in those processes? At some point, the marginal return of optimizing those processes would diminish. The EUV materials community is not the first to confront such dilemma and NLP techniques have brought progress in complex processes such as bio-molecular pathway identification[207], cancer research[208], material synthesis[209, 210], automatic hypothesis generation [211] and more. In the author's opinion, when it comes to hypothesis identification or new platform exploration NLP appear to present less risk to material developers in the EUV material community. Proven results in other subjects with similar challenges mean that investments into such has a good chance of paying off. Also, even if this tool is adopted, it will not displace anybody or cause big changes to material development workflow. Conceivably, such techniques would ideally make the jobs of material researchers in the community more streamlined.

Back to the bigger context of EUV material research. It appears that once a platform has been identified and preliminary hypothesis of its mechanism is formed, existing computational chemistry techniques, in conjunction with experiments, are good at elucidating mechanisms and optimizing material design as in the theory–experiment collaboration that has taken place over the past few decades. After working on a few research problems using computational chemistry, the author quite ironically realized that it has both strengths and weaknesses, and is not always the best tool. It is versatile but it has its limits. The bottom line, however, is always about identifying the best match between tools and problems so the only “method” that will always work is being diligent on the lookout.

It is the best of times, it is the worst of times. Like all tectonic changes in history, some finds themselves in an epoch of peril, for the others, an epoch of opportunity. It has been quite a ride, like a roller coaster. It might be too exciting for some but the author thoroughly enjoys every single minute of it.

## REFERENCES

- [1] G. M. Gallatin, P. Naulleau, and R. Brainard, “Fundamental limits to EUV photoresist,” in *Advances in Resist Materials and Processing Technology XXIV* (Q. Lin, ed.), vol. 6519, pp. 387 – 396, International Society for Optics and Photonics, SPIE, 2007.
- [2] P. Naulleau and G. Gallatin, “Relative importance of various stochastic terms and EUV patterning,” *Journal of Micro/Nanolithography, MEMS, and MOEMS*, vol. 17, no. 4, pp. 1 – 7, 2018.
- [3] M. E. CASIDA, *Time-Dependent Density Functional Response Theory for Molecules*, pp. 155–192. 1995.
- [4] W. D. Hinsberg and G. M. Wallraff, *Lithographic Resists*. John Wiley and Sons, Inc., 2012.
- [5] D. R. McKean, R. D. Allen, P. H. Kasai, U. P. Schaedeli, and S. A. MacDonald, “Acid generation and acid diffusion in photoresist films,” in *Advances in Resist Technology and Processing IX* (A. E. Novembre, ed.), vol. 1672, pp. 94 – 103, International Society for Optics and Photonics, SPIE, 1992.
- [6] K. Closser, D. Ogletree, P. Naulleau, and D. Prendergast, “The importance of inner-shell electronic structure for enhancing the euv absorption of photoresist materials,” *Journal of Chemical Physics*, vol. 146, no. 16, 2017. cited By 12.
- [7] L. Long, A. R. Neureuther, and P. P. Naulleau, “Modeling of novel resist technologies,” in *Advances in Patterning Materials and Processes XXXVI* (R. Gronheid and D. P. Sanders, eds.), vol. 10960, pp. 117 – 129, International Society for Optics and Photonics, SPIE, 2019.
- [8] N. Mardirossian and M. Head-Gordon, “Thirty years of density functional theory in computational chemistry: an overview and extensive assessment of 200 density functionals,” *Molecular Physics*, vol. 115, no. 19, pp. 2315–2372, 2017.
- [9] J. H. Ma, H. Wang, D. Prendergast, A. Neureuther, and P. Naulleau, “Investigating EUV radiation chemistry with first principle quantum chemistry calculations,” in *International Conference on Extreme Ultraviolet Lithography 2019* (T. Itani, P. A. Gargini, P. P. Naulleau,

- and K. G. Ronse, eds.), vol. 11147, pp. 103 – 113, International Society for Optics and Photonics, SPIE, 2019.
- [10] S. W. J. Scully, J. A. Wyer, V. Senthil, M. B. Shah, and E. C. Montenegro, “Autodissociation of doubly charged water molecules,” *Phys. Rev. A*, vol. 73, p. 040701, Apr 2006.
- [11] Z. Cai, S. Chen, and L.-W. Wang, “Dissociation path competition of radiolysis ionization-induced molecule damage under electron beam illumination,” *Chem. Sci.*, vol. 10, pp. 10706–10715, 2019.
- [12] L.-W. Wang, M. Califano, A. Zunger, and A. Franceschetti, “Pseudopotential theory of auger processes in cdse quantum dots,” *Phys. Rev. Lett.*, vol. 91, p. 056404, Jul 2003.
- [13] T. Kozawa and S. Tagawa, “Radiation chemistry in chemically amplified resists,” *Japanese Journal of Applied Physics*, vol. 49, no. 3 PART 1, 2010.
- [14] A. Narasimhan, L. Wisheart, S. Grzeskowiak, L. E. Ocola, G. Denbeaux, and R. L. Brainard, “What We Don’t Know About EUV Exposure Mechanisms,” *Journal of Photopolymer Science and Technology*, vol. 30, no. 1, pp. 113–120, 2017.
- [15] R. F. Egerton, *Electron energy-loss spectroscopy in the electron microscope*. Springer, 2011.
- [16] M. Dapor, *Computer simulation of electron transport in solids with applications to materials analysis and characterization*. PhD thesis, University of Trento, 2013.
- [17] O. Kostko, B. Xu, M. Ahmed, D. S. Slaughter, D. F. Ogletree, K. D. Closser, D. G. Prendergast, P. Naulleau, D. L. Olynick, P. D. Ashby, Y. Liu, W. D. Hinsberg, and G. M. Wallraff, “Fundamental understanding of chemical processes in extreme ultraviolet resist materials,” *The Journal of Chemical Physics*, vol. 149, no. 15, p. 154305, 2018.
- [18] G. Kasperski, P. Mozejko, and C. Szmytkowski, “Electron scattering on c6f6 and sf6 molecules,” *Zeitschrift für Physik D Atoms, Molecules and Clusters*, vol. 42, pp. 187–191, Sep 1997.
- [19] H. Tanaka, T. Masai, M. Kimura, T. Nishimura, and Y. Itikawa, “Fluorination effects in electron scatterings from ch<sub>4</sub>, ch<sub>3</sub>f<sub>1</sub>, ch<sub>2</sub>f<sub>2</sub>, ch<sub>1</sub>f<sub>3</sub>, and cf<sub>4</sub>,” *Phys. Rev. A*, vol. 56, pp. R3338–R3341, Nov 1997.
- [20] A. Gauf, L. R. Hargreaves, A. Jo, J. Tanner, M. A. Khakoo, T. Walls, C. Winstead, and V. McKoy, “Low-energy electron scattering by tetrahydrofuran,” *Phys. Rev. A*, vol. 85, p. 052717, May 2012.

- [21] F. Blanco and G. García, “Screening corrections for calculation of electron scattering from polyatomic molecules,” *Physics Letters A*, vol. 317, no. 5, pp. 458–462, 2003.
- [22] F. Blanco and G. García, “A screening-corrected additivity rule for the calculation of electron scattering from macro-molecules,” *Journal of Physics B: Atomic, Molecular and Optical Physics*, vol. 42, p. 145203, jun 2009.
- [23] F. Blanco, A. Muñoz, D. Almeida, F. Ferreira da Silva, P. Limão-Vieira, M. C. Fuss, A. G. Sanz, and G. García, “Modelling low energy electron and positron tracks in biologically relevant media,” *The European Physical Journal D*, vol. 67, p. 199, Sep 2013.
- [24] P. c. v. Kolorenč, V. Brems, and J. c. v. Horáček, “Computing resonance positions, widths, and cross sections via the feshbach-fano  $r$ -matrix method: Application to potential scattering,” *Phys. Rev. A*, vol. 72, p. 012708, Jul 2005.
- [25] C. S. Trevisan, A. E. Orel, and T. N. Rescigno, “Resonant electron-CF collision processes,” *Phys. Rev. A*, vol. 72, p. 062720, Dec 2005.
- [26] M. A. Khakoo, M. A. P. Lima, and J. Tennyson, “Advances and challenges in electron–molecule scattering physics—a report of the 14th international symposium on electron–molecule collisions and swarms,” *Physica Scripta*, vol. 74, pp. C7–C14, jun 2006.
- [27] F. Jensen, *Introduction to Computational Chemistry*. Wiley, 2017.
- [28] M. A. Fennimore and S. Matsika, “Electronic resonances of nucleobases using stabilization methods,” *The Journal of Physical Chemistry A*, vol. 122, no. 16, pp. 4048–4057, 2018. PMID: 29614226.
- [29] Y.-K. Kim and M. E. Rudd, “Binary-encounter-dipole model for electron-impact ionization,” *Phys. Rev. A*, vol. 50, pp. 3954–3967, Nov 1994.
- [30] I. Abril, R. Garcia-Molina, C. D. Denton, F. J. Pérez-Pérez, and N. R. Arista, “Dielectric description of wakes and stopping powers in solids,” *Phys. Rev. A*, vol. 58, pp. 357–366, Jul 1998.
- [31] J. Lindhard, “J. lindhard, mat. fys. medd. k. dan. vidensk. selsk. 28, 8 (1954).,” *Mat. Fys. Medd. K. Dan. Vidensk. Selsk.*, vol. 28, p. 8, 1954.
- [32] F. Gianturco and A. Jain, “The theory of electron scattering from polyatomic molecules,” *Physics Reports*, vol. 143, no. 6, pp. 347–425, 1986.

- [33] H. Ehrhardt and L. A. Morgan, *Electron collisions with molecules, clusters, and surfaces*. Plenum Press, 1994.
- [34] V. M. Bermudez, “Low-energy electron-beam effects on poly(methyl methacrylate) resist films,” *Journal of Vacuum Science and Technology B: Microelectronics and Nanometer Structures Processing, Measurement, and Phenomena*, vol. 17, no. 6, pp. 2512–2518, 1999.
- [35] C. P. Ennis and R. I. Kaiser, “Mechanical studies on the electron-induced degradation of polymethylmethacrylate and kapton,” *Phys. Chem. Chem. Phys.*, vol. 12, pp. 14902–14915, 2010.
- [36] B. Sun and W. Dorp, “Low-energy electron-induced chemistry of pmma,” 2014.
- [37] Y. Zhang, J. Haitjema, X. Liu, F. Johansson, A. Lindblad, S. Castellanos, N. Ottosson, and A. Brouwer, “Photochemical conversion of tin-oxo cage compounds studied using hard x-ray photoelectron spectroscopy,” *Journal of Micro/Nanolithography, MEMS, and MOEMS*, vol. 16, no. 2, 2017. cited By 13.
- [38] H. Yamamoto, T. Kozawa, S. Tagawa, H. B. Cao, H. Deng, and M. J. Leeson, “Polymer-structure dependence of acid generation in chemically amplified extreme ultraviolet resists,” *Japanese Journal of Applied Physics*, vol. 46, pp. L142–L144, feb 2007.
- [39] M. Dampc, P. Mozejko, and M. Zubek, “Electron impact ionization and cationic fragmentation of the pyridazine molecules,” *The European Physical Journal D*, vol. 72, p. 216, Dec 2018.
- [40] S. Tagawa, S. Nagahara, T. Iwamoto, M. Wakita, T. Kozawa, Y. Yamamoto, D. Werst, and A. D. Trifunac, “Radiation and photochemistry of onium salt acid generators in chemically amplified resists,” in *Advances in Resist Technology and Processing XVII* (F. M. Houlihan, ed.), vol. 3999, pp. 204 – 213, International Society for Optics and Photonics, SPIE, 2000.
- [41] A. Narasimhan, S. Grzeskowiak, J. Ostrander, J. Schad, E. Rebeyev, M. Neisser, L. E. Ocola, G. Denbeaux, and R. L. Brainard, “Studying electron-PAG interactions using electron-induced fluorescence,” in *Advances in Patterning Materials and Processes XXXIII* (C. K. Hohle and R. Uchida, eds.), vol. 9779, pp. 34 – 49, International Society for Optics and Photonics, SPIE, 2016.
- [42] H. Lee, S. Park, M. Kim, J. Moon, B. Lee, and M. Cho, “Multiscale simulation of extreme ultraviolet nanolithography: impact of acid–base reaction on pattern roughness,” *J. Mater. Chem. C*, vol. 9, pp. 1183–1195, 2021.

- [43] S. Grzeskowiak, J. Kaminsky, S. Gibbons, A. Narasimhan, R. L. Brainard, and G. Denbeaux, "Electron trapping: a mechanism for acid production in extreme ultraviolet photoresists," *Journal of Micro/Nanolithography, MEMS, and MOEMS*, vol. 17, no. 3, pp. 1 – 7, 2018.
- [44] H.-Y. Cheng and C.-W. Chen, "Energy and lifetime of temporary anion states of uracil by stabilization method," *The Journal of Physical Chemistry A*, vol. 115, no. 35, pp. 10113–10121, 2011. PMID: 21819093.
- [45] S. Bhattarai, "Study of Line Edge Roughness and Interactions of Secondary Electrons in Photoresists for EUV Lithography," 2017.
- [46] R. Pal, L. Bourgeois, M. Weyland, A. K. Sikder, K. Saito, A. M. Funston, and J. R. Bellare, "Chemical fingerprinting of polyvinyl acetate and polycarbonate using electron energy-loss spectroscopy," *Polym. Chem.*, vol. 11, pp. 5484–5492, 2020.
- [47] D. C. Joy, *Monte Carlo Modeling for Electron Microscopy and Microanalysis*. New York, UNITED STATES: Oxford University Press, Incorporated, 1995.
- [48] H. R. Alty, S. M. Lewis, S. G. Yeates, and R. E. P. Winpenny, "Using 3D Monte Carlo simulation to develop resists for next-generation lithography," in *Photomask Technology 2018* (E. E. Gallagher and J. H. Rankin, eds.), vol. 10810, pp. 132 – 140, International Society for Optics and Photonics, SPIE, 2018.
- [49] A. Fay, N. A. Thiam, M.-L. Cordini, I. Servin, C. Constancias, L. Lattard, and L. Pain, "'Fast' and 'thick' e-beam resists exposed with multi-beam tool at 5 keV for implants and mature nodes: experimental and simulated model study," in *Alternative Lithographic Technologies VII* (D. J. Resnick and C. Bencher, eds.), vol. 9423, pp. 417 – 431, International Society for Optics and Photonics, SPIE, 2015.
- [50] J. Ma, A. R. Neureuther, and P. P. Naulleau, "Investigating EUV radiochemistry with condensed phase photoemission," in *Extreme Ultraviolet (EUV) Lithography X* (K. A. Goldberg, ed.), vol. 10957, pp. 392 – 400, International Society for Optics and Photonics, SPIE, 2019.
- [51] J. H. Ma, H. Wang, D. Prendergast, A. Neureuther, and P. Naulleau, "Excitation selectivity in model tin-oxo resist: a computational chemistry perspective," in *Extreme Ultraviolet (EUV) Lithography XI* (N. M. Felix and A. Lio, eds.), vol. 11323, pp. 349 – 355, International Society for Optics and Photonics, SPIE, 2020.



- [52] O. Kostko, T. R. McAfee, J. Ma, and P. Naulleau, “Characterization of secondary electron blur via determination of electron attenuation length,” in *Extreme Ultraviolet (EUV) Lithography XII* (N. M. Felix and A. Lio, eds.), vol. 11609, International Society for Optics and Photonics, SPIE, 2021.
- [53] S. Hufner, *Very High Resolution Photoelectron Spectroscopy*.
- [54] S. Hufner, *Photoelectron Spectroscopy*.
- [55] O. Kostko, B. Xu, D. S. Slaughter, M. Ahmed, K. D. Closser, D. L. Olynick, D. G. Prendergast, P. D. Ashby, D. F. Ogletree, Y. Liu, P. Naulleau, W. D. Hinsberg, and G. M. Wallraff, “Fundamental understanding of chemical processes in EUV lithography,” *J. Chem. Phys.*, vol. 149, p. 154305, 2018.
- [56] M. P. Seah, “Background subtraction: I. General behaviour of Tougaard-style backgrounds in AES and XPS,” *Surface Science*, vol. 420, no. 2-3, pp. 285–294, 1999.
- [57] J. Yeh and I. Lindau, “Atomic subshell photoionization cross sections and asymmetry parameters:  $1 \leq z \leq 103$ ,” *Atomic Data and Nuclear Data Tables*, vol. 32, no. 1, pp. 1 – 155, 1985.
- [58] M. Heni and E. Illenberger, “Electron attachment by saturated nitriles, acrylonitrile (c2h3cn), and benzonitrile (c6h5cn),” *International Journal of Mass Spectrometry and Ion Processes*, vol. 73, no. 1, pp. 127–144, 1986.
- [59] J. K. Olthoff, J. A. Tossell, and J. H. Moore, “Electron attachment by haloalkenes and halobenzenes,” *The Journal of Chemical Physics*, vol. 83, no. 11, pp. 5627–5634, 1985.
- [60] S. Grzeskowiak, R. L. Brainard, and G. H. Denbeaux, 2019.
- [61]
- [62] N. R. *Chem. Rev.*, vol. 107, p. 1553, 2007.
- [63] J. A. *J. Electron Spectrosc. Relat. Phenom.*, vol. 100, p. 137, 1999.
- [64] C. Y. C. *J. Chem. Phys.*, vol. 61, p. 2727, 1974.
- [65] H. S. *J. Chem. Phys.*, vol. 67, p. 4139, 1999.
- [66] M. F. C. *Appl. Surf. Sci.*, vol. 422, p. 504, 2017.
- [67] J. M. I. *Phys. Chem. Chem. Phys.*, vol. 19, p. 13372, 2017.

- [68] P. C. J. *Surf. Sci.*, vol. 44, p. 29, 1974.
- [69] L. I. *J. Electron Spectrosc. Relat. Phenom.*, vol. 3, p. 409, 1974.
- [70] M. C. *J. Electron Spectrosc. Relat. Phenom.*, vol. 35, p. 307, 1985.
- [71] C. E. *Phys. Rev. B*, vol. 34, p. 8822, 1986.
- [72] S. M. P. *Surf. Interface Anal.*, vol. 1, p. 2, 1979.
- [73] G. D. *Phys. Rev. Lett.*, vol. 123, p. 086802, 2019.
- [74] M. M. *Radiat. Res.*, vol. 159, p. 3, 2003.
- [75] O. Y. *J. Electron Spectrosc. Relat. Phenom.*, vol. 197, p. 17, 2014.
- [76] T. S. *Phys. Rev. Lett.*, vol. 111, p. 173005, 2013.
- [77] S. Y.-I. *Phys. Rev. E*, vol. 90, p. 010302, 2014.
- [78] K. O. *J. Chem. Phys.*, vol. 151, p. 184702, 2019.
- [79] B. C. D. *J. Phys. Chem.*, vol. 93, p. 1670, 1989.
- [80] L. C. L. A. *Langmuir*, vol. 15, p. 2037, 1999.
- [81] C. R. *J. Phys. Chem. B*, vol. 107, p. 10216, 2003.
- [82] A. M. *Nanotechnology*, vol. 30, p. 025704, 2019.
- [83] H. B. L. *At. Data Nucl. Data Tables*, vol. 54, p. 181, 1993.
- [84] B. L. Henke, J. A. Smith, and D. T. Attwood, “0.1–10-keV x-ray-induced electron emissions from solids—Models and secondary electron measurements,” *Journal of Applied Physics*, vol. 48, no. 5, pp. 1852–1866, 1977.
- [85] B. L. Henke, J. Liesegang, and S. D. Smith, “Soft-x-ray-induced secondary-electron emission from semiconductors and insulators: Models and measurements,” *Physical Review B*, vol. 19, no. 6, pp. 3004–3021, 1979.
- [86] A. A. *Nucl. Instrum. Methods Phys. Res. Sect. A*, vol. 308, p. 219, 1991.
- [87] S. J. J. *Philips J. Res.*, vol. 50, p. 375, 1996.
- [88] G. G. *Europhys. Lett.*, vol. 31, p. 163, 1995.

- [89] J. J. D. *Phys. Rev. B*, vol. 7, p. 2644, 1973.
- [90] K. T. *J. Photopolym. Sci. Technol.*, vol. 20, p. 577, 2007.
- [91] J.-G. J.-P. *Can. J. Chem.*, vol. 71, p. 287, 1993.
- [92] O. Kostko, T. R. McAfee, J. Ma, and P. Naulleau, “Experimental characterization of resist materials,” in *International Conference on Extreme Ultraviolet Lithography 2021* (K. G. Ronse, P. P. Naulleau, P. A. Gargini, T. Itani, and E. Hendrickx, eds.), vol. 11854, International Society for Optics and Photonics, SPIE, 2021.
- [93] J. Jiang, G. Giordano, R. Fallica, D. DeSimone, and G. Vandenberghe, “Sensitizer for euv chemically amplified resist: Metal versus halogen,” *Journal of Photopolymer Science and Technology*, vol. 32, no. 1, pp. 21–25, 2019.
- [94] H.-P. Fenzlaff and E. Illenberger, “Low energy electron impact on benzene and the fluorobenzenes. formation and dissociation of negative ions,” *International Journal of Mass Spectrometry and Ion Processes*, vol. 59, no. 2, pp. 185–202, 1984.
- [95] S. Agostinelli, J. Allison, K. Amako, J. Apostolakis, H. Araujo, P. Arce, M. Asai, D. Axen, S. Banerjee, G. Barrand, F. Behner, L. Bellagamba, J. Boudreau, L. Broglia, A. Brunengo, H. Burkhardt, S. Chauvie, J. Chuma, R. Chytracsek, G. Cooperman, G. Cosmo, P. Degtyarenko, A. Dell’Acqua, G. Depaola, D. Dietrich, R. Enami, A. Feliciello, C. Ferguson, H. Fesefeldt, G. Folger, F. Foppiano, A. Forti, S. Garelli, S. Giani, R. Giannitrapani, D. Gibin, J. Gómez Cadenas, I. González, G. Gracia Abril, G. Greeniaus, W. Greiner, V. Grichine, A. Grossheim, S. Guatelli, P. Gumplinger, R. Hamatsu, K. Hashimoto, H. Hasui, A. Heikkinen, A. Howard, V. Ivanchenko, A. Johnson, F. Jones, J. Kallenbach, N. Kanaya, M. Kawabata, Y. Kawabata, M. Kawaguti, S. Kelner, P. Kent, A. Kimura, T. Kodama, R. Kokoulin, M. Kossov, H. Kurashige, E. Lamanna, T. Lampén, V. Lara, V. Lefebure, F. Lei, M. Liendl, W. Lockman, F. Longo, S. Magni, M. Maire, E. Medernach, K. Minamimoto, P. Mora de Freitas, Y. Morita, K. Murakami, M. Nagamatu, R. Nartallo, P. Nieminen, T. Nishimura, K. Ohtsubo, M. Okamura, S. O’Neale, Y. Oohata, K. Paech, J. Perl, A. Pfeiffer, M. Pia, F. Ranjard, A. Rybin, S. Sadilov, E. Di Salvo, G. Santin, T. Sasaki, N. Savvas, Y. Sawada, S. Scherer, S. Sei, V. Sirotenko, D. Smith, N. Starkov, H. Stoecker, J. Sulkimo, M. Takahata, S. Tanaka, E. Tcherniaev, E. Safai Tehrani, M. Tropeano, P. Truscott, H. Uno, L. Urban, P. Urban, M. Verderi, A. Walkden, W. Wander, H. Weber, J. Wellisch, T. Wenaus, D. Williams, D. Wright, T. Yamada, H. Yoshida, and D. Zschesche, “Geant4—a simulation toolkit,” *Nuclear Instruments and Methods in Physics Research Section A: Accelerators, Spectrometers, Detectors and Associated Equipment*, vol. 506, no. 3, pp. 250–303, 2003.

- [96] R. H. Ritchie, "Plasma losses by fast electrons in thin films," *Phys. Rev.*, vol. 106, pp. 874–881, Jun 1957.
- [97] N. D. Mermin, "Lindhard dielectric function in the relaxation-time approximation," *Phys. Rev. B*, vol. 1, pp. 2362–2363, Mar 1970.
- [98] M. A. Khakoo, D. Orton, L. R. Hargreaves, and N. Meyer, "Electron-impact vibrational excitation of tetrahydrofuran," *Phys. Rev. A*, vol. 88, p. 012705, Jul 2013.
- [99] R. W. Gurney and N. F. Mott, "The theory of the photolysis of silver bromide and the photographic latent image," *Proceedings of the Royal Society of London. Series A - Mathematical and Physical Sciences*, vol. 164, no. 917, pp. 151–167, 1938.
- [100] C. S. D. Castro, S. Dimitrov, H. D. Burrows, P. Douglas, and M. L. Davies, "Photoinduced charge transfer: From photography to solar energy," *Science Progress*, vol. 100, no. 2, pp. 212–230, 2017. PMID: 28693679.
- [101] G. M. Wallraff, W. D. Hinsberg, L. Resists, G. M. Wallraff, W. D. Hinsberg, L. Resists, and G. M. Wallraff, "Lithographic Resists," *Encyclopedia of Polymer Science and Technology*, vol. 6, no. 8, pp. 660–696, 2002.
- [102] S. Grzeskowiak, R. L. Brainard, and G. H. Denbeaux, "Measuring extreme-ultraviolet secondary electron blur (Conference Presentation)," in *Advances in Patterning Materials and Processes XXXVI* (R. Gronheid and D. P. Sanders, eds.), vol. 10960, International Society for Optics and Photonics, SPIE, 2019.
- [103] K. T. *Jpn. J. Appl. Phys.*, vol. 50, p. 030209, 2011.
- [104] W. Kohn and L. J. Sham, "Self-consistent equations including exchange and correlation effects," *Phys. Rev.*, vol. 140, pp. A1133–A1138, Nov 1965.
- [105] O. Sinanoglu, "Many-electron theory of atoms and molecules. i. shells, electron pairs vs many-electron correlations," *The Journal of Chemical Physics*, vol. 36, no. 3, pp. 706–717, 1962.
- [106] K. Yamashita, S. Kamimura, H. Takahashi, and N. Nishikawa, "A resist material study for lwr and resolution improvement in euv lithography," *Journal of Photopolymer Science and Technology*, vol. 21, no. 3, pp. 439–442, 2008.
- [107] D. L. Goldfarb, A. Afzali-Ardakani, and M. Glodde, "Acid generation efficiency: EUV photons versus photoelectrons," in *Advances in Patterning Materials and Processes XXXIII*

- (C. K. Hohle and R. Uchida, eds.), vol. 9779, pp. 6 – 18, International Society for Optics and Photonics, SPIE, 2016.
- [108] S. W. Staley and J. T. Strnad, “Calculation of the energies of  $\pi^*$  negative ion resonance states by the use of Koopmans’ theorem,” *The Journal of Physical Chemistry*, vol. 98, no. 1, pp. 116–121, 1994.
- [109] K. Aflatooni, G. A. Gallup, and P. D. Burrow, “Electron attachment energies of the DNA bases,” *The Journal of Physical Chemistry A*, vol. 102, no. 31, pp. 6205–6207, 1998.
- [110] J. P. Perdew, M. Ernzerhof, K. Burke, J. P. Perdew, M. Ernzerhof, and K. Burke, “Rationale for mixing exact exchange with density functional approximations Rationale for mixing exact exchange with density functional approximations,” vol. 22, no. 105, pp. 9982–9985, 1996.
- [111] F. Weigend and R. Ahlrichs, “Balanced basis sets of split valence, triple zeta valence and quadruple zeta valence quality for h to rn: Design and assessment of accuracy,” *Phys. Chem. Chem. Phys.*, vol. 7, pp. 3297–3305, 2005.
- [112] V. Barone and M. Cossi, “Quantum calculation of molecular energies and energy gradients in solution by a conductor solvent model,” *The Journal of Physical Chemistry A*, vol. 102, no. 11, pp. 1995–2001, 1998.
- [113] S. Hirata and M. Head-Gordon, “Time-dependent density functional theory within the Tamm–Dancoff approximation,” *Chemical Physics Letters*, vol. 314, no. 3, pp. 291–299, 1999.
- [114] J. C. Tully, “Molecular dynamics with electronic transitions,” *The Journal of Chemical Physics*, vol. 93, no. 2, pp. 1061–1071, 1990.
- [115] J. L. Dektar and N. P. Hacker, “Photochemistry of triarylsulfonium salts,” *Journal of the American Chemical Society*, vol. 112, no. 16, pp. 6004–6015, 1990.
- [116] E. Despagnet-Ayoub, W. W. Kramer, W. Sattler, A. Sattler, P. J. LaBeaume, J. W. Thackeray, J. F. Cameron, T. Cardolaccia, A. A. Rachford, J. R. Winkler, and H. B. Gray, “Triphenylsulfonium topophotochemistry,” *Photochem. Photobiol. Sci.*, vol. 17, pp. 27–34, 2018.
- [117] Y. Shao, M. Head-Gordon, and A. I. Krylov, “The spin–flip approach within time-dependent density functional theory: Theory and applications to diradicals,” *The Journal of Chemical Physics*, vol. 118, no. 11, pp. 4807–4818, 2003.

- [118] A. V. Marenich, C. J. Cramer, and D. G. Truhlar, “Universal solvation model based on solute electron density and on a continuum model of the solvent defined by the bulk dielectric constant and atomic surface tensions,” *The Journal of Physical Chemistry B*, vol. 113, no. 18, pp. 6378–6396, 2009. PMID: 19366259.
- [119] Z. Marković, J. Tošović, D. Milenković, and S. Marković, “Revisiting the solvation enthalpies and free energies of the proton and electron in various solvents,” *Computational and Theoretical Chemistry*, vol. 1077, pp. 11–17, 2016. Antioxidants vs. Oxidative Stress: Insights from Computation.
- [120] A. Narasimhan, S. Grzeskowiak, C. Ackerman, T. Flynn, G. Denbeaux, and R. L. Brainard, “Mechanisms of EUV exposure: electrons and holes,” in *Extreme Ultraviolet (EUV) Lithography VIII* (E. M. Panning, ed.), vol. 10143, pp. 195 – 203, International Society for Optics and Photonics, SPIE, 2017.
- [121] D. F. Ogletree, “Chapter 2 - molecular excitation and relaxation of extreme ultraviolet lithography photoresists,” in *Materials and Processes for Next Generation Lithography* (A. Robinson and R. Lawson, eds.), vol. 11 of *Frontiers of Nanoscience*, pp. 91 – 113, Elsevier, 2016.
- [122] J. K. Stowers, A. Telecky, M. Kocsis, B. L. Clark, D. A. Keszler, A. Grenville, C. N. Anderson, and P. P. Naulleau, “Directly patterned inorganic hardmask for EUV lithography,” *Extreme Ultraviolet (EUV) Lithography II*, vol. 796915, no. April 2011, p. 796915, 2011.
- [123] W. D. Hinsberg and S. Meyers, “A numeric model for the imaging mechanism of metal oxide EUV resists,” in *Advances in Patterning Materials and Processes XXXIV* (C. K. Hohle, ed.), vol. 10146, pp. 14 – 24, International Society for Optics and Photonics, SPIE, 2017.
- [124] B. Cardineau, R. Del Re, M. Marnell, H. Al-Mashat, M. Vockenhuber, Y. Ekinici, C. Sarma, D. A. Freedman, and R. L. Brainard, “Photolithographic properties of tin-oxo clusters using extreme ultraviolet light (13.5nm),” *Microelectronic Engineering*, vol. 127, pp. 44 – 50, 2014.
- [125] I. Bepalov, Y. Zhang, J. Haitjema, R. Tromp, S. Van Der Molen, A. Brouwer, J. Jobst, and S. Castellanos, “Key role of very low energy electrons in tin-based molecular resists for extreme ultraviolet nanolithography,” *ACS Applied Materials and Interfaces*, vol. 12, no. 8, pp. 9881–9889, 2020. cited By 3.
- [126] J. Haitjema, Y. Zhang, N. Ottosson, and A. Brouwer, “Photoreactions of tin oxo cages, model euv photoresists,” *Journal of Photopolymer Science and Technology*, vol. 30, no. 1, pp. 99–102, 2017. cited By 16.

- [127] J. Haitjema, L. Wu, A. Giuliani, L. Nahon, S. Castellanos, and A. Brouwer, "Photo-induced fragmentation of a tin-oxo cage compound," *Journal of Photopolymer Science and Technology*, vol. 31, no. 2, pp. 243–247, 2018. cited By 8.
- [128] D. Hutchison, R. Stern, M. Olsen, L. Zakharov, K. Persson, and M. Nyman, "Alkyltin clusters: The less symmetric keggin isomers," *Dalton Transactions*, vol. 47, no. 29, pp. 9804–9813, 2018. cited By 11.
- [129] Y. Zhu, M. Olsen, M. Nyman, L. Zhang, and J. Zhang, "Stabilizing  $\gamma$ -alkyltin-oxo keggin ions by borate functionalization," *Inorganic Chemistry*, vol. 58, no. 7, pp. 4534–4539, 2019. cited By 5.
- [130] R. D. Stern, D. C. Hutchison, M. R. Olsen, L. N. Zakharov, M. Nyman, and K. A. Persson, "Alkyltin Keggin clusters as EUVL photoresist technology," in *International Conference on Extreme Ultraviolet Lithography 2019* (T. Itani, P. A. Gargini, P. P. Naulleau, and K. G. Ronse, eds.), vol. 11147, pp. 181 – 188, International Society for Optics and Photonics, SPIE, 2019.
- [131] F. Banse, F. Ribot, P. Tolédano, J. Maquet, and C. Sanchez *Inorganic Chemistry*.
- [132] V. W. Day, T. A. Eberspacher, W. G. Klemperer, and C. W. Park, "Dodecatitanates: a new family of stable polyoxotitanates," *Journal of the American Chemical Society*, vol. 115, no. 18, pp. 8469–8470, 1993.
- [133] A. Müller, R. Rohlfing, E. Krickemeyer, and H. Bögge, "Control of the linkage of inorganic fragments of v-o compounds: From cluster shells as carcerands via cluster aggregates to solid-state structures," *Angewandte Chemie International Edition in English*, vol. 32, no. 6, pp. 909–912, 1993.
- [134] C. Eychenne-Baron, F. Ribot, and C. Sanchez, "New synthesis of the nanobuilding block  $(\text{BuSn})_{12}\text{O}_{14}(\text{OH})_6$  and exchange properties of  $(\text{BuSn})_{12}\text{O}_{14}(\text{OH})_6(\text{o}3\text{sc}6\text{h}4\text{ch}3)_2$ ," *Journal of Organometallic Chemistry*, vol. 567, no. 1, pp. 137 – 142, 1998.
- [135] J. Haitjema, Y. Zhang, M. Vockenhuber, D. Kazazis, Y. Ekinici, and A. Brouwer, "Extreme ultraviolet patterning of tin-oxo cages," vol. 10143, SPIE, 2017. cited By 6.
- [136] H. Puff and H. Reuter, "Zur hydrolyse von monoorganylzinn-trihalogeniden iii. isolierung und röntgenstrukturanalyse von verbindungen mit dem neuartigen käfig-ion  $[(\text{i-prsn})_{12}\text{o}_{14}(\text{oh})_6]^{2+}$ ," *Journal of Organometallic Chemistry*, vol. 373, no. 2, pp. 173 – 184, 1989.

- [137] L. Plasseraud, H. Cattey, and P. Richard, “[ $(\text{PhCH}_2\text{Sn})_{12}(\mu^3\text{-O})_{14}(\mu\text{-OH})_6(\text{F}_3\text{CSO}_3)_2$ ]: A new dodecanuclear organostannoxane,” *Zeitschrift für Naturforschung B*, vol. 66, no. 3, pp. 262 – 268, 01 Mar. 2011.
- [138] J. Chalabala, O. Dvořák, and P. Slavíček, “Ab initio photodynamics of model euv photoresists,” *Chemical Physics*, vol. 515, pp. 221–230, 2018. cited By 3.
- [139] D. S. Levine, D. Hait, N. M. Tubman, S. Lehtola, K. B. Whaley, and M. Head-Gordon, “Casscf with extremely large active spaces using the adaptive sampling configuration interaction method,” *Journal of Chemical Theory and Computation*, vol. 16, no. 4, pp. 2340–2354, 2020. PMID: 32109055.
- [140] S. Grimme, J. Antony, S. Ehrlich, and H. Krieg, “A consistent and accurate ab initio parametrization of density functional dispersion correction (dft-d) for the 94 elements hpu,” *The Journal of Chemical Physics*, vol. 132, no. 15, p. 154104, 2010.
- [141] S. Grimme, S. Ehrlich, and L. Goerigk, “Effect of the damping function in dispersion corrected density functional theory,” *Journal of Computational Chemistry*, vol. 32, no. 7, pp. 1456–1465, 2011.
- [142] Y. Shao, Z. Gan, E. Epifanovsky, A. T. Gilbert, M. Wormit, J. Kussmann, A. W. Lange, A. Behn, J. Deng, X. Feng, D. Ghosh, M. Goldey, P. R. Horn, L. D. Jacobson, I. Kaliman, R. Z. Khaliullin, T. Kuś, A. Landau, J. Liu, E. I. Proynov, Y. M. Rhee, R. M. Richard, M. A. Rohrdanz, R. P. Steele, E. J. Sundstrom, H. L. W. III, P. M. Zimmerman, D. Zuev, B. Albrecht, E. Alguire, B. Austin, G. J. O. Beran, Y. A. Bernard, E. Berquist, K. Brandhorst, K. B. Bravaya, S. T. Brown, D. Casanova, C.-M. Chang, Y. Chen, S. H. Chien, K. D. Closser, D. L. Crittenden, M. Diedenhofen, R. A. D. Jr., H. Do, A. D. Dutoi, R. G. Edgar, S. Fatehi, L. Fusti-Molnar, A. Ghysels, A. Golubeva-Zadorozhnaya, J. Gomes, M. W. Hanson-Heine, P. H. Harbach, A. W. Hauser, E. G. Hohenstein, Z. C. Holden, T.-C. Jagau, H. Ji, B. Kaduk, K. Khistyayev, J. Kim, J. Kim, R. A. King, P. Klunzinger, D. Kosenkov, T. Kowalczyk, C. M. Krauter, K. U. Lao, A. D. Laurent, K. V. Lawler, S. V. Levchenko, C. Y. Lin, F. Liu, E. Livshits, R. C. Lochan, A. Luenser, P. Manohar, S. F. Manzer, S.-P. Mao, N. Mardirossian, A. V. Marenich, S. A. Maurer, N. J. Mayhall, E. Neuscamman, C. M. Oana, R. Olivares-Amaya, D. P. O’Neill, J. A. Parkhill, T. M. Perrine, R. Peverati, A. Prociuk, D. R. Rehn, E. Rosta, N. J. Russ, S. M. Sharada, S. Sharma, D. W. Small, A. Sodt, T. Stein, D. Stück, Y.-C. Su, A. J. Thom, T. Tsuchimochi, V. Vanovschi, L. Vogt, O. Vydrov, T. Wang, M. A. Watson, J. Wenzel, A. White, C. F. Williams, J. Yang, S. Yeganeh, S. R. Yost, Z.-Q. You, I. Y. Zhang, X. Zhang, Y. Zhao, B. R. Brooks, G. K. Chan, D. M. Chipman, C. J. Cramer,



- W. A. G. III, M. S. Gordon, W. J. Hehre, A. Klamt, H. F. S. III, M. W. Schmidt, C. D. Sherrill, D. G. Truhlar, A. Warshel, X. Xu, A. Aspuru-Guzik, R. Baer, A. T. Bell, N. A. Besley, J.-D. Chai, A. Dreuw, B. D. Dunietz, T. R. Furlani, S. R. Gwaltney, C.-P. Hsu, Y. Jung, J. Kong, D. S. Lambrecht, W. Liang, C. Ochsenfeld, V. A. Rassolov, L. V. Slipchenko, J. E. Subotnik, T. V. Voorhis, J. M. Herbert, A. I. Krylov, P. M. Gill, and M. Head-Gordon, “Advances in molecular quantum chemistry contained in the q-chem 4 program package,” *Molecular Physics*, vol. 113, no. 2, pp. 184–215, 2015.
- [143] R. Frederick, S. Saha, J. Trey Diulus, F. Luo, J. Amador, M. Li, D.-H. Park, E. Garfunkel, D. Keszler, and G. Herman, “Thermal and radiation chemistry of butyltin oxo hydroxo: A model inorganic photoresist,” *Microelectronic Engineering*, vol. 205, pp. 26–31, 2019. cited By 6.
- [144] M. Sharps, R. Frederick, M. Javitz, G. Herman, D. Johnson, and J. Hutchison, “Organotin carboxylate reagents for nanopatterning: Chemical transformations during direct-write electron beam processes,” *Chemistry of Materials*, vol. 31, no. 13, pp. 4840–4850, 2019. cited By 2.
- [145] W. L. Marshall and E. U. Franck, “Ion product of water substance, 0-1000 °c, 1-10,000 bars new international formulation and its background,” *Journal of Physical and Chemical Reference Data*, vol. 10, no. 2, pp. 295–304, 1981.
- [146] A. V. Bandura and S. N. Lvov, “The ionization constant of water over wide ranges of temperature and density,” *Journal of Physical and Chemical Reference Data*, vol. 35, no. 1, pp. 15–30, 2006.
- [147] T. Zuo, L. Xu, C. M. Beavers, M. M. Olmstead, W. Fu, T. D. Crawford, A. L. Balch, and H. C. Dorn, “M<sub>2</sub>@c<sub>79</sub>n (m = y, tb): Isolation and characterization of stable endohedral metallofullerenes exhibiting m-m bonding interactions inside aza[80]fullerene cages,” *Journal of the American Chemical Society*, vol. 130, no. 39, pp. 12992–12997, 2008. PMID: 18774804.
- [148] G. Gryn’ova, M. L. Coote, and C. Corminboeuf, “Theory and practice of uncommon molecular electronic configurations,” *WIREs Computational Molecular Science*, vol. 5, no. 6, pp. 440–459, 2015.
- [149] A. Kumar and M. D. Sevilla, “Somo–homo level inversion in biologically important radicals,” *The Journal of Physical Chemistry B*, vol. 122, no. 1, pp. 98–105, 2018. PMID: 29240424.

- [150] T. N. Truong and E. V. Stefanovich, “A new method for incorporating solvent effect into the classical, ab initio molecular orbital and density functional theory frameworks for arbitrary shape cavity,” *Chemical Physics Letters*, vol. 240, no. 4, pp. 253–260, 1995.
- [151] D. L. Goldfarb, O. Wang, C. R. Thomas, H. Polgrean, M. C. Lawson, A. E. Hess, and A. D. Silva, “EUV chemically amplified resist component distribution and efficiency for stochastic defect control,” in *Advances in Patterning Materials and Processes XXXVII* (R. Gronheid and D. P. Sanders, eds.), vol. 11326, pp. 17 – 31, International Society for Optics and Photonics, SPIE, 2020.
- [152] A. D. Silva, L. Meli, J. Guo, J. Church, N. M. Felix, D. L. Goldfarb, B. Kumar, R. J. Wojtecki, M. Mettry, and A. Hess, “Study of resist hardmask interaction through surface activation layers,” in *International Conference on Extreme Ultraviolet Lithography 2018* (K. G. Ronse, E. Hendrickx, P. P. Naulleau, P. A. Gargini, and T. Itani, eds.), vol. 10809, pp. 168 – 176, International Society for Optics and Photonics, SPIE, 2018.
- [153] P. Brichon, E. Despiau-Pujo, and O. Joubert, “Md simulations of low energy clx+ ions interaction with ultrathin silicon layers for advanced etch processes,” *Journal of Vacuum Science and Technology A*, vol. 32, no. 2, p. 021301, 2014.
- [154] Q. Tao, G. Jursich, and C. Takoudis, “Selective atomic layer deposition of hfo2 on copper patterned silicon substrates,” *Applied Physics Letters*, vol. 96, no. 19, p. 192105, 2010.
- [155] S. M. George, B. Yoon, and A. A. Dameron, “Surface chemistry for molecular layer deposition of organic and hybrid organic-inorganic polymers,” *Accounts of Chemical Research*, vol. 42, no. 4, pp. 498–508, 2009. PMID: 19249861.
- [156] A. J. M. Mackus, M. J. M. Merckx, and W. M. M. Kessels, “From the bottom-up: Toward area-selective atomic layer deposition with high selectivity,” *Chemistry of Materials*, vol. 31, no. 1, pp. 2–12, 2019.
- [157] E. Stevens, Y. Tomczak, B. T. Chan, E. Altamirano Sanchez, G. N. Parsons, and A. Delabie, “Area-selective atomic layer deposition of tin, tio2, and hfo2 on silicon nitride with inhibition on amorphous carbon,” *Chemistry of Materials*, vol. 30, no. 10, pp. 3223–3232, 2018.
- [158] S. E. Atanasov, B. Kalanyan, and G. N. Parsons, “Inherent substrate-dependent growth initiation and selective-area atomic layer deposition of tio2 using “water-free” metal-halide/metal alkoxide reactants,” *Journal of Vacuum Science and Technology A*, vol. 34, no. 1, p. 01A148, 2016.

- [159] E. Färm, M. Kemell, M. Ritala, and M. Leskelä, “Selective-area atomic layer deposition using poly(methyl methacrylate) films as mask layers,” *The Journal of Physical Chemistry C*, vol. 112, no. 40, pp. 15791–15795, 2008.
- [160] I. Zyulkov, E. Voronina, M. Krishtab, D. Voloshin, B. T. Chan, Y. Mankelevich, T. Rakhimova, S. Armini, and S. De Gendt, “Area-selective ru ald by amorphous carbon modification using h plasma: from atomistic modeling to full wafer process integration,” *Mater. Adv.*, vol. 1, pp. 3049–3057, 2020.
- [161] I. Zyulkov, V. Madhiwala, E. Voronina, M. Snelgrove, J. Bogan, R. O’Connor, S. De Gendt, and S. Armini, “Area-selective ald of ru on nanometer-scale cu lines through dimerization of amino-functionalized alkoxy silane passivation films,” *ACS Applied Materials and Interfaces*, vol. 12, no. 4, pp. 4678–4688, 2020. PMID: 31913003.
- [162] X. Jiang and S. F. Bent, “Area-selective atomic layer deposition of platinum on YSZ substrates using microcontact printed SAMs,” *Journal of The Electrochemical Society*, vol. 154, no. 12, p. D648, 2007.
- [163] F. S. M. Hashemi and S. F. Bent, “Sequential regeneration of self-assembled monolayers for highly selective atomic layer deposition,” *Advanced Materials Interfaces*, vol. 3, no. 21, p. 1600464, 2016.
- [164] R. Wojtecki, J. Ma, I. Cordova, N. Arellano, K. Lioni, T. Magbitang, T. G. Pattison, X. Zhao, E. Delenia, N. Lanzillo, A. E. Hess, N. F. Nathel, H. Bui, C. Rettner, G. Wallraff, and P. Naulleau, “Additive lithography—organic monolayer patterning coupled with an area-selective deposition,” *ACS Applied Materials and Interfaces*, vol. 13, no. 7, pp. 9081–9090, 2021. PMID: 33471496.
- [165] O. Lugier, A. Troglia, N. Sadegh, L. van Kessel, R. Bliem, N. Mahne, S. Nannarone, and S. Castellanos, “Extreme ultraviolet photoelectron spectroscopy on fluorinated monolayers: towards nanolithography on monolayers,” *Journal of Photopolymer Science and Technology*, vol. 33, no. 2, pp. 229–234, 2020.
- [166] D. Cahen, R. Naaman, and Z. Vager, “The cooperative molecular field effect,” *Advanced Functional Materials*, vol. 15, no. 10, pp. 1571–1578, 2005.
- [167] J. B. Rivest, G. Li, I. D. Sharp, J. B. Neaton, and D. J. Milliron, “Phosphonic acid adsorbates tune the surface potential of tio<sub>2</sub> in gas and liquid environments,” *The Journal of Physical Chemistry Letters*, vol. 5, no. 14, pp. 2450–2454, 2014. PMID: 26277814.

- [168] C. C. Fernández, E. Pensa, P. Carro, R. Salvarezza, and F. J. Williams, “Electronic structure of a self-assembled monolayer with two surface anchors: 6-mercaptopurine on au(111),” *Langmuir*, vol. 34, no. 20, pp. 5696–5702, 2018. PMID: 29715033.
- [169] S.-H. Liu, T. Balankura, and K. A. Fichthorn, “Self-assembled monolayer structures of hexadecylamine on cu surfaces: density-functional theory,” *Phys. Chem. Chem. Phys.*, vol. 18, pp. 32753–32761, 2016.
- [170] G. Kresse and J. Hafner, “Ab initio molecular dynamics for liquid metals,” *Phys. Rev. B*, vol. 47, pp. 558–561, Jan 1993.
- [171] G. Kresse and J. Hafner, “Ab initio molecular-dynamics simulation of the liquid-metal–amorphous-semiconductor transition in germanium,” *Phys. Rev. B*, vol. 49, pp. 14251–14269, May 1994.
- [172] G. Kresse and J. Furthmüller, “Efficiency of ab-initio total energy calculations for metals and semiconductors using a plane-wave basis set,” *Computational Materials Science*, vol. 6, no. 1, pp. 15–50, 1996.
- [173] G. Kresse and J. Furthmüller, “Efficient iterative schemes for ab initio total-energy calculations using a plane-wave basis set,” *Phys. Rev. B*, vol. 54, pp. 11169–11186, Oct 1996.
- [174] J. P. Perdew, K. Burke, and M. Ernzerhof, “Generalized gradient approximation made simple,” *Phys. Rev. Lett.*, vol. 77, pp. 3865–3868, Oct 1996.
- [175] P. E. Blöchl, “Projector augmented-wave method,” *Phys. Rev. B*, vol. 50, pp. 17953–17979, Dec 1994.
- [176] A. Hojabri, F. Hajakbari, N. Soltanpoor, and M. S. Hedayati, “Annealing temperature effect on the properties of untreated and treated copper films with oxygen plasma,” *Journal of Theoretical and Applied Physics*, vol. 8, p. 132, Jun 2014.
- [177] A. K. Mishra, A. Roldan, and N. H. de Leeuw, “Cu<sub>2</sub>O surfaces and CO<sub>2</sub> activation: A dispersion-corrected dft+u study,” *The Journal of Physical Chemistry C*, vol. 120, no. 4, pp. 2198–2214, 2016.
- [178] L. I. Bendavid and E. A. Carter, “First-principles predictions of the structure, stability, and photocatalytic potential of Cu<sub>2</sub>O surfaces,” *The Journal of Physical Chemistry B*, vol. 117, no. 49, pp. 15750–15760, 2013. PMID: 24138294.

- [179] A. Soon, M. Todorova, B. Delley, and C. Stampfl, “Thermodynamic stability and structure of copper oxide surfaces: A first-principles investigation,” *Phys. Rev. B*, vol. 75, p. 125420, Mar 2007.
- [180] L. I. Bendavid and E. A. Carter, “Co<sub>2</sub> adsorption on cu<sub>2</sub>o(111): A dft+u and dft-d study,” *The Journal of Physical Chemistry C*, vol. 117, no. 49, pp. 26048–26059, 2013.
- [181] S. L. Dudarev, G. A. Botton, S. Y. Savrasov, C. J. Humphreys, and A. P. Sutton, “Electron-energy-loss spectra and the structural stability of nickel oxide: An lsd+u study,” *Phys. Rev. B*, vol. 57, pp. 1505–1509, Jan 1998.
- [182] D. C. Edwards, S. B. Nielsen, A. A. Jarzęcki, T. G. Spiro, and S. C. Myneni, “Experimental and theoretical vibrational spectroscopy studies of acetohydroxamic acid and desferrioxamine b in aqueous solution: Effects of ph and iron complexation,” *Geochimica et Cosmochimica Acta*, vol. 69, no. 13, pp. 3237–3248, 2005.
- [183] D. Cheshmedzhieva, N. Toshev, M. Gerova, O. Petrov, and T. Dudev, “Hydroxamic acid derivatives as histone deacetylase inhibitors: a dft study of their tautomerism and metal affinities/selectivities,” *Journal of Molecular Modeling*, vol. 24, p. 114, Apr 2018.
- [184] J. El Yazal and Y.-P. Pang, “Novel stable configurations and tautomers of the neutral and deprotonated hydroxamic acids predicted from high-level ab initio calculations,” *The Journal of Physical Chemistry A*, vol. 103, no. 41, pp. 8346–8350, 1999.
- [185] L. F. Zagonel, M. Bäurer, A. Bailly, O. Renault, M. Hoffmann, S.-J. Shih, D. Cockayne, and N. Barrett, “Orientation-dependent work function of in situ annealed strontium titanate,” *Journal of Physics: Condensed Matter*, vol. 21, p. 314013, jul 2009.
- [186] G. A. Haas and R. E. Thomas, “Distribution of crystal orientation and work function in tungsten ribbons,” *Journal of Applied Physics*, vol. 40, no. 10, pp. 3919–3924, 1969.
- [187] L. Gao, J. Souto-Casares, J. R. Chelikowsky, and A. A. Demkov, “Orientation dependence of the work function for metal nanocrystals,” *The Journal of Chemical Physics*, vol. 147, no. 21, p. 214301, 2017.
- [188] B. Krahl-Urban, E. Niekisch, and H. Wagner, “Work function of stepped tungsten single crystal surfaces,” *Surface Science*, vol. 64, no. 1, pp. 52–68, 1977.
- [189] K. Besocke, B. Krahl-Urban, and H. Wagner, “Dipole moments associated with edge atoms; a comparative study on stepped pt, au and w surfaces,” *Surface Science*, vol. 68, pp. 39–46, 1977.

- [190] R. Rulken, A. J. Lough, I. Manners, S. R. Lovelace, C. Grant, and W. E. Geiger, "Linear oligo(ferrocenyldimethylsilanes) with between two and nine ferrocene units: Electrochemical and structural models for poly(ferrocenylsilane) high polymers," *Journal of the American Chemical Society*, vol. 118, no. 50, pp. 12683–12695, 1996.
- [191] P. W. Cyr, M. Tzolov, I. Manners, and E. H. Sargent, "Photooxidation and photoconductivity of polyferrocenylsilane thin films," *Macromolecular Chemistry and Physics*, vol. 204, no. 7, pp. 915–921, 2003.
- [192] W. Thornley, H. D. Truong, M. I. Sanchez, D. P. Sanders, G. M. Wallraff, O. Kostko, D. F. Ogletree, and D. S. Slaughter, "Model reactivity of inorganic and organometallic materials in EUV (Conference Presentation)," in *Advances in Patterning Materials and Processes XXXVI* (R. Gronheid and D. P. Sanders, eds.), vol. 10960, International Society for Optics and Photonics, SPIE, 2019.
- [193] Y. Tomkiewicz, E. M. Engler, J. D. Kuptsis, R. G. Schad, V. V. Patel, and M. Hatzakis, "Organic conductors as electron beam resist materials," *Applied Physics Letters*, vol. 40, no. 1, pp. 90–92, 1982.
- [194] D. C. Hofer, F. B. Kaufman, S. R. Kramer, and A. Aviram, "New high-resolution charge transfer x-ray and electron beam negative resist," *Applied Physics Letters*, vol. 37, no. 3, pp. 314–316, 1980.
- [195] G. De Santis, L. Fabbrizzi, M. Licchelli, C. Mangano, and D. Sacchi, "Redox switching of anthracene fluorescence through the cuii/cui couple," *Inorganic Chemistry*, vol. 34, no. 14, pp. 3581–3582, 1995.
- [196] L. Fabbrizzi, "The ferrocenium/ferrocene couple: a versatile redox switch," *ChemTexts*, vol. 6, p. 22, Oct 2020.
- [197] U. Salzner, "Quantitatively correct uv-vis spectrum of ferrocene with tdb3lyp," *Journal of Chemical Theory and Computation*, vol. 9, no. 9, pp. 4064–4073, 2013. PMID: 26592400.
- [198] I. Manners, "Poly(ferrocenylsilanes): novel organometallic plastics," *Chem. Commun.*, pp. 857–865, 1999.
- [199] R. T. Perry, *Synthesis and properties of polysilane-poly(ferrocenylsilane) random copolymers and oxidized poly(ferrocenylsilane)s*. PhD thesis, 1997. Copyright - Database copyright ProQuest LLC; ProQuest does not claim copyright in the individual underlying works; Last updated - 2021-05-26.

- [200] J.-D. Chai and M. Head-Gordon, “Long-range corrected hybrid density functionals with damped atom–atom dispersion corrections,” *Phys. Chem. Chem. Phys.*, vol. 10, pp. 6615–6620, 2008.
- [201] K. Muther, P. Hrobárik, V. Hrobáriková, M. Kaupp, and M. Oestreich, “The family of ferrocene-stabilized silylium ions: Synthesis,  $^{29}\text{Si}$ -nmr characterization, lewis acidity, substituent scrambling, and quantum-chemical analyses,” *Chemistry – A European Journal*, vol. 19, no. 49, pp. 16579–16594, 2013.
- [202] A. F. Cunningham, “Mechanism of mercuration of ferrocene: General treatment of electrophilic substitution of ferrocene derivatives,” *Organometallics*, vol. 16, no. 6, pp. 1114–1122, 1997.
- [203] Q. Yan, J. Yu, S. K. Suram, L. Zhou, A. Shinde, P. F. Newhouse, W. Chen, G. Li, K. A. Persson, J. M. Gregoire, and J. B. Neaton, “Solar fuels photoanode materials discovery by integrating high-throughput theory and experiment,” *Proceedings of the National Academy of Sciences*, vol. 114, no. 12, pp. 3040–3043, 2017.
- [204] V. Tshitoyan, J. Dagdelen, L. Weston, A. Dunn, Z. Rong, O. Kononova, K. A. Persson, G. Ceder, and A. Jain, “Unsupervised word embeddings capture latent knowledge from materials science literature,” *Nature*, vol. 571, pp. 95–98, Jul 2019.
- [205] J. Jumper, R. Evans, A. Pritzel, T. Green, M. Figurnov, O. Ronneberger, K. Tunyasuvunakool, R. Bates, A. Žídek, A. Potapenko, A. Bridgland, C. Meyer, S. A. A. Kohl, A. J. Ballard, A. Cowie, B. Romera-Paredes, S. Nikolov, R. Jain, J. Adler, T. Back, S. Petersen, D. Reiman, E. Clancy, M. Zielinski, M. Steinegger, M. Pacholska, T. Berghammer, S. Bodenstein, D. Silver, O. Vinyals, A. W. Senior, K. Kavukcuoglu, P. Kohli, and D. Hassabis, “Highly accurate protein structure prediction with alphafold,” *Nature*, vol. 596, pp. 583–589, Aug 2021.
- [206] P. Ball, “Behind the screens of alphafold,” Dec 2020.
- [207] C. Friedman, P. Kra, H. Yu, M. Krauthammer, and A. Rzhetsky, “GENIES: a natural-language processing system for the extraction of molecular pathways from journal articles,” *Bioinformatics*, vol. 17, pp. S74–S82, 06 2001.
- [208] H.-M. Müller, E. E. Kenny, and P. W. Sternberg, “Textpresso: An ontology-based information retrieval and extraction system for biological literature,” *PLOS Biology*, vol. 2, p. null, 09 2004.

- [209] S. Eltyeb and N. Salim, “Chemical named entities recognition: a review on approaches and applications,” *Journal of Cheminformatics*, vol. 6, p. 17, Apr 2014.
- [210] E. Kim, K. Huang, A. Saunders, A. McCallum, G. Ceder, and E. Olivetti, “Materials synthesis insights from scientific literature via text extraction and machine learning,” *Chemistry of Materials*, vol. 29, no. 21, pp. 9436–9444, 2017.
- [211] S. Spangler, A. D. Wilkins, B. J. Bachman, M. Nagarajan, T. Dayaram, P. Haas, S. Regenbogen, C. R. Pickering, A. Comer, J. N. Myers, I. Stanoi, L. Kato, A. Lelescu, J. J. Labrie, N. Parikh, A. M. Lisewski, L. Donehower, Y. Chen, and O. Lichtarge, “Automated hypothesis generation based on mining scientific literature,” in *Proceedings of the 20th ACM SIGKDD International Conference on Knowledge Discovery and Data Mining*, KDD ’14, (New York, NY, USA), p. 1877–1886, Association for Computing Machinery, 2014.



## LIST OF PUBLICATIONS

1. Kostko, O., McAfee, T., Ma, J., and Naulleau, P. (2021, February). Characterization of secondary electron blur via determination of electron attenuation length. In Extreme Ultraviolet (EUV) Lithography XII (Vol. 11609, p. 116091V). International Society for Optics and Photonics.
2. Wojtecki, R., Ma, J., Cordova, I., Arellano, N., Lioni, K., Magbitang, T., ... and Naulleau, P. (2021). Additive Lithography–Organic Monolayer Patterning Coupled with an Area-Selective Deposition. *ACS applied materials and interfaces*, 13(7), 9081-9090.
3. Conti, G., Martins, H. P., Cordova, I. A., Ma, J., Wojtecki, R. J., Naulleau, P., and Nemšák, S. (2021). Chemical and structural characterization of EUV photoresists as a function of depth by standing-wave x-ray photoelectron spectroscopy. *Journal of Micro/Nanopatterning, Materials, and Metrology*, 20(3), 034603.
4. Kostko, O., McAfee, T., Ma, J., and Naulleau, P. (2021, February). Characterization of secondary electron blur via determination of electron attenuation length. In Extreme Ultraviolet (EUV) Lithography XII (Vol. 11609, p. 116091V). International Society for Optics and Photonics.
5. Ma, J. H., Wang, H., Prendergast, D. G., Neureuther, A. R., and Naulleau, P. P. (2020). Investigating extreme ultraviolet radiation chemistry with first-principles quantum chemistry calculations. *Journal of Micro/Nanolithography, MEMS, and MOEMS*, 19(3), 034601.
6. Ma, J. H., Wang, H., Prendergast, D., Neureuther, A., and Naulleau, P. (2020, April). Excitation selectivity in model tin-oxo resist: a computational chemistry perspective. In Extreme

Ultraviolet (EUV) Lithography XI (Vol. 11323, p. 113231F). International Society for Optics and Photonics.

7. Conti, G., Martins, H. P., Cordova, I. A., Ma, J., Wojtecki, R. J., Naulleau, P., and Nemsak, S. (2020, November). Sub-nm depth characterization of EUV nanoscale photoresist films by standing-wave photoemission spectroscopy. In *Extreme Ultraviolet Lithography 2020* (Vol. 11517, p. 115170I). International Society for Optics and Photonics.
8. Ma, J. H., Wang, H., Prendergast, D., Neureuther, A., and Naulleau, P. (2019, November). Investigating EUV radiation chemistry with first principle quantum chemistry calculations. In *International Conference on Extreme Ultraviolet Lithography 2019* (Vol. 11147, p. 111470X). International Society for Optics and Photonics.
9. Ma, J., Neureuther, A. R., and Naulleau, P. P. (2019, May). Investigating EUV radiochemistry with condensed phase photoemission. In *Extreme Ultraviolet (EUV) Lithography X* (Vol. 10957, p. 109571Y). International Society for Optics and Photonics.

#### **CONFERENCE PRESENTATIONS WITHOUT PUBLICATIONS**

1. Ma, J. H., Naulleau, P. P., Prendergast, D., and Neureuther, A. (2021, February). Elucidating the radiation chemistry of prototypical tin-oxo resist with first-principles computations. In *Extreme Ultraviolet (EUV) Lithography XII* (Vol. 11609, p. 116091B). International Society for Optics and Photonics.
2. Ma, J. H., Cordova, I. A., Wojtecki, R., Neureuther, A., and Naulleau, P. P. (2020, September). Engineering resist-substrate interface: a quantum chemistry study of self-assembled monolayers. In *Extreme Ultraviolet Lithography 2020* (Vol. 11517, p. 115170H). International Society for Optics and Photonics.